Thesis

Multi-messenger signatures of high energy sources

TCHERNIN, Céline

Abstract

Les rayons cosmiques sont des particules chargées, principalement des protons, dont le spectre énergétique s'étend de quelques GeV à 1e20 eV. Les trajectoires de ces particules étant déviées par les champs magnétiques entre la source et l'observateur, l'information sur la position de la source accélératrice est perdue. Cependant, l'étude de la direction de propagation des particules neutres (neutrinos et rayons gamma) produites lors de l'interaction des rayons cosmiques au sein de la source pourrait amener à l'identification de ces sites d'accélération. Dans ma thèse, je combine les données du détecteur de neutrinos IceCube, avec les donnés de rayons gamma récoltées par le satellite Fermi. J'applique cette méthode "multi-messagers" à différentes sources potentielles de rayons cosmiques: le plan Galactique, les blazars et les amas de galaxies. Dans un autre registre, je m'intéresse aussi à la distribution de matière noire dans les amas de galaxies et j'applique un algorithme qui me permet de reconstruire le profile radial du potentiel gravitationnel de l'amas Abell 1689 à partir du profile [...]

Reference

TCHERNIN, Céline. *Multi-messenger signatures of high energy sources*. Thèse de doctorat : Univ. Genève, 2014, no. Sc. 4728

URN : urn:nbn:ch:unige-432686
DOI : 10.13097/archive-ouverte/unige:43268

UNIVERSITÉ DE GENÈVE **FACULTÉ DES SCIENCES**
Département d'astronomie **Professeur A. Neronov**

Multi-messenger signatures of high energy sources

THÈSE

présentée à la Faculté des sciences de l'Université de Genève
pour obtenir le grade de Docteur ès sciences,
mention astronomie et astrophysique

par

Céline Alexandra TCHERNIN

de

Cologny (GE)

Thèse N° 4728

GENÈVE
Atelier d'impression ReproMail
2014

UNIVERSITÉ
DE GENÈVE
FACULTÉ DES SCIENCES

Doctorat ès sciences
Mention astronomie et astrophysique

Thèse de *Madame Céline TCHERNIN*

intitulée :

"Multi-messenger Signatures of High Energy Sources"

La Faculté des sciences, sur le préavis de Monsieur A. NERONOV, professeur assistant et directeur de thèse (International Science Data Center, Département d'astronomie), Monsieur T. COURVOISIER, professeur ordinaire (Département d'astronomie), Madame T. MONTARULI, professeure ordinaire (Département de physique nucléaire et corpusculaire) et Monsieur M. BARTELMANN, professeur (Institut für Theoretische Astrophysik, Zentrum für Astronomie, Universität Heidelberg, Deutschland), autorise l'impression de la présente thèse, sans exprimer d'opinion sur les propositions qui y sont énoncées.

Genève, le 30 octobre 2014

Thèse - 4728 -

Le Décanat

N.B. - La thèse doit porter la déclaration précédente et remplir les conditions énumérées dans les "Informations relatives aux thèses de doctorat à l'Université de Genève".

CETTE THÈSE A FAIT L'OBJET DES PUBLICATIONS SUIVANTES:
voir Liste des Publications en section 10.

Contents

Chapter 1

Résumé / Summary

Les rayons cosmiques sont des particules chargées, principalement des protons, dont le spectre énergétique s'étend sur plusieurs ordres de grandeur en énergie: de quelques GeV à 10^{20} eV. Dû à la présence de champs magnétiques entre la source et l'observateur, les trajectoires de ces particules sont déviées et l'information sur la position de la source accélératrice est perdue. Plus de 100 ans après leur découverte, l'origine des rayons cosmiques reste encore un mystère.

Il existe néanmoins une méthode alternative pour contraindre l'origine des rayons cosmiques. En effet, la trajectoire des particules neutres n'étant pas affectée par la présence de champs magnétiques, l'analyse de la direction de propagation des particules neutres produites lors de l'interaction des rayons cosmiques avec la matière environnante au sein de la source accélératrice est un moyen prometteur pour identifier les sites d'accélération de rayons cosmiques. Ces particules neutres sont les neutrinos et les rayons γ.

Dans ma thèse, je combine les données de neutrinos collectées par le détecteur de neutrinos IceCube, avec les données de rayons γ récoltées par le satellite Fermi. Dans des conditions optimales, on s'attendrait à ce que la combinaison de ces données nous dévoile les sites d'accélération de rayons cosmiques. Cependant, jusqu'à présent aucune source ponctuelle de neutrinos n'a pu être détectée et seules des limites supérieures sur le flux de neutrinos ont pu être posées (voir par exemple l'analyse de Aartsen et al. 2014c). Dans l'étude que je présente dans cette thèse, en me basant sur les relations connues entre les flux de neutrinos et rayons γ produits lors des interactions de rayons cosmiques, j'utilise les observations faites dans le domaine des rayons γ pour estimer le flux attendu de neutrinos. Connaissant la réponse du détecteur IceCube à un tel flux de neutrinos et sous l'hypothèse que l'émission γ observée est d'origine hadronique, cela me permet d'imposer d'importantes contraintes sur la source considérée. J'applique cette méthode dite "multi-messagers" à différentes sources.

La première source que je considère est le plan Galactique. L'émission γ du plan Galactique a une composante diffuse très lumineuse qui est modélisée comme provenant majoritairement d'interactions hadroniques. Par conséquent, une émission de neutrinos qui accompagne l'émission γ est attendue. En estimant le flux de neutrinos par les observations γ, je cherche à déterminer le temps d'observation nécessaire à la détection de ce flux de neutrinos avec le détecteur IceCube. Le détecteur IceCube étant situé au pôle Sud, il est davantage sensible aux sources situées dans l'hémisphère Nord. Mon résultat montre qu'après 20 ans d'exposition, parmi toutes les sources situées dans l'hémisphère Nord, seule La Région de Cygnus pourrait être éventuellement détectée à un niveau de confiance de 3σ. Dans une analyse complémentaire, afin d'analyser le potentiel de détection des sources situées dans l'hémisphère Sud, le détecteur IceCube a été placé virtuellement au pôle Nord. Cet exercice mène à un résultat très intéressant: avec un tel détecteur, plusieurs sources pourraient être détectées à un niveau de 5σ, après seulement 5 années d'observation. Parallèlement, la collaboration d'IceCube a développé une méthode d'analyse de données dont la sensibilité de détection pour les sources situées dans l'hémisphère Sud est améliorée par rapport à la méthode sur laquelle je me base dans mon analyse. En utilisant cette méthode, la collaboration

IceCube a détecté plusieurs neutrinos d'énergie supérieure à 30 TeV, pour qui l'hypothèse d'une origine purement atmosphérique est rejetée à un niveau de 4σ. Parmi ces neutrinos, certains pourraient provenir du plan Galactique. Cette découverte a été le sujet d'une analyse complémentaire dont vous pourrez trouver les détails dans ma thèse.

Me projetant à plus grande échelle, j'étudie également de potentielles sources extra-galactiques de rayons cosmiques. La première classe de sources extra-galactiques que je considère est celle des blazars. Les blazars sont des noyaux actifs de galaxies (aussi nommé AGN, pour l'acronyme de Active Galactic Nuclei), dont le jet de particules relativistes est orienté dans la direction de l'observateur. De fait, l'émission est intensifiée par les effets relativistes et les blazars font partie des sources γ les plus lumineuses. Cependant, l'origine de cette émission γ n'est pas établie (elle peut être hadronique ou leptonique). Dans l'hypothèse où cette émission γ est produite lors de l'interaction de rayons cosmiques dans le jet, on s'attend à ce qu'un flux de neutrinos, lui aussi intensifié par les effets relativistes, l'accompagne. Par conséquent, parmi tous les AGN, la classe des blazars devrait produire le flux de neutrinos le plus facilement détectable par IceCube. Dans cette analyse, je combine les données des rayons γ et des neutrinos collectées pour les blazars les plus brillants détectés par le satellite Fermi pendant ses deux premières années de mission. Je considère les données correspondantes à une période d'un an, pour laquelle les informations nécessaires à mon analyse étaient publiques et pendant laquelle le détecteur d'IceCube ne faisait que la moitié de sa taille finale. Avec seulement un an de données et un demi-IceCube, cette combinaison neutrino-γ me permet déjà de mettre d'importantes contraintes sur le spectre des protons accélérés dans ces blazars et par conséquent, sur les modèles hadroniques d'émission de blazars. Par conséquent, avec la configuration finale du détecteur IceCube et un plus long temps d'exposition, de plus fortes contraintes sur les modèles hadroniques d'émission de blazars sont attendues. Ce travail met, de fait, en lumière le potentiel de l'approche multi-messager pour contraindre les modèles hadroniques d'émission de blazars.

La dernière classe de sources potentielles de rayons cosmiques que je considère est celle des amas de galaxies. Les rayons cosmiques pourraient y être accélérés lors de l'accrétion de matière dans l'amas, pendant la fusion de deux amas ou par l'activité de l'AGN central, si présent. En se basant sur l'exemple de notre Galaxie et sur certains modèles de diffusion de particules chargées dans le champs magnétique, les rayons cosmiques devraient rester confinés dans l'amas de galaxies qui les a accélérés pendant un temps supérieur à l'âge de l'Univers. Cependant, bien que les évidences de la présence d'électrons relativistes dans les amas sont nombreuses, celles suggérant la présence des protons relativistes manquent encore. Les amas de galaxies sont de brillantes sources de rayons X, une émission qui révèle la présence d'un gaz chaud dans le milieu intergalactique. Par conséquent, des interactions entre les rayons cosmiques confinés dans l'amas et ce gaz sont attendues et devraient mener à des émissions diffuses de rayons γ et de neutrinos. Ainsi, la détection de l'émission diffuse de rayons γ (et de neutrinos) serait une preuve de la présence de rayons cosmiques dans ces systèmes. Cependant, de telles émissions n'ont pas encore été détectées et seules des limites supérieures ont été posées pour chacun des flux de ces deux messagers. Dans le travail que je présente dans ma thèse, j'utilise la limite supérieure sur le flux de rayons γ, obtenue pour un échantillon d'amas de galaxies très brillant en rayons X, pour y contraindre la quantité de rayons cosmiques. J'obtiens une limite supérieure sur le rapport entre la pression des rayons cosmiques et celle du gaz qui est au niveau des prédictions des simulations numériques. Ce résultat observationnel pose d'importantes contraintes sur les modèles d'accélération de rayons cosmiques dans les amas.

De plus, les amas de galaxies sont les systèmes gravitationnellement liés les plus grands de

l'Univers. Pour cette raison, l'étude de l'évolution de ces systèmes peut mener à une meilleure compréhension de la formation des structures. Cependant, pour ce faire, une bonne compréhension des amas de galaxies est nécessaire. Cet objectif pourrait être atteint grâce à la combinaison des différentes observations effectuées sur les amas de galaxies. Un tel projet est actuellement mené par l'équipe de recherche dirigée par le Prof. Bartelmann. J'ai eu la chance de prendre part à ce projet et d'utiliser un algorithme qui combine des observations obtenues par lentilles gravitationnelles et rayonnement X dans le but de reconstruire le potentiel gravitationnel projeté d'amas de galaxies. Dans ma thèse, j'applique cet algorithme à l'amas de galaxies Abell 1689 et montre qu'une grande quantité d'information devient accessible par la comparaison du potentiel gravitationnel reconstruit à partir des observations des rayons X, avec celui obtenu à partir des observations de lentilles gravitationnelles.

Cosmic rays are charged particles (mainly protons) that are observed over a large range of energy, from a few GeV up to 10^{20} eV. Due to the presence of a magnetic fields between us and the source, the arrival direction of these particles is isotropized and the information about their origin is lost. Nevertheless, information on their origin can still be obtained through the study of the ultra high energy cosmic rays (UHECRs, of energy larger than $\sim 10^{19}$ eV), for which the trajectories are not too affected by the presence of the magnetic field (which induces a deflection of about few degrees for a proton). Therefore the composition and arrival direction measurements of UHECRs should help the identification of the cosmic ray sources. Unfortunately the statistics of these measurements is too scarce to be conclusive.

An alternative way to constrain the cosmic ray origin is to use the fact that cosmic rays interact at the sources and produce secondary particles. Because their trajectories are not deflected by the magnetic fields, the study of the neutral secondary particles (γ-rays and neutrinos) should carry information on the acceleration sites. This is the guideline I follow in my thesis.

In my thesis, I combine the neutrino measurements of the recently built IceCube neutrino detector with the γ-ray data collected with the Fermi γ-ray satellite. By performing a full sky survey, ideally the combination of the data of these two instruments should draw regions in the sky where the cosmic rays are accelerated. However, neutrinos are very difficult to detect and only upper-limits on the neutrino flux have been claimed so far in the searches for point-like sources of neutrinos with the IceCube detector (Aartsen et al. 2014c). In the study I present in my thesis, I use the known relations between the γ-ray and neutrino flux produced in hadronic interactions, to estimate the neutrino flux from the observed γ-ray flux. I apply this multi-messenger approach to different sources. Knowing the answer of the IceCube detector to a such neutrino flux, this allows me to set interesting constraints to the considered source.

The Galactic plane is a bright γ-ray source. The diffuse γ-ray emission arising from the Galactic plane is modeled to be mainly produced in hadronic interactions. As a result, the Galactic plane should also be a bright neutrino emitter. In this study, based on γ-ray measurements, I estimate the expected neutrino flux and derive what should be the exposure time necessary to the detection of this expected neutrino emission by the IceCube detector. Due to the location of the IceCube detector at the Southern Pole, the detector is more sensitive to the detection of muon neutrinos coming from the Northern Hemisphere. Among all the northern sources, the analysis shows that the neutrino data need to be collected over at least 20 years to claim a neutrino detection at a 3σ level of the Cygnus region only. Interestingly, in a complementary analysis sensitive to the Southern Hemisphere, with a hypothetic IceCube like detector located at the Northern Pole, I find with my co-authors that many sources located in the Southern Hemisphere could be detected at a 5σ

level within an exposure time of only 5 years. This prediction may be consistent with the recent detection of high energy neutrinos with the IceCube detector (IceCube Collaboration 2013; Aartsen et al. 2014b). However given the poor angular resolution of this data analysis, any conclusion about the exact arrival direction of this signal is difficult and many other models for the origin of these high energy neutrinos are possible.

Moving to larger scales, I study some potentially extragalactic cosmic ray acceleration sites. The first extragalactic sources that I considere are blazars. Blazars are active galactic nuclei (AGN) whose jet is oriented in the direction of the observer. As a result, the γ-ray emission is beamed and blazars belong to the brightest and more energetic detected γ-ray sources. The hadronic origin of this γ-ray emission is however not established. Nevertheless, some models suggest that this γ-ray emission is produced in the interaction of cosmic rays in the source. Adopting this scenario, a neutrino flux should also be present and beamed in the direction of the observer. Therefore the neutrino flux from blazars is expected to be easier to detect than the neutrino flux emitted by other non-beamed AGN. In this study, I use the configuration of the IceCube detector which represents the half of its final size (IC-40), because by the time of this analysis, the information required for my analysis were only published for this configuration of the detector. To be consistent with the combined neutrino and γ-ray observations collected during one year (which corresponds to the IC-40 period), strong limits on the possible values of the primary proton spectrum parameters have been set for a sample of selected bright blazars. The constraints presented in my thesis have been obtained for only one year of data and half of the IceCube detector, with the full IceCube and a longer exposure time, stronger constraints are expected to be imposed on hadronic models for blazar activity. This study is therefore a proof of concept of the constraining power of the multi-messenger approach for the hadronic models for blazar activity.

Moving to even larger scale, I consider galaxy clusters. Cosmic rays are expected to be accelerated in galaxy clusters during matter accretion at the cluster outskirts, during cluster mergers and also by the central AGN, when it is present. Based on the model of our Galaxy and on diffusion models of charged particles in the magnetic fields, cosmic rays are expected to be confined in galaxy clusters over a time larger than the Hubble time for the lowest energy protons. Even though the presence of relativistic electrons is attested in galaxy clusters, evidence of the presence of cosmic rays in these systems is still lacking. Galaxy clusters are bright X-ray sources. As this X-ray emission reveals the presence of a gas between the galaxies in the clusters, the interaction of the confined cosmic rays with the gas is expected to produce a diffuse γ-ray and neutrino emission. As a result, the detection of a diffuse γ-ray (and neutrino) emission from galaxy clusters would be an evidence of the presence of cosmic rays in these systems. However, up to now, these emissions have not been detected and only upper-limits have been set on the diffuse γ-ray and neutrino flux. In this work, I use the γ-ray flux upper-limit obtained by a stacked analysis of a sample of bright X-ray clusters to set an upper-limit on the cosmic ray to thermal pressure ratio in this sample. The obtained upper-limit is at the level of the lower-limit expected in numerical simulations. Therefore, this study probes the models of particle acceleration in galaxy clusters.

Furthermore, galaxy clusters are the largest gravitationally bound systems in the Universe and therefore, their study can lead to a better understanding of the large-scale structure formation. However, to this end their internal constitution needs to be thoroughly understood. Such a goal may be achieved when different observations of galaxy clusters are combined in a joint analysis. This project is under study in the team led by Prof. Bartelmann. In the work I present in my thesis, I use an algorithm which joins the lensing and X-ray observations to reconstruct the projected gravitational potential of galaxy clusters. I apply this algorithm to the known galaxy cluster Abell

1689 and show that a substantial amount of information on the physical state of the intracluster gas becomes available by the direct comparison of the lensing potential with the projected potential reconstructed from X-ray emission.

Chapter 2

Acknowledgments/Remerciements

Je souhaiterais remercier de nombreuses personnes.

Tout d'abord, ma famille pour m'avoir apporté tout son soutien, pour avoir toujours été présente et pour m'avoir toujours poussé vers l'avant. Je souhaiterais aussi remercier Ido, qui m'a soutenu sans relâche pendant cette période et sans qui ces dernières années de thèse auraient été bien différentes. Je tiens aussi à remercier Eluned, pour les corrections d'anglais.

I would also like to thank my colleagues for all our interesting scientific discussions. I think of Andrea, Enrico, Dominique, Stéphane and many others. I really appreciated these interactions, each of them brought me a new perspective on the subject and the happiness of sharing this passion.

En particulier, je souhaiterais remercier Dominique, Stéphane Paltani et Prof. Stéphane Udry pour l'opportunité qu'ils m'offrent de travailler avec eux encore quelques mois après mon doctorat.

J'aimerais remercier Prof. Courvoisier pour son écoute et son soutien tout au long de mon cursus. Je souhaiterais le remercier pour sa confiance et pour m'avoir permis et aidé à organiser mon ERASMUS à Heidelberg lorsque j'étais encore étudiante, ce séjour m'a beaucoup apporté personnellement et professionnellement.

I would like to thank Prof. Montaruli, to have trusted me, to have opened the door to our collaboration and for always giving me time and answers to my questions. This collaboration led us to work on astro-particles, using the newly born neutrino astronomy science and this, in a very trustful and friendly atmosphere.

I would like thank Prof. Bartelmann for our interesting discussions, for always answering my questions and for letting me be part of the interesting project he is leading. I would like to thank him for his patience, for his trust, for his quick reactions to my wish to enter his working group and for giving in my hands all the tools I would need to start working in cosmology.

Et bien-entendu, je souhaiterais remercier Andrii, pour m'avoir donné la chance de travailler dans son groupe et pour tout ce que j'ai pu apprendre sous sa direction.

Merci aussi à toutes les personnes qui ont participé à faire de l'institut un endroit convivial et agréable, je pense en particulier à Rozenn, Martine, Franca et bien d'autres!! Merci à tous!

Chapter 3

High energy messengers

3.1 Cosmic rays

3.1.1 Detection mechanisms and observations

Cosmic rays are charged particles (mainly protons) that were discovered by Victor Hess more than a century ago, in 1912. Since their discovery, two complementary detection methods have been developed.

At energy lower than $\sim 10^{14}$ eV, the flux of particles is high enough to allow direct detections above the atmosphere. This can be done by *space satellite* experiments, like for instance PAMELA (Casolino et al. 2003) and AMS-1/2 (Alcaraz 1999; Aguilar et al. 2013) and also at lower altitude, by *balloon experiments*, like TIGER (Link et al. 2000), RUNJOB (Zayarnaya 2008), JACEE (Asakimori et al. 1993), ATIC (Guzik 1999), CAPRICE (Barbiellini et al. 1995), BESS (Nozaki et al. 1995) and CREAM (Beatty 1999).

For cosmic rays of higher energy, the decreasing flux with energy becomes too low to allow direct detection. In this case, one uses instead ground detector arrays and the Earth atmosphere as calorimeter. Once a cosmic ray enters the atmosphere, it initiates an extensive air shower (EAS): i.e. a zoo of secondary particles is generated, which consists mainly in pions, neutrinos, electrons, positrons, photons, and muons, as shown in Fig. 3.1. From the detection and study of the secondary particles, information on the primary can be recovered.

At high energy ($> 10^{17}$ eV and 10^{12} eV, respectively), two different signatures left by the secondary particles in the atmosphere are commonly used: the fluorescence light and the Cerenkov light. The fluorescence light is emitted isotropically by the nitrogen atoms in the atmosphere once they de-excite along the path of the charged particles. This light carries information on the primary charged particle direction and allows a calorimetric measurement of its energy: the primary cosmic ray energy is proportional to the number of charged particles in the shower. Fluorescence detectors (FD) are used in the Pierre Auger Observatory (PAO, Gemmeke et al. 2001), Telescope Array (TA, 2008-current, Jui & the Telescope Array Collaboration 2012), and their predecessors HiRes (1997-2006, Sokolsky & HiRes Collaboration 2011a), Fly's Eye (1981-1993, Bird et al. 1995). This technique is sketched Fig. 3.2, right panel, in the case of HiRes, where one can see the roundish fluorescence detector which is made of multi faced sub-detectors and is able to detect the fluorescence light from any direction.

The other expected signature is the Cerenkov light. This light is emitted when a charged particle travels faster than the light in the medium. This radiation is emitted in a cone whose opening angle depends on the density of the air and thus on the height in the atmosphere (with a maximal opening angle of 1.4°). The particles in the cascade stop propagating, while the Cerenkov light continues its travel and overlaps on the ground, as shown in the left panel of Fig. 3.2. For instance, the Yakutsk observatory (Glushkov et al. 1993), the Chicago Air Shower Array-Broad Lateral Non-imaging Cerenkov Array (CASA-BLANCA, Cassidy et al. 1997) and the Tunka-133 experiment (Budnev et al. 2010) detect the atmospheric Cerenkov light using arrays of photomultipliers

tubes (PMT) and measure the lateral photon distribution on the ground.

Fluorescence and Cerenkov detectors can collect light in moonless nights with clear atmospheric conditions only. In both techniques, the total flux of light deposited in the atmosphere is used as an estimator of the primary particle energy. However, the fluorescence technique is dedicated to the detection of cosmic rays of larger energy, because the amount of energy deposited in the atmosphere is proportional to the number of charged secondaries produced, and therefore the diffuse fluorescence emission must be triggered by a primary of high energy to be detected.

If the particles are energetic enough to reach the ground with relativistic energies, they may be detected directly by surface detectors (SD) at the ground. Different kinds of surface detectors can be found. Some SDs are made of water tanks in which the charged particles emit Cerenkov light, like the Haverah Park (Ave 1999) or the PAO experiment (Gemmeke et al. 2001). Other SDs are made of scintillator counters, which detect the scintillation light emitted when the ionizing radiation passes through the scintillator (which is made of a transparent medium, like gas, liquid or plastic). For instance, the Chicago Air Shower Array (CASA, Borione et al. 1993), the Akeno Giant Air Shower Array (AGASA, Chiba et al. 1991), the Tibet AS-Gamma Experiment (Amenomori et al. 2000), KASCADE-Grande (Huangs et al. 2003) and TA (Jui & the Telescope Array Collaboration 2012) are/were using scintillator arrays. Some surface detectors, like ARGO-YBJ (Surdo et al. 2003), are made of resistive plate chambers. In such detectors, the charged particles ionize the gas and the produced ions are collected by a system of cathode-anode and converted into an electronic signal. Then depending on the size of the array, the detector is sensitive to a different energy range. For instance, while the KASCADE-Grande is dedicated to the detection of cosmic rays of energy between 10^{14} eV and $2 \cdot 10^{18}$eV, the TA observatory is sensitive to cosmic rays of energy above 10^{18} eV. Most of these surface array detectors also have special detectors designed for the detection of muons. As we will see latter, the detection of muons helps the identification of the nature of the primary particle.

Hybrid experiments use the detection of particles in the air and at the ground. These two techniques are complementary: while surface detectors allow the measurement the two-dimensional lateral structure of the shower at ground level and the arrival time of particles, the fluorescence detectors measure the longitudinal profile of the shower during its development across the atmosphere (ie the number of charged particles in the shower as a function of the depth in the atmosphere). From this combination, information on the primary cosmic ray composition, direction and energy can be obtained (see e.g., Healy 2008). For instance, the PAO and the TA experiments are hybrid experiments which combine FD with SD techniques. While the TA experiment combines FD with plastic scintillators, the AUGER observatory combines FD with water-tank Cerenkov detector arrays. In the case of the PAO, the fluorescence light and the detection of the charged particles on the ground by water tanks are schematized in Fig. 3.2, left panel. The upcoming LHAASO (the Large High Altitude Air Shower Observatory Zha 2012) is planned to combine all these different techniques: FD, SD (gas scintillators and water tanks) and Cerenkov detectors.

A superposition of measurements of different experiments is presented in Fig. 3.3 (from Berezinsky 2013, where the results of the different experiments are reviewed). As shown, the cosmic ray spectrum measured at Earth extends over 12 orders of magnitude in energy, up to 10^{20}eV.

The cosmic ray spectrum shown in Fig. 3.3 (upper panel) can be roughly described by a power-law with a few spectral changes. These features are enhanced in the lower panel of Fig. 3.3, where the spectrum has been multiplied by $E^{2.7}$. In this representation we can see that the cosmic ray spectrum can be divided in three parts. Each of these parts can be characterized by a different

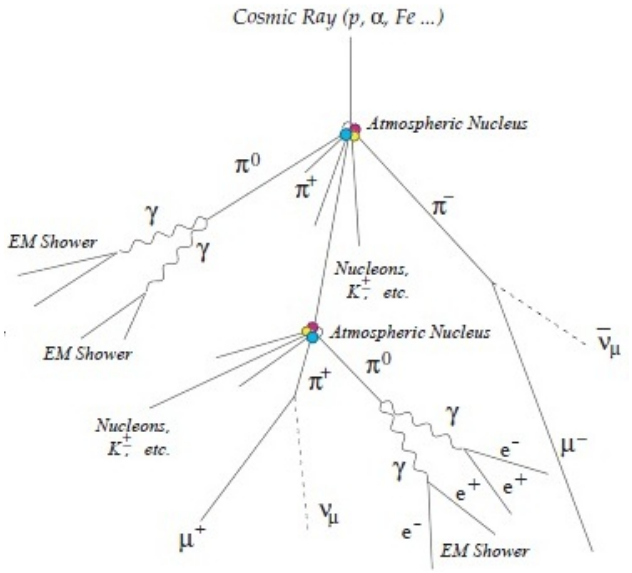

Figure 3.1: Development of the extensive air shower induced by a UHECR entering the atmosphere. Taken from the PAO web page (from http://www.lip.pt/ jespada/Research/PhysPAO.php).

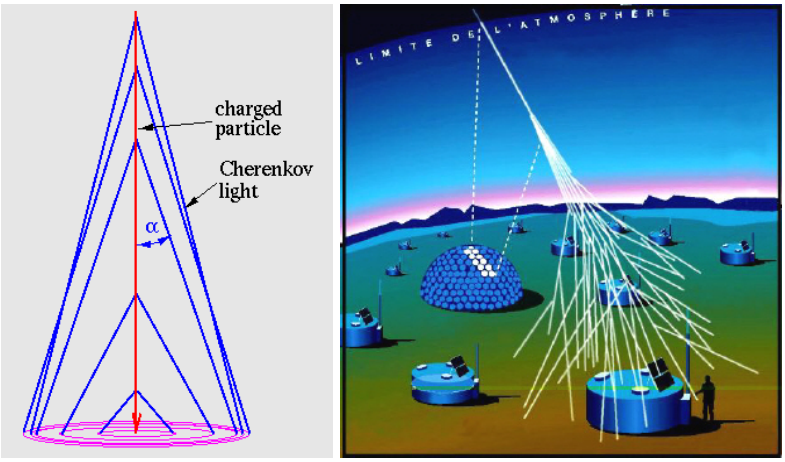

Figure 3.2: On the left panel: Development of the extensive air shower induced by a UHECR entering the atmosphere. Taken from the PAO web page (from http://www.lip.pt/ jespada/Research/PhysPAO.php). Right panel: Sketch of the detection techniques of the signature left by the UHECR in the Earth atmosphere: the fluorescence detector measures the longitudinal profile of the shower and the surface detector measures the lateral structure of the EAS at ground level. Illustration taken from the PAO web page (http://www.mpi-hd.mpg.de/hfm/CosmicRay/ChLight/Cherenkov.html).

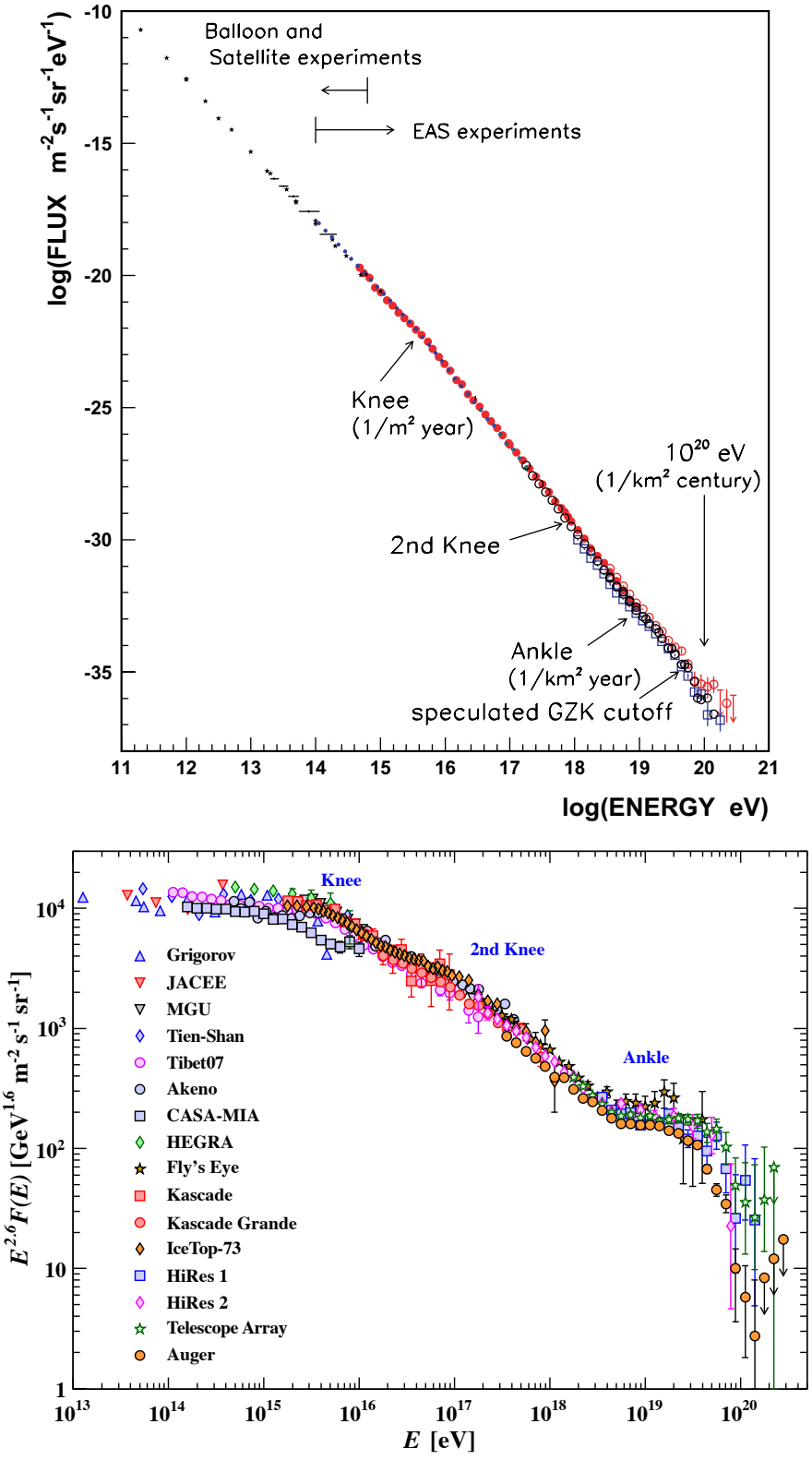

Figure 3.3: Top panel: the all particle cosmic ray flux (see Nagano 2009, for the references of the experiments). Bottom panel: all particle spectra zoomed in the high energy range and multiplied by $E^{2.6}$ to enhance the three spectral features: at $\sim 5 \cdot 10^{15}$ eV, at $\sim 10^{17}$ eV and at $\sim 10^{19}$ eV. Taken from Beringer et al. (2012).

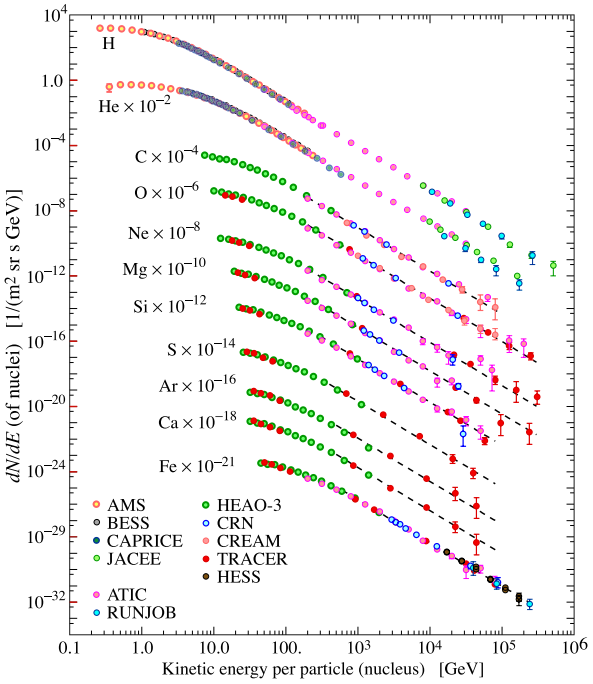

Figure 3.4: Flux of the low energy (up to 100 TeV) cosmic rays. Taken from Beringer et al. (2012).

power-law index: below $\sim 3-5\cdot 10^{15}$eV, the spectral index is equal to ~ 2.7, then between $\sim 3-5\cdot 10^{15}$eV and $\sim 4\cdot 10^{18}$eV the distribution steepens to a ~ 3.1 spectrum, and finally, at energies above $\sim 4\cdot 10^{18}$eV the distribution becomes flatter again with a spectral index of ~ 2.6. The first transition is called the *knee* and the second transition is called the *ankle*. A less pronounced feature, called the *second knee*, can be seen at energy of $\sim 4-7\cdot 10^{17}$eV. At this energy, the spectrum steepens slightly and the spectral index increases from ~3.1 to ~3.3. Also, we can notice a flux suppression at energy above 10^{20} eV. This latter has been observed by many experiments like HiRes (Abbasi et al. 2008), TA (Tsunesada & for the Telescope Array Collaboration 2011) and PAO (Abraham et al. 2008), but not by the AGASA experiment (Takeda et al. 1998), certainly due to lack of statistics or calibration issues. Each of these observed features may potentially provide information about the cosmic ray acceleration sites and mechanisms.

Complementary to this information, enlightenment on the cosmic ray origin can also arise from the study of the arrival direction and of the composition of the cosmic ray flux. Here below I will review some recent results.

It has been observed that the composition of the cosmic ray flux changes with energy. At energies below $\sim 10^{14}$ *eV* the composition is dominated by the light elements, with about 70% of free protons (Beringer et al. 2012), as shown in Fig. 3.4 (taken from Beringer et al. 2012). At higher energy, in the region between the two *knees*, measurements favor a model in which the spectra of nuclei of increasing charge Ze are superposed on each other. This model is based on the assumption that an element of charge Ze can not be accelerated above the maximal energy $E_{max}(Z) = R_{source}BZe$. The superposition of these intrinsic cut-off energy spectra reproduces well the cosmic ray spectrum obtained by the KASCADE-Grande experiment (Apel et al. 2011). However, an updated analysis of the KASKADE-Grande results (Apel et al. 2013), as well as the

CREAM (Seo 2012) and the IceTop (a water tank array on the surface of the IceCube experiment, Aartsen et al. 2013b) data may require the presence of several populations of Galactic sources with cut-off energy to explain the observed spectral features at energy below the *second knee* (see e.g., Gaisser 2012, for a model). Then at the largest energies, the composition is debated: the results from HiRes (Abbasi et al. 2010b) and TA (Jui & the Telescope Array Collaboration 2012) differ from the ones of PAO (Abraham et al. 2010). Indeed, while the results of TA and HiRes can be described by a purely proton composition, the ones of PAO show a transition towards heavier nuclei at $\sim 10^{19}$eV. Those results are shown in Fig. 3.5, where the composition is represented by the quantity X_{max}, which represents the average depth in the atmosphere (in g/cm^2) at which a shower initiated by a nucleus of energy E contains the largest number of particles. This quantity depends on two parameters: the mass and the energy of the primary particle. This energy dependence can be understood qualitatively by the fact that secondary particles produced by a high energy primary particle will have larger energy and will be able to propagate up to a larger distance in the atmosphere. Regarding the sensitivity of X_{max} to the composition of the cosmic rays, this quantity is expected to decrease as the mass of the primary increases. This is due to the fact that when a heavy nuclei of mass A enters the atmosphere, in first approximation it fragments into A hydrogen nuclei of energy E_Z/A. Each of the A protons will induce a cascade of the same X_{max} in the atmosphere. These expectations are shown in Fig. 3.5 (top left and bottom panels), where we can see that the predicted values for X_{max} are smaller for the heaviest nuclei and increase with the energy. The width of the X_{max} distribution (RMS(X_{max})) is also sensitive to the composition of cosmic rays. Indeed, the RMS(X_{max}) is expected to be smaller for the heaviest nuclei with respect to the lightest ones. This is related to the fragmentation mechanism introduced earlier: the larger A is, the larger is the statistics of the X_{max} and the smallest is the RMS(X_{max}). In Fig. 3.5 are shown the predictions for different hadronic models. As we can attest, the divergence between these different predictions may cause uncertainties on the composition measurements. Such different predictions arise from the uncertainties of the inelastic proton-proton interaction cross-section at such energies and from the fact that the proton-air interaction cross-section is derived from the inelastic proton-proton interaction cross-section using scaling factors (see e.g., Norbury & Townsend 2007). Indeed, these are derived from cross-sections tested in man-made accelerators which have been extrapolated to higher energies based on different descriptions of the hadronic interactions (see Rebel & Sima 2012, for a complete discussion about this issue). For instance, in the case of the PAO measurement (top panels), the hadronic models QGS-JET (Kalmykov et al. 1997), SYBILL (Ahn et al. 2009) and EPOS (Werner et al. 2006) are used to analyse the data.

The information contained in the cosmic ray composition measurements is related to the level of anisotropy of the cosmic ray arrival direction. Indeed, we expect that lighter cosmic rays should be less deflected than heavier cosmic rays by the presence of the magnetic field between the source and us. As a result, the trajectory of an iron nucleus would be deflected 26 times more than a proton of the same energy.

In 2007 the PAO collaboration claimed the detection of a correlation between the location of nearby AGNs (at a distance smaller than 100 Mpc) from the catalog of Veron-Cetty and Veron (Véron-Cetty & Véron 2006) and the arrival direction of cosmic rays of energy larger than 55 EeV (Pierre Auger Collaboration et al. 2007). This correlation with AGNs weakened with improved statistics (Pierre Auger Collaboration et al. 2011). In the same data analysis, the PAO collaboration discovered a clump of high energy events in the direction of the radio loud AGN Cen A (see Fig. 3.6 from Pierre Auger Collaboration et al. 2011). Sensitive to the Northern hemisphere, the TA experiment did not confirm the PAO anisotropy pattern but measured a clump of events within

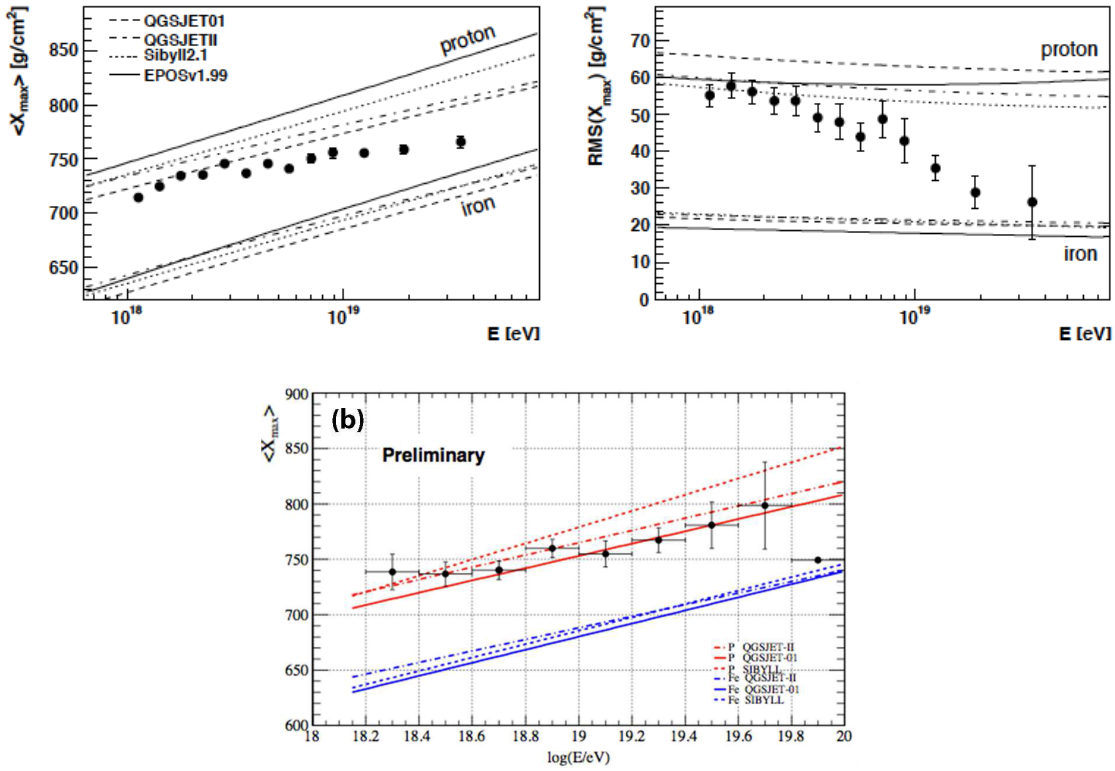

Figure 3.5: Top panel: PAO composition measurements using two different techniques described in the text (Abraham et al. 2010); Bottom panel: TA composition measurements (Jui & the Telescope Array Collaboration 2012). Predictions from different hadronic interaction models are shown.

20° radius circle centered at the location R.A.=146.7, Dec=43.2 at a 3.4σ significance level (The Telescope Array Collaboration et al. 2014). Interestingly, Fang et al. (2014) found that from the twenty-eight high energy neutrinos detected with the HESE technique (High Energy Starting Events, see Sect. 3.2.3) by the IceCube collaboration (IceCube Collaboration 2013), two have a direction consistent with this cosmic rays excess. In Fang et al. (2014), the authors also suggested that the AGN Mrk 421 could be the source of the detected UHECRs and neutrinos. However, both the region delimited by the 20° radius circle of the UHECR clustering detected by TA and the fact that the reconstruction of the direction of these detected neutrino events has a quite large angular resolution (as we will see later in this chapter, see Sect. 3.2.3), imply that a significant number of different models and sources can be allowed by these data.

The deflection of UHECR protons in the Galaxy is expected to reach a few degrees, depending on the magnetic field configuration (see e.g., Osborne et al. 1973). If UHECRs are protons, the low level of anisotropy reported in these measurements may indicate that such particles are accelerated in extragalactic sources. This argument however would not hold for heavy nuclei, because their Larmor radii are Z times smaller than the ones of the protons and any initial clustering in arrival direction is diluted by the Galactic magnetic field (see e.g., Kachelrieß et al. 2007). However, the lack of statistics of UHECRs (see the flux suppression in the cosmic ray spectrum, Fig. 3.3) is also expected to contribute to this low level of anisotropy. Anyway, other explanations tend to indicate that UHECRs have an extragalactic origin. For instance, the Larmor radius of a 10^{18} eV proton is about 3 kpc in the Galactic μG magnetic field. As the height of the Galactic plane is about 400 pc and its radius, about 30 kpc, a 10^{18} eV proton is not expected to stay confined in the Galaxy long enough to be accelerated to such high energies (we will see more about it in the next chapter). Therefore, these broad band energy measurements suggest that the observed cosmic ray spectrum is a superposition of cosmic rays having a Galactic and an extragalactic origin.

As a first guess, we would expect that the transition occurs at one of the observed features of the spectrum, like at the *knee*, the *second knee* or the *ankle* (see Fig. 3.3).

One of the proposed models to explain the transition between the Galactic and extragalactic origin is called the *dip*-scenario referring to the valley which is formed between the *ankle* and the *second knee*. This model is valid only if the protons dominate the composition at energies between the *ankle* and the *second knee*, which is consistent with the observations performed with TA (Jui & the Telescope Array Collaboration 2012), HiRes (Sokolsky & HiRes Collaboration 2011b) and PAO (Abraham et al. 2010). In this model, the protons interact with the Cosmic Microwave Background radiation (CMB) during their propagation towards the Earth and create the *dip* feature via the e^+e^-pair production ($p + \gamma_{CMB} \rightarrow p + e^+e^-$) process.

If the protons dominate the cosmic ray spectrum at higher energies, this model can also explain the high energy flux suppression with the photo-meson production process ($p + \gamma_{CMB} \rightarrow p + \pi$). This proton composition is consistent with the TA (Jui & the Telescope Array Collaboration 2012) and HiRes (Sokolsky & HiRes Collaboration 2011b), but not with the PAO (Abraham et al. 2010) measurements. In this case, the flux suppression is known under the name of the Greisen-Zatsepin-Kuzmin cutoff (GZK cutoff, Greisen 1966; Zatsepin & Kuz'min 1966). Due to this interaction, the UHECR protons must come from a distance smaller than about 100 Mpc to be observed (the so-called GZK horizon, which corresponds to the mean distance that protons of energy larger than 10^{19}eV can travel before being absorbed by the CMB photons).

At the opposite, if we assume that UHECRs are heavy nuclei like Iron (which would be consistent with the PAO observations), the high energy flux suppression might be explained as a *nuclei-photodisintegration* cut-off. In this case, the nuclei interact with the low energy radiation

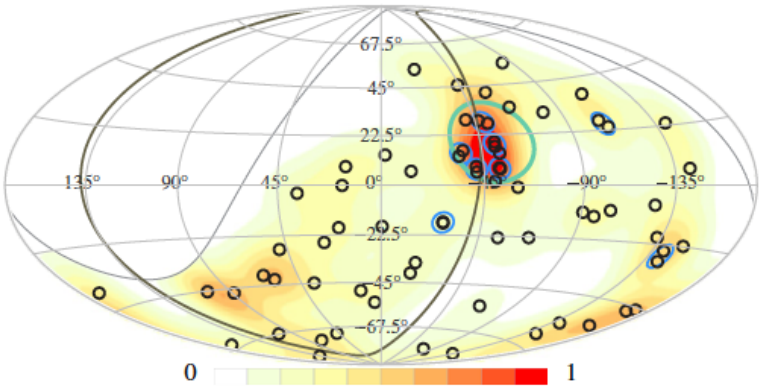

Figure 3.6: Map of anisotropy in Galactic coordinates measured with the Pierre Auger Observatory. The arrival directions of events with E> $5.5 \cdot 10^{19}$eV are shown by black circles. A cluster of events has been identified in the direction of the center of the radio galaxy Cen A. Taken from (Yüksel et al. 2012).

during their propagation and produce lighter nuclei. However, a precise model of the produced lighter particles is difficult, because it depends on the different involved nuclei.

Alternatively, the composition change observed by the PAO observatory may suggest a mixed composition model, in which the observed features are produced by the superposition of spectra of cosmic rays of different charge and maximal energy ($E_{max}(Z)$, see e.g. Aloisio et al. 2011). In such a model, the transition from Galactic to extragalactic sources occurs at the *second knee*, while the *ankle* is a feature produced by the extragalactic proton to extragalactic iron transition. The transition from Galactic to extragalactic sources could also happen at the *ankle* but in this case several populations of Galactic cosmic rays would be required (see e.g., Gaisser 2012).

As a matter of fact, due to the low statistics of UHECRs, it is not obvious if cosmic ray data alone could provide enough information to allow the identification of the accelerating sources. An alternative method would be to study the secondary particles produced by the interaction of the cosmic rays with their surrounding medium. Indeed, as some of these secondaries are not charged and point toward their source location, they are of particular interest for the cosmic ray sources identification.

3.1.2 Cosmic ray interactions with the surrounding medium: γ-ray and neutrino production

In this section, we will consider the interactions of the high energy protons with the low energy radiation in photo-meson production ($p\gamma$ interactions) and with low energy protons via inelastic proton-proton interactions (pp interactions). In both cases, a hadronic shower is produced (π, γ, ν, e^-, ... as shown in Fig. 3.1). For instance, an application of the pp interactions was given in the previous section, where the protons interact with the Earth's atmosphere and produce secondary particles shower (EAS). Depending on the energy of the primary particles and on the density of the target particles, any of these interaction channels could dominate.

For the two interaction channels (pp and $p\gamma$), well defined relations exist to link the spectra of the secondary particles (neutrino and γ-ray flux) between each-other and with the primary particle. To describe the secondary particle spectra produced in pp interaction, I use the parametrizations of Kelner et al. (2006), which is based on the SIBYLL code (Fletcher et al. 1994) and partly on the QGSJET code (Kalmykov et al. 1997). Whereas to describe the secondary particle spectra produced in photo-meson production, I use the parametrizations described in Kelner & Aharonian (2008), which are based on the Monte-Carlo code SOPHIA (Mucke et al. 1999). These parametrizations are based on phenomenological models incorporated with experimental data obtained at particle accelerators and extrapolated to higher energies.

The inelastic proton proton interaction

In *inelastic proton-proton interaction* (pp), a proton interacts with another proton and produces secondary particles. The interaction can be described by

$$p + p \rightarrow p + N + k_i\pi^i, \tag{3.1}$$

where k_i is the pion multiplicity for the charges $i = \{+, -, 0\}$ and N the outgoing nucleon (proton or neutron).

The minimal required energy of the primary proton to produce a single pion can be estimated using the Mandelstam variables. Let us call $P^\mu_{p1} = (E_{p1}/c, \vec{p}_{p1})$ and $P^\mu_{p2} = (E_{p2}/c, \vec{p}_{p2})$, the four-vectors of the particles before the collision, where $E_{p1,2}, \vec{p}_{p1,2}$ are the energy and momentum of the proton 1 and 2 and c the speed of light. With P^μ_{final} the four-vector after the collision, in the frame where the final particles are at rest, we have $P^\mu_{final} = ((2m_p + m_\pi)c, \vec{0})$, m_p and m_π being the masses of the proton and of the pion respectively. Being a conserved quantity, $s = (P^\mu_{p1} + P^\mu_{p1})^2$ must be equal to $(P^\mu_{final})^2$; i.e., $2m_p^2c^2 + 2/c^2(E_{p1}E_{p2} - \beta_1\beta_2 cos(\theta)) = (2m_pc + m_\pi c)^2$, β_i being the velocity of the particle i. Solving this equation for E_{p1} in the reference frame where the proton P^μ_{p2} is at rest, this leads to (with $E_{th} \equiv E_{p1}$):

$$E_{th} = m_pc^2 + m_\pi c^2(2 + m_\pi/(2m_p)) \sim 1.22 \text{ GeV}. \tag{3.2}$$

This minimal energy corresponds to the energy of the proton at rest plus a small correction.

Once produced, the pions decay to produce electrons, neutrinos and photons, as follows. The γ-ray photons are produced by the neutral pion decay:

$$\pi^0 \rightarrow \gamma + \gamma, \tag{3.3}$$

and the electrons and neutrinos are produced by the decay of the charged pion and the subsequent muon decay,

$$\pi^{+/-} \rightarrow \mu^{+/-} + \nu_\mu(\bar{\nu_\mu}) \qquad \mu^{+/-} \rightarrow e^{+/-} + \bar{\nu_\mu}(\nu_\mu) + \nu_e(\bar{\nu_e}). \tag{3.4}$$

As a result, at the source, we expect the ratio between the flux of neutrinos of different flavors to be $F_{\nu_e} : F_{\nu_\mu} : F_{\nu_\tau}$ =1:2:0. This flavor ratio is only expected in the case of pion decay. However, at higher energies, the contribution of heavier mesons, like kaons and charmed mesons, is expected to modify the neutrino flavor ratio produced at the source (Sarcevic 2009). Nevertheless, in my study I use the parametrization of (Kelner et al. 2006; Kelner & Aharonian 2008), where only the pion, kaon and eta meson decay are taken into account. Due to flavor oscillations, this ratio is expected to be 1:1:1 at Earth (Learned & Pakvasa 1995).

I will now derive the secondary particle spectra using the parametrization of (Kelner et al. 2006). In pp interactions, the charged pions π^- and π^+ are produced in about the same amount. Therefore, the distribution of both the particles and their anti-particles are expressed in Kelner et al. (2006) in term of the particle only. Consequently, I will refer to the flux of neutrinos of all flavors as: $F_\nu = F_{\nu_e} + F_{\nu_\mu}$, where F_{ν_μ} is the sum of the contribution of the muon neutrino coming from the charged pion decay and from the muon decay (Eq. [3.4]). I will also consider separately the flux coming from the neutral pion decay, F_{γ,π^0}, from the flux of the electromagnetic cascade, $F_{\gamma,em}$, where the contribution of the electrons is added to the one of the neutral pion decay. In $F_{\gamma,em}$ the electrons are assumed to lose all their kinetic energy in radiation: $F_{\gamma,em} = F_{\gamma,\pi^0} + F_e$.

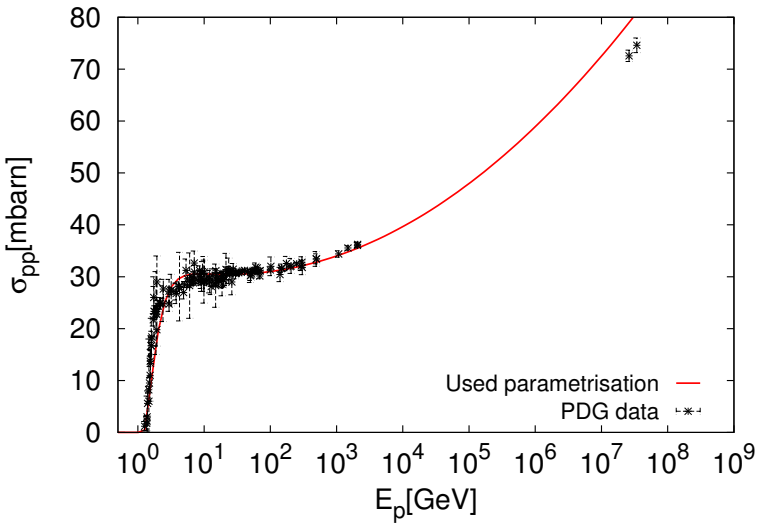

Figure 3.7: Comparison of the parametrization of the total inelastic cross-section of pp interaction from Kelner et al. (2006) to the cross-section data from (Beringer et al. 2012), as function of the proton total energy.

The total cross-section of the pion production is shown in Fig.3.7, with the parametrization of Kelner et al. (2006)

$\sigma_{pp} = (34.3 + 1.88\ln(E_p/1\text{ TeV}) + 0.25[\ln(E_p/1\text{ TeV})]^2)[1 - (E_{th}/E_p)^3]^2$mb. As shown, this parametrization is slightly higher than the cross section data from (Beringer et al. 2012) at the highest energies reached by handmade collider ($E_p \sim 10^{17}$ eV). I will come back to the effect of this over-estimation in Sect. 6.6.

The cross-section grows sharply at the threshold energy of the pion production, forms a plateau at energies between $E_p \in [5 \cdot 10^9; 10^{12}]$ eV and grows logarithmically at larger energy. As we will see, this behavior leaves an imprint in the spectra of the produced particles.

Following Kelner et al. (2006), the differential secondary particle flux can be obtained as

$$F_{sec} = \int_{E_{sec}}^{\infty} n_H \cdot \frac{dN_p}{dE_p} \cdot \sigma_{pp}(E_p) \cdot v_p(E_p) f_{sec}(E_{sec}, E_p) \frac{dE_p}{E_p}, \tag{3.5}$$

where we can recognize the collision rate per unite volume: $\sigma_{pp} v_p(E_p) n_P n_H$, with $\sigma_{pp}(E_p)$ the cross-section of the interaction, n_H and n_p the density of the target particles and of the primary proton respectively and $v_p(E_p)$ the velocity of the primary proton. In the above equation, n_p is substituted by the differential primary proton spectrum in a unite volume dN_p/dE_p and is multiplied with the factor $f_{sec}(E_{sec}, E_p)$, given in Kelner et al. (2006), which represents the number of secondary particles of energy E_{sec} produced in one pp interaction by a proton of energy E_p. To count for all the secondary particles produced in these interactions, the collision rate is then integrated over the energy of the primary protons. These parametrizations are given for protons of total energy in the range $10^{11} - 10^{17}$ eV. In order to produce the secondary particle spectra at lower energy, I use what the authors referred to as the δ-function approximation, in which each proton of the distribution produces only one pion in average during the interaction.

I will now describe the main features of the secondary particle spectra, derived using Eq [3.5] with the parametrization of Kelner et al. (2006), in the case where the primary proton spectrum is described by a cut-off power-law distribution

$$dN_p/dE_p = N_{0,p} \left(\frac{E}{E_0} \right)^{-\gamma_p} \exp(-E/E_{max,p}), \tag{3.6}$$

where $N_{0,p}$ is the normalization at E_0, γ_p the spectral index and $E_{max,p}$ the cut-off energy.

The resulting secondary particle spectra, obtained for a proton distribution of spectral index $\gamma_p = 2$, are illustrated in Fig. 3.8. The low energy end of the secondary particle spectra follows the behavior of the cross-section. At higher energy, as we can notice, the secondary particle spectra are slightly harder than the one of the primary protons due to the logarithmic increase of the cross-section. The high energy end of the secondary particle distribution can be described by a cut-off power-law with the two parameters $E_{max,sec} \approx 10\% E_{max,p}$ and $\gamma_{sec} \approx \gamma_p - 0.1$. It implies that if we manage to observe the secondary particle spectra, we can obtain information on the primary proton spectrum (slope and cut-off energy).

We can also see that the γ-ray flux (pink curve) is of the same order of magnitude as the flux of all flavor neutrinos (green curve), therefore, the energy injected in both channels is comparable in first approximation. This is a very important feature which I would like to test now more quantitatively.

To start with, I would like to estimate the relation between the muon neutrino flux, F_{ν_μ} and the γ-ray flux produced by neutral pion decay, $F_{\gamma_{\pi^0}}$, in the case of single pion production. I chose this simple case because it can be more easily compared to the output of the parametrization. In a second time, I would use the full parametrization to compare the all flavor neutrino flux with the electromagnetic cascade, where the electron kinetic energy is also taken into account. Those fluxes are of particular interest, as they are accessible from Earth.

Roughly, the secondary particle spectrum can be related to the primary spectrum as:

$$F_i \approx \frac{N_i}{N_p} \frac{dN_p}{dE_p} \frac{E_p}{E_i}, \tag{3.7}$$

where i represents the secondary particle: neutrinos or γ-rays. It means that for each interaction, the secondary particle distribution can be derived from (the number of particle i produced per proton) $\times$ (the distribution of primary protons per energy bin) $\times$ (the energy transferred to each particle i from its parent proton in one collision).

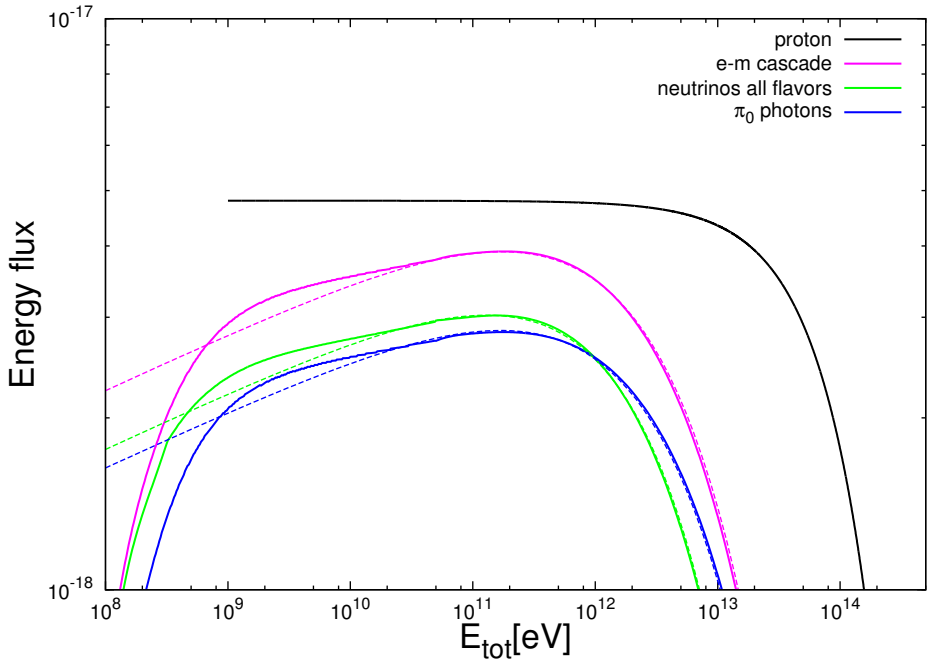

Figure 3.8: Spectra of secondary particles obtained using the parametrization of Kelner et al. (2006) for a primary proton spectrum described by Eq. [3.6] with $\gamma_p = 2$, $E_{max,p} = 10^{14}$eV and an arbitrary normalization. The flux of the electromagnetic cascade is defined as $F_{\gamma,em} = F_{\gamma,\pi^0} + F_e$ and the flux of neutrino all flavors is defined by $F_\nu = F_{\nu_e} + F_{\nu_\mu}$. The spectra of the parent proton is re-scaled to help the comparison with the secondary particle spectra. The high energy end of the secondary particle spectra can be well described by a cut-off power-law distribution (see text for details).

In first approximation, we assume that the pions of all charges are produced in equal quantities, i.e., $\pi^+ : \pi^0 : \pi^- = 1 : 1 : 1$ and that the inelasticity is ~ 0.2. It implies that for each pp interaction, a pion of any charge can be produced with a probability (1/3) and carries the energy $E_{max,\pi} = 0.2 \times E_{max,p}$.

Assuming that each π^0 meson decays in 2 photons of energy $E_{\gamma,\pi^0} = E_\pi/2$, the energy fraction transferred by the proton to one photon is $E_p/E_{\gamma,\pi^0} = (E_p/E_\pi)(E_\pi/E_{\gamma,\pi^0}) = (1/0.2)(2) = 10$ and the differential number of photons produced for each proton is $N_{\gamma,\pi^0}/N_p = (1/3) \cdot 2 = 2/3$. The same can be done for the muon neutrino, knowing that for each interaction one has the probability (1/3) to produce a charged pion (π^+ and π^-) and that each charged pion will decay into 2 muon neutrinos, each of them carrying 1/4 of the pion energy, we obtain $E_p/E_\nu = (1/0.2)(4) = 20$ and $N_{\nu,\mu}/N_p = (1/3)(2)(2) = 4/3$.

For a primary proton spectrum with a power law distribution of spectral index γ_p: $dN_p/dE_p \propto (E_p)^{-\gamma_p}$, the power injected into the electromagnetic cascade by the neutral pion and muon neutrino decay can be estimated as

$$E^2_{\gamma,\pi^0} F_{\gamma,\pi^0} \approx E^2_{\gamma,\pi^0}(2/3) \cdot (10 \cdot E_{\gamma,\pi^0})^{-\gamma_p} \cdot 10 = (20/3) \cdot 10^{-\gamma_p} \cdot E^{-(\gamma_p-2)}_{\gamma,\pi^0}. \tag{3.8}$$

While the expected power injected in muon neutrinos is

$$E^2_{\nu,\mu} F_{\nu,\mu} \approx E^2_{\nu,\mu}(4/3) \cdot (20 \cdot E_\nu)^{-\gamma_p} \cdot 20 = (80/3) \cdot 20^{-\gamma_p} \cdot E^{-(\gamma_p-2)}_{\nu}. \tag{3.9}$$

It implies that the relation between the secondary particles is a function of the spectral index of the primary proton spectrum. As we can deduce from the two last equations, $E^2_{\nu,\mu} F_{\nu,\mu} \sim E^2_{\gamma,\pi^0} F_{\gamma,\pi^0}$ for γ_p=2 and differs by a factor 2 at most for $\gamma_p \in [1 : 3]$. From this simple estimate, we can conclude that the muon neutrino flux is roughly comparable to the neutral pion decay γ-ray flux. In the parametrizations of Kelner et al. (2006), the γ-ray spectrum is obtained by summing the contribution of the π^0 and η-meson decays, such that the power injected in both messengers is slightly different from the one derived above, even though, they are still quite comparable. For instance, in the case of γ_p=2, one obtains $(E^2_{\gamma,\pi^0} F_{\gamma,\pi^0})/(E^2_{\nu,\mu} F_{\nu,\mu}) \sim 1.41$ and this ratio lies between 1 and 2 for $\gamma_p \in [1;\ 3]$.

Now that the output of the parametrization has been cross-checked in the simplest case, we can consider the relation between the neutrinos of all flavors and the electromagnetic cascade. For these secondaries, we obtain comparable results, ie $(E^2_{\gamma,em} F_{\gamma,em})/(E^2_\nu F_\nu) \in [1;\ 1.6]$ for $\gamma_p \in [1;\ 3]$. This relation is very important because it implies that the injected electromagnetic power can be used as an estimate of the injected neutrino power.

To sum up: if we are able to observe the secondary particle spectra, we can have information on the shape of the primary proton spectrum by using the relations: $E_{max,sec} \approx 10\% E_{max,p}$ and $\gamma_{sec} \approx \gamma_p - 0.1$. However, if the spectra of the secondaries is not observable, as it would be the case if an electromagnetic cascade develops and reprocesses the injected flux to lower energy, the spectral information (slope and cut-off energy) of the injected particle spectra cannot be recovered from the γ-ray observations. Nevertheless, we can still use that the bolometric electromagnetic flux ($F_{\gamma,em}$) and the neutrino flux (F_ν) have a comparable injected power to set constraints on the expected neutrino flux and of the primary proton spectrum.

I will now derive similar relations for the $p\gamma$ interactions.

The photo-meson production

In *photo-meson production* ($p\gamma$), high energy protons interact with low energy photons to produce pions. This pion production process can be symbolized as

$$p + \gamma \rightarrow N + k_i \pi^i, \tag{3.10}$$

where k_i is the multiplicity of the pion of charge $i = \{+, -, 0\}$ and N the nucleon (proton or neutron). As in the case of pp interactions, the same final particles, neutrinos, electrons and photons, are produced by pion decays (Eq. [3.3] - [3.4]).

One can compute the energy threshold for the single pion production with $P_p^\mu = (E_p/c, \vec{p}_p)$ and $P_\gamma^\mu = (\epsilon_{ph}/c, \vec{p}_\gamma)$, respectively the four-vector of the proton and of the photon before the collision and P_{final}^μ the four-vector after the collision. By conservation of the square of the total momentum, we have: $(P_p^\mu + P_\gamma^\mu)^2 = (P_{final}^\mu)^2$. In the rest frame of the final particles, it leads to $m_p^2 c + 2E_p \epsilon_{ph}/c^2(1 - \beta cos(\theta)) = (m_p c + m_\pi c)^2$, θ being the angle between the direction of the proton and photon before the collision. The minimal energy of a proton of velocity β to produce a pion by interacting with photon of energy ϵ_{ph} is

$$E_{th} = \frac{2 m_p m_\pi c^4 + m_\pi^2 c^4}{2\epsilon_{ph}(1 - \beta cos(\theta))}. \tag{3.11}$$

In the case of head-on collision ($cos(\theta) = -1$) with a relativistic proton ($\beta \rightarrow 1$), the minimal energy for the production of a single pion ($n = 1$) is

$$E_{th} \simeq 7 \times 10^{16} \left[\frac{\epsilon_{ph}}{1\ \text{eV}}\right]^{-1}. \tag{3.12}$$

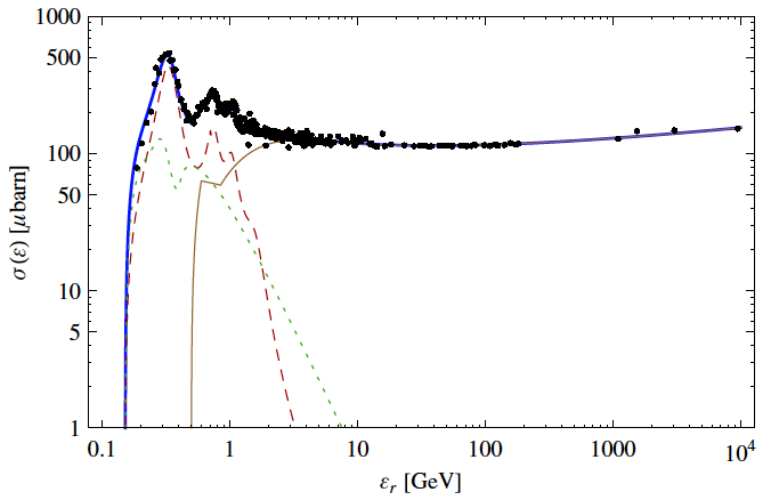

Figure 3.9: Cross-section for $p\gamma$ interaction as function of the target photon energy in the rest frame of the proton. Key: the baryon resonances is shown in dashed red, the direct channel in dotted green and the multi-pion production, in brown. Taken from (Hümmer et al. 2010).

The cross-section of the $p\gamma$ interactions is shown in Fig. 3.9 as function of the energy of the photon in the rest frame of the proton (taken from Mucke et al. 1999). As we can see, there is a

sharp increase at the energy of $\epsilon_{ph} = c^2(2m_p m_\pi + m_\pi^2)/2m_p \approx$ 145 MeV, this increase corresponds to the direct pion production, while the first peak, at $\sim$ 0.2 GeV, is known as the Δ-resonance and has important implications on the secondary particle spectra, as we will see.

The secondary particle spectra can be derived in a similar way as in the case of pp interactions (Eq. 3.5), except that this time the target particles have a non uniform distribution in energy. It implies that an additional integration needs to be performed on the photon target energy distribution. This procedure can be sketched as

$$F_{sec} = \int_{E_p}\int_{\epsilon_{ph}} \frac{dN_p}{dE_p}\frac{dN_{ph}}{d\epsilon_{ph}} \cdot \sigma_{p\gamma}(E_p) \cdot v_p(E_p) f_{sec}(E_{sec}, E_p)\frac{1}{E_p} dE_p d\epsilon_{ph}, \tag{3.13}$$

where dN_p/dE_p and $dN_{ph}/d\epsilon_{ph}$ are the proton and target photon differential spectra per unit of volume, $f_{sec}(E_{sec}, E_p)$ the particle parametrization given by (Kelner & Aharonian 2008) and $\sigma_{p\gamma}(E_p)$ the cross-section (Fig. 3.9).

In photo-meson production there is an "asymmetry" between the production of π^+ and π^-, such that the amount of produced particles is different to the one of their antiparticles. Indeed, in the so-called Δ-resonance approximation, only one pion is produced and we expect that (see e.g., Hümmer et al. 2010)

$$p + \gamma \rightarrow \Delta^+ \rightarrow n + \pi^+ \ \ (1/3) \ \ \text{and} \ \ p + \gamma \rightarrow \Delta^+ \rightarrow p + \pi^0 \ \ (2/3). \tag{3.14}$$

Where the factor in parentheses represents the probability of this decay channel. This probability "asymmetry" is a consequence of isospin and charge conservation, which require that the produced Δ meson, of total isospin of 3/2, has a positive electromagnetic charge. From the four possible Δ mesons which belong to the same isospin multiplet, charge conservation implies that only Δ^+ can be produced. A table of the different allowed decay of the Δ mesons is shown in Table 3.10, where the decay branching ratios are given by the Clebsch-Gordan coefficients. As shown, Δ^+ has a probability of 1/3 to decay in $n + \pi^+$ and a probability of 2/3, to decay in $p + \pi^0$, as indicated in Eq. [3.14].

	$p\pi^+$	$p\pi^0$	$p\pi^-$	$n\pi^+$	$n\pi^0$	$n\pi^-$
Δ^{++}	1					
Δ^+		2/3		1/3		
Δ^0			1/3		2/3	
Δ^-						1

Figure 3.10: Table of the branching ratio within the isospin multiplet of the Δ meson. Taken from (Romeyer 2003).

As a result, the expected pion ratio is $\pi^+ : \pi^0 : \pi^- = 1 : 2 : 0$ and no electrons and electron anti-neutrino are expected. On the opposite, during the multi-pion production, the pions are produced with all charges. Therefore, we need a different parametrization for each produced particle and

anti-particle ($F_{\pi^0,\gamma}$, F_{e^+}, F_{e^-}, F_{ν_e}, $F_{\bar{\nu_e}}$, F_{ν_μ} and $F_{\bar{\nu_\mu}}$). As a result, the total neutrino flux is given by: $F_\nu = F_{\nu_e} + F_{\bar{\nu_e}} + F_{\bar{\nu_\mu}} + F_{\nu_\mu}$, while the flux of the electromagnetic cascade, $F_{em,\gamma}$, is obtained as the sum of the flux injected in the electrons, positrons, and photon produced by neutral pion decay, $F_{\pi^0,\gamma}$: $F_{em,\gamma} = F_{e^-} + F_{e^+} + F_{\pi^0,\gamma}$.

The secondary particle spectra produced in both cases of single pion production and of multi-pion production are represented in Fig. 3.11. In these figures, the single pion production is obtained using a proton energy cutoff close to the energy threshold of the single pion production, i.e. $E_{max,p} \approx E_{th}$, where E_{th} is described by Eq. [3.12]. If $E_{max,p} = 10^{19}$ eV, such a relation can be obtained for a low energy target photon field described by a black body radiation of temperature $T = 10^2$K; while the multi-pion regime ($E_{max,p} \gg E_{th}$) can be obtained with $T = 10^4$K. To help the reading of the plots, the energy thresholds are shown as vertical lines for the two regimes. As we can see, in the multiple pion production case, even though the secondary spectra seem to follow the behavior of the parent protons spectra in a narrow energy bin around the pion production threshold energy, the overall distribution of the secondary particles produced in the single and multiple pion regimes are quite similar and they are all hard and peaked at the energy threshold of the pion production, independently of the primary proton spectral index (from γ_p =1 to 3). Therefore, the information of the primary proton spectrum (slope and cut-off energy) is not accessible by the observations of the secondary particle spectra. This is different to the case of the pp interactions (see Fig. 3.8) and this is due to the presence of the resonance in the cross-section for $p\gamma$ interaction. As a result, the only available information is the power injected by the source.

Therefore, it is important to know how to relate the power injected in neutrinos of all flavors and in the electromagnetic cascade. As in the previous subsection, I will consider first the simplest case, the Δ-resonance, to relate the muon neutrinos and the γ-ray spectra from neutral pion decay.

The spectrum of the produced γ-rays and neutrinos can be estimated as shown in Eq. [3.7]. The main difference to the computation performed above for the pp interaction, is that in the Δ-resonance approximation, instead of having the same probability to produce all pions, we expect a ratio $\pi^+ : \pi^0 : \pi^- = 1 : 2 : 0$. It implies that the number of π^0 decay photon for each proton is $N_{\gamma,\pi^0}/N_p = (2/3) \cdot 2 = 4/3$ while the number of muon neutrinos is $N_{\nu_\mu}/N_p = (1/3) \cdot 2 = 2/3$.

In the Δ-resonance approximation, the inelasticity is ~ 0.2, so that the energy transferred to each secondary particle is $E_p/E_{\gamma,\pi^0} = 10$, for a π^0 decay photon and $E_p/E_\nu = 20$, for a neutrino. It implies that for a primary proton spectrum with a power law distribution of spectral index γ_p: $dN_p/dE_p \propto (E_p)^{-\gamma_p}$, the energy stored in the π^0 decay photon can be estimated as

$$E^2_{\gamma,\pi^0} F_{\gamma,\pi^0} \approx (4/3) \cdot (10 \cdot E_{\gamma,\pi^0})^{-\gamma_p} \cdot 10 = (40/3) \cdot 10^{-\gamma_p} \cdot E^{-(\gamma_p-2)}_{\gamma,\pi^0}, \tag{3.15}$$

and in the muon neutrino spectrum

$$E^2_{\nu,\mu} F_{\nu,\mu} \approx (2/3) \cdot (20 \cdot E_\nu)^{-\gamma_p} \cdot 20 = (40/3) \cdot 20^{-\gamma_p} \cdot E^{-(\gamma_p-2)}_{\nu}. \tag{3.16}$$

As a result, we obtain $(E^2_{\gamma,\pi^0} F_{\gamma,\pi^0})/(E^2_{\nu,\mu} F_{\nu,\mu}) \sim 4$ in the Δ-resonance approximation for $\gamma_p = 2$ and $(E^2_{\gamma,\pi^0} F_{\gamma,\pi^0})/(E^2_{\nu,\mu} F_{\nu,\mu}) \in [2;\ 8]$ for $\gamma_p \in [1;\ 3]$. Using the parametrization with the full cross-section (Fig. 3.9), the ratio $(E^2_{\gamma,\pi^0} F_{\gamma,\pi^0})/(E^2_{\nu,\mu} F_{\nu,\mu})$ for $\gamma_p = 2$ is closer to 3 than to 4: for spectral indices between 1 and 3, this ratio lies between 3.4 and 2.8. This difference could be explained by the contribution of the K and η meson decays to the γ-ray and neutrino flux, which are taken into account in the parametrization but not in the above computation.

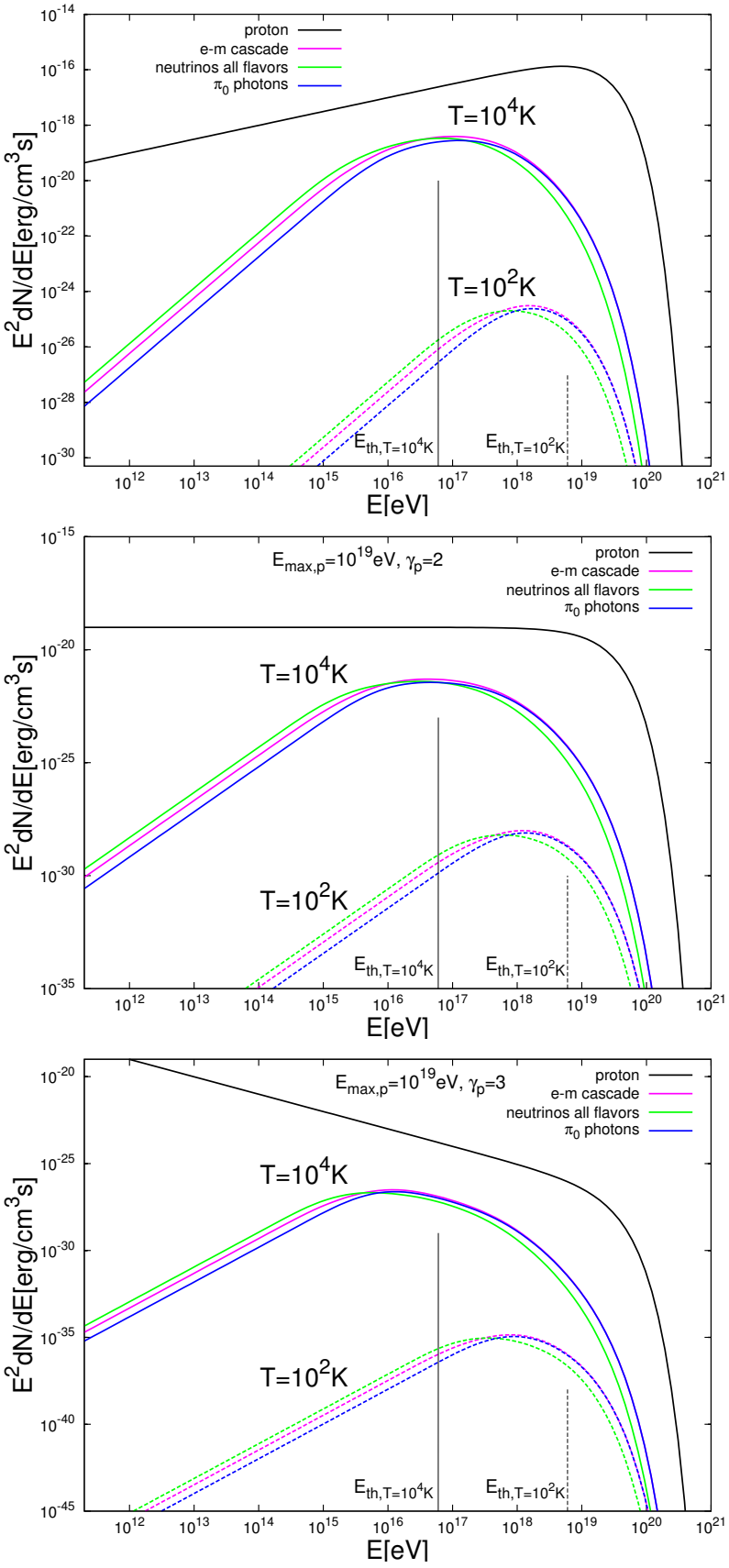

Figure 3.11: Energy distribution of secondary particle spectra in the case of $p\gamma$ interaction of high energy protons which interact with two different target particles (distributed with a Planck function): $T = 10^2$K and $T = 10^4$K. The spectra for $F_{em,\gamma}$, F_ν and $F_{\pi^0,\gamma}$ are shown with solid lines for $T = 10^4$K and with dashed lines for $T = 10^2$K. The energy threshold for each target energy distribution is shown as vertical line. The proton distribution is described by the Eq. [3.13] with $E_{max,p} = 10^{19}$ eV and different values of the spectral index, top: $\gamma_p = 1.5$, middle: $\gamma_p = 2$; bottom: $\gamma_p = 3$.

Finally, if we consider the relations between the power injected in the total neutrino spectra and in the electromagnetic cascade, we find an energy ratio close to 1 (see also Mucke et al. 1999). Indeed, the ratio $(E_\nu^2 F_\nu)/(E_{\gamma,em}^2 F_{\gamma,em})$ lies between 1.4 and 1.3 for proton spectral indices between 1 and 3. This is an important result, as it shows that the power injected in the γ-ray flux can be used as an estimate of the power injected in the total neutrino flux.

In the following sections, I will introduce these secondary particles.

3.2 Neutrinos

Neutrinos have a low mass, no electric charge and interact only through weak forces. The cross-section of neutrinos with nucleons is shown in Fig. 3.2.1. As we can attest, the probability of interaction of neutrinos with the matter is very small (for comparison, the Thomson cross-section is 9 order of magnitude larger at a particle energy of 10^5 GeV). Thanks to their small interaction cross-section, they can travel over very large distances without loosing energy. Therefore, their detection could teach us about the spectrum of the accelerated proton at the source. Furthermore being electrically neutral particles, they are not affected by the magnetic field and point toward their source. As a result, neutrinos are interesting in many aspects. Nevertheless, this low probability of interaction makes their detection a challenge.

3.2.1 Production mechanisms of neutrinos

In the Standard Model of particle physics, neutrinos are produced in weak interactions only: in the radioactive decay of unstable particles (as we saw above) or in nuclear interactions.

Neutrinos can be produced in astrophysical sources, by nuclear fusion in the sun or in supernova explosions. The maximal energy of neutrinos produced by these mechanisms is of order of a few MeV.

In this study, we are interested in the neutrinos produced in cosmic ray interactions. These neutrinos are very energetic and are expected to reach an energy of few % of the highest cosmic ray energy observed (see Fig. 3.8 and Fig. 3.11). One can distinguish two kinds of neutrinos: one is produced by the cosmic ray interactions with the Earth's atmosphere and is called *atmospheric* neutrino, while the second one, produced directly in the accelerating source, is called *astrophysical* neutrino. One usually aims at detecting the *astrophysical* neutrinos against the *atmospheric* neutrinos, which constitute an important background contribution to the neutrino source detection.

3.2.2 Detection principle of very high energy neutrinos

Neutrinos of very high energy are detected indirectly by the secondary particles they produced in the detector. A neutrino can interact with a nucleon N through two channels: the charged (CC) and neutral current (NC). In both cases, a shower of hadrons is created at the neutrino interaction vertex by the production and decay of unstable mesons, with the subsequent production of muons, neutrinos, electrons and photons (see Sect. 3.1.2).

- In a CC channel, a charged lepton is produced. The interaction can be expressed as $\nu_l + N \rightarrow l + X$, where X represents the hadronic shower and l any kind of leptons: electron, muon, or tau. The same processes but involving an anti-neutrino will then produce the corresponding anti-particle. The kind of lepton produced depends on the flavor of the interacting neutrino.

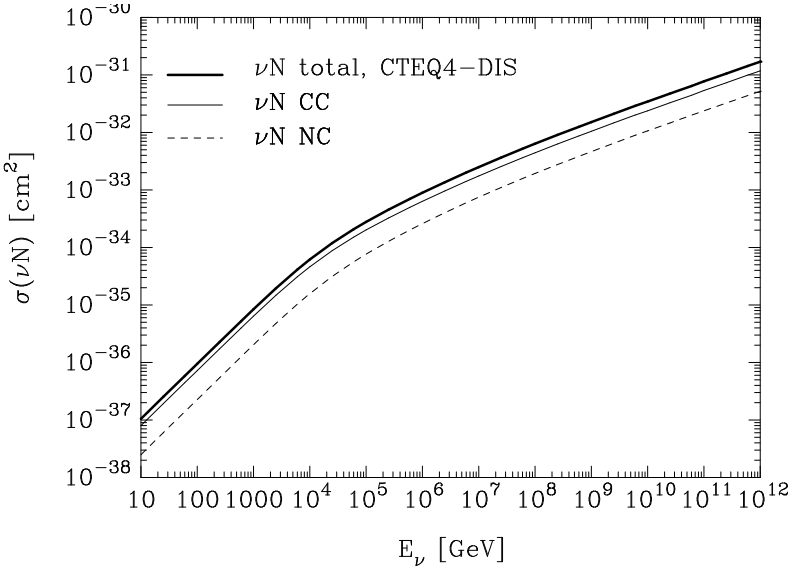

Figure 3.12: Neutrino cross-section with nuclei in charged (interaction with exchange of a charged boson $W^{+/-}$) and neutral current (interaction with exchange of the Z^0 boson). Taken from (Gandhi 2001).

If this charged particle is relativistic, it can emit Cerenkov light in the detector (see 3.2.2). Then, depending on the light pattern left in the detector, information on the incoming neutrino can be inferred, like its direction and flavor. In the case where the hadronic shower at the interaction vertex and the Cerenkov light left by the secondary particle are both detected, a calorimetric measurement of the neutrino energy becomes possible (assuming that the secondary looses all its energy in the detector).

- In a NC channel: $\nu_l + N \rightarrow \nu_l + X$, only the hadronic shower is detected while the neutrino escapes with an unknown fraction of the incident neutrino energy. As a result, the energy deposited in the detector is only a lower limit to the initial neutrino energy.

Both *CC* and *NC* channels can be used to infer information on the parent neutrinos. While the hadronic shower leaves an almost spherical light pattern in the detector at the interaction vertex, the signature left by the charged lepton in the detector depends on its flavor. I will now introduce the characteristics of the Cerenkov light emitted by the electron, muon and tau leptons produced in the *CC* interaction channel.

Cerenkov light

When a charged particle travels faster than the speed of light in a dielectric medium, this particle radiates Cerenkov photons. Let us assume that the relativistic particle has a velocity (in units of speed of light) β and crosses the distance $d = \beta ct$ during the time t, then, if during this time the light only traverses the distance $l = tc/n$, the condition that the particle traverse a larger distance than the light ($d > l$) can be expressed in term of a condition over the velocity of the charged particle: $\beta > 1/n$, where n the refractive index of the medium.

As a result, a charged particle of mass m needs a kinetic energy larger than

$$E_k = mc^2 \left(\frac{1}{\sqrt{1 - (\frac{1}{n})^2}} - 1 \right), \tag{3.17}$$

to emit Cerenkov light. Here we used the fact that the total energy of the particle is equal to $E = \Gamma mc^2$ where the Lorentz factor of the particle, $\Gamma = 1/\sqrt{1-\beta^2}$, is computed for the threshold velocity $\beta = 1/n$. The Cerenkov photons are optical photons and are emitted in a cone of opening angle defined by $cos(\theta) = 1/\beta n$ around the direction of propagation of the particle. The refraction index in ice and water is approximately $n \approx 1.33$, so that the opening angle is ~41°around the direction of propagation of the relativistic particle ($\beta \to 1$) in both medium.

- **Cerenkov light of relativistic electrons:**
  The Cerenkov energy threshold of the electrons is $E_k \approx 0.26$ MeV (Eq [3.17]). This energy threshold is below the critical energy[1] of the electron in the ice/water $E_{crit} = 78.60$ MeV (Rädel & Wiebusch 2013). Below this critical energy, electrons start to scatter in the medium. Therefore the final pattern of the Cerenkov light emitted by electrons has a broad angular distribution.

  Electrons lose energy rapidly and the typical length of a shower is less than 10 meters for a TeV electron (Rädel & Wiebusch 2013). Depending on the instrumentation of the detector, a ~ 10 meter scale cannot be resolved and the electromagnetic cascade cannot be distinguished from the hadronic shower initiated at the interaction vertex. This is shown in Fig. 3.13, panel (a), in the case of the km^3 IceCube detector. In this case, all the energy of the electron is radiated and the total energy deposited in the detector is approximatively equal to the energy of the incident electron neutrino (IceCube Collaboration et al. 2013b). However, as it is in general not possible to distinguish the light pattern left by an electron neutrino from the hadronic shower produced in *NC* channels, the energy deposited in the detector is only a lower limit to the energy of the incident neutrino.

- **Cerenkov light of relativistic muons:**
  Muons of energy larger than $E_k \approx 55$ MeV (Eq [3.17]) emit Cerenkov photons. The life time of the muon in the rest frame is of the order of $2.2 \cdot 10^{-6}$ s, with a mass of about 106 MeV, the distance travelled by a GeV muon is ~ 6 km, which is large enough to cross the largest built neutrino detectors, the km^3 IceCube detector (see Sect. 3.2.3). The Cerenkov radiation is emitted in a cone along their direction of propagation. As illustrated in Fig. 3.13, panel (b), the light pattern left in the detector has a track shape, such that a muon can be detected even if the interaction vertex is not contained in the detector.

  Using the direction of the track left in the detector, the direction of the incoming muon can be reconstructed. However, the energy of the muon neutrino is poorly constrained.

- **Cerenkov light of relativistic taus**
  The energy threshold of a tau lepton with respect to the Cerenkov emission is $E_k \approx 924$ MeV (Eq [3.17]). The tau lepton is an unstable particle of 1.78 GeV and $2.9 \cdot 10^{-13}$ s life time. As a

[1]The critical energy is the energy at which the electrons losses per ionization dominate over the losses per bremsstrahlung .

2 PeV tau can travel ∼100 m before decaying, the light pattern deposited in a detector where the optical modules are distant of ∼100 m is expected to be resolvable. In the case where both the interaction vertex and the tau decay occur in the detector, the light pattern deposited in the detector is composed by two showers separated by a track. This light pattern is called the *tau double bang* and is illustrated in Fig. 3.13, panel (c). For tau leptons of lower energy, the distance travelled by the tau in the detector is not resolvable and the two showers can not be distinguished from one another, such that the light pattern deposited in the detector is similar to the one left by the electron, except if the tau decays in a muon and in this case, the event cannot be distinguished from the muon track produced by muon neutrino in *CC* interaction (Chiarusi & Spurio 2010).

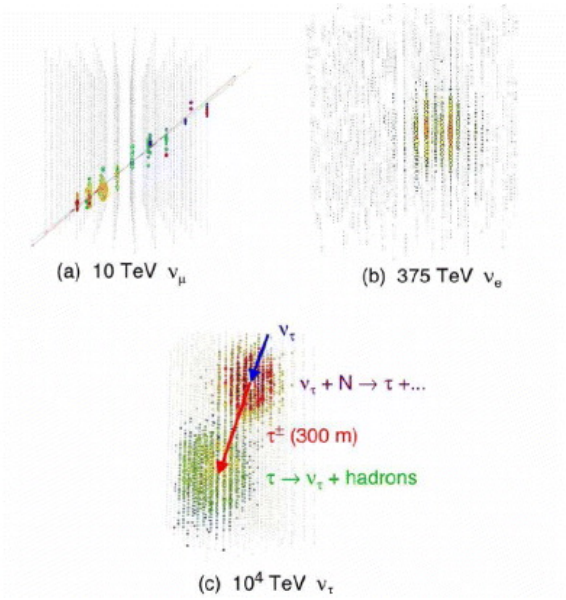

Figure 3.13: Simulation of the signatures of the three neutrino flavors in the IceCube detector. (a) the muon track from muon neutrino interacting outside the detector volume. (b) electron neutrino interacting in the detector volume. (c) 'double-bang' signature of a tau neutrino. Taken from (Hoffman 2009).

Main high energy neutrino detectors

As the Cerenkov radiation is emitted in the optical band, high energy neutrino detectors must be built in media with suitable optical properties to be able to detect the optical photons. A medium with the best optical properties should have the largest absorption and scattering lengths, such that the Cerenkov photons are not absorbed nor scattered. The absorption/scattering length of a medium corresponds to the distance a beam of light will travel to see its intensity I_0 decrease by e: $I(x) = I_0 e^{-x/L_i}$, where L_i corresponds to any of the mentioned lengths and x is the distance trav-

elled. These optical properties of a medium are called *transparent* and *homogeneous*, respectively. Transparent media are for instance water and ice.

The scattering length for the ice is smaller than for the water. As the scattering changes the direction of propagation and the distribution of arrival time, the angular resolution in the ice is poorer with respect to the one in the water. Scattering in the ice is mainly due to air bubbles and dust particles, whose quantity varies with the depth. A technique to solve this issue is to measure the absorption and scattering length in the ice at different depths, using a source of light as calibration (Chiarusi & Spurio 2010). On the other hand, the absorption length is larger in the ice than in the water, which implies that the total amount of light arriving at the detector is smaller for the water. Also, in water the detector is not solid and suffers from the current (an algorithm to determine the location of each detector with a high precision is required, see for instance (Adrián-Martínez et al. 2012)). Furthermore, bioluminescence light can be produced in sea water by bacteria and animals and the distribution of bioluminescence organisms varies with location and depth. This additional optical background is irreducible and absent in the ice.

The main high energy neutrino detectors have been built in water and ice, in natural sites in order not to be limited by the size.The Deep Underwater Muon and Neutrino Detection (DUMAND) Project is the first neutrino detector located in the deep sea (Stenger 1978). This project started already in 1975 and has been used as basis for other neutrino detectors located in natural sites. For instance, The Neutrino Extended Submarine Telescope with Oceanographic Research (NESTOR, Resvanis & Nestor Collaboration 2006), which is in early stage; ANTARES (ANTARES Collaboration 1999), which is completed since 2008 and taking data since 2007, and The NEutrino Mediterranean Observatory (NEMO, de Marzo et al. 2000), which is in operation since 2007, are three neutrino detectors built in the Mediterranean Sea. Another detector located in water, The Baikal Neutrino Telescope (Balkanov et al. 2000), is since 1998 in the Russian Lake Baikal and takes data since then.

Other projects are using the ice as transparent medium. For instance, the AMANDA detector (Antarctic Muon and Neutrino Detector Array, Andres et al. 2000), completed since 2000 and the IceCube detector, completed since 2011 (Ahrens et al. 2004, see also Sect. 3.2.3) are located at the South Pole, in the Antarctic ice. The AMANDA detector is part of the km^3 IceCube detector since 2005.

The IceCube's field of view is complementary to the one of ANTARES: while the IceCube detector is optimized for the detection of neutrinos coming from sources located in the Northern hemisphere, ANTARES is optimized for the sources located in the Southern hemisphere. There exists also a project to build a 1 km^3 neutrino detector in the mediterranean sea. This latter, called The KM3NeT project (Kappes & KM3NeT Consortium 2007), is based on the three neutrino experiments ANTARES, NEMO and NESTOR. Compared to the IceCube neutrino detector, a better exposure to the Galactic center region and a better angular resolution on the measurement of the neutrino direction are expected. On the other hand, the diffuse flux of neutrinos of extragalactic origin should be better detected with IceCube (because IceCube is optimized for the detection of neutrinos from the outer part of our Galaxy).

The atmospheric muon neutrino flux, produced by the interactions of the cosmic rays in the atmosphere, has been measured by most of these neutrino detectors, for instance, by ANTARES (The ANTARES Collaboration et al. 2013), FREJUS (Daum 1995), AMANDA (Abbasi et al. 2010a) and IceCube (IceCube Collaboration et al. 2013a). Recent observations collected by the

IceCube detector are shown in Fig. 3.14. Historically, this muon atmospheric neutrino flux has been described by a power law of spectral index of 3.6 between 1TeV and 1PeV (Gandhi et al. 1996)

$$\frac{dN}{dEd\Omega}|_{\nu_\mu,\,atm} = 7.8 \cdot 10^{-11} \left(\frac{E}{1\mathrm{TeV}}\right)^{-3.6} \mathrm{cm}^2\mathrm{s}^{-1}\mathrm{sr}^{-1}\mathrm{GeV}^{-1}. \quad (3.18)$$

However, the current data of the atmospheric muon neutrino flux are better fitted by a power law of spectral index of 3.7 with some corrections due to the presence of spectral features in the cosmic ray spectrum and to the contribution of the heavy mesons, which contribute to a hard tail of the neutrino flux at the highest energies (see e.g, Honda et al. 2007; Gaisser 2012). The different predictions leave an uncertainty of about 20% on the neutrino flux. In the study that I present in this thesis, I use the atmospheric muon neutrino flux of Honda et al. (2007). This neutrino flux needs to be disentangled from the astrophysical neutrino flux. The sensitivity of a neutrino detector is mostly based on its ability to select the astrophysical neutrinos among the numerous atmospheric neutrinos.

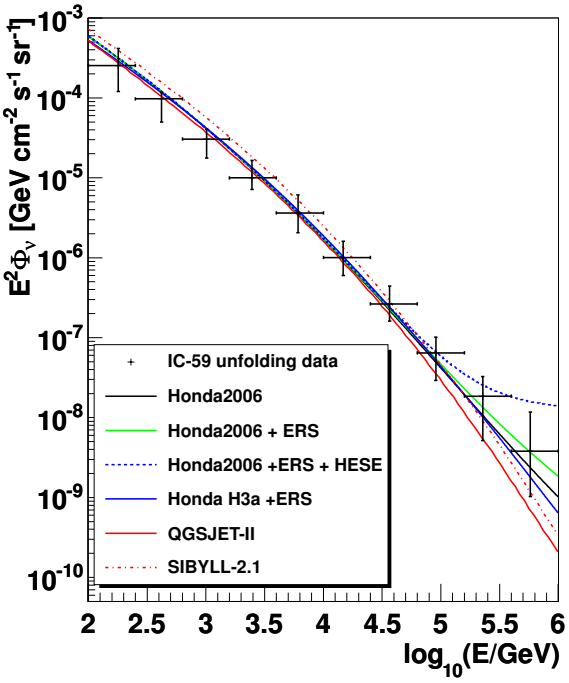

Figure 3.14: IceCube data for the atmospheric muon neutrino flux compared to theoretical predictions. Taken from (Aartsen et al. 2014a).

In the following section, I will introduce in more detail the IceCube neutrino detector, which I use in my study.

3.2.3 The IceCube neutrino detector

The IceCube neutrino detector is a km^3 size detector frozen in the ice at the geographic South Pole. The Cerenkov light emitted by the secondary particles is detected by strings of optical detectors,

which contain photomultipliers (PMTs) that convert the Cerenkov photons to an electric signal. The distance separating each neighbouring strings is of about 125m. IceCube has been completed in 2011 and is made of 86 strings (IC86), but it was already operating with only part of the strings. In my study, I use both the half IceCube configuration (IC40, see Sect. 6) and the almost completed IceCube configuration (IC79, see Sect. 5).

The IceCube data analysis can be performed by two complementary methods: A) the so-called *muon track channel analysis*, which is optimized for the analysis of the muon neutrinos produced in *CC* channel; and B) the so-called *veto channel analysis*, which is optimized for the cascade-like events produced by electron and tau neutrinos in *CC* channels and by all neutrino flavors in *NC* channel. In this section, I will introduce these two methods.

A) The muon detection channel

The muon detection channel is based on the analysis of the track left by the relativistic muons in the detector. The muon track is directional and collinear with the direction of the parent muon neutrino, with an energy dependent angle between the muon neutrino and the generated muon $< \theta >=< \frac{0.6^\circ}{\sqrt{E_\nu/TeV}} >$ (Chiarusi & Spurio 2010), where E_ν is the energy of the incoming neutrino.

Atmospheric muons are produced together with the atmospheric neutrinos. These relativistic muons can emit Cerenkov light in the detector and be mis-reconstructed as muons produced by the interaction of astrophysical neutrinos in the detector.

Due to its location, the IceCube detector uses the Earth as a filter to suppress the background of atmospheric muons. However, the atmospheric muons coming from the Southern hemisphere are not shielded by the Earth and hit the detector. As a result, in the Southern hemisphere the background is composed by both the atmospheric muons and the atmospheric muon neutrinos. To open the detection to sources located in the Southern hemisphere, a low energy cut is applied to reduce the flux of atmospheric muons, which are known to have a soft spectrum. Therefore, with this technique, the detection of astrophysical muon neutrinos from sources located in the Northern hemisphere is optimized in the TeV-PeV energy range, while from the Southern hemisphere, in the PeV energy range only.

This is illustrated in the declination dependence of the effective area. This latter represents the size of the detector if it were 100% efficient. It is computed taking into account the probability that an astrophysical muon neutrino of a given energy crosses the Earth and produces a detectable muon given that the Earth is opaque to PeV neutrinos. The effective area of the IceCube detector obtained in the IC-40 configuration is shown in Fig. 3.16. From this plot, we can clearly see the higher cut in energy applied in the Southern hemisphere in order to reject the atmospheric muons. Also, due to the neutrino absorption in the Earth, the effective area decreases at high energy for sources located at large declination (green curve).

In my study, I use both the effective area and the point spread function (PSF) of the detector. This latter describes the ability of a detector to reconstruct the true neutrino direction from the light pattern left in the detector. The angular resolution of the detector in the IC-40 configuration is of the order of 1° for 10 TeV-100 TeV neutrinos and gets better as the energy increases (see Fig. 3.15). It also gets better with the completion of the detector: in its final configuration, the IceCube detector reaches an angular resolution $< 1^\circ$(IceCube Collaboration et al. 2013b).

As a result, due to its good angular resolution the muon detection channel is optimized to the point-source search, where one aims at detecting an excess of astrophysical neutrinos concentrated

at a point source position on the top of an isotropic background.

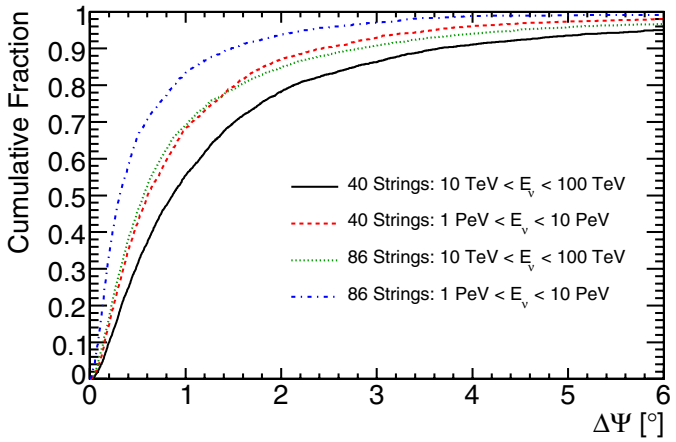

Figure 3.15: Cumulative PSF, or cumulative fraction of well reconstructed events, of the IceCube detector in the IC40 configuration. Taken from (Abbasi et al. 2011).

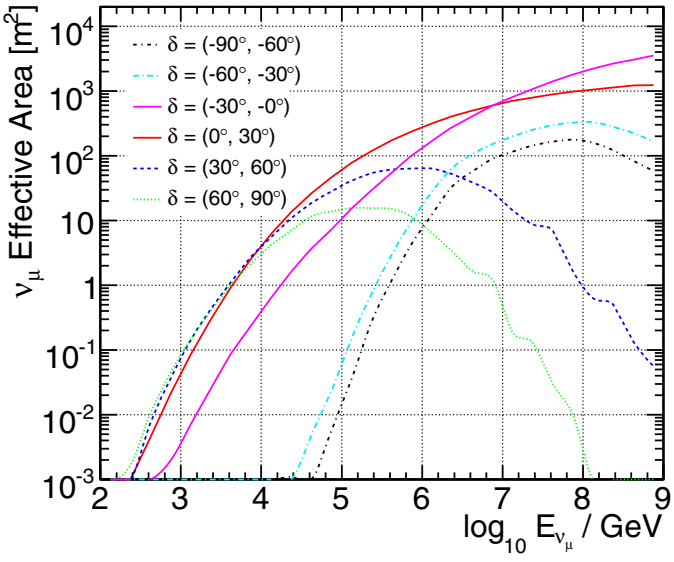

Figure 3.16: Effective area of the IceCube detector in the IC40 configuration for the muon neutrino detection. Taken from (Abbasi et al. 2011).

B) The veto detection channel

The veto detection channel (or High Energy Starting Events (HESE), Aartsen et al. 2013a) is based on the analysis of cascade-like events rather than track-like events. Cascade events are produced by electron and tau neutrinos in *CC* channel (see Sect. 3.2.2) and by all neutrino flavors in *NC*

channel. This is an alternative method to the track analysis, which is based on the selection of events which are fully contained inside the detector. A sketch of the veto technique is shown in Fig. 3.17, from (Aartsen et al. 2013a).

By selecting only events contained in the detector, this technique opens the analysis to sources located in the Southern hemisphere and to the highest energy neutrinos, which do not need to cross the Earth to reach the detector (the Earth being opaque to PeV neutrinos). This is illustrated in Fig. 3.18, where the effective area for the cascade-like events is represented.

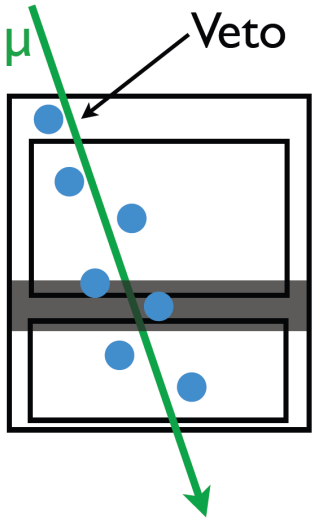

Figure 3.17: Sketch of the veto technique. The grey shaded region corresponds to a region in the ice where dust is present and increases the scattering of the light. Those data of poorer quality are also removed in the veto procedure. From Aartsen et al. (2013a).

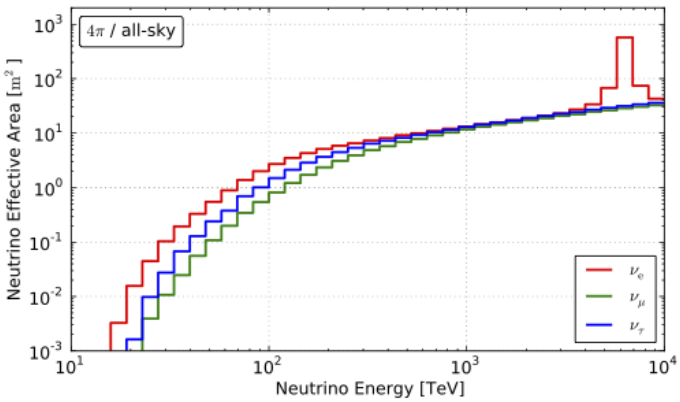

Figure 3.18: Effective area in the veto channel averaged over all arrival angles. At 6.3 PeV, the increase of the effective area for the electron neutrino is due to the Glashow resonance. Taken from IceCube Collaboration (2013).

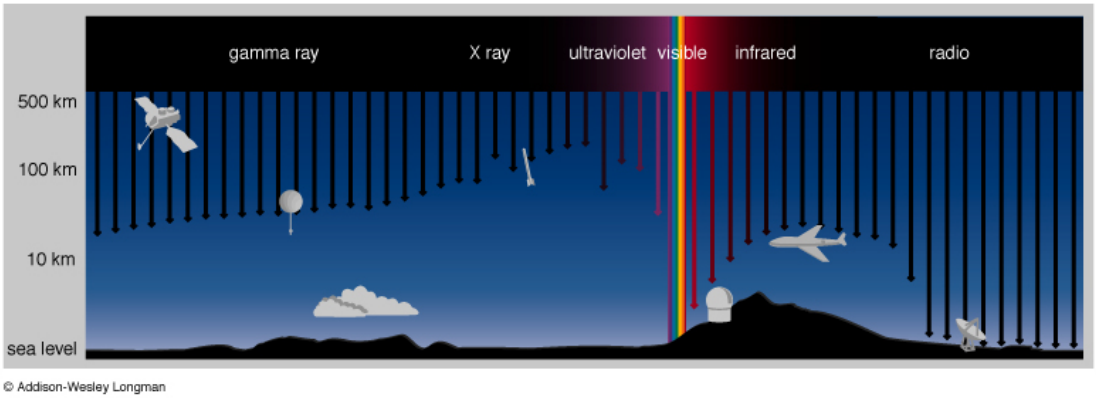

Figure 3.19: Atmospheric absorption of the electromagnetic spectrum. Taken from (http://atmos.nmsu.edu/~nchanove/A105S04/lecture_11.html).

Due to the spherical shape of the cascade-like events, the information about the primary neutrino direction is almost lost. The angular resolution is between 10 and 15°(Kurahashi & for the IceCube Collaboration 2014), which is worse than the angular resolution of track-like events (around 1°or better, depending on the energy). Therefore the veto technique is not dedicated to the point source analysis. However, the energy resolution is better than in the track analysis, as the shower is contained in the instrumental volume. Furthermore, its large effective area at the highest energies (where the background is inexistent) makes the search for a hard astrophysical neutrino energy spectrum advantageous compared to the muon tracks analysis.

3.3 γ-rays

Photons are copiously produced and observed across the complete electromagnetic spectrum. The γ-ray photons belong to the highest energy photons observed ($E_\gamma > 10^6$eV).

In astronomical sources there exist several competitive mechanisms able to produce γ-ray photons. These can be classified into two categories: the so-called leptonic and hadronic models. In leptonic emission mechanisms, only electrons (and positrons) are involved; while in hadronic interactions, protons and atomic nuclei are also implicated. The production mechanisms for γ-rays through pp end $p\gamma$ interactions have been described in section 3.1.2. In this section, I will focus on the other production mechanisms.

3.3.1 Production mechanisms

An electron in the Coulomb field of a nucleus emits *bremsstrahlung* radiation. The energy loss of a relativistic electron in the field of nuclei of number density n_N and charge Ze is proportional to the energy of the emitting electron, such that the cooling time is energy independent

$$t_{brem} \approx \frac{m_e^2}{16Z(Z+1)e^6 n_N} \approx 4 \cdot 10^7 \left(\frac{n_N}{1\ \mathrm{cm}^{-3}}\right)^{-1} \ \mathrm{yr}. \tag{3.19}$$

Therefore, the losses per bremsstrahlung do not change the initial electron spectrum. The spectrum of radiation peaks at the energy of the electron. If the electrons are distributed with a power law of spectral index p, the bremsstrahlung radiation spectrum is also a power law with the same spectral index p. For the protons, the cooling time is increased by a factor $(m_p/m_e)^2$ and the cooling time becomes: $t_{brem} = 4 \cdot 10^{13} \left(n_N/1\ \mathrm{cm}^{-3}\right)^{-1}$ yr.

Alternatively, electrons in a dense radiation field produce γ-ray photons by Inverse Compton scattering processes on these photons. The cross-section of the interaction depends on ratio between the initial energy of the photon (ϵ_{ph}) and of the rest energy of the electron ($m_e c^2$). In the case where $\epsilon_{ph} << m_e c^2$, one is in the Thomson regime, while in the case $\epsilon_{ph} \geq m_e c^2$, one is in the Klein-Nishina (KN) regime.

In the Thomson regime, the cross-section tends to the Thomson cross-section and the energy loss of the electron is proportional to the square of the electron energy: $-dE_e/dt = 4/3\sigma_T c u_{ph}(E_e/m_e c^2)^2$, where u_{ph} is the energy density of the low energy radiation. Therefore, the Compton cooling time of an electron is inversely proportional to the electron energy

$$t_{IC,T} \approx \frac{3m_e^2 c^3}{4\sigma_T u_{ph} E_e} \approx 3 \cdot 10^7 \left(\frac{u_{ph}}{1\ \mathrm{eV/cm}^3}\right)^{-1} \left(\frac{E_e}{10\ \mathrm{GeV}}\right)^{-1} \mathrm{yr}. \tag{3.20}$$

As the cooling time decreases linearly with E_e, the process is more effective at the highest electron energies. The average energy of the up-scattered photon is $\epsilon'_{ph} \sim \epsilon_{ph} E_e^2 \approx 0.5(\epsilon_{ph}/1\ \mathrm{eV})(E_e/10\ \mathrm{GeV})^2$ GeV. For a power law distribution of electrons with spectral index p, the up-scattered γ-ray spectrum has a power-law index $\alpha = (p-1)/2$. The energy loss rate is suppressed by a factor $(m_e/m_p)^4$ for the protons and the cooling time becomes: $t_{IC,T} \approx 3{\cdot}10^{20} \left(u_{ph}/1\ \mathrm{eVcm}^{-3}\right)^{-1} \left(E_p/10\ \mathrm{GeV}\right)^{-1}$ yr.

In the KN regime, the photon takes away a large fraction of the electron energy, such that $\epsilon'_{ph} \approx E_e$ independently of the incident photon energy. Nevertheless, in this regime, the cross-section decreases with the electron energy, as $(ln(2x) + 1/2)/x$, where $x = \epsilon_{ph}/m_e c^2$ (Longair 2011) and the produced γ-ray emission is suppressed.

Finally, a relativistic electron in a magnetic field emits *synchrotron* radiation. The energy loss of an electron in a magnetic field is proportional to the square of the electron energy: $-dE_e/dt = 4/3\sigma_T c u_B (E_e/m_e c^2)^2$, where $u_B = B^2/8\pi$ is the magnetic energy density.

Therefore, the cooling time of an electron emitting synchrotron radiation is inversely proportional to the electron energy (Sarazin 1999)

$$t_{syn} \approx \frac{3m_e^2 c^3}{4\sigma_T u_B E_e} \approx 2 \cdot 10^9 \left(\frac{B}{\mu\mathrm{G}}\right)^{-2} \left(\frac{E_e}{10\ \mathrm{GeV}}\right)^{-1} \mathrm{yr}. \tag{3.21}$$

Each electron emits a photon spectrum peaked at the characteristic frequency $\nu_{c,e} = 3/2(eB/m_e c 2\pi)(E/m_e c^2)^2$ and the characteristic energy of the synchrotron photons is $\epsilon_{syn} = h\nu_{c,e} \approx 5 \cdot 10^{-6}(B/\mu\mathrm{G})(E_e/10\ \mathrm{GeV})^2$ eV. For a power-law distribution of electrons, the resulting photon flux can be approximated as the sum of each individual spectra and draws a power law distribution of spectral index $\alpha = (p-1)/2$. For the protons, the energy loss rate is suppressed by a factor $(m_e/m_p)^4$ and the cooling time becomes $t_{syn} \approx 2 \cdot 10^{10}(B/1\ \mathrm{G})^{-2}(E_p/10\ \mathrm{GeV})^{-1}$ yr and the synchrotron photons peak energy is shifted by a factor $(m_e/m_p)^3$ toward lower energy.

Each of these mechanisms can dominate, depending on the gas number density (Eq. 3.19), the energy density of the low energy radiation (Eq. 3.20) and the energy density of the magnetic field (Eq. 3.21). For these three emission mechanisms, if the parent electron spectrum follows a power law distribution, the produced γ-ray spectrum has also a power law distribution.

This makes the distinction from the hadronic scenario difficult, as the spectra of the γ-ray neutral pion decay photons produced in cosmic ray interactions are also distributed with a power-law (see Fig. 3.8 and Fig. 3.11). Therefore the detection of a clear signature of any of these models (like for instance the π^0 decay bump at GeV energy or the detection of γ-rays above the Klein-Nishina suppression) would be helpful in this identification.

3.3.2 Detection principle

As shown in Fig. 3.19, the atmosphere is opaque to infrared, ultraviolet, X-ray and γ-ray photons. As a result, to observe γ-ray emission one needs to go above the atmosphere.

The first γ-ray space telescopes were SAS-2 (1972-1973, sensitive to photons between 20 MeV and 1 GeV, Fichtel et al. 1975) and COS-B (1975-1982, sensitive to photons between 30 MeV and 10 GeV, Bignami et al. 1974), then EGRET (Thompson et al. 1993, 1991-2000, sensitive to photons between 20 MeV and 30 GeV,) on the Compton-Gamma-Ray Observatory performed the first all sky survey in the energy range 50 MeV to 30 GeV. The currently flying and data-taking detectors are the Fermi γ-ray detector (Atwood et al. 2009) and AGILE (Pittori 2003) (see Bruel 2010, for a review of the main differences between Fermi and AGILE). Direct detection is however only possible for γ-ray of energy below a few 100 GeV, for which the flux is high enough.

Due to their low flux, the highest energy photons can only be detected indirectly though the cascade of secondary particles that they produce by entering the Earth's atmosphere, ie in the same way as we detect UHECRs. Therefore, the detectors meant to detect γ-rays also detect cosmic rays (and vice versa), such that depending on whether one aims to detect high energy γ-rays or cosmic rays, the other kind of particles appears as a background one should get rid of. Fortunately, based on shower development simulations, the electromagnetic cascade development in the atmosphere (which consists in pair creation and bremsstrahlung radiation) is expected to be different than the one of the cosmic rays. For instance, the difference of lateral distribution is a useful quantity to distinguish the EAS generated by γ-rays from the ones generated by cosmic rays. An illustration of the signature left by γ-rays and cosmic rays entering at the ground is shown in Fig. 3.21. These differences come from the fact that the hadronic EAS contain also pions, muons, neutrinos and thus have a more scattered profile than the purely leptonic EAS. The longitudinal profile is also used for this purpose: as the γ-rays undergo less scatter and can penetrate a larger distance in the atmosphere, they are characterized by a larger X_{max} than cosmic rays of the same energy.

The Cerenkov light emitted in the air can be detected via imaging Air Cerenkov Telescope (IACT). The typical field of view of a IACT is of $\sim$3.5°, therefore IACT needs to be pointed to the source one wants to study. The first IACT was the Whipple Gamma-Ray Telescope, constructed in 1968 (Finley & VERITAS Collaboration 2001), while the HEGRA telescope array (Aharonian et al. 1991), constructed in 1987, was the first stereoscopic Cerenkov telescope, i.e. it uses multiple telescopes to reconstruct the development of the shower in the air (ie, the longitudinal distribution). Since then, other IACTs have been built like H.E.S.S. (Hofmann & H.E.S.S. Collaboration 2001), VERITAS (is located at the Whipple's site VERITAS Collaboration et al. 2011), MAGIC (is located at the HEGRA's site Albert et al. 2008), CANGAROO (Edwards et al. 1993) and the incoming Cherenkov Telescope Array (CTA Actis et al. 2011). Those detectors only work

during clear and dark nights. Using IACT techniques, one is sensitive to γ-rays between 50 GeV and about 50 TeV (Hofmann 2012), but the upcoming CTA is expected to have an energy threshold below 50 GeV and a larger field of view than other IACTs.

Finally, the highest energy γ-rays can be detected directly by surface detectors. For instance, high energy γ-rays are detected with water tank detectors like MILAGRO (Atkins et al. 1999) and its successor HAWC (The High Altitude Cerenkov Experiment HAWC Collaboration et al. 2013). High energy γ-rays create relativistic electron-positron pairs in the purified water, which is detected via their Cerenkov emission. Such detectors are operational days and nights.

A good sensitivity is required for the detection of the highest energy γ-ray, as their flux is attenuated during their propagation by the pair creation process on the low energy radiation. The energy threshold for this interaction is $E\epsilon_{ph} \approx 2(m_e c^2)^2 \approx 0.5 \cdot 10^{12}$ (eV)^2, where ϵ_{ph} is the energy of the target radiation and E, the energy of the γ-ray photons. The mean distance travelled by a photon in a low energy radiation field is computed as $(n_{ph}\sigma_{\gamma\gamma})^{-1}$, where $\sigma_{\gamma\gamma}$ is the cross-section of the interaction and n_{ph} the density of the target photons. For instance, as the cross-section for this interaction peaks at 10^{-25}cm^2 (Gould & Schreder 1967), PeV photons will interact with CMB photons of density $n_{ph} \sim 400$ cm^{-3} and energy $\sim 10^{-3}$ eV, and can only travel a mean distance of ~ 8 kpc. This is illustrated in Fig. 3.20 for the case of a low radiation field composed by the CMB and by the optical and infrared radiation (known as extragalactic background light, EBL). As shown, γ-rays with energy below 100 GeV are expected to be able to travel several pc and to reach us without being absorbed.

Compared to IACTs, water tank detectors have a larger field of view and duty cycle. But also a higher energy threshold and a reduced sensitivity. This is shown in Fig. 3.22, where the sensitivity to a γ-ray spectrum of -2.3 slope is represented for the different γ-ray experiments mentioned: The Fermi γ-ray space telescope, the IACTs, the water tank Cerenkov telescopes and the upcoming CTA. As mentioned earlier, space telescopes cannot detect the highest energy γ-rays whose flux is very low and only accessible to ground based telescope. Indeed, the effective area of IACT is of 0.1 km^2, due to the Cerenkov light which develops in a cone of about 1° in the atmosphere at an altitude of about 10 km and reaches the ground to form a 130 m radius Cerenkov pool. So, compared to the 1m^2 effective area of the Fermi satellite, the IACTs could detect fluxes which are 100 times fainter than space satellites. Nevertheless, given that IACTs and space telescopes do not consider the same energy range and that the flux of γ-rays decreases with increasing energy, this effective area improvement does not imply that the sensitivity of the IACTs is 100 times better than the one of the space satellite, as illustrated in Fig. 3.22. The expected sensitivity of the CTA observatory is also shown for comparison. With this instrument, one expects to close the energy gap between the energy ranges covered by the ground based IACTs and the space satellites and to open the study to the highest energy range, where important results are expected. For instance, the detection of γ-rays at energy larger than the Klein-Nishina suppression would be an evidence of the hadronic origin of the γ-ray emission.

In my analysis, I use γ-ray data collected with the Fermi telescope (Atwood et al. 2009). I will introduce this detector in the following section.

3.3.3 The Fermi γ-ray telescope

The Fermi γ-ray telescope (formerly called GLAST) has been launched in June 2008 and is made of two instruments: the large area telescope (LAT) and the Gamma-ray Burst Monitor (GBM). The LAT instrument is the main instrument on board of the satellite.

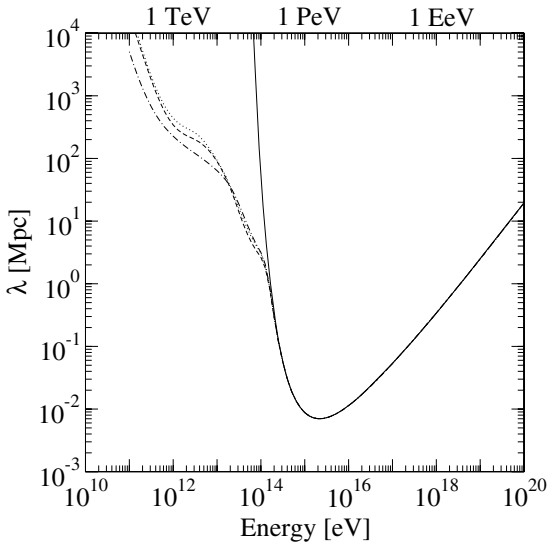

Figure 3.20: Mean free path of the high energy photons of energy between 10GeV and 1EeV for pair creation with the low radiation photons for four different models of the background. Key: the solid line represents the γ-ray photons mean free path through CMB photons only, while for the dashed, dotted and dot-dached lines, the background radiation field consists in CMB and EBL photons, for three different models of EBL. Taken from (Venters 2010).

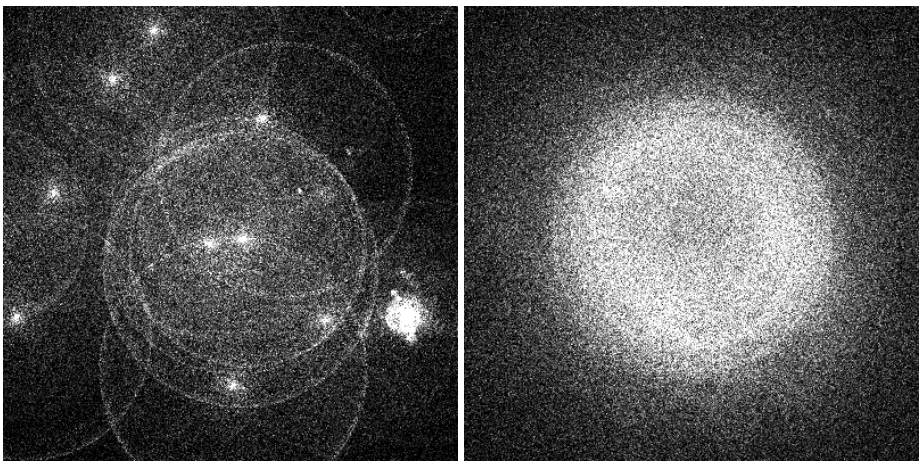

Figure 3.21: Simulation of lateral distribution of Cherenkov light of air showers with CORSIKA, left by a proton of 1 TeV (left panel) and by a photon of 300 GeV (right panel). Taken from http://www.mpi-hd.mpg.de/hfm/CosmicRay/ChLight/ChLat.html.

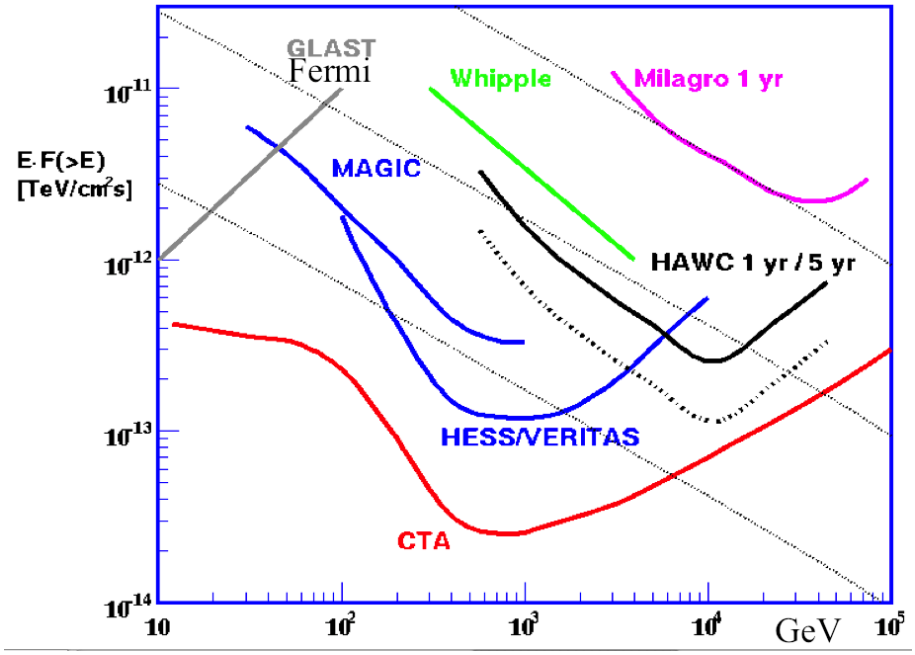

Figure 3.22: Sensitivity of the different γ-ray detectors. Diagonal lines show the reference flux of (from top to bottom): 1 Crab, 0.1 Crab and 0.01 Crab. Adapted from the webpage: http://umdgrb.umd.edu/hawc/science.php.

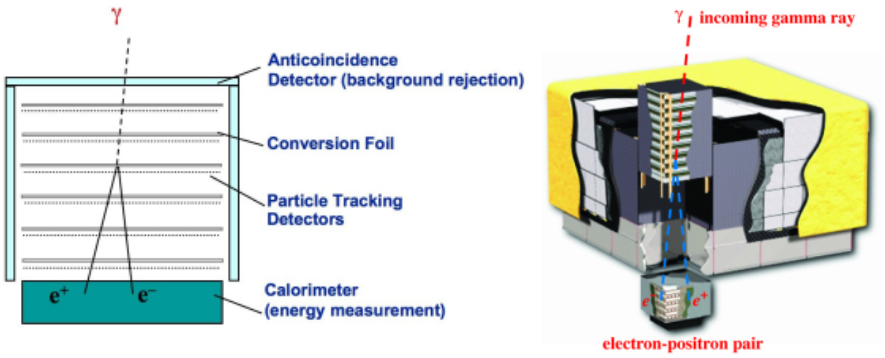

Figure 3.23: Description of the Fermi-LAT detector. The Fermi-Lat instrument, shown in the right panel, is made of 16 detector towers similar to the one shown in the left panel. Taken from the Fermi webpage.

The LAT has a size of 1.8 m square and 0.72 m high. Thanks to its large field of view (1/5 of the all sky), it is able to scan the entire sky in two orbits. It is sensitive to γ-rays of energy above 30 MeV and up to 300 GeV. It is a pair-converter detector and the detection of γ-rays is performed as follows (see Fig. 3.23): when a γ-ray enters the LAT, it first passes through a shield called the Anticoincidence Detector (ACD) which produces a signal when it is crossed by a charged particle. As a result, the ACD allows to discard the data produced by cosmic rays. It is important to identify such events as they may emit background γ-rays. Then the γ-ray enters the main body of the detector, which consists in sheets of absorbent material incorporated in a tracker. While the absorbent sheets induce the electron-positron pair creation, the tracker records their arrival direction. The energy of the photo-electrons is then measured in the calorimeter, which is made of absorbent material.

The GBM is a complementary instrument to the LAT which is meant to detect Gamma-ray bursts (GRBs). As GRBs are coming from random direction in a wide range of time scales, the GBM is made of 12 sub-detectors which are located on opposite sides and face different directions in the sky. From a comparison between the detection rate coming from these sub-detectors, the GMB can infer the arrival direction of the burst. The GBM is sensitive to energies between 8 keV and 30 MeV. As a result, GBM is a low energy instrument with a large field of view.

The performances of the LAT are based on Monte Carlo simulations (see Rando & for the Fermi LAT Collaboration 2009, for details). The peak effective area is larger than 0.8 m^2 and is reached at energy between [2;200] GeV. The angular resolution is $\lesssim 3.5°$ at 100 MeV and $\lesssim 0.15°$ at energies above 10 GeV for a 68% containment (this represents the fraction of events detected). The energy resolution reaches $\Delta E/E < 10\%$ for γ-rays of energy between [1;30] GeV.

After two years only, the Fermi-LAT detector observed already 1873 sources, associated with known or new sources (Nolan et al. 2012). This can be compared with the number of sources detected with its predecessor EGRET and reported in the third EGRET catalogue (Hartman et al. 1999), where 271 sources have been detected in about 4 years. The all-sky map of the Fermi-LAT telescope obtained after five years of mission is illustrated in Fig. 3.24.

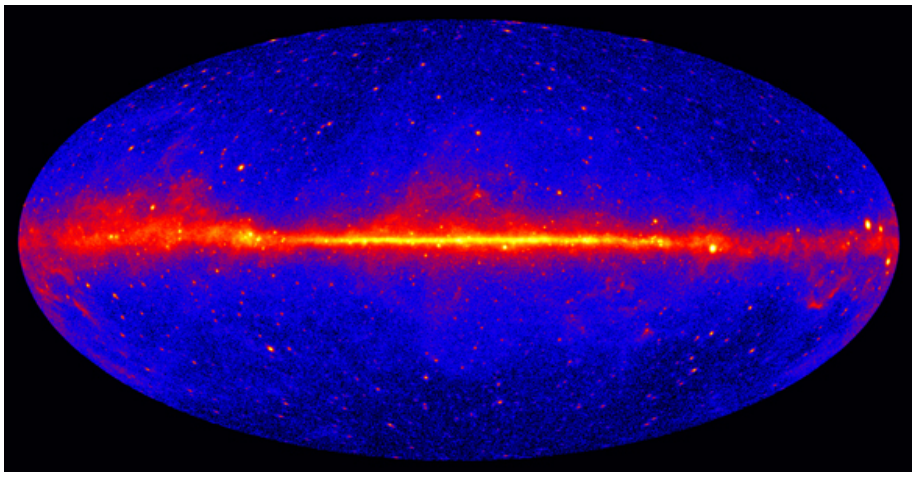

Figure 3.24: All-sky map after five years of data acquisition with the Fermi-LAT instrument. Taken from the Fermi webpage.

Chapter 4

High energy sources

The origin of cosmic rays is still unclear and many models have been proposed since their discovery. In some of them, cosmic rays appear as the decay product of very massive exotic particles (*top-down model*), while in others, they are charged particles accelerated to high energy in astrophysical sources (*bottom-up model*). In this study, I consider the second possibility only.

Hereafter I will review different astrophysical sources which are potential cosmic ray accelerators. To do so, I will start by introducing the conditions that a cosmic ray accelerator needs to fulfill.

4.1 Requirements on a source of high energy cosmic rays

Due to the presence of the magnetic field between the source of cosmic rays and the Earth, the identification of the accelerating source based on the observations of the cosmic rays arrival direction is difficult. As a result, one needs to rely on theoretical expectations to determine the potential sources of cosmic rays.

Based on geometrical considerations, Hillas suggested 30 years ago that a particle must be confined in the accelerating region to be accelerated up to a given energy (Hillas 1984). This condition implies that each astrophysical source of given size (R_{source}) and magnetic field strength (B) can only accelerate charged particles up to a maximal energy: $E_{max} = R_{source}BZe$, where Ze is the charge of the particle. This relation, based on the requirement that the Larmor radius of the particle (R_{lar}) is smaller than the size of the source, is shown in Fig. 4.1. In this figure, the diagonal lines are the maximal energy reached for 10^{20} eV protons and iron nuclei and for 10^{21} eV protons. As we saw in the previous chapter, based on the anisotropy and composition measurements, the observed cosmic ray spectrum (see Fig. 3.3) appears like a superposition of cosmic ray flux of Galactic and extra-galactic origin. In this frame work, the Hillas criterion allows us to select which extragalactic sources are potentially able to accelerate protons up to 10^{20}eV. Among them, we find active galactic nuclei (AGN), galaxy clusters and gamma-ray burst (GRB). Due to their large magnetic field, neutron stars, which can be Galactic objects, are also potential UHECR accelerator.

The Hillas criterion does not take into account the energy losses. Indeed, the maximal energy reached by the cosmic ray as it leaves the source is determined by the balance between the energy losses and gains. The most commonly used acceleration mechanism is the first order Fermi acceleration or Diffuse Shock Acceleration mechanism (DSA Fermi 1949; Bell 1978; Blandford & Eichler 1987), which describes the energy gain of a charged particle which is magnetically confined in the vicinity of a shock and diffuses back and forth across the shock surface on the magnetic field lines, gaining energy at each cycle (a more detailed description of the DSA process can be found in appendix .1). This theory predicts a spectrum of accelerated particles which is a

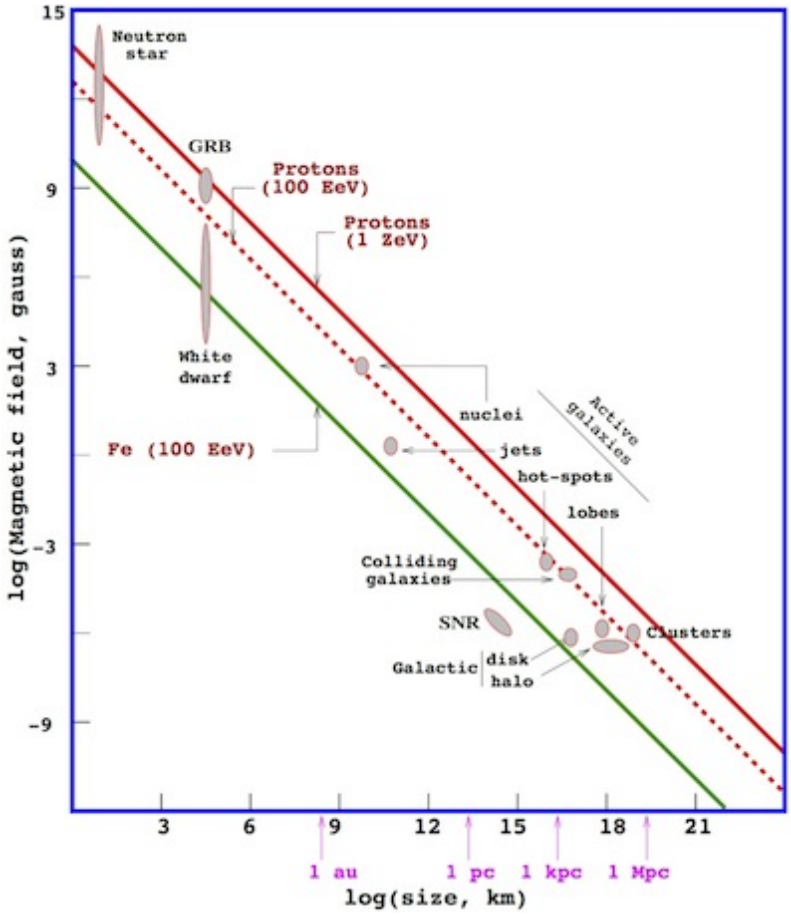

Figure 4.1: Hillas plot taken from (Hooper & Serpico 2007).

power-law of spectral index equal to 2, which can explain the observed cosmic ray spectrum below the knee for given models of propagation of cosmic rays in the Galaxy (ie for a given energy dependent escape time). For this reason, the DSA mechanism is one of the favorite acceleration mechanism in astrophysical sources. Regarding the energy losses, as we saw in Sect. 3.3.1, the dominant energy loss channel depends on the characteristics of the medium and the energy losses are more efficient for lighter particles. This is due to the mass dependency of the energy loss expressions (see for instance Eq. [3.21] for the loss per synchrotron radiation, Inverse Compton (Eq. [3.20]) or bremsstrahlung (Eq. [3.19])).

Another relevant criterium for the selection of the potential accelerating sources is based on the energy budget. Indeed, a cosmic ray source candidate must be powerful enough to provide the necessary energy to the accelerated particles. For instance, to sustain the observed cosmic ray energy density of 1 eV/cm^3, in the Galaxy volume of 10^{67} cm^3 and a typical escape time of 10^7 yr, an energy rate input of 10^{41} erg/s is required.

4.2 Galactic sources

Explosions of massive stars in supernovae (SN) are predicted to be able to provide enough energy to explain the cosmic ray flux observed from Earth (Ginzburg & Syrovatskii 1964). The kinetic energy released by a supernovae explosion has been estimated to be of the order of $E_{SN} \sim 10^{51}$ erg (Chevalier 1977). With a rate of 3 new SNe per century deduced from the star formation rate, one can reproduce the observed local cosmic ray energy density, provided that 10% of the total kinetic energy of the supernovae is transferred to the cosmic rays. Furthermore, the ejected envelope of the SN explosion, known as Supernovae Remnant (SNR), satisfies the Hillas criterion for proton up to 10^{15} eV. For these reasons, SNRs are usually considered as the best Galactic candidate for acceleration of cosmic rays.

However, in Lagage & Cesarsky (1983), the authors computed that the maximal energy obtained in SNR using the DSA mechanism does not reach the *knee* due to the short time of the SNR in the accelerating phase (known as the Sedov phase), compared to the acceleration time needed to reach such high energies. As a result, a modified version of the DSA model, called the non-linear DSA (NLDSA) has been developed (see e.g., Drury 1983; Bell 1978). By including the feedback of the cosmic ray interaction on the magnetic field, it increases the maximal energy reached during acceleration (see e.g., Malkov & O'C Drury 2001, for a review).

Furthermore, the observations of SNRs show evidence of the presence of relativistic particles in the remnant. For instance, the detection of γ-ray, radio, and X-ray emission provides direct evidence of the presence of a shock and of high energy electrons in SNRs. Indeed, while the radio emission is produced by the interactions of relativistic electrons with the magnetic fields, the X-ray emission shows the interstellar gas heated by the shock wave at the SNR boundary. Regarding the γ-ray emission two origins are possible: either the origin is hadronic and the high energy cosmic rays interact with the interstellar medium, producing neutral pions which decay in photons; or the origin is leptonic and the high energy electrons interact with low energy synchrotron radiation through inverse Compton processes. If one can attest that the γ-ray emission is hadronic, then we have found one of the Galactic sources of cosmic rays. A typical hadronic feature is the 'neutral pion bump' at about 1 GeV: while some SNRs emission exhibit this neutral pion signature (like the Tycho SNR (Morlino & Caprioli 2012), IC 443 and W 44 (Ackermann et al. 2013)), some others do not (like RX J1713.7-3946, Abdo et al. 2011b), but these latter observations are still debated (Gabici & Aharonian 2014).

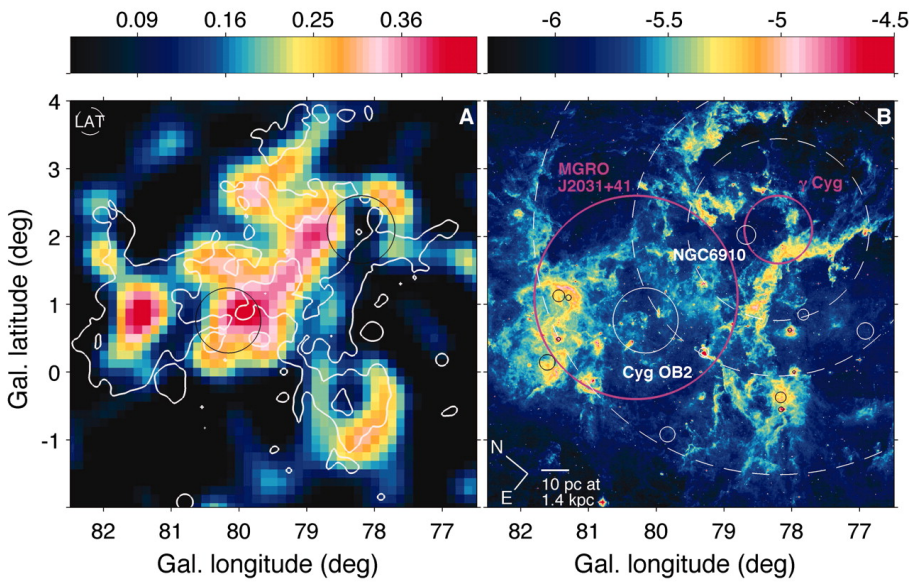

Figure 4.2: Left: The Cygnus region detected in γ-ray with the Fermi-LAT telescope in energy 10-100 GeV and contours of 8μm [Wm-2sr-1] MIR Dust emission (MSX). Right: 8μm [Wm-2sr-1] MIR Dust emission (MSX) with the name of the sources superimposed. As shown, the γ-ray emission matchs with the emission of ionized dust and molecular cloud. Taken from (Ackermann et al. 2011b).

It has been also suggested that rather than isolated SNe, the collective effects of many massive stars explosions in SNe can accelerate cosmic rays to high energies. This is motivated by the fact that massive stars are concentrated in OB stars association. As they have a very short lifetime compared to the escape time from the association, they explode before having the time to move significantly from their birth location. As a result, the explosion of one star triggers the explosion of the other massive stars. The strong winds of massive stars (see e.g., Meynet & Maeder 2003) are also believed to contribute to the formation of this large accelerating structure called *superbubble* (Parizot 2000; Higdon et al. 1998).

For instance, in an analysis performed by the Fermi-LAT satellite (Ackermann et al. 2011b), γ-rays are detected from the Cygnus region. This emission has a cocoon shape elongated by 50 pc whose intensity contours match with the intensity contours of the interstellar gas (visible in the mid-infrared, see Fig. 4.2). In this analysis, they interpreted this γ-ray emission as being produced by the freshly accelerated cosmic rays through pp interactions with the interstellar gas and subsequent neutral pion decay. As this γ-ray emission is located at the star forming region Cygnus X which hosts the Cygnus OB2 association, these cosmic rays are suggested to be accelerated by the collective processes which take place in the star forming region. An undeniable proof of the presence of accelerated cosmic rays in the Cygnus region would be the detection of a neutrino flux with a spectrum comparable to the γ-ray spectrum detected with Fermi. In a recent analysis performed by the IceCube collaboration, the authors obtained that the signal of six stacked Milagro TeV sources is consistent at a 2% level with the background fluctuation (IceCube Collaboration et al. 2014). As four of these sources are located in the Cygnus region, this may indicate that cosmic rays are accelerated in the Cygnus region.

Some SNRs host a pulsar. Pulsars are spinning neutron stars which convert their rotational kinetic energy into a particle wind. The power injected in the relativistic particles can be inferred from the spin down rate of the pulsar, which is observed thanks to the curvature radiation emitted by the electrons. The pulsar is surrounded by a nebula, called Pulsar Wind Nebula (PWN). This latter emits over the all electromagnetic spectrum by the following mechanism: the accelerated electrons emit curvature radiation in the magnetic field of the neutron star. These curvature photons interact with the low energy photons in the nebula to create an electron-positron pair, which triggers an electromagnetic cascade. The resulting PWN emission extends from radio to γ-rays in synchrotron and Inverse Compton processes (see e.g., Gaensler & Slane 2006). In Neronov & Semikoz (2012) the authors noticed that most of the known SNRs detected with the Fermi satellite above 100 GeV are spatially associated with pulsars, which indicates that the presence of pulsars may be a key ingredient in the cosmic ray acceleration process, even though, there is no evidence that protons are accelerated in these sources.

4.2.1 The confinement of cosmic rays in the Galaxy

Once the cosmic rays are accelerated, they interact with the Galactic magnetic field irregularities and stay confined in our Galaxy. There exist many evidence of the confinement of cosmic rays in our Galaxy. For instance, assuming that the amount of boron is null before spallation (an argument which is motivated by the fact that the boron abundance is suppressed in the solar system compared to the carbon abundance, but is as abundant as carbon among cosmic rays, indicating that the boron is almost absent as end product of stellar nucleosynthesis), the relative abundance of the boron-to-carbon ratio as a function of the energy can provide an estimate of the quantity of matter the cosmic ray carbon needs to cross before leaving the Galaxy (see e.g., Obermeier et al. 2012). Figure 4.3 shows the most recent published results of the boron-to-carbon ratio from AMS-02 (Oliva & on behalf of the AMS collaboration 2013). As one can notice, this decreasing function of the energy implies that the highest energy carbon elements leave the Galaxy first. The confinement time can also be estimated by the study of the ratio of abundance of unstable over stable isotope as function of the energy. For instance, ^{9}Be is a stable isotope, while ^{10}Be is unstable and undergoes beta decay to ^{10}B. At production, the ratio ^{9}Be:^{10}Be should be about 2:1. However, the observed ratio is 10:1 (see e.g, Yanasak et al. 2001). This implies that ^{10}Be has sufficient time to decay. Knowing that the ^{10}Be undergoes β^{-} decay with a half life time of $1.5{\cdot}10^{6}$yrs, the confinement time of the cosmic rays in the Galaxy is deduced to be of about $\sim 1.5 \cdot 10^{7}$ yrs (Yanasak et al. 2001).

Therefore, one expects that the accelerated cosmic rays do not leave the Galaxy straight away, but are scattered by the magnetic field inhomogeneities. The *leaky box* model (see e.g., Cesarsky 1980) is a simplified model which treats the Galaxy as an homogeneous box, from which the cosmic rays escape after a time t_{esc}, defined as $t_{esc} \approx H^2/D$, where D is the diffusion coefficient and H the height of the Galaxy.

There are different models to estimate the diffusion coefficient. For instance, assuming a magnetic field turbulence power spectrum characterized by a Kolmogorov spectrum, in Berezinsky et al. (1997) the authors obtained that the diffusion coefficient decreases with the energy as $D(E) \propto E^{1/3}$, such that the escape time of a particle of energy of 1GeV is
$t_{esc} \approx 3 \cdot 10^{7}(L/1\mathrm{kpc})^{2}(10^{28}\mathrm{cm}^{2}\mathrm{s}^{-1}/D)(E/1\mathrm{GeV})^{-1/3}$ yr and reduces to $3 \cdot 10^{3}$ yr for a 10^{19} eV cosmic ray. This energy dependent diffusion coefficient implies that the lower energy particles stay confined longer than the higher energy particle. This energy dependence is consistent with

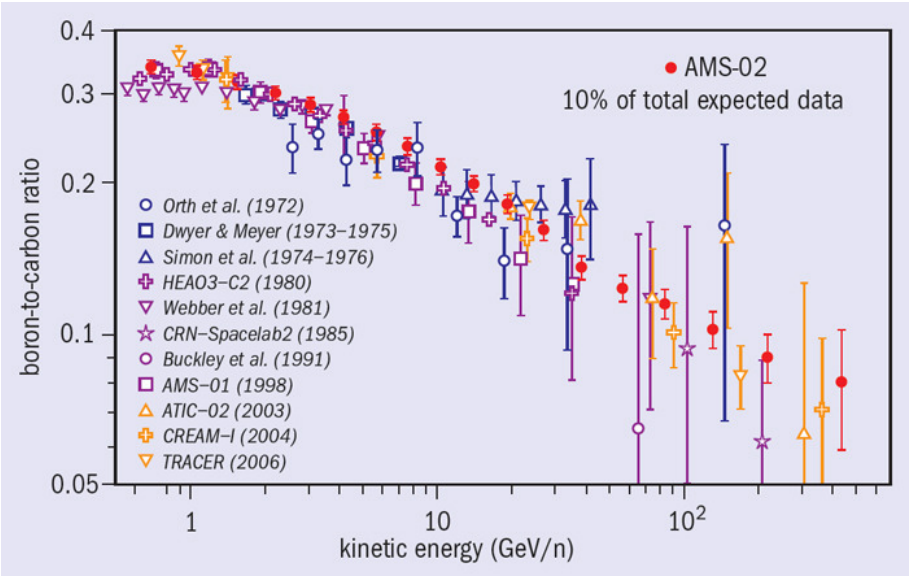

Figure 4.3: Boron-to-carbon ratio measurement as function of the energy. Taken from (Oliva & on behalf of the AMS collaboration 2013).

the energy dependence of the AMS-02 data of boron-to-carbon ratio (see Fig. 4.3 from Oliva & on behalf of the AMS collaboration 2013). Indeed, as we can attest from this figure, the diffusion coefficient derived from the AMS-02 data can be approximated by $D(E) \propto E^{\zeta}$, with $\zeta \sim 1/3$. This implies that the energy dependence assuming Bohm diffusion ($D \sim R_{lar}c \propto E$) would be too steep to reproduce these observations. This argument is also valid for the energy dependent diffusion coefficient $D \propto E^{0.7}$, which is required to explain the observed Galactic cosmic ray spectrum below the *knee* for an injected cosmic ray spectrum of spectral index equal to 2.

4.2.2 Diffuse γ-ray emission of the Galactic plane

The confined cosmic ray protons interact with the gas of the interstellar medium and produce a diffuse gamma-ray flux.

The Galactic plane of our Milky Way Galaxy is the brightest source of γ-rays (see e.g., The Fermi-LAT Collaboration 2012). The diffuse γ-ray emission of the Galactic plane detected above 100 MeV is dominated by the neutral pion decay radiation produced in the cosmic ray protons interactions with the gas of the interstellar medium (e.g., Stecker 1971). This is illustrated in Fig. 4.4 (from Abdo et al. 2009a), where the cosmic ray propagation in the Galaxy has been modeled using an updated version of the GALPROP code (Strong et al. 2004). At the highest γ-ray energies, the ground based γ-ray telescopes, HESS, MAGIC, and VERITAS, have recently started to explore the Galactic plane. The HESS survey of the inner part of the Galactic plane has revealed a number of bright extended γ-ray sources (Aharonian et al. 2005a, 2008), but no continuous diffuse emission from the entire Galactic plane, except for the Galactic ridge region (Aharonian et al. 2006a). The same bright extended sources are also seen in the survey of the Galactic plane above 100 GeV performed by Fermi-LAT (Neronov & Semikoz 2012). In Neronov & Semikoz (2012), this is interpreted as a consequence of the energy dependent escape time of cosmic rays, based on the fact that high energy cosmic rays can diffuse on small distances only

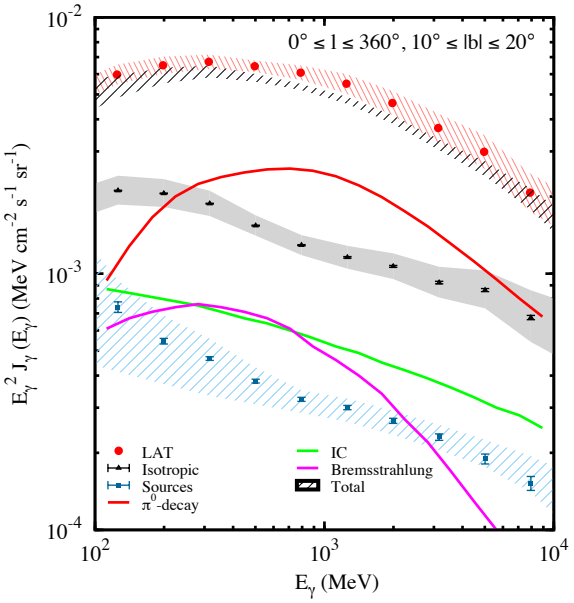

Figure 4.4: Results of the Fermi analysis performed in (Abdo et al. 2009a), where the cosmic ray propagation in the Galaxy has been modeled using an updated version of the GALPROP code (Strong et al. 2004). Taken from (Abdo et al. 2009a).

and cannot spread homogeneously throughout the disk. Due to the short escape time of high energy cosmic rays, these TeV emitting regions are location of recent cosmic ray acceleration (10^4 – 10^5 yr) (Neronov & Semikoz 2012). Verification of this hypothesis implies establishment of the hadronic nature of these sources by the detection of neutrinos. Indeed, as the cosmic ray interactions with the molecular gas result in the production of neutral and charged pions which subsequently decay into γ-rays, electrons/positrons, and neutrinos (Dermer 1986; Stecker 1979; Berezinsky et al. 1993), a diffuse neutrino flux is also expected from the Galactic plane, with an overall power and spectral characteristics very similar to the γ-ray flux (see Sect. 3.1.2, and also Stecker 1979; Kamae et al. 2006; Kelner et al. 2006).

4.3 Extragalactic sources

4.3.1 Blazars

Based on phenomenological considerations, an Active Galactic Nucleus (AGN) is composed of a supermassive black hole surrounded by an accretion disk and a dusty torus (see Fig. 4.5). At larger latitudes from the plane formed by the accretion disk, one can find narrow line (NLR) and broad line (BLR) regions, which become visible to the observer depending on the orientation of the observer with respect to the AGN. Perpendicular to the accretion disk, a jet of relativistic particles can be present. Depending if a jet is observed or not, the AGN is defined as a radio-loud, or radio-quiet AGN, respectively. According to the unified model, only the orientation differs between the different kinds of AGN (Urry & Padovani 1995).

There exist two classes of radio-loud AGNs (Fanaroff & Riley 1974): Fanaroff-Riley type 1 (FR I) and Fanaroff-Riley type 2 (FR II). FR I AGNs are characterized by a radio emission

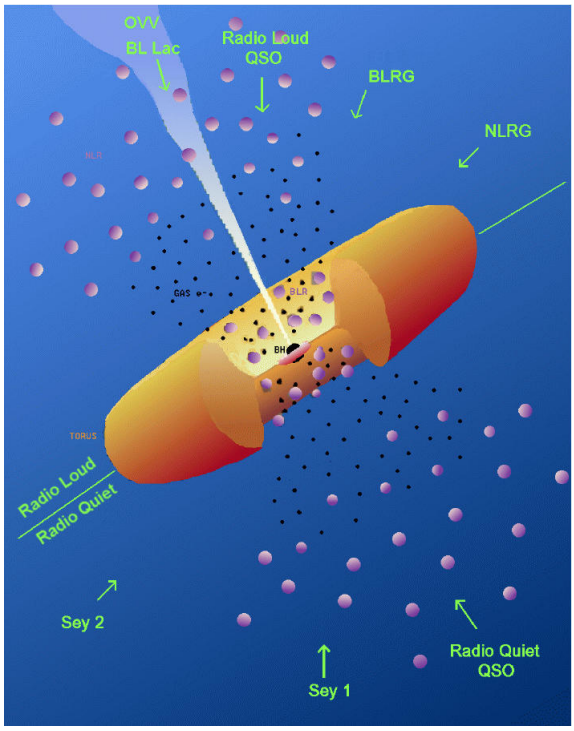

Figure 4.5: Unified model for AGN. Taken from (Urry & Padovani 1995).

brighter in the center and FR II by bright radio lobes. The beam of FR II is powerful enough to propagate through the host galaxy without being decelerated by the matter (see for instance the radio measurement of the radio-loud FR II galaxy Cygnus A shown in Fig. 4.6). The radio luminosity of FR II is larger than that of the FR I, therefore the radio luminosity is used as a criterion to classify radio loud AGN between these two classes.

Blazars are a special type of radio-loud AGN, whose jet is aligned with the line of sight (Urry & Padovani 1995). As a result, the observed emission is beamed and the blazars are among the brightest TeV sources ever detected. Indeed, the typical γ-ray luminosity of blazars observed with the Fermi-LAT satellite is $L \sim 10^{44-49}$ erg/s (Ackermann et al. 2011a). There are two populations of blazar: the Flat Spectrum Radio Quasars (FSRQ) and the BL Lac objects. A main difference between the two classes can be established by the study of their spectral energy distribution (SED). On average, the FSRQ are more luminous, more distant and have stronger emission lines than the BL Lac objects (Urry & Padovani 1995). In the SED of FSRQ, the emission of the accretion disk is observable in the UV band, which implies that such AGNs are accreting material with a high rate. On the other hand, BL Lac objects have a stronger jet emission and their SED is characterized by the lack of strong lines and accretion disk emission. Therefore the structure of the accretion flow in BL Lacs is, most probably, significantly different from the one in the FSRQ. According to the unified model, the less luminous BL Lacs may belong to the family of FR I, while the high luminous FSRQs to the one of FR II.

An illustration of a typical SED of blazar is shown Fig. 4.7. The SED shown in this figure is the result of a multi-wavelength campaign of the BL Lac 3C 66A during the year 2008. As shown the SED of a blazar is composed by two broad components: one at low and the other one at high

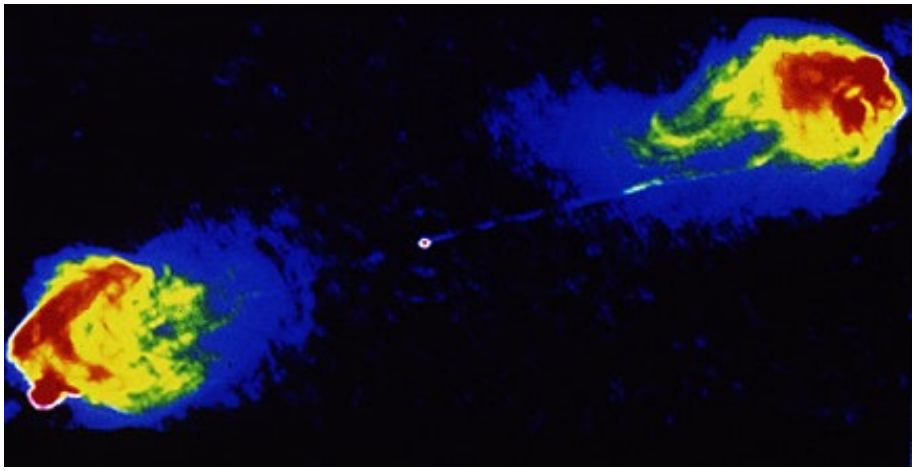

Figure 4.6: Cygnus A radio emission. Copyright 1995: Board of Trustees, University of Illinois. Taken from the webpage: http://archive.ncsa.illinois.edu/Cyberia/NumRel/RelUniverse2.html.

energy.

The low energy component is attributed to synchrotron radiation from relativistic electrons. This synchrotron emission extends from radio to the optical/X-ray region and is evidence that electrons are accelerated to extremely high energies (in a magnetic field of a few Gauss, TeV electrons are needed to produce X-ray synchrotron photons). However, the origin of these electrons and their production sites are still not understood. Different sites are suggested, such at the blazar central engine or at the shocks propagating through the parsec-scale jets. Observations of fast variability of the highest energy emission tend to favor an acceleration site close to the blazar central engine, the supermassive black hole (see e.g., Celotti et al. 1998), while invoking the absorption of the γ-rays by low energy radiation (see e.g., Ghisellini & Madau 1996a), the acceleration at some distance of the central engine is favored.

On the other hand, the high energy component of the SED can have different origins: hadronic or leptonic models (or both) can be favored depending on the collected data. While in leptonic models only electrons, positrons and photons are required, in hadronic models, protons, muons and pions are also involved.

One of the simplest leptonic model (in the sense of number of free parameters) is the synchrotron-self Compton model (SSC, see e.g., Bloom & Marscher 1996). In this model, the high energy part of the blazar SED is produced by low energy synchrotron photons up-scattered to higher energy via Inverse Compton process, with the particularity that the synchrotron photons are emitted and up-scattered by the same population of electrons. Therefore, a correlation is expected between the flux in the different energy band. As this correlation is not always observed, more parameters have been added to this model to fit the data, for instance, models with several populations of electrons have been suggested (see e.g., Graff et al. 2008). Other models suggest Inverse Compton emission processes on low energy photons external to the jet (see Fig. 4.5), e.g. originating from the accretion disk, from the jet/accretion disk radiation reprocessed in the BLR or from the radiation of the dusty torus. This model is known as external Compton model (EC, see e.g., Ghisellini & Madau 1996b; Reimer 2012). For instance, a combination of SSC and EC models are used in Fig. 4.7 to

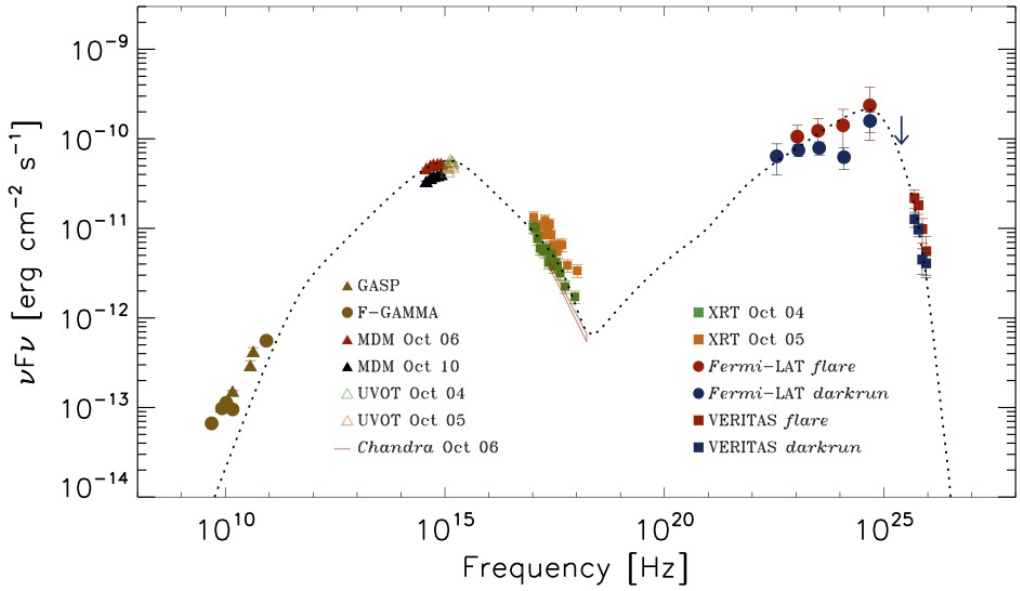

Figure 4.7: Broadband SED of the BL lac 3C 66A during a multi-wavelength campaign in 2008. The SED is fitted here with a leptonic model composed by SSC and EC contributions. Taken from (The Fermi-LAT collaboration et al. 2010).

fit the SED of the blazar 3C66A (The Fermi-LAT collaboration et al. 2010).

Hadronic models are based on the assumption that protons are accelerated together with electrons, presumably with higher efficiency due to less important energy losses. The main energy loss channels for the high-energy protons in the AGN environment are pion production in interactions with the low-energy protons (pp, see e.g., Nellen et al. 1993; Bednarek & Protheroe 1997) or in the interactions with radiation fields ($p\gamma$, see e.g., Mannheim & Biermann 1992; Mannheim 1993). An additional possibility is proton synchrotron radiation energy losses (Mücke & Protheroe 2001; Aharonian 2000; Mücke et al. 2003). The pp and $p\gamma$ interactions were already considered in Sect. 3.1.2. At the opposite to these interactions, in the case of synchrotron radiation of the accelerated protons, no neutrino emission is expected. Furthermore, to explain the observed emission with proton synchrotron a high magnetic field is required (of the order of 10^{13} times the one required with electrons of the same energy, see Sect. 3.3.1). For instance, in a study made by Aharonian (2000) for the case of Mrk 501, the observed γ-ray emission could be explained by the synchrotron radiation of protons if the compact region of size $R \sim 10^{15}$ cm is magnetized with magnetic fields of the order of $B \sim 30 - 100$ G, and if the energy of the protons exceeds $E_p \gtrsim 10^{19}$ eV. In this case, the synchrotron energy loss time for protons, $t_{syn,p} \sim 5 \times 10^4\,[B/100\,\mathrm{G}]^{-2}\left[E_p/10^{19}\mathrm{eV}\right]^{-1}$ s, could be comparable or shorter than the energy loss time via competing pp and $p\gamma$ interactions mechanisms. The characteristic energy of proton synchrotron photons would be $\epsilon_{syn,p} \sim 1\,[B/100\,\mathrm{G}]\left[E_p/10^{19}\,\mathrm{eV}\right]^2$ GeV. There are also other models which take into account the contribution of the synchrotron radiation emitted by the produced muon and pions to the high energy part of the SED (Rachen & Mészáros 1998).

Even if the multi-wavelength measurement of the SED is becoming more and more precise, it is difficult to distinguish in the high energy region the primary accelerated e^+e^- from the secondary e^+e^- induced by proton-initiated cascades via pp and $p\gamma$ interactions. Therefore, there exist hybrid

models, where both electrons and protons are accelerated directly at the source. For instance, in the *Proton Induced Cascade* model (PIC, Mannheim & Biermann 1992; Mannheim 1993), the protons undergo $p\gamma$ interactions on the synchrotron photon emitted by the primary electrons and trigger synchrotron-pair cascades in the jet via pion decay. On the other hand, in "purely hadronic" models, the fraction of primary electrons is negligible and all the power of electromagnetic emission from the source is supposed to originate from the interactions of high-energy protons. Based on this assumption, a neutrino emission comparable to the electromagnetic emission is expected (see Sect. 3.1.2 and Kelner et al. (2006); Kelner & Aharonian (2008)). The electromagnetic+leptonic part develops into an electromagnetic cascade that transfers all source energy to radio-to-γ-ray radiation. Therefore, within this model, the total power of neutrino emission is comparable to the power of the bolometric electromagnetic emission. A direct verification of the hadronic origin of blazar could be achieved by the observation of high-energy neutrinos from charged pion decays and would attest of the cosmic rays acceleration in AGNs. However, up to now no neutrinos have been detected from AGN in point-sources analysis (IceCube Collaboration et al. 2014).

4.3.2 Galaxy clusters

Galaxy clusters are mainly composed of three components: galaxies, hot gas (intracluster medium, ICM) and dark matter (DM). As they are the largest gravitationally bound structures in the Universe, according to the hierarchical structure formation scenario, they should be the latest structures to form and should continue to grow by accreting dark matter and baryonic gas. This structure formation scenario is predicted by the cold dark matter (CDM) model, which is favored by substantial theoretical and observational evidence (e.g., Komatsu et al. 2011).

Galaxy clusters can be used as tracers of the large-scale structure formation. For instance, the study of the redshift evolution of the galaxy cluster mass function is commonly used to this purpose. Based on equilibrium assumptions, the study of the luminous component (galaxies and hot gas) of galaxy clusters can provide information on the dark matter component and on the total mass of the cluster (see Allen et al. 2011, for a review). In this section, I would like to review how the mass of the cluster can be estimated from direct observables, like the X-ray emissivity of the ICM, or the galaxy kinematics in the cluster.

As galaxy clusters are virialized systems, one expects the accreted gas to be heated up to the virial value in the potential well of the cluster (Voit 2005). For a gas particle of mass $m_p\mu$ and kinetic energy $3/2k_BT_{gas}$ which is inside the potential of the cluster $-GM_{cl}m_p\mu/R_{cl}$ (where μ is the mean molecular weight and M_{cl} is the mass of the cluster), the virial theorem leads to

$$3k_BT_{cl} = \frac{GM_{cl}m_p\mu}{R_{cl}}. \tag{4.1}$$

Where the quantities are integrated over the radius of the cluster R_{cl}, ie $T_{cl} \equiv T_{gas}(R_{cl})$ and $M_{cl} \equiv M(R_{cl})$. The gas radiates in X-rays through bremsstrahlung and emission lines, which are sensitive to the temperature of the plasma. Therefore, the integrated mass within the radius R_{cl} can be inferred from X-ray measurements. By definition, R_{cl} corresponds to the virial radius, within which, the virial theorem is expected to hold.

Equivalently, one can infer the mass of the cluster by studying the kinematics of the galaxies inside the clusters. Indeed, the potential energy of a galaxy of mass M_{gal} in the cluster is $-GM_{cl}M_{gal}/(R_{cl})$ and its kinetic energy is $1/2M_{gal}\sigma^2$, where σ is the velocity dispersion of the galaxies in the cluster. Thus, the velocity dispersion of the galaxies in the cluster can be used to infer the total mass enclosed in the radius R_{cl}, as

$$M_{cl} \approx \frac{R_{cl}\sigma^2}{G}. \tag{4.2}$$

The mass of the cluster enclosed in the radius R_{cl} can be estimated, if either the average temperature T_{cl} or the velocity dispersion of the galaxies in the cluster are measured.

The mass profile can be estimated using the hydrostatic equilibrium equation. This assumes that the gravitational force is balanced by a pressure gradient force such that the system is in equilibrium. Assuming spherical symmetry, a system in hydrostatic equilibrium satisfies

$$\frac{dP}{dr} = -\rho\frac{d\Phi}{dr} = -\rho\frac{GM(r)}{r^2}, \tag{4.3}$$

where G is the gravitational constant and $M(r)$ is the mass enclosed within a radius r from the cluster center. This equation is usually used for an ideal gas, whose pressure can be expressed as: $P_{gas} = n_{gas}k_B T_{gas}$, where n_{gas} is the gas number density, k_B is Stefan Boltzmann constant and T_{gas} is the plasma temperature. Assuming that the equation of state of the medium is given by the ideal gas equation at each radius r, one can determine the mass enclosed in the radius r (see e.g. Sarazin 2008), as

$$M(r) = -\frac{k_B T_{gas}(r) r}{\mu m_p G}\left[\frac{dln\rho(r)}{dlnr} + \frac{dlnT_{gas}(r)}{dlnr}\right]. \tag{4.4}$$

where n_{gas} has been expressed in term of $\rho/\mu m_p$. This equation is valid if thermal pressure and gravity are the only forces at play in the system. If the non thermal pressure component is not negligible, the derived mass is an underestimation of the total mass.

Complementarily to these mass estimations, the mass of a cluster can be derived using gravitational lensing. Gravitational lensing effects are produced when photons propagate through an inhomogeneous gravitational field. Such measurements give information on the matter distribution between the emitting sources and the observer along the line of sight (see Bartelmann & Schneider 2001, for a review). As it is determined by the density distribution of the matter only, gravitational lensing measurements provide information on the total matter without requiring assumptions on the dynamical state of the matter (like virial equilibrium or hydrostatic equilibrium). There are different types of gravitational lensing. Here we will focuse on *weak* and *strong* lensing. In the case of weak lensing, the distortion of the images of individual background galaxies is too weak to be observed. However, in a large enough sample, the effects induced by the gravitational effect can be measured statistically and information on the large-scale mass distribution of the foreground galaxy cluster can be obtained. In the case of strong lensing, the distorted images of the background galaxies can be distinguished by their peculiar arc-like shapes (see Fig. 4.10). The dedicated study of these images gives information on the mass of the lensing cluster enclosed within these arcs. As large image distortions only appear when the background source is aligned with the center of the foreground cluster, strong lensing is only sensitive to the core of the lensing cluster. Therefore, the combination of weak and strong lensing allows the derivation of the projected mass distribution of the foreground cluster over different scales, from the center to the outskirts of the cluster.

Based on any of these mass estimation methods, one can count the number of clusters of a given mass at a given redshift and probe models of large-scale structure formation. For instance,

based on the cold dark matter model, massive clusters are not expected at large redshift, as they do not have time to accrete enough matter. Up to now, a few massive clusters have been detected at high redshift, like "el Gordo" at a redshift of ∼0.87 (see e.g., Menanteau et al. 2012). However, their presence is not in tension with the CDM cosmological model, as they belong to the very end tail of the mass function (Menanteau et al. 2012; Williamson et al. 2011).

Interestingly, the value of the estimated mass depends on the method used for its derivation. For instance, the mass of the cluster "el Gordo" through the Sunyaev-Zel'dovich effect only (Williamson et al. 2011) or from a multi-wavelength study of Menanteau et al. (2012), are respectively estimated to be $(1.89 \pm 0.45)10^{15}M_{sun}$ and $(2.16 \pm 0.32)10^{15}M_{sun}$. Although these two mass estimates agree within the error bars, if one is interested in the ranking of clusters as function of their mass, this could have consequences on the outcome of the analysis. For instance, in Waizmann et al. (2013), the authors reported that this difference in mass changed the rank of the cluster from the fifth to the third most massive cluster. Furthermore, discrepancies between masses estimated from X-rays and gravitational lensing have been also found by several authors (e.g., von der Linden et al. 2014). Therefore, the use of cluster masses as cosmological probe could lead to uncertainties in the constraints one could set on cosmological models. As a result, galaxy clusters may be strong cosmological probes, but to this end, the statistical methods may need some improvements. We will come back to this subject in Chapter 7.

During structure formation, galaxy clusters are expected to accelerate particles. Indeed, cosmic rays are thought to be accelerated in shock waves induced by cluster mergers and during the accretion of material from the cluster environment (e.g., Kang et al. 1996, 1997). Numerical simulations modeling the injection of cosmic rays at merger shocks during the formation of large-scale structures always report the presence of strong accretion shocks (i.e. with a Mach number $M \sim 10$) in the outer regions of galaxy clusters by the accretion of gas or low-mass systems, and weaker ($2 \leq M \leq 5$) and more energetic merger shocks induced by structure-formation processes in the central cluster regions (e.g. Miniati et al. 2000, 2001; Ryu et al. 2003; Pfrommer et al. 2008; Vazza et al. 2012).

Clusters can be subdivided into two classes, the cool-core (CC) and non-cool-core (NCC) clusters (Cavagnolo et al. 2009b). These two classes may correspond to different stages of the cluster evolution (e.g. Rossetti et al. 2011). Indeed, on the one hand, CC galaxy clusters are observed to contain a large amount of cold gas at their center. It implies that the gas has the time to condensate in the gravitational potential and therefore that CC galaxy clusters remain unperturbed on the scale of the cooling time of the gas. Interestingly, as the bremsstrahlung emission of the gas depends on the square of the gas density, the temperature of the gas is expected to drop at the center due to efficient cooling and to give rise to star formation processes at the cluster center (Fabian 1994). However, this is not observed (Peterson & Fabian 2006). This puzzle is known as the "cooling flow problem", which may be related to the fact that most of the CC clusters host active galactic nuclei at their center (e.g. McNamara & Nulsen 2007). On the other hand, NCC galaxy clusters are disturbed systems which have undergone a major merger in their recent past.

The observations of galaxy clusters at radio wavelengths (see e.g. Sarazin 1986; Feretti et al. 2012, for reviews) indicate the presence of relativistic particles confined in the cluster volume through large-scale magnetic fields (Völk et al. 1996; Berezinsky et al. 1997; Völk & Atoyan 1999). From Faraday rotation measurements of the synchrotron emission, the magnetic field in galaxy clusters is of the order of $0.1 - 10\ \mu$G (Feretti et al. 2012; Murgia et al. 2004), and implies the presence of GeV electrons. Several classes of extended radio sources are observed in galaxy

clusters, known as radio halos, relics and mini-halos: while radio halos are extended over the entire size of the cluster, radio relics are confined to the outer regions of the cluster and mini-halos are of smaller extension than the cluster size. For instance, the radio halo of the Coma cluster is shown in Fig. 4.8. It has been observed that the clusters hosting a radio halo are undergoing violent mergers and belong therefore to the NCC class (Cassano et al. 2011). Radio relics are also only observed in NCC clusters and seem to be produced by the acceleration of electrons in shocks (e.g., Enßlin & Brüggen 2002). An illustration of a radio relic is shown in Fig. 4.9, taken from van Weeren et al. (2010). One can clearly see the shock shape of the emitting region, indicating the acceleration of particles through DSA mechanism in a major merger event (van Weeren et al. 2010). Further investigations of this radio relic have shown that the distribution of the spectral indices of the emitting electrons is consistent with a outward-moving shock. Considering now mini-halos, they have been detected only in CC clusters. In Mazzotta & Giacintucci (2008), the presence of mini-halos has been explained as the consequence of a minor merger in CC clusters, which re-accelerate electrons by turbulence. They discard the implication of a central AGN as the cause of the mini-halo, based on the fact that the radiative lifetime of the relativistic electrons is too short to let the electrons be transported from the central galaxy up to the emission region. Only the presence of electrons is attested by these observations, nevertheless, protons are expected to be accelerated together with the electrons.

In galaxy clusters, cosmic rays are not expected to be only accelerated in cosmological shocks but they can also be injected into the cluster volume by central AGN (see e.g., Vazza et al. 2013). The latter are ubiquitous in the central galaxies of CC clusters (Burns 1990; Mittal et al. 2009). In some models (see e.g., Colafrancesco & Marchegiani 2008), cosmic rays are required to explain the cooling flow problem, by transferring part of their energy to the gas, which may heat the gas and therefore quench the star formation process. Furthermore, based on the model of our Galaxy, the cumulative effects of multiple supernovae explosion should also accelerate cosmic rays (see e.g., Völk & Atoyan 2000; Völk et al. 1996). However, based on the measurements of the gas metallicity in galaxy clusters, the rate of SNe seems to be lower than previously expected (see e.g., Zeimann et al. 2013; de Plaa et al. 2007).

Based on the model of our own Galaxy, after being accelerated, cosmic ray protons are expected to stay confined in galaxy clusters and to accumulate in the cluster's volume starting from the formation epoch (e.g., Berezinsky et al. 1997; Völk & Atoyan 1999). As a result, galaxy clusters are thought to be a huge reservoir of cosmic rays. This confinement may lead to proton-proton (pp) collisions between CR protons and the ambient thermal plasma. Indeed, the cooling time of GeV energy protons in the gas density is larger than the cluster age ($\sim$10 Gyr), such that the protons interact, but stay confined in the cluster. Therefore, as in the case of the diffuse γ-ray emission from the Galactic plane (see Sect. 4.2.2), an expected signature of the presence of cosmic ray protons in a galaxy cluster would be the detection of a diffuse gamma ray emission from the cluster volume (e.g. Blasi et al. 2007; Pfrommer et al. 2008; Pinzke & Pfrommer 2010). However, up to now this emission has not been detected (see also Pinzke et al. 2011) and numerous observational studies (e.g. Reimer et al. 2003; Perkins 2008; Aharonian et al. 2009; Aleksić et al. 2010; Ackermann et al. 2010; Arlen et al. 2012; Dutson et al. 2013) have only resulted in upper limits on the gamma-ray emission from clusters of galaxies.

If the diffuse γ-ray emission is so faint, one expects the detection of the accompanying neutrino diffuse flux from galaxy clusters to be even more challenging, due to the smaller neutrino cross section. For instance, in Murase et al. (2008), the authors predict that a detectable neutrino flux

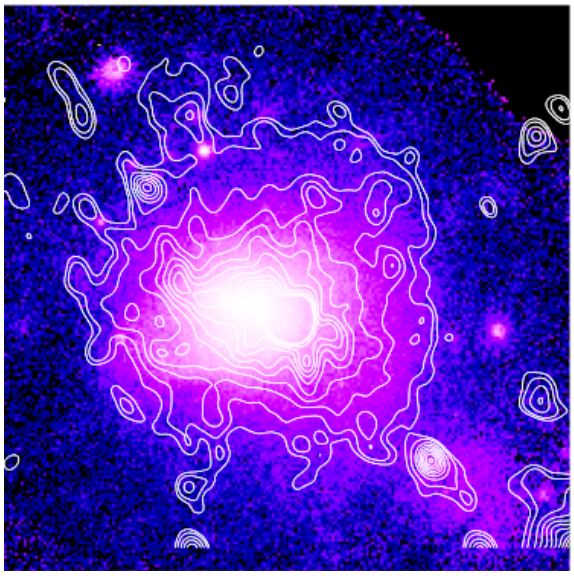

Figure 4.8: X-ray observations and contours of the radio halo of the COMA cluster. Taken from (Markevitch 2010).

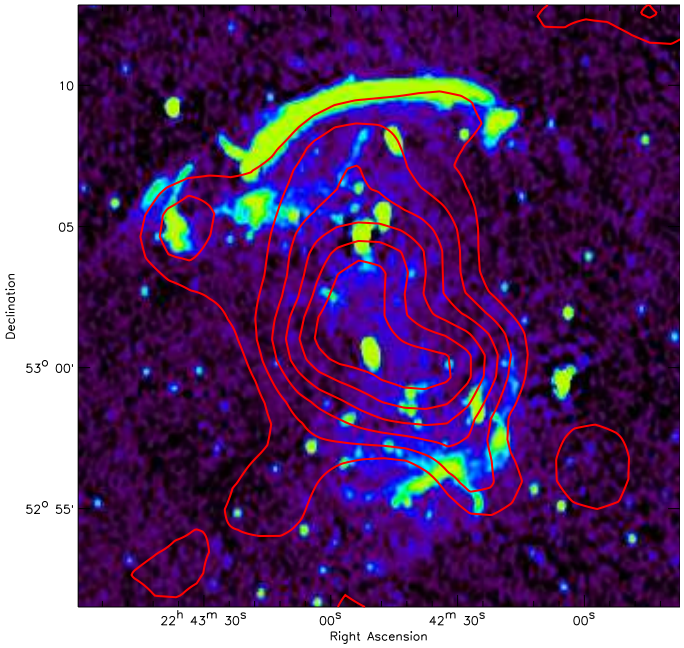

Figure 4.9: Radio relic in the northern outskirt of the galaxy cluster CIZA J2242.8+5301. Radio image at 1.4 GHz with X-ray emission from the ICM detected by ROSAT superimposed. Taken from (van Weeren et al. 2010).

Figure 4.10: Strong and weak lensing of the cluster Abell 2218. Image obtained with the Hubble Space Telescope. Credit: NASA, ESA, and Johan Richard (Caltech, USA).

should be present in galaxy clusters if these latter contribute to the acceleration of UHECRs. Based on this model, in (Abbasi et al. 2011; IceCube Collaboration et al. 2014) the IceCube collaboration studied the stacked signal of six close galaxy clusters and have set upper limits to the neutrino signal, which lie above the predictions of Murase et al. (2008). Therefore, in my thesis, I will not use the multi-messenger approach to study galaxy clusters, but I will instead combine X-ray and γ-ray observations to constrain the cosmic ray content in galaxy clusters.

4.4 Summary

As we have seen in this chapter, the sources of cosmic rays can be Galactic and extra-galactic.

Regarding the Galactic candidates, cosmic rays are expected to be produced in our Galaxy by supernovae explosions (isolated or in superbubbles) and by pulsars. The presence of cosmic rays in these sources has been attested for instance by the spatial correspondence between the γ-ray emission regions and the target molecular cloud emission regions (see for instance Fig. 4.2 of the Cygnus Region) or by the neutral pion decay signature in SNR.

Considering the extragalactic sources, AGN and galaxy clusters are potential sources. However, evidence of the presence of cosmic rays in these sources are still missing. The presence of accelerated nuclei and protons in extragalactic sources could be attested by the detection of a very-high-energy (VHE) neutrino flux which would match with the expectations derived from γ-ray and radio observations (if one assumes that the emitting electrons are secondaries produced in hadronic interactions). Finally, as we saw, galaxy clusters are not only potential source of cosmic rays, but also tracers of the large-scale structures formation.

Chapter 5

γ-rays and neutrinos from the Galactic plane

5.1 Motivations

As introduced in Chap. 4, the Galactic plane is the strongest γ-ray source in the sky (see also Fig. 3.24). This γ-ray emission is due to isolated γ-ray point sources superimposed on a diffuse γ-ray emission. In this chapter, I will consider only the diffuse γ-ray emission. This latter is dominated by the cosmic ray interactions with the interstellar medium (pp interactions), which result in production and subsequent two-photon decays of neutral pions (see introduction, Sect. 4.2). The same interactions also lead to neutrino emission from the Galaxy, via production and decays of charged pions (Stecker 1979; Berezinsky et al. 1993). As a result, a neutrino flux is also expected from the Galactic plane. The neutrino and γ-ray signals from the cosmic ray interactions are expected to have comparable flux and energy distributions (Stecker 1979; Kamae et al. 2006; Kelner et al. 2006, see also Chapt.3.1.2). Therefore, the Galaxy is expected to be (one of) the strongest astronomical source of high-energy neutrinos.

In this section, I aim to determine within which exposure time, the IceCube detector, which is the largest neutrino detector ever built, would be able to detect the expected neutrino signal. This study has been published in Tchernin et al. (2013b).

5.2 Scan of the Galactic plane with the Fermi-LAT telescope

The diffuse γ-ray (and neutrino) emission is extended along the Galactic plane. As the angular resolution of the IceCube detector is of about 1° (see Fig. 3.15), the diffuse γ-ray emission (and neutrino) is collected on degree scale circular regions centered on each Galactic longitude l. We choose two different angular radii for the analysis: 2°and 4°. We do not know a priori what would be the optimal size of the extended region on which the neutrino data need to be collected, but the best size of the collecting area will be determined by the extension of the diffuse γ-ray emission.

The γ-ray spectra obtained with Fermi-LAT over the energy 10-300 GeV can be described by a power-law

$$\frac{dN}{dE}|_\gamma = A_{100,\gamma}\left(\frac{E}{100\ \mathrm{GeV}}\right)^{-\gamma_\gamma}. \tag{5.1}$$

With γ_γ the spectral index and $A_{100,\gamma}$ the normalization at 100 GeV. The spectral indices of the γ-ray spectra have been derived from the ratio of the integrated fluxes in two energy bins of equal width in log scale: $N_{10-31.6}$ and $N_{31.6-100}$, respectively in the $10 - 31.6$ GeV and $31.6 - 100$ GeV energy ranges (i.e. from the hardness ratio between the two bands, neglecting the flux above 100 GeV because of its low statistics):

$$\gamma_\gamma = 1 - 2\log\left(N_{31.6-100}/N_{10-31.6}\right). \tag{5.2}$$

The uncertainties on the spectral index corresponding to 1σ are computed with (using $\log(x) = ln(x)/ln(10)$):

$$\Delta\gamma_\gamma = [(\frac{-2}{(N_{31.6-100})^{0.5}\ln(10)})^2 + (\frac{2}{(N_{10-31.6})^{0.5}\ln(10)})^2]^{0.5}. \quad (5.3)$$

Figures 5.1 and 5.2 show the profiles of the intensity of the emission from the Galactic plane as a function of Galactic longitude for circular regions of radii 2° and 4° around each Galactic longitude of the Galactic plane. To produce these figures, the Fermi data have been collected over the period from August 2008 to October 2012 and filtered using the *gtselect* and gtmktime tools. Following the recommendations of the LAT collaboration[1], only events belonging to the so-called clean class (`evclass=3`), which are the more likely to be γ-ray, have been retained. The flux has been estimated by dividing counts by exposure calculated using the *gtexposure* tool.

5.3 Estimation of the neutrino flux from the γ-ray observations

Based on the known relations between the γ-ray and neutrino emission produced in pp interactions: (see e.g., Stecker 1979, and Sect. 3.1.2), the VHE neutrino signal from the Galactic plane can be reliably estimated based on the observed γ-ray signal.

As the γ-ray flux can be described by a power-law of parameters γ_γ and $A_{100,\gamma}$ (see Eq. [5.2]), the expected neutrino signal can also be described by a power-law of parameters $A_{100,\nu}$ and γ_ν (the normalization of the neutrino flux at 100 GeV, and the spectral index of the neutrino spectrum), as

$$\frac{dN}{dE}|_\nu = A_{100,\nu}\left(\frac{E}{100\ \mathrm{GeV}}\right)^{-\gamma_\nu}. \quad (5.4)$$

In this study, I use the relations between the normalization and the slopes of the spectra of the parent protons, muon neutrinos and γ-rays from π^0 decay from Kappes et al. (2007): $\gamma_\nu \approx \gamma_\gamma \approx (\gamma_p - 0.1)$ and $A_{100,\nu} \approx A_{100,\gamma}(0.71 - 0.16\gamma_p)$. These relations are based on the secondary spectra parametrizations of Kelner et al. (2006), see also Sect. 3.1.2.

I estimate the neutrino flux in this way for each Galactic longitude l and for the two angular radii ψ =2 and 4°. As the Fermi detector is sensitive to energy between 30 MeV and 300 GeV, which lies below the energy band in which IceCube is most sensitive, the neutrino spectra are interpolated to higher energy, assuming that the spectral index remains constant.

5.4 Computation of the probability of detection

Let us first determine qualitatively which part of the Galactic plane could be detected with the IceCube detector. For the sources located in the Northern Hemisphere, one can see from the γ-ray profiles shown in Fig. 5.1 and 5.2 that the brightest γ-ray (and hence neutrino) emission comes from two equally bright locations: from the Galactic longitude $\simeq$ 33°, around HESS J1857+028, and from the Cygnus region at Galactic longitude $\simeq$ 80°. So as a first guess, this indicates that the Galactic plane will appear as isolated extended excesses at the positions of the Cygnus region and/or l = 33° in the IceCube detector.

Furthermore, as the atmospheric neutrino flux is measured to have a power law distribution of spectral index close to 3.7 between 1 TeV and 1 PeV (Honda et al. 2007), it implies that the harder the astrophysical neutrino spectra is, the easiest the source can be detected on the top

[1] `http://fermi.gsfc.nasa.gov/ssc/data/analysis/`

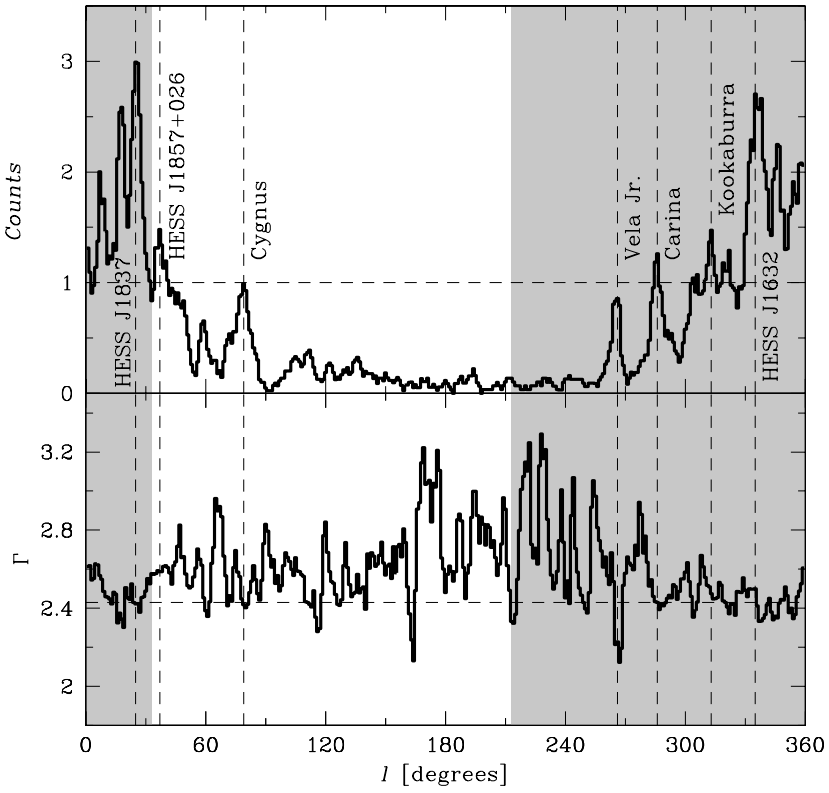

Figure 5.1: Profiles of the intensity (top) in the energy band above 100 GeV and the spectral index (bottom) of the γ-ray power-law emission obtained with Eq. [5.2]. Fermi-LAT counts are collected from the circular regions of radius $\psi = 2^\circ$ around each Galactic longitude of the Galactic plane. The fluxes are normalized on the flux from the Cygnus region above 100 GeV at longitude $l = 79 - 80^\circ$ (used value: $3.75 \cdot 10^{-12}$ 1/cm^{2}s). The shaded region marks the part of the Galactic plane in the Southern Hemisphere. Vertical lines with the names show locations of bright extended VHE γ-ray sources. Taken from (Tchernin et al. 2013b).

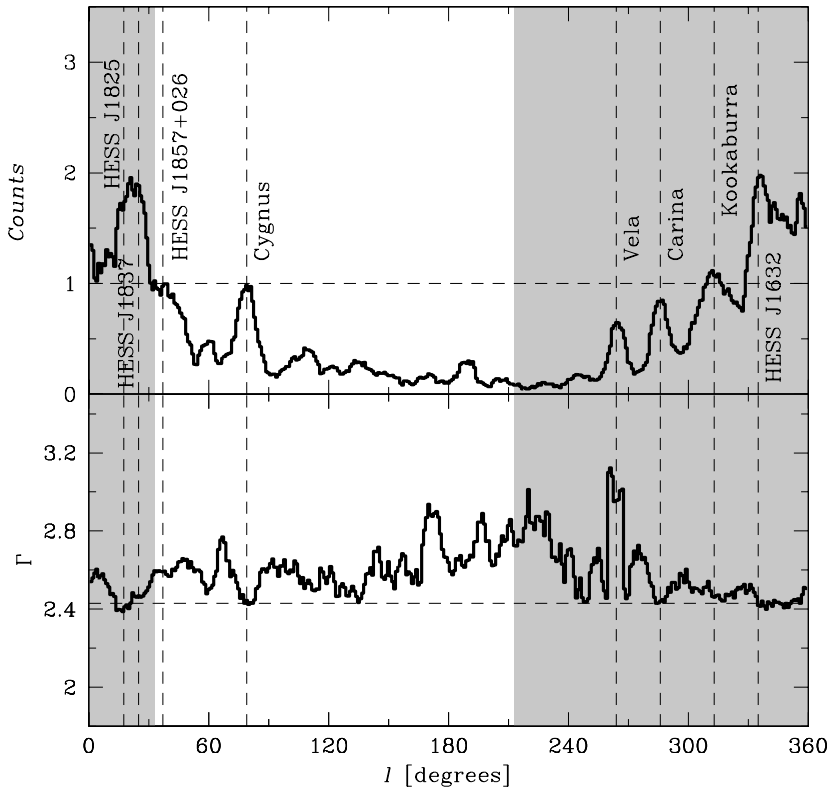

Figure 5.2: The same as in Fig. 5.1, but for the source region of angular radius $\psi = 4°$. The intensity profile has been normalized to the flux of the Cygnus region above 100GeV ($6.25 \cdot 10^{-12}$ $1/\mathrm{cm}^2\mathrm{s}$). Taken from (Tchernin et al. 2013b).

of the atmospheric neutrino flux. Therefore, as the Cygnus region spectrum is harder than that corresponding to the excess located at $l = 33°$, the neutrino signal in IceCube from the direction of Cygnus should be significantly stronger than that from the $l = 33°$ region. We will now test this prediction in a more quantitative way.

The number of expected detected signal events in a given time T in a circular region of extension ψ around the Galactic longitude l is

$$N_{signal}(E)|_{\psi,l} = T \int_{E_{min}}^{E_{max}} A_{eff}(E, \delta(l)) \frac{dN}{dE}|_{\psi}(E, l) dE. \tag{5.5}$$

$dN/dE|_{\psi}(E, l)$ is the neutrino flux integrated in the region of angular radius ψ which has been estimated from γ-ray observations in the previous section and $A^{eff}(E_{\nu}, \delta)$ is the detector effective area at the source declination δ (similar to the one shown in Fig. 3.16, but for IC-79 instead of IC-40). The expected number of background events can be derived in the same way

$$N_{bgd}(E)|_{\psi,l} = \pi\psi^2 T \int_{E_{min}}^{E_{max}} A_{eff}(E, \delta(l)) \frac{dN_{atm}}{dE d\Omega}(E, \delta(l)) dE. \tag{5.6}$$

Where $dN_{atm}(E, \delta)/(dE d\Omega)$ is the spectrum of the atmospheric neutrinos arriving from a declination δ in a solid angle $d\Omega$ (Honda et al. 2007, see Eq. 3.18).

The number of expected signal events, N_{signal}, and background event, N_{bgd}, are computed around each Galactic longitude for the two angular radius sizes introduced above: ψ=2°and 4°.

We want now to compute the probability to have at least $(N_{signal} + N_{bgd})$ neutrino counts from a given direction on the sky while the expected level of the atmospheric neutrino background is N_{bgd}. Giving that the detection of neutrinos follows Poisson statistics, the background fluctuations around N_{bgd} can be expressed with the help of the probability mass function, $f(N_{obs}; N_{bgd}) = (e^{-N_{bgd}}(N_{bgd})^{N_{obs}})/N_{obs}!$, where $N_{obs} = (N_{signal} + N_{bgd})$ is the observed value. This probability can be obtained as

$$P(N \geq N_{obs}) = 1 - P(N < N_{obs}) = 1 - \sum_{N=0}^{N_{obs}} \frac{e^{-N_{bgd}}(N_{bgd})^N}{N!}. \tag{5.7}$$

This corresponds to the probability that the observed number of events N_{obs} can be produced by background fluctuations. The smallest is this probability, the more significant is the source detection.

From Eq. [5.5]-[5.6], we can see that the number of signal and background events depend on the energy range at which we consider the events. More specifically, they depend on the lower bound of the energy range, as the statistics at E_{max} is too low to affect significantly the result. In this analysis, the value of E_{max} is fixed to 10^9 GeV. It implies that for each ψ, one can find the value of E_{min} such that the signal-to-noise ratio is maximal or equivalently, for which the probability (Eq. [5.7]) is minimal. This value of E_{min} depends on the spectrum of the astrophysical signal (on its spectral index and normalization, see Eq. [5.4]). For instance, if the spectral index of the astrophysical neutrino spectrum is hard, the optimal value of E_{min} can be large because the atmospheric neutrino flux is negligible at high energy. On the other hand, for a soft astrophysical neutrino spectra, a too small value of E_{min} would dilute the signal in the more abundant background counts and would strongly reduce the detection efficiency of the source.

A scan to obtain the optimal E_{min} for each l has been performed for the two values of ψ (2 and 4°), with the additional condition that N_{signal} is required to be larger than one. Once the optimal value of E_{min} is found, the exposure time is set by the condition that the probability falls below $3 \cdot 10^{-7}$ (which corresponds to the 5σ confidence level threshold).

5.5 Results: the neutrino signal from the Galactic plane

The Poisson probability described by Eq. [5.7] and minimized by the optimal choice of E_{min} is shown in Figs 5.3-5.6 for different exposure times of 10 and 20 years, and different circular radius $\psi = 2$ and 4°.

From Figs. 5.3 and 5.4 one can see that the strongest excess (i.e. the strongest inconsistency with the background-only hypothesis) is found in the Cygnus region. A ten-year exposure is, however, not sufficient for a detection of the Cygnus region at the 3σ level, except if the spectral index remains as hard as the one detected with Fermi at higher energies. As shown in Fig. 5.4, the low-declination region at $l = 33°$ with a stronger flux in the 100 GeV band (see Fig. 5.1) gives a weaker excess. This is explained by a softer spectrum of the source, which results in a lower number of source counts in the IceCube energy range. This result is consistent with our expectations. Furthermore, a source at a Galactic longitude of 60° is also present. This is probably due to its hard spectrum, but due to its low normalization, a ten-year exposure do not seem enough for its detection.

Figures. 5.5 and 5.6 show that a 20-year exposure of IceCube should be sufficient for a detection of the Cygnus region at 3σ level, for both source regions of radius $\psi = 2°$ and $\psi = 4°$(marginally). The probability of detection is higher if the source region is smaller, which is explained by a higher level of atmospheric neutrino background than signal events in this larger region. It is interesting to note that apart from the Cygnus, none of the other regions in the part of the Galactic plane in the Northern Hemisphere will be detectable even with a 20-year exposure of IceCube in the muon neutrino channel. It appears that the part of the Galactic plane in the Northern Hemisphere is not a bright neutrino source.

The calculations are done for the 79 string configuration of the IceCube detector (IC-79), using the IceCube performances published in (Aguilar 2013). The IC-79 effective areas are close to those of the final configuration with 86 strings (IC-86), so that the potential of IceCube for the detection of the neutrino emission from the Galactic plane can be correctly estimated based on the known IC-79 instrument characteristics.

5.5.1 The neutrino signal from the Cygnus region

Figure 5.7 shows a Fermi-LAT countmap of the Cygnus region in the energy band above 100 GeV, smoothed with a 1 degree Gaussian to highlight the extended structures. As one can notice, the dominant source in the Cygnus region in this energy range is the γ-Cygni supernova remnant, which contains a pulsar wind nebula and a shell-type supernova remnant. The overall extent of the remnant is about 1°.

The spectrum of the γ-ray emission from a circular region of radius $\psi = 1°$ centered on the γ-Cygni supernova remnant position is shown in Fig. 5.8. At the energies below $\sim$ 10 GeV, the emission from the source is strongly dominated by the emission from the pulsar PSR J2021+4026 (Abdo et al. 2009d). Above 10 GeV the pulsar emission is suppressed and a separate power-law-type emission component is present. The same power-law components are present also on a larger

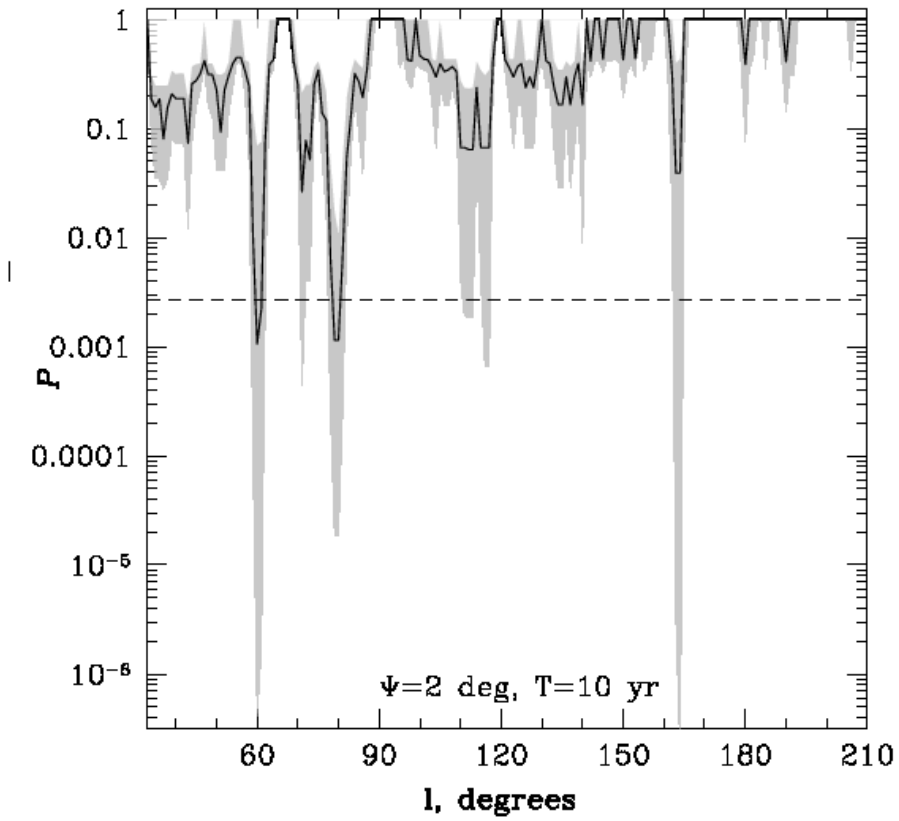

Figure 5.3: Poissonian probability that the neutrino signal expected from the gamma-ray observations are due to the fluctuations of the atmospheric neutrino background (Eq. 5.7) for 10 years exposure time with IceCube in the IC-79 configuration and a 2 degree region of interest around each longitude of the Galactic plane (l) in the Northern Hemisphere ($l \in [34 : 220]^\circ$). A line corresponding to the probability of 3σ has been added to help the readability. Key: in black, the probability using the spectral index computed with the equation 5.2; in grey, the uncertainties of the probability corresponding to 1 σ. Taken from (Tchernin et al. 2013b).

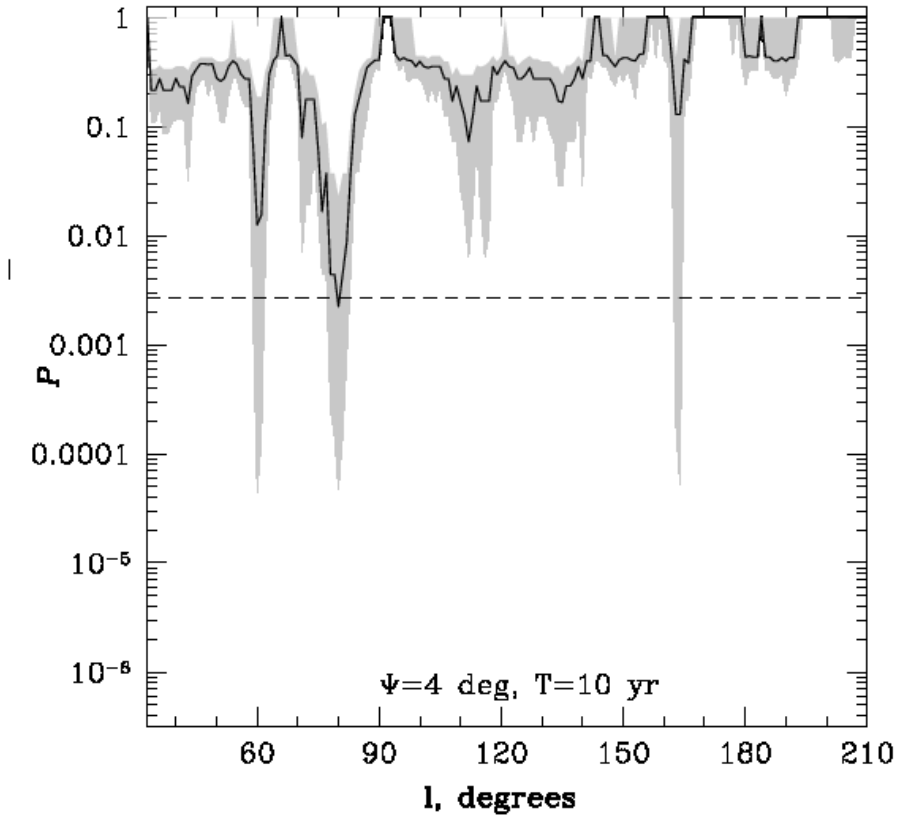

Figure 5.4: The same as in Fig. 5.3, but for a 4 degree region of interest. Taken from (Tchernin et al. 2013b).

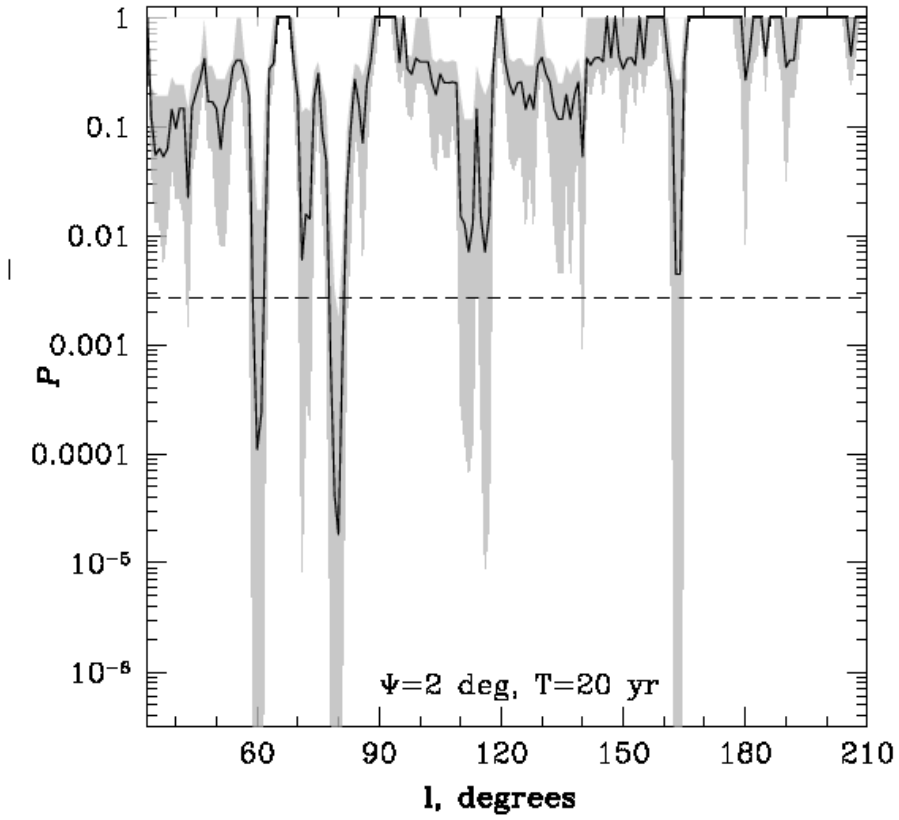

Figure 5.5: The same as in Fig. 5.3, but for a 20-year exposure. Taken from (Tchernin et al. 2013b).

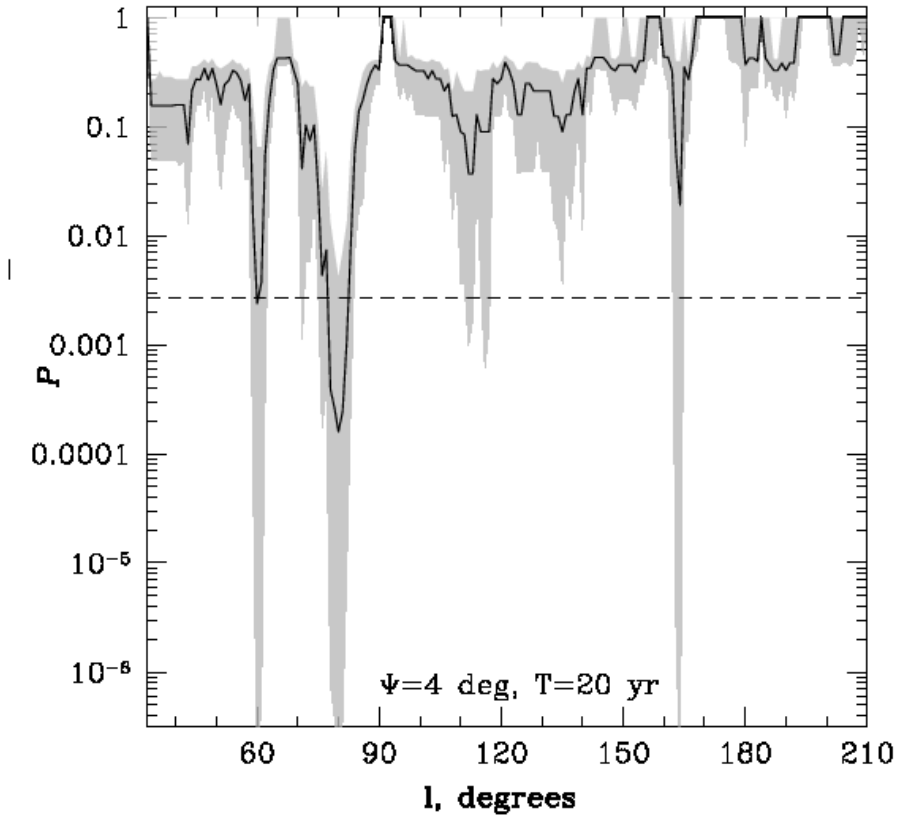

Figure 5.6: The same as in Fig. 5.5, but for a 4 degree region of interest. Taken from (Tchernin et al. 2013b).

ψ	RA	DEC	l	b	E_{thr}	$A_{100,\nu}$	γ_ν
2°	306.6°	40.7°	79.0°	1.5°	$4.0 \cdot 10^4$	$1.05 \cdot 10^{-12}$	2.40
4°	308.3°	41.7°	80.5°	1.0°	$3.2 \cdot 10^4$	$1.65 \cdot 10^{-12}$	2.42

Table 5.1: Optimal positions and energy thresholds of the source signal regions for the search of neutrino emission from extended regions. The Col. 1 shows the radius of the source region circle; positions in equatorial and Galactic coordinates are given in Cols. 2-4. Column 6 shows the optimal energy threshold (in GeV), while the two last columns show the expected muonic neutrino signal deduced from the observed γ-ray signal using Kappes et al. (2007): normalization at 100 GeV in units 1/GeVcm^{2}s and spectral index, respectively (see Eq. [5.4]). Taken from (Tchernin et al. 2013b).

angular scale ($\psi = 2°$ and $\psi = 4°$, as shown in Fig. 5.8) and the spectral index of the power-law $\gamma_\gamma \simeq 2.4$ remains remarkably stable across all the different angular scales. No sign of high-energy cut-off of this component is found in the Fermi data up to 300 GeV. Moreover, observations of the region in the multi-TeV energy band by VERITAS (Weinstein & for the VERITAS Collaboration 2009) and MILAGRO (Abdo et al. 2007) reveal a strong emission at the energies up to tens of TeV. The measurement of the flux of multiple sources in the Cygnus region seen by MILAGRO in the 10 TeV band agrees well with a simple power-law extrapolation of the Fermi-LAT spectrum of extended emission from the Cygnus region. This agreement allows us to make a conjecture that the emission found by MILAGRO is just the high-energy counterpart of the cosmic ray powered γ-ray emission from the freshly accelerated cosmic rays injected either by the Cygnus OB2 association (Ackermann et al. 2011b) or by the γ-Cygni / PSR J2021+4026 composite supernova remnant (Neronov & Semikoz 2012).

This interpretation is consistent with the analysis performed by the Fermi collaboration. Indeed, as seen in Sect. 4.2, the multi-wavelength observations (γ-ray and mid infrared) of the Cygnus region indicate the presence of cosmic rays which interact with the interstellar medium (see Fig. 4.2). This automatically implies the presence of a hard spectrum neutrino emission from this region which accompanies the observed hard γ-ray spectrum (of spectral index $\gamma_\gamma \sim 2.4$).

Since the γ-ray emission from the Cygnus region is produced via cosmic ray interactions with the gas of the interstellar medium, the imaging characteristics of the neutrino signal could also be derived directly from the γ-ray data. We have inspected the γ-ray data with the goal of localizing the circular source regions of the radii $\psi = 2°$, and 4°, which produce the highest gamma-ray (and hence neutrino) signal above 100 GeV. Figure 5.9 shows the locations of the highest signal circles on the sky. Table 5.1 lists the positions and expected neutrino fluxes in these circles. The information of these two *a priori* coordinates of highest signal could be useful for IceCube to maximize the strength of the neutrino signal by correctly localizing the region used as the source region in the analysis of the data, and limiting in this way the trial factor associated with scanning the entire Cygnus region.

These predictions may potentially be confirmed by the IceCube collaboration in a recent analysis (IceCube Collaboration et al. 2014). The authors performed a stacking analysis of six MILAGRO TeV sources and obtained a stacked signal consistent with a probability of 2% with background fluctuations. As four of these six sources are located in the Cygnus region, this may confirm our prediction that the Cygnus region should become a detectable neutrino source after a

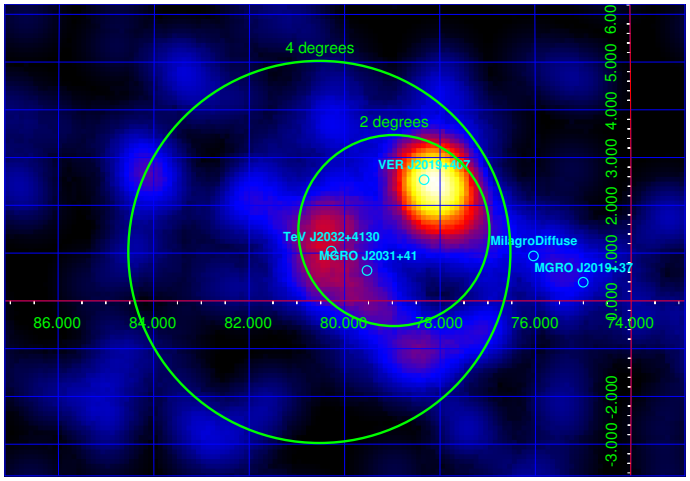

Figure 5.7: The Fermi-LAT countmap of the Cygnus region in the energy band above 100 GeV, smoothed with a Gaussian kernel of 1 degree. The regions indicated by the green circles are used for the spectral extraction of Fermi-LAT data and have radii of 2 and 4 degrees (from small to large). Positions and names on known VHE γ-ray sources are marked. Taken from (Tchernin et al. 2013b).

longer exposure time.

5.5.2 The neutrino signal from the inner Galaxy with a hypothetical detector in the Northern Hemisphere

Our results show that from the whole Northern Hemisphere, only the Cygnus region would be detectable. Nevertheless, as shown in Fig. 5.1-5.2, the strongest γ-ray and neutrino signal come from the inner part of the Galactic plane which is entirely situated in the Southern Hemisphere.

To demonstrate the potential of neutrino astronomy which might be done with a km^3 class neutrino detector in the Northern Hemisphere, I performed with my co-authors an analysis identical to that reported in the previous subsection, but assuming a hypothetical IceCube-like neutrino detector situated at the North rather than the South Pole. One candidate for this km^3 class neutrino detector in the Northern Hemisphere is the KM3NeT project to be located in the Mediterranean Sea and which is currently in the design phase (Kappes & KM3NeT Consortium 2007).

The results of the calculations for the Northern IceCube are shown in Figs. 5.10 and 5.11 for a five-year exposure. A detector identical to IceCube, but in the Northern Hemisphere would detect some ~ 3 sources at the 5σ level with just five years of operation (compared with the ten to twenty years needed for a 3σ evidence of single source in real IceCube), if the region of interest is of 2 degrees. For some of the detected sources, the imaging analysis might be possible with a five-year data set: one can see that several sources would be significantly detectable in both $\psi = 2^\circ$ and $\psi = 4^\circ$ regions.

In general, all the isolated extended sources detectable at the 5σ level within a five-year exposure by the Northern IceCube are locations with a hard emission spectrum. It is interesting to note that the Galactic center itself would not be detected by the Northern IceCube. This is explained by the relatively soft spectrum of the source in the Galactic center (see Fig. 5.1 and 5.2). Table 5.2

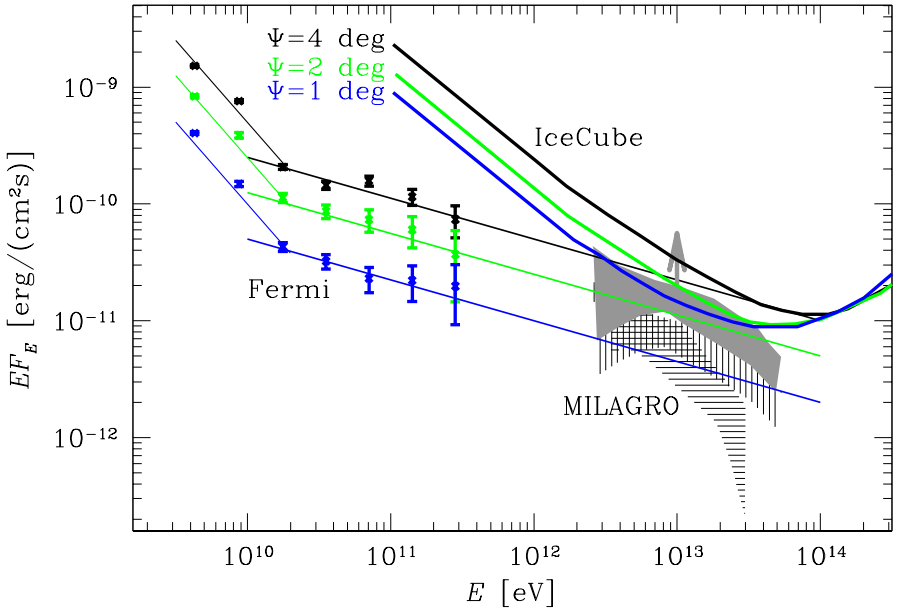

Figure 5.8: Data points: Fermi-LAT spectra of the 1, 2 and 4 degree regions in the Cygnus region (from bottom to top). Straight lines show fits to the spectra with extrapolations to higher energies. Curves represent the 90% confidence level sensitivities of IceCube (2 yr exposure) for the extended sources of the size 1, 2 and 4 degree (from bottom to top) for all neutrino flavors, assuming that at Earth, after oscillations, the muonic neutrino flux is one third of the total neutrino flux (Learned & Pakvasa 1995). See Chapter 6.3 for the derivation of these sensitivity curves. The horizontal hatched region shows the spectrum of the VHE γ-ray source MGRO J2019+37. The vertical hatched region shows the spectrum of MGRO J2031+41. The gray shading shows the sum of the fluxes of MGRO J2019+37 and MGRO J2031+41 (Abdo et al. 2012). Taken from (Tchernin et al. 2013b).

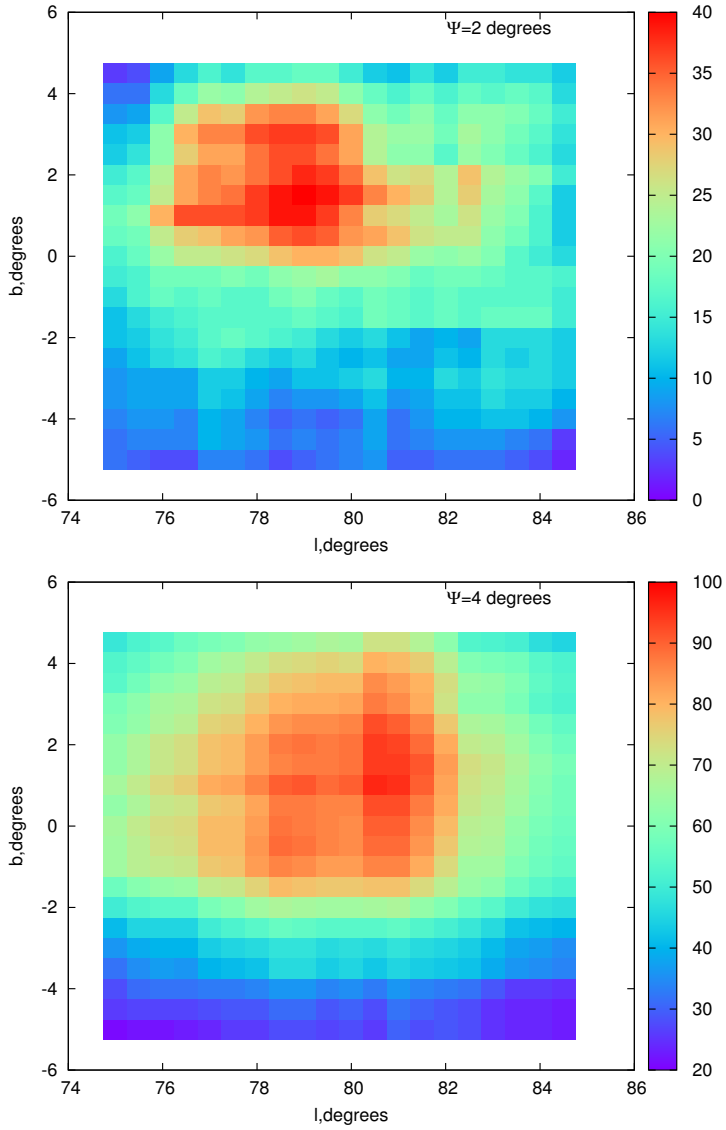

Figure 5.9: Top: The strength of the γ-ray (and hence neutrino) signal within circles of radius $\psi = 2^\circ$ at different locations inside the Cygnus region. Each pixel shows the position of the center of the circle. The color scale shows the number of gamma-ray counts in the circles. Bottom: The same as the left panel, but for $\psi = 4^\circ$. Taken from (Tchernin et al. 2013b).

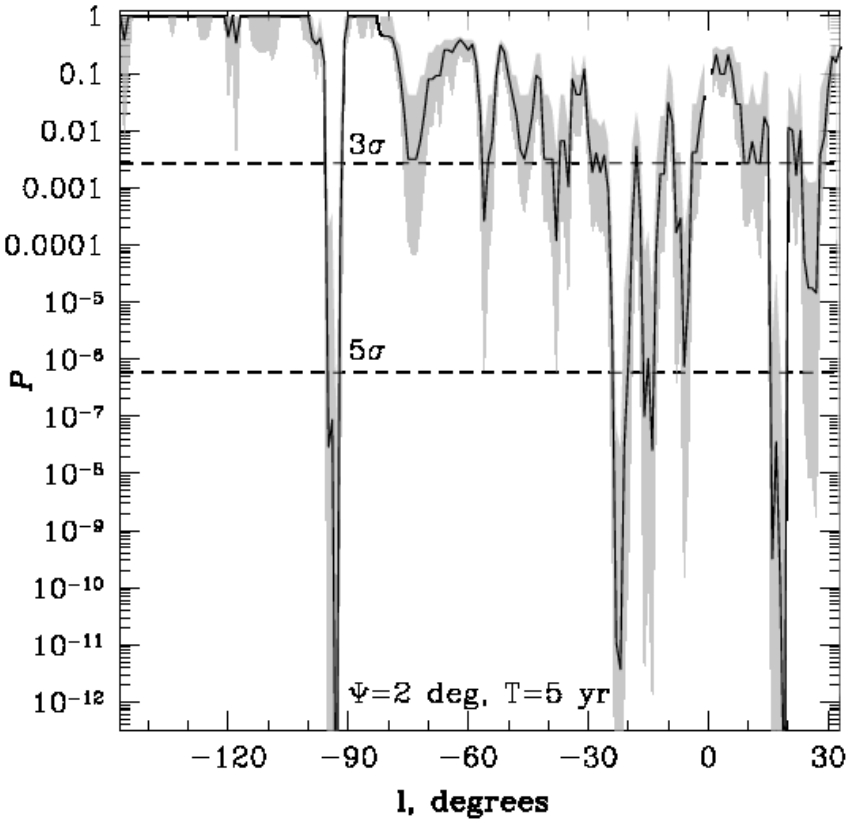

Figure 5.10: The same as in Fig. 5.3, but for a hypothetical Northern IceCube detector situated at the North Pole and sensitive for the sources in the Southern Hemisphere. For five years of exposure. Taken from (Tchernin et al. 2013b).

summarizes the position and neutrino spectral information of the sources that could be detectable by a neutrino telescope located in the Northern Hemisphere such as KM3NeT. In the following I will describe each of these potential neutrino sources.

Located at a Galactic longitude of 19°, the source *HESS J1825-137* has been detected with the HESS telescope (Aharonian et al. 2005a) as an extended source. This source could be associated with the X-ray pulsar wind nebula G18.0–0.7 (Aharonian et al. 2005c) and with the pulsar PSR B1823-13 (de Jager et al. 2005). In de Jager et al. (2005) the authors suggest that the extended emission of *HESS J1825-137* is the result of the expansion of a supernova remnant in an inhomogeneous medium.

The second source I would like to introduce is the supernova remnant *Vela Jr.* It has been discovered in 1998 using X-ray images performed by ROSAT (Aschenbach 1998). It is one of the most luminous Galactic sources in the VHE energy band and the only potential source which is not located in the Galactic ridge region ($l \in$[-30;30]°). Its flux has been reported to be of about 10% of Crab at 1 TeV by Katagiri et al. (2005). The distance to *Vela Jr.* has been estimated to be on the order of 200 pc (Aschenbach et al. 1999). The CANGAROO-II imaging atmospheric Cerenkov telescope detected the source at the 6 σ level in 100 hours (Katagiri et al. 2005). This

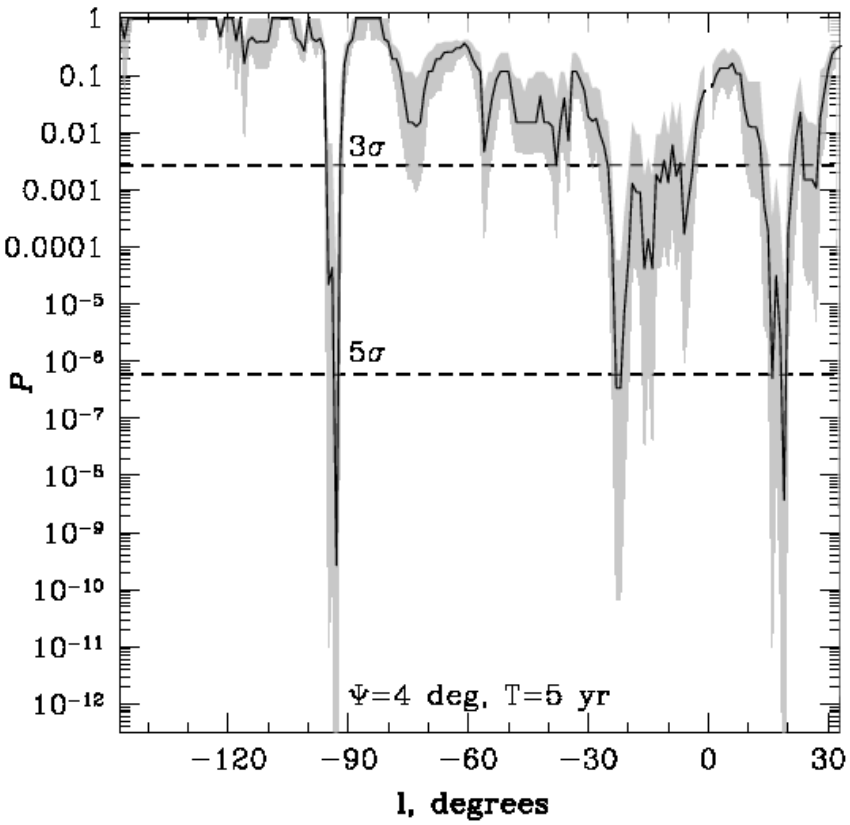

Figure 5.11: The same as in Fig. 5.10, but for a 4 degree region of interest around each Galactic longitude. Taken from (Tchernin et al. 2013b).

Gal. longitude (l)	*Name*	E_{thr}	$A_{100,\nu}$	γ_ν
19°	HESS J1825-137	$2.5{\cdot}10^4$	$3.0{\cdot}10^{-12}$	2.30
267°	Vela Jr.	$3.2{\cdot}10^4$	$1.1{\cdot}10^{-12}$	2.12
337-338°	HESS cluster	$2.0{\cdot}10^4$	$\sim 3.2{\cdot}10^{-12}$	2.33

Table 5.2: List of the sources located in the Southern Hemisphere potentially detectable with a detector similar to the IceCube detector located in the North Pole (see Fig. 5.10). The name and position of these sources are given in column 1 and 2. The third column shows the optimal energy threshold for the detection, while the two last columns show the expected neutrino flux (see Eq. (5.4)) for a considered region of 2 degrees around the Galactic longitude listed in the Col. 1. Units for E_{thr} and $A_{100,\nu}$ are the same as in Table 5.1. The so-called HESS cluster is a generic term for the sources detected by HESS in the region around $l = 337 - 338°$. Taken from (Tchernin et al. 2013b).

source has been also detected by the H.E.S.S. telescope (Aharonian et al. 2005b; Paz Arribas et al. 2012) with a differential gamma-ray spectrum that follows a power-law distribution of a spectral index ~2.1. This flux measurement is consistent with the flux obtained at lower energy with the Fermi telescope (see Table 5.2). According to Aschenbach et al. (1999), this remnant is quite young, with an age of 680 years, and thus could be the site of recently accelerated cosmic rays.

Finally the extended emission detected by the Fermi telescope at Galactic longitude around $l = 337 - 338°$ has a counterpart at higher energy. The inner Galactic plane survey of H.E.S.S. (Aharonian et al. 2006b) has revealed several sources located in the considered region: *HESS J1632-478* ($l = 336.38°$, $b = 0.19°$), *HESS J1634-472* ($l = 337.11°$, $b = 0.22°$), and *HESS J1640-465* ($l = 338.32°$, $b = 0.02°$). Close to the position of *HESS J1632-478* ($l = 336.08°$, $b = -0.21°$), the pulsar *PSR J1632-4818* has been detected with an age estimated to be on the order of 20 kyr (Manchester et al. 2002). Another close pulsar, *PSR J1632-4757*, has been detected close to this source. Both pulsars could be marginally associated to the source *HESS J1632-478* (Aharonian et al. 2006b). It seems thus possible that the emission from this region is composed of contributions from many sources. The second source of the "HESS cluster" is *HESS J1634-472*. It has been detected during this same survey (Aharonian et al. 2006b) as an extended gamma-ray source with a flux of 6% of the Crab Nebula and with a position that agrees with the supernova remnant *G337.2+0.1*. Finally, the multi-wavelength observations of the gamma-ray source *HESS J1640-465* associate this source with the supernova remnant *G338.3-0.0* (using radio observations in 843 MHz (Whiteoak & Green 1996)) and with a pulsar wind nebula (using the X-ray observations obtained with Chandra (Lemiere et al. 2009) and XMM (Funk et al. 2007), together with the gamma-ray observations collected with Fermi (Sugizaki et al. 2001)).

As we can attest, all the listed sources have a counterpart at higher energy and are most probably associated with SNR and pulsars. As also noticed in (Neronov & Semikoz 2012), these sources are potentially sites of recent injection of cosmic rays and therefore are good candidates for the production of neutrinos.

5.6 Neutrino detection with the IceCube detector: start of multi-messenger astronomy

As we just saw, the neutrino flux coming from the Southern Hemisphere should be detectable by a neutrino detector similar to the IceCube detector, but sensitive to the Southern Hemisphere. However, using the muon neutrino detection channel, the IceCube detector sensitivity is not optimized in the Southern Hemisphere (see the effective area Fig. 3.16). This issue could be overcome using the veto technique introduced in Sect. 3.2.3. With this method, the detection of neutrino is open to the Southern Hemisphere with a larger sensitivity (see the effective area Fig. 3.18). In this analysis, one considers the shower-like events produced by charged current interactions of electron neutrinos and tau neutrinos, and by neutral current interactions of neutrinos of all flavors. As a result, the angular resolution is poorer than for muon track, due to the difficulty to reconstruct the direction of shower like events (about 10-15 degrees).

Recently, using the veto detection channel (HESE, see Sect. 3.2.3), the IceCube collaboration reported the detection of twenty-eight high energy neutrinos (with energy larger than 30 TeV) that are inconsistent with a purely atmospheric origin at a 4σ level (IceCube Collaboration 2013). From these events, seven are muon track and twenty-one are shower events. From the highest energy detected neutrinos, nine of the events have an energy larger than 100 TeV and two have an

deposited energy larger than 1 PeV.

Their exist many models for the origin of the detected neutrinos. For instance, the high Galactic latitude events could be produced by e.g. extragalactic sources, like blazars (see Chapt. 6), while the events closer to the Galactic plane may be from individual Galactic sources or be a part of diffuse emission from the Galaxy. In IceCube Collaboration (2013), the authors noticed that at the energy above 100 TeV, the background event fraction of the detected events is reduced from 70% to 10% (IceCube Collaboration 2013). Therefore, in the present analysis (Neronov et al. 2013), I perform with my co-authors a dedicated study of the neutrino events of energy above 100 TeV.

Figure 5.12 shows the distribution of arrival directions of the highest energy ($E > 100$ TeV) neutrinos detected by IceCube, superimposed onto a Fermi γ-ray image of the sky in the energy band above 100 GeV. One could see that among the nine neutrino events with energy larger than 100 TeV, three are distributed around the Galactic ridge, a bright γ-ray emission region in the Galactic longitude range $-30^\circ < l < 30^\circ$. Two more events are arriving from the directions close to the Galactic plane and four events are arriving from high Galactic latitude.

Motivated by the coincidence of arrival directions of a subset of $E > 100$ TeV neutrinos with the direction toward the inner Milky Way disk, we put forward a conjecture that the Galactic ridge is a source of those neutrinos. In Fig. 5.13, we perform a zoom of the Galactic ridge region by scanning the spectral properties of the γ-ray emission from the $8^\circ \times 8^\circ$ regions centered at different Galactic longitudes. The grey band in this Figure marks the Galactic ridge region, defined by $-30^\circ < l < 30^\circ$ and $b = 0^\circ$. As one could see, the highest flux in the range of Galactic longitudes $-30^\circ < l < 30^\circ$ is measured from the parts of the Galactic plane centered at the positions of the sources *HESS J1837-069* (an unidentified extended source), *HESS J1825-137* (a pulsar wind nebula), *G 0.9+0.1* (a composite supernova remnant), *HESS J1731-347* (a shell type SNR), and an unidentified extended source *HESS J1632-478*.

To verify the self-consistency of the assumption that the Galactic ridge is a source of those neutrinos, we estimate the $E > 100$ TeV neutrino flux detected with the IceCube detector and compare it with an extrapolation of the measured γ-ray spectrum of the Galactic ridge. If both γ-rays and neutrinos are produced via the same mechanism (cosmic ray interactions resulting in pion production and decays), the neutrino flux and spectrum is expected to be nearly identical with the γ-ray flux and spectrum. After oscillations neutrinos are expected to reach the Earth with a flavor ratio different to the one emitted at the source (see Sect. 3.1.2) and neutrinos of all flavors are expected to reach the detector. Therefore, shower-like and track-like events are both expected in the detector. The result of this study is shown in Fig. 4.14, where we can see the detected flux of neutrinos having an origin compatible with the Galactic Ridge region. On the same figure is represented the gamma-ray flux of the Galactic Ridge, for comparison.

For the γ-ray emission, the overall spectrum of emission from the Galactic ridge is well represented by a broken power law with a hardening in the 20 GeV range. The harder component of the spectrum is characterized by the photon index $\gamma_\gamma \simeq 2.4$, while the softer component has the spectrum with the slope $\gamma_\gamma \simeq 2.5$. The TeV band spectra of individual sources contributing to the Galactic ridge emission, shown by grey curves, have been taken from Aharonian et al. (2006b). The 1σ uncertainties on the spectrum detected with Fermi-Lat are obtained by an equivalent method as in Eq. [5.3].

To estimate the flux and spectrum of the three neutrinos whose arrival direction matchs with the Galactic ridge region, we use the performances of the detector. Therefore, we need to know the

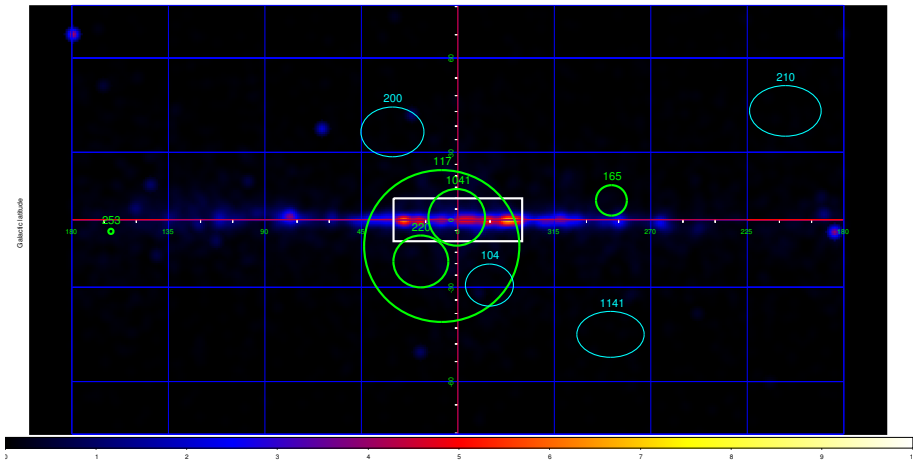

Figure 5.12: Fermi count map in the energy range above 100 GeV, smoothed with 4° Gaussian. Elliptical regions show the arrival direction and its uncertainty of the IceCube neutrino events with energies above 100 TeV. Green (blue) color marks the neutrinos coming from directions close (far) to the Galactic Plane. Numbers next to each ellipse mark the energy of neutrino events in TeV. White rectangle shows the spectral extraction region for the Galactic ridge. Taken from (Neronov et al. 2013).

effective area of the detector in the Southern Hemisphere at the energy of 117, 220 and 1041 TeV (see Fig. 5.12). However, IceCube Collaboration (2013) provides only a sky-averaged effective area for electron, tau and muon neutrinos (see Fig. 3.18). This effective area grows rapidly in the energy range above 100 TeV, such that the difference between the effective area at 200 TeV and 1 PeV is of a factor of three (i.e. half-an-order of magnitude). In an order of magnitude estimate, we divide the energy range 100 TeV - 3 PeV onto energy bins in which the effective area can be considered as almost constant. We choose to divide the energy range in three energy bins of equal width in the logarithmic scale: 100-316 TeV, 316 TeV-1 PeV and 1-3.16 PeV. For each energy bin, we calculate the effective area corresponding to the range of declinations of interest using the declination dependence of the count rate reported in IceCube Collaboration (2013, right panel of the Fig. 4) for an isotropic source. As this count rate is almost declination-independent in the Southern Hemisphere, the effective area can be estimated as declination-independent in the Southern Hemisphere with a value 1.3 times larger than the 4π-averaged affective area reported in IceCube Collaboration (2013).

From Fig. 5.14 one could see that the IceCube flux estimate lies right at the power law extrapolation of the γ-ray spectrum of the Galactic ridge to the 100 TeV energy range. At the same time, the estimate of the neutrino flux is inconsistent with the extrapolations of the spectra of individual sources contributing to the Galactic ridge. This inconsistency could not be explained by possible absorption of the highest energy γ-rays in the source because (a) normalization of the flux at lower energies is already much lower than the neutrino flux estimate and (b) all Galactic sources, as well as the interstellar medium around the sources are expected to be transparent for the 100 TeV γ-rays: the density of the soft photon backgrounds is largely insufficient for significant attenuation of the γ-ray flux due to the pair production (see Fig. 3.20). This suggests a model in which the hard component of the γ-ray flux from the entire Galactic ridge and the neutrino flux from the inner Galaxy direction are produced via one and the same mechanism: interactions of cosmic rays

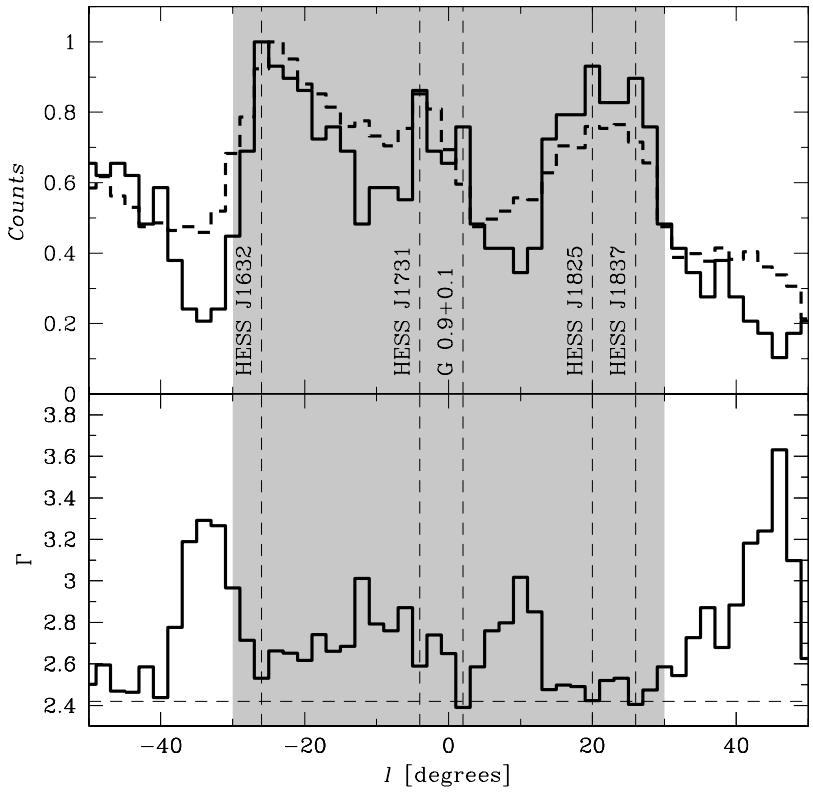

Figure 5.13: Top: Normalized intensity profile of γ-ray emission from $8^\circ \times 8^\circ$ regions centered at a given l position along the Galactic plane. Solid line shows the profile in the 0.3-1 TeV band. Dashed line is for the 0.1-0.3 TeV band. Bottom panel shows the slope of the spectrum calculated from the ratio of the counts in the two bands. Shaded range shows the boundaries of the Galactic ridge spectral extraction region. Vertical dashed lines mark positions of brightest sources. Taken from (Neronov et al. 2013).

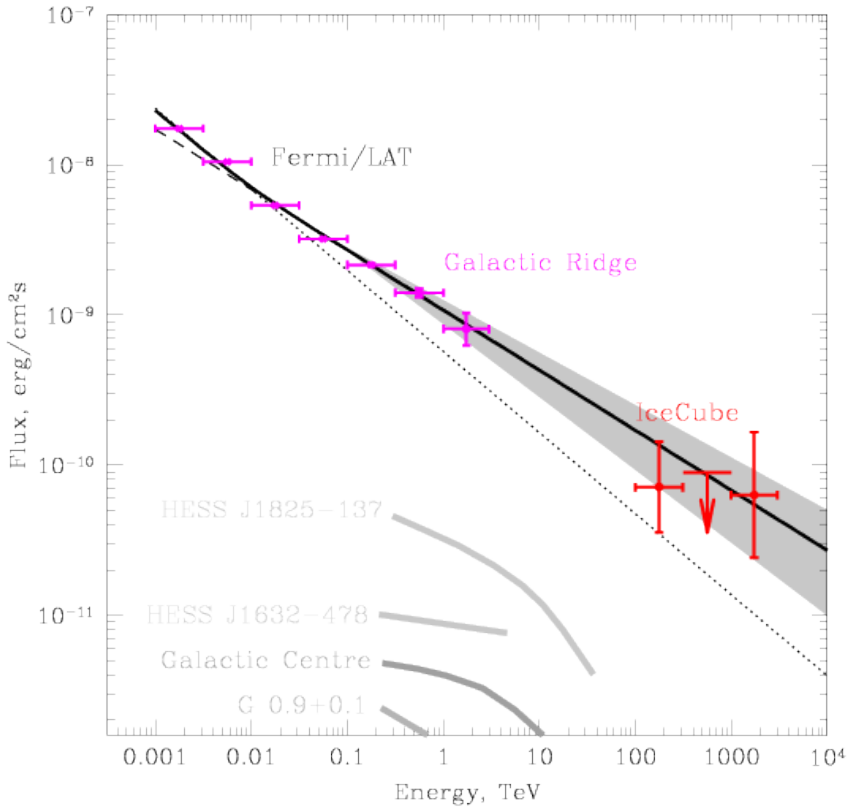

Figure 5.14: Comparison of Fermi-LAT and IceCube spectra of sources in the direction of the inner Galaxy. Magenta data points show the overall γ-ray spectrum of a $-30° < l < 30°$, $-4° < b < 4°$ part of the Galactic plane. Red data points show the estimates of IceCube neutrino flux above 100 TeV. Black thick solid line shows a broken power law model for the γ-ray spectrum with soft (thin dotted) and hard (thin dashed) components. Grey band shows the uncertainty of the spectrum of the hard component. The individual spectra of TeV sources taken from (Aharonian et al. 2006b) contributing to the Galactic ridge emission are shown by grey curves. Taken from (Neronov et al. 2013).

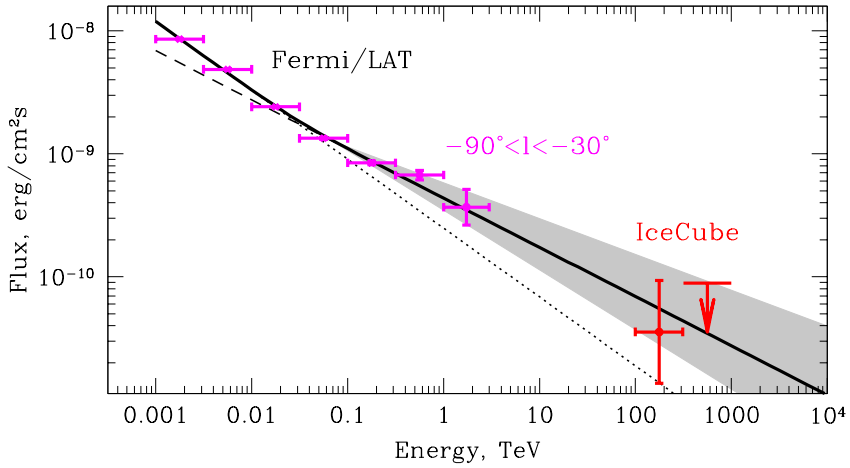

Figure 5.15: Same as in Fig. 5.14, but for the region $-90° < l < -30°$. Taken from (Neronov et al. 2013).

with the interstellar medium.

The relation between the γ-ray and neutrino signal from cosmic ray interactions in the interstellar medium should hold not only in the Galactic ridge region, but everywhere along the Galactic Plane. To verify the self-consistency of the model in which the observed $E > 100$ TeV neutrinos at low Galactic latitudes are coming from the cosmic ray interactions, we also extracted the γ-ray spectrum and estimated the neutrino flux from the region $-90° < l < -30°$, which is entirely contained in the Southern Hemisphere, so that our estimate of the IceCube exposure is also applicable. From Fig. 5.15 one could see that the detection of one $E > 100$ TeV neutrino from the direction toward this part of the Galactic Plane is consistent with the expectations based on the extrapolation of the γ-ray spectrum.

Furthermore, it is interesting to notice that the γ-ray flux from the outer part of the Galactic Disk ($90° < l < 270°$) in the energy band above 100 GeV is approximately three times lower than the flux from the inner Galactic Disk (Ackermann et al. 2012). If both γ-rays and neutrinos coming from the direction of the Galactic Plane are produced by cosmic ray interactions, the ratio of neutrino flux from the outer Galactic Plane to that from the inner Galactic plane is also expected to be approximately $1 \div 3$. This is what is observed in the IceCube data (see Fig. 5.12). There are four neutrinos with energies above 100 TeV from the inner Galactic Disk and one from the outer Galactic Disk. This demonstrates the self-consistency of the hypothesis that low Galactic latitude astronomical neutrinos with energies above 100 TeV detected by IceCube could be a part of diffuse neutrino emission from the Galaxy.

Our result suggests a model where the cosmic rays responsible for the γ-ray and neutrino flux are characterized by a hard spectrum with a cut-off energy higher than 10 PeV. Such an interpretation would indicate that at least some Galactic sources may be able accelerate cosmic rays to energies beyond the *knee*. Furthermore, the projection of the Galactic Bar and of the Norma arm lies in the range of Galactic longitudes $|l| < 30°$ (see Fig. 5.16). This implies that the Galactic ridge spans the range of Galactic longitudes delimited by the projection of the innermost Norma arm of the Galaxy and of the Galactic Bar. As cosmic rays only extend along the regular component of the magnetic field (Giacinti et al. 2012), cosmic rays spreading from sources in the

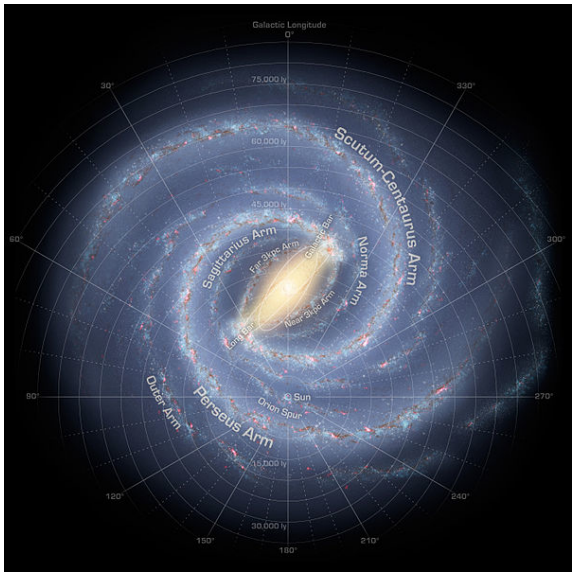

Figure 5.16: Sketch of the Milky Way. Taken from http://www.mgvoss.de/92.html.

Norma arm and /or in the Galactic Bar could not spread into $|l| > 30°$, they only extend along the arm. This might explain the distinct appearance of the brighter Galactic ridge in the γ-ray map and should lead to a similar extension of the neutrino source in the inner Galaxy, a conjecture which could be verified with a deeper IceCube exposure.

5.7 Discussion

Summary and outlook

The Galactic plane is the brightest γ-ray source in the sky. As the diffuse counterpart of this γ-ray emission is dominated by neutral pion decay, the Galactic plane is expected to be also a bright neutrino source. In (Tchernin et al. 2013b), I have investigated with my co-authors the detectability of this expected neutrino emission with the IceCube detector (IC-79). The flux of the neutrino signal has been estimated from the γ-ray flux detected with Fermi. Among all the sources located in the Northern Hemisphere, we found a possible evidence of neutrino detection after about ten-twenty years of exposure in the Cygnus region. Interestingly, this result could potentially be confirmed by the recent analysis performed by the IceCube collaboration on the four years of collected data (IceCube Collaboration et al. 2014). In this analysis, the IceCube collaboration performed a stacking analysis of six MILAGRO TeV sources and obtained that the stacked signal was consistent with a probability of 2% with background fluctuations. Four of these six sources are located in the Cygnus region, which may indicate that with a longer exposure time, the Cygnus region could be detected by the IceCube detector.

In the second part of this study, I performed with my co-authors the same analysis, but with an hypothetic detector sensitive to the Southern Hemisphere. Our results show that the detection of neutrino sources located in the Southern Hemisphere seems more favorable. Indeed, in our analysis, we found that an IceCube-like detector located in the Northern Hemisphere could detect several neutrino sources within a $\sim$ 5 yr exposure time. This prediction may be consistent with

the recent detection of high energy neutrinos with the IceCube detector (IceCube Collaboration 2013; Aartsen et al. 2014b). Indeed, using a data analysis sensitive to the Southern Hemisphere, the IceCube collaboration detected a neutrino signal from a direction consistent with the Galactic ridge. However given the poor angular resolution of this analysis method, any conclusion about the exact arrival direction of this signal is difficult and many other models for the origin of these neutrinos are possible (see e.g., Anchordoqui et al. 2013, for a review).

Remarks and limitations of this analysis

In this chapter two complementary studies have been performed. In both studies, the γ-ray flux is used as an estimate of the expected neutrino flux.

In the first study, we were interested in the emission from the Galactic plane. This γ-ray emission is the sum of the diffuse and the point sources emission (Ackermann et al. 2012). However, only the diffuse emission has been confirmed to be of hadronic origin. As we obtained our results assuming that the entire γ-ray emission is only produced by pp interactions, the obtained results are optimistic and the resulting exposure times are only lower bounds to the required time for detection.

In the second study, we considered the possibility that the recently detected high energy neutrino events and γ-rays are products of cosmic ray interactions in the Galactic ridge. However, at energy $E > 100$ GeV, some models suggest that the diffuse γ-ray emission from the Galactic plane is dominated by inverse Compton emission from electrons instead by the neutral pion decay (see e.g., Ackermann et al. 2012). As a result, the flux of pion decay contribution to the γ-ray flux measured by Fermi would be lower than the total flux of the Galactic ridge region shown in Fig. 5.14. In this case, the neutrino flux in the $E > 100$ TeV band may be inconsistent with the high-energy extrapolation of the pion decay component of the γ-ray spectrum. Therefore, for our analysis to be valid, one must assume that the γ-ray emission results from pp interaction.

Furthermore, in these studies, we combined a neutrino flux with a γ-ray flux which were not observed in the same energy range. We assumed that the γ-ray flux exhibits no cut-off and we extrapolated the γ-ray flux observed with Fermi-LAT to higher energies, where the IceCube detector is sensitive. The uncertainties coming from this extrapolation could be avoided if the γ-ray data were taken in the energy range where IceCube is sensitive. This could be achieved with the help of the CTA telescope, which is planned to be sensitive in the energy range of IceCube (Actis et al. 2011).

Chapter 6

γ-rays and neutrinos from blazars

6.1 Motivation

Based on the Hillas criterion, Active Galactic Nuclei (AGN) should be able to accelerate protons up to the highest energies (see Fig. 4.1, Hillas 1984). As introduced in Sect. 4.3.1, blazars belong to a subclass of AGN, whose relativistic jet is orientated in the direction of the Earth. These sources are of particular importance in the search for neutrinos because assuming that the electromagnetic emission has an hadronic origin, the neutrino emission should be beamed together with the γ-ray emission. Therefore, among the AGN, the neutrino signal from blazars should the easiest to detect.

In the present analysis, I combine the IceCube sensitivity curves with the γ-ray observations of the brightest γ-ray blazars detected with the Fermi-LAT satellite to set constraints on the parameter space of hadronic models. This analysis has been published in Tchernin et al. (2013a).

6.2 'Purely hadronic' models for blazars

In order to estimate the neutrino flux from the observed γ-ray emission, one needs to make some assumption about the origin of this γ-ray emission. As introduced in Sect. 4.3.1, the spectral energy distribution of blazars is composed of two peaks, one at high and the other at low energy (see for instance Fig. 4.7, where the SED of the blazar 3C 66A is shown). This emission is dominated by the emission from the jet, due to the beaming effect.

While all models agree in explaining the low energy bumps by the synchrotron emission of the relativistic electrons in the magnetic field of the jet, the origin of the high energy bump, which peaks in the γ-ray regime, is still debated. There exist two competing scenarios, known as the leptonic and the hadronic models. In the leptonic scenario, only electrons/positrons are required to reproduce the observed γ-ray emission. For instance, in the SSC model, the γ-ray emission develops in an electromagnetic cascade: the relativistic electrons/positrons emit synchrotron photons and up-scatter them to TeV energy by Inverse Compton scattering. On the other hand, in hadronic scenarios, protons are also involved. In such models, the γ-ray emission can be emitted by different mechanisms, like the synchrotron emission (Aharonian 2000), the photo-meson ($p\gamma$ Sikora et al. 1987) and the inelastic proton-proton interactions (pp). In the two latter cases, pions are produced, which subsequently decay into neutrinos and γ-rays. As a result, neutrinos are expected in some hadronic models, while they are absent in all leptonic models. It implies that the detection of neutrinos would be an evidence of the acceleration of cosmic rays in AGN.

To simplify the analysis and to take advantage of the known relations between the expected neutrino and γ-ray spectra in the hadronic scenarios (see Sect. 3.1.2), in the present study we assume that the broad band emission of blazars has a "purely hadronic" origin and is produced only via pp and $p\gamma$ interactions, where one of these two channels dominates.

In such scenarios, the secondary electrons produced in the charged pion decays and the high energy photons coming from the neutral pion decay initiate an electromagnetic cascade and reprocess the initial power to lower energy, while the neutrinos escape freely from the source. As the power injected in the neutrinos is comparable to the one injected in the electromagnetic cascade for both interaction channels (see Figs. 3.8, for the pp and 3.11, for the $p\gamma$ interactions), the observed bolometric luminosity can be used to estimate the luminosity of the neutrinos.

6.3 Determination of the IceCube detector sensitivity curve

In the literature, quoted neutrino limits (upper-limits and sensitivity curves) are usually given assuming an astrophysical neutrino spectrum with a power-law shape $dN/dE \propto E^{-\gamma_\nu}$ with γ_ν equals to 2. Historically, this choice has been based on the fact that a E^{-2} spectrum can be obtained with acceleration model like the DSA mechanism (Bell 1978) which is consistent with the observed $E^{-2.7}$ cosmic ray spectrum below the *knee*, assuming a given energy-dependent diffusion coefficient. However, for UHECRs, whose spectrum is as soft as $\sim$ 3.3, the relation to an injected spectrum equal to 2 is not obvious. Moreover, based on non-linear treatment of the DSA mechanism, the spectral index can be different from 2 and there are a-priori no reason to assume a spectral index equal to 2. Therefore, in this analysis I do not restrain the analysis to a spectral index equal to 2, but I derive the neutrino sensitivity curves for any value of the spectral index γ_ν lying in the range 1 to 3.

To this end I use the approach developed in (Neronov & Ribordy 2009), which is similar to the one introduced in the previous chapter (Sect. 5). I compute the expected number of signal and background events and search for the optimal parameters for which the signal-to-noise ratio is maximized in the direction of the source. The main difference with the previous section is that blazars are point sources (their extension is smaller than the angular resolution of the IceCube neutrino detector, see Fig. 3.15, taken from Abbasi et al. 2011), while in the previous section, we were considering the extended diffuse emission of the Galactic plane. As a result, in the present analysis both the source angular extension in the sky and the energy information contained in the neutrino source spectrum can be used to detect the signal on the top of the background. In order to exploit the information contained in the source direction, I use the muon detection channel introduced in Sect. 3.2.3, which is characterized by its good angular resolution (see Sect. 3.2.3).

Optimization of the signal-to-noise ratio of a given source

Firstly, we compute the expected number of background events N_{bgd}, of energy E within $[E_{min}; E_{max}]$ expected to be detected within a given time, T, at the position δ with the IceCube detector in a circular region of the sky of angular radius ψ, as

$$N_{bgd}(E,\psi) = \pi\psi^2 T \int_{E_{min}}^{E_{max}} A_{eff}(E,\delta)\frac{dN_{atm}(E,\delta)}{dEd\Omega}dE. \tag{6.1}$$

Where $A_{eff}(E_\nu,\delta)$ is the effective area of the detector shown in Fig. 3.16 and $dN_{atm}/dEd\Omega(E,\delta)$, the measured atmospheric neutrino flux which can be described by a power law of spectral index $\sim$3.7 (see Sect. 3.2.3, Honda et al. 2007). Because the atmospheric neutrino flux is isotropic, its expected detection rate increases with the size of the considered region with ψ^2.

The number of astrophysical neutrinos (N_{signal}) expected to be detected with the IceCube detector in a given time T for a blazar located at the position δ, and for a given neutrino source

spectrum, $(dN/dE)|_{\nu,\ ast}$, can be obtained as

$$N_{signal}(E,\psi) = T \int_{E_{min}}^{E_{max}} \int_{\Omega} A_{eff}(E,\delta) \cdot \frac{dN}{dE}|_{\nu,\ ast} \cdot f_{PSF}(E,\psi) dE d\Omega. \tag{6.2}$$

Here the factor $f_{PSF}(E,\psi)$ is the PSF of the detector, which is a function of both the angular size of the considered region and of the particle energy (see Fig. 3.15). As mentioned above, in this analysis we assume that the astrophysical neutrino spectrum follows a power-law shape of spectral index γ_ν going from 1 to 3, as

$$\frac{dN}{dE}|_{\nu,ast} = \Phi_0 \left(\frac{E}{E_0}\right)^{-\gamma_\nu}, \tag{6.3}$$

with Φ_0 the normalization at an arbitrary energy E_0.

For the sources located in the Northern Hemisphere, the atmospheric neutrino flux is the only one source of background we need to consider. In this analysis, the fluctuations of the background are taken into account by using the Feldman Cousins approach (FC, Feldman & Cousins 1998). Generally, we observe the total count $N_{obs} = N_{signal} + N_{bgd}$, which consists in an unknown number of signal events N_{signal} and in a known number of background events N_{bgd}. The FC method helps us to derive, for a given background rate and observed number count N_{obs}, what is the confidence interval $[N_{signal_{min}}; N_{signal_{max}}]$ of the unknown parameter N_{signal} at a confidence level of 90%. In the FC method, the selection of the N_{obs} to be included in the acceptance region $[N_{obs_{min}}; N_{obs_{max}}]$ is based on an ordering principle, where for a fixed value of the unknown parameter N_{signal}, one computes the likelihood ratio $R = P(N_{obs}|N_{signal})/P(N_{obs}|N_{signal,best})$, where $N_{signal,best}$ is the value of N_{signal} which maximizes the likelihood ($\mathcal{L}(N_{signal}) \equiv P(N_{obs}|N_{signal})$) for a fixed value of N_{obs}. Starting from $N_{obs} = 0$, one increments the value of N_{obs} and computes the new likelihood ratio while keeping the unknown parameter N_{signal} fixed. For each value of N_{signal}, the values of N_{obs} are added to the acceptance region for decreasing values of R, until the sum of $P(N_{obs}|N_{signal})$ reaches the chosen C.L., in our case, 0.9. By construction, for an observed count rate N_{obs}, this method returns the confidence interval of the parameter N_{signal} at the chosen C.L. By ranking the values by $P(N_{obs}|N_{signal,best})$, one weights the parameters as function of their deviation to the best fit value. Due to the discrete nature of N_{obs}, the sum will be greater than 90% and the confidence intervals are conservative.

In the present case, the point source search performed in Abbasi et al. (2011) reveals that the number of detected events is consistent with background fluctuations. This implies that $N_{obs} = N_{bgd}$ and the FC method provides[1] an upper-limit to the possible values of N_{signal}, meaning that any value of N_{signal} larger than this limit should have been detected at a 90% C.L. I will use the notation $N_{signal}^{90\%CL}$ to refer to this upper-limit in the following.

With Eq. [6.2] and [6.3], we can define the maximal value of the astrophysical neutrino flux normalization which is allowed by the non-detection of neutrinos at a 90%C.L., $\Phi_0^{90\%CL}$, as

$$\Phi_0^{90\%CL}(\psi, E_{min}) = \frac{N_{signal}^{90\%CL}(\psi, E_{min})}{T \cdot F_{PSF}(E,\psi) \cdot \int_{E_{min}}^{E_{max}} A_{eff}(\delta, E)\,(E/E_0)^{-\gamma_\nu}\, dE}. \tag{6.4}$$

[1] I used the code which has been implemented at CERN (in C++: TFeldmanCousins) to obtain these upper-limits.

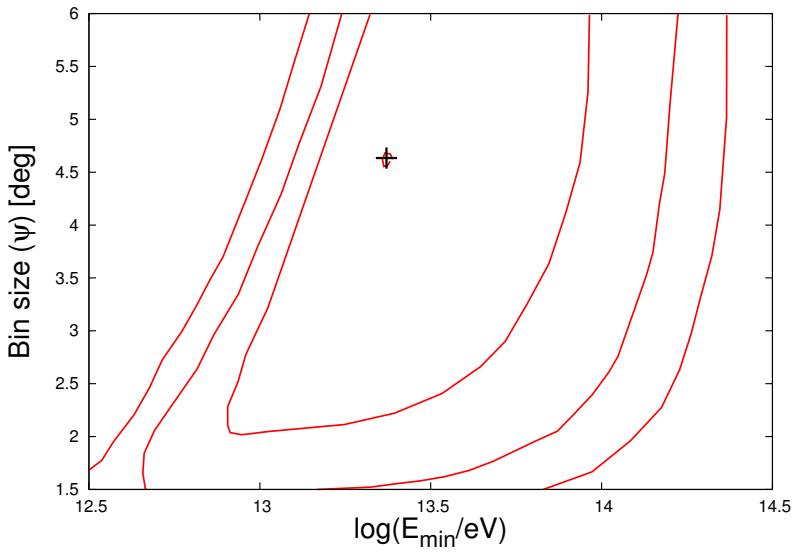

Figure 6.1: Contour plot of the normalization factor $\Phi_0^{90\%CL}(\psi, E_{min})$ for $\gamma_\nu = 1$ and a declination of 38°. Contours represent the constant levels of $\Phi_0^{90\%CL}(\psi, E_{min})$: from $2.5 \cdot 10^{-19}$[1/GeVcm$^2 s$] to $3.25 \cdot 10^{-19}$[1/GeVcm$^2 s$] with step of 0.25, from center to the border, for a scale factor of $E_0 = 10^{17} eV$. The optimal choice of ψ, E_{min} corresponding to the minimum of $\Phi_0^{90\%CL}(\psi, E_{min})$ marked by the cross. Taken from (Tchernin et al. 2013a).

Where $F_{PSF}(E, \psi)$ is the cumulative PSF. By definition this normalization corresponds to the upper-limit of the astrophysical neutrino counts which is consistent with the non-detection at 90%CL. This normalization can be minimized with the optimal choice of the parameters ψ and E_{min}. This optimal value of $\Phi_0^{90\%CL}$, depends on ψ and E_{min} in the following way. Let us consider first the dependence on ψ. One can notice that the dependence in ψ is different between the two expressions for the expected rate of atmospheric neutrinos (Eq. [6.1]) and for the expected rate of astrophysical neutrinos (Eq. [6.2]). This is due to the fact that the signal in point sources is concentrated in a region the size of the detector angular resolution, while for extended sources, the detected number of events increases with the square of the angular size. As a result, there exists an optimal angular size around the source which maximizes the signal-to-noise ratio by suppressing the background without reducing the statistics of the signal. Then, this information can be combined with the energy information such that the optimization is done simultaneously on both E_{min} and ψ. For instance, the detection of a hard astrophysical neutrino spectrum on the top of the soft atmospheric neutrino flux could be achieved for any value of ψ, by a choice of a high cut-off energy. On the other hand, if we consider a source with a softer spectrum, the signal-to-noise ratio would be maximized by reducing the angular extension ψ and by choosing a low value of E_{min}. Figure 6.1 illustrates the procedure: the parameter space of (E_{min}, ψ) is represented for the case of a hard power-law spectrum of spectral index $\gamma_\nu = 1$ at a source declination of 38°. In this figure, curves represent the regions of constant values of $\Phi_0^{90\%CL}$, while the value of (E_{min}, ψ) at which $\Phi_0^{90\%CL}$ reaches its minimal value is represented by a cross. For softer neutrinos spectra, the cross point corresponding to the optimal choice of (E_{min}, ψ) moves to the lower left corner of the parameter space plot.

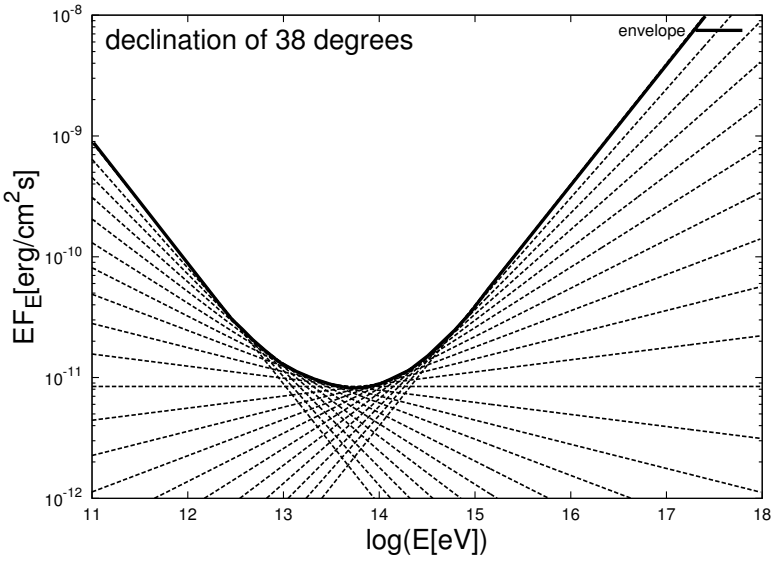

Figure 6.2: A set of the power-law source spectra $\Phi_0^{90\%CL}(E/E_0)^{\gamma}$ with minimal values of $\Phi_0^{90\%CL}$ for different choices of γ. Black thick curve is an envelope drawn by all the power-law curves. The declination of the source is assumed to be $\delta = 38°$. Taken from (Tchernin et al. 2013a).

These upper-limits are actually sensitivity curves, as we do not use the data, but the expected atmospheric neutrino flux from (Honda et al. 2007) as an observed quantity. The sensitivity curves for astrophysical neutrino spectra defined by Eq. [6.3] with the optimized $\Phi_0^{90\%CL}$ (Eq. [6.4]) and derived for the set of spectral indices in the range $\gamma_\nu \in [1;3]$ are shown in Fig. 6.2. In this figure, each straight line represents an upper limit on the neutrino flux. From this figure one could see that a convenient way to represent the upper limit for an arbitrary choice of γ_ν would be to plot an envelope-shape curve for all the straight lines (the black thick curve). The sense of this curve is the following: for any value of γ_ν, the maximal allowed value of the source spectrum is tangent to the envelope curve. In this representation, the upper-limit for $\gamma_\nu = 2$ is represented by the horizontal line. As a consistency check, I have verified that those values correspond to the median sensitivity given in Abbasi et al. (2011).

Due to the declination dependence on the effective area, a different envelope curve is given for each source declination. A comparison of curves derived for different declination is shown in Fig. 6.3. The sensitivity of the detector to the highest energy neutrinos is better close to the horizon. It is interesting to note that the sensitivity at low energy is similar for all the Northern declinations. This is due to the effective area of the IceCube detector, which has a comparable shape for all the Norther sources at energy lower than about 10 TeV.

These envelopes are derived for the muon neutrino only. To obtain the envelopes for the all flavor neutrino flux, we use the fact that even if at the source, neutrinos of each flavor are produced with the ratio: $F_{\nu_e} : F_{\nu_\mu} : F_{\nu_\tau}$ =2:1:0, after oscillations the ratio observed at Earth is: $F_{\nu_e} : F_{\nu_\mu} : F_{\nu_\tau}$ =1:1:1 (Learned & Pakvasa 1995). Therefore, to derive the sensitivity curve for neutrinos of all flavors, we rescale the sensitivity curve by a factor of 3 (because we expect that the all-flavor neutrino flux is 3 times the muon neutrino flux observed at Earth).

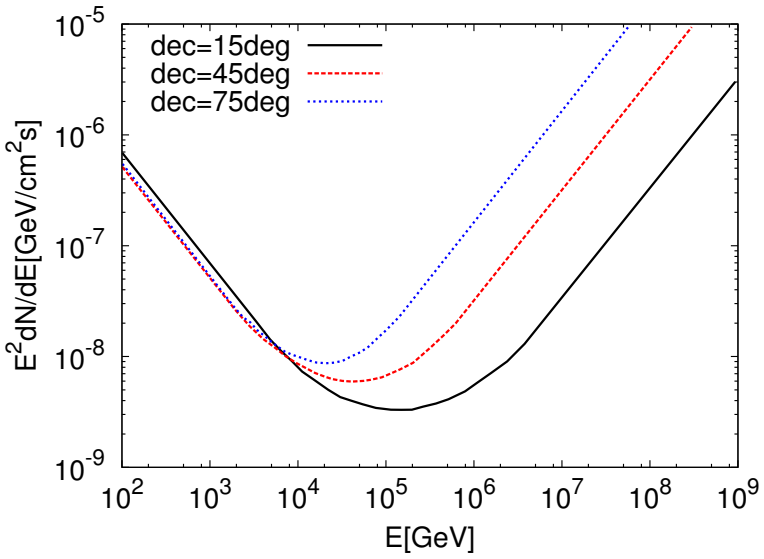

Figure 6.3: Comparison of the derived IceCube sensitivity curves for different declination. As shown, at the highest considered energy, the detector is optimized for point sources located close to the horizon. Taken from (Tchernin et al. 2014).

6.4 Selection of the brightest GeV gamma-ray sources

In this study we consider the γ-ray data collected with the Fermi-LAT telescope (Atwood et al. 2009) during the period August 4, 2008 – May 9, 2009, which corresponds to the period where the IceCube detector was in its 40 strings configuration (Abbasi et al. 2011). In this way, γ-ray and neutrino data are simultaneous.

A preselection of brightest γ-ray blazars from the two-year Fermi catalog (Nolan et al. 2012) has been done by requiring an average flux (over the 0.1 - 100 GeV) greater than 10^{-10} erg/cm^{2}s during the two years. This condition allows us to consider only the brightest blazars of the Fermi catalogue, knowing that the Fermi-LAT sensitivity reaches 10^{-12} erg/cm^{2}s at $\sim$ 10 GeV energies. The list of northern sources which satisfy this condition is shown in Table 6.1. Figure 6.4 shows the light curves for the selected sources. Some sources, like AO 0235+164 and PKS 1502+10, were particularly active during the period of interest (indicated by the vertical red dashed lines in Fig. 6.4). However, the presence of bright flares does not affect significantly the average flux during the IC-40 observation period, which is higher than the average flux by just a factor $1.1 - 1.5$ (see Tab. 6.1). This means that the initial selection of the bright blazars based on the high two-year average fluxes already provides a representative 'brightest blazar" set for our period of interest.

The sources listed in Tab. 6.1 belong to two different sub-classes of the blazar population: BL Lac and FSRQ (see Sect. 4.3.1). BL Lac and FSRQ are characterized by different spectra in the γ-ray range. As the properties of accretion flows in these two types of objects are different, the efficiency of pp and $p\gamma$ interactions in the two types of objects could also be very different. It is not clear in advance in which of the two types of objects the hadronic interactions are more efficient.

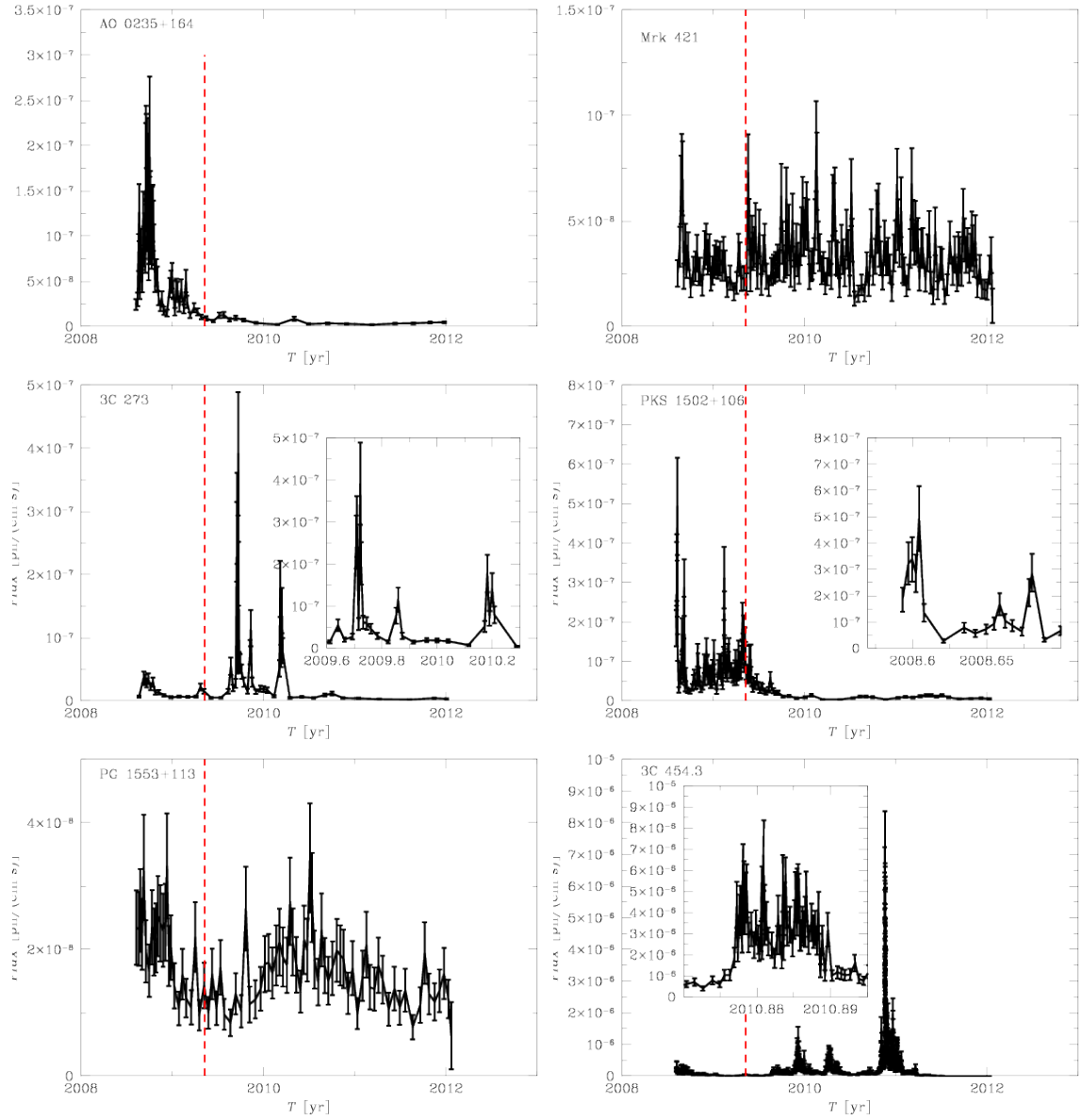

Figure 6.4: LAT light curves of some of the selected blazars (Tables 6.1) in the energy band above 1 GeV. Vertical dashed line shows the end date of IC-40 exposure. Adapted from (Tchernin et al. 2013a).

Name	Type	z	$F_{\mathrm{IC-40\,period}}$	$F_{\mathrm{2-years}}$
3C 66A	BL Lac	0.444∗	17.7	25.8
AO 0235+164	BL Lac	0.94	24.3	16.5
Mrk 421	BL Lac	0.030	30.1	30.8
3C 273	FSRQ	0.158	21.2	11.2
PKS 1502+106	FSRQ	1.839	39.8	30.9
B2 1520+31	FSRQ	1.487	16.1	13.3
PG 1553+113	BL Lac	-	19.8	17.2
BZB J2001+4352	BL Lac	-	11.3	10.0
3C 454.3	FSRQ	0.859	49.2	86.3

Table 6.1: Selected sources for the northern hemisphere (declination $\delta > 0°$) with average fluxes $F_{\mathrm{2-years}} > 10^{-10}$ erg/cm^{2}s in the 2-year Fermi catalogue (Nolan et al. 2012). $F_{\mathrm{IC40-period}}$ is the average flux over the IC-40 period. Both fluxes are in 10^{-11} erg/cm^{2}s units.
∗ From SIMBAD database. The source redshift is uncertain, see Aleksić et al. (2011). Taken from (Tchernin et al. 2013a).

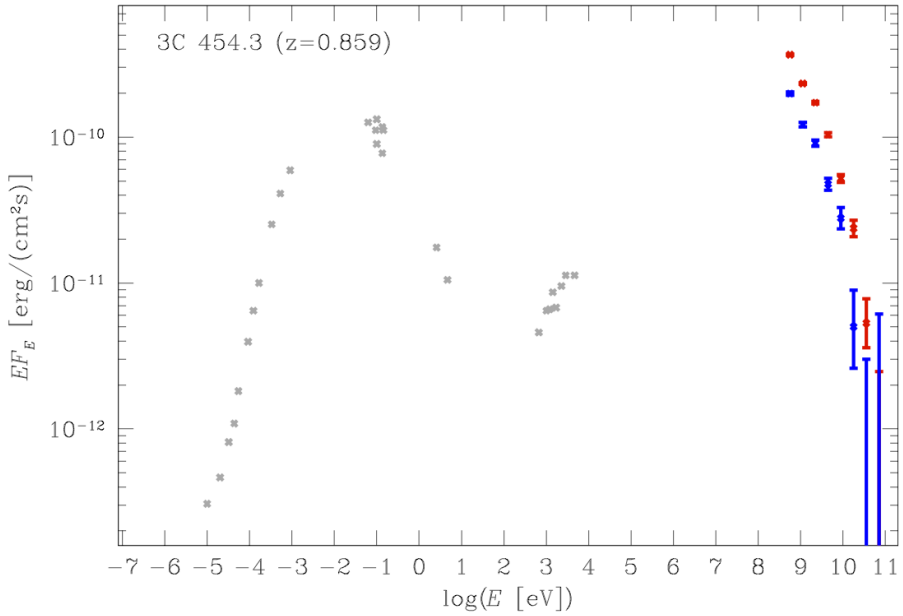

Figure 6.5: Fermi data in the context of the broad-band spectral energy distribution of 3C 454.3. Blue color shows the spectrum during the period of IC-40 observations, red is the average over three-year Fermi data spectrum. Grey data points are from Abdo et al. (2009c). Taken from (Tchernin et al. 2013a).

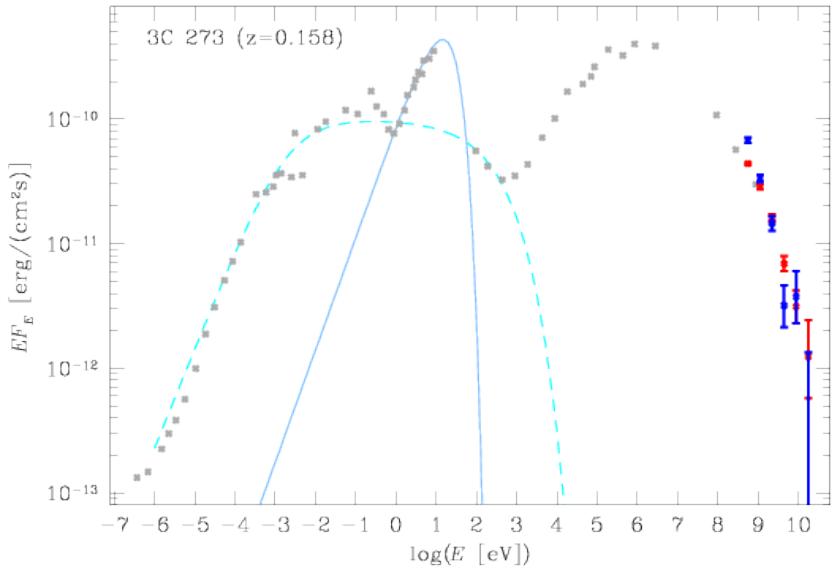

Figure 6.6: Fermi data in the context of the broad-band spectral energy distribution of 3C 273. Red/blue data points are the same as in Fig. 6.5. Grey data points are from Courvoisier (1998). The dashed curve represents the fit for the synchrotron emission, while the continuous curve is the contribution due to the accretion disk. Taken from (Tchernin et al. 2013a).

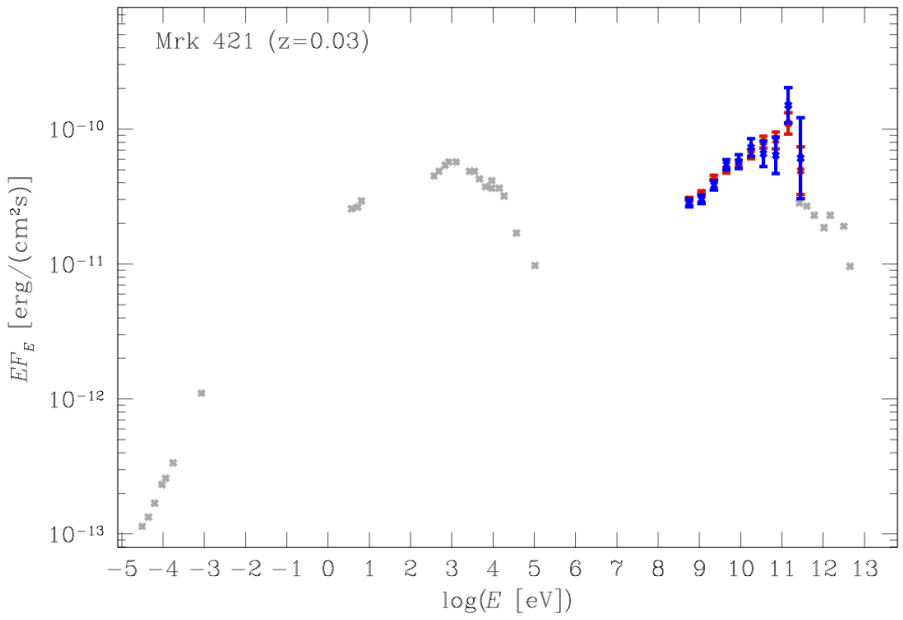

Figure 6.7: Fermi data in the context of the broad-band spectral energy distribution of Mrk421. Red/blue data points are the same as in Fig. 6.5. Grey data points are from Abdo et al. (2011a). Taken from (Tchernin et al. 2013a).

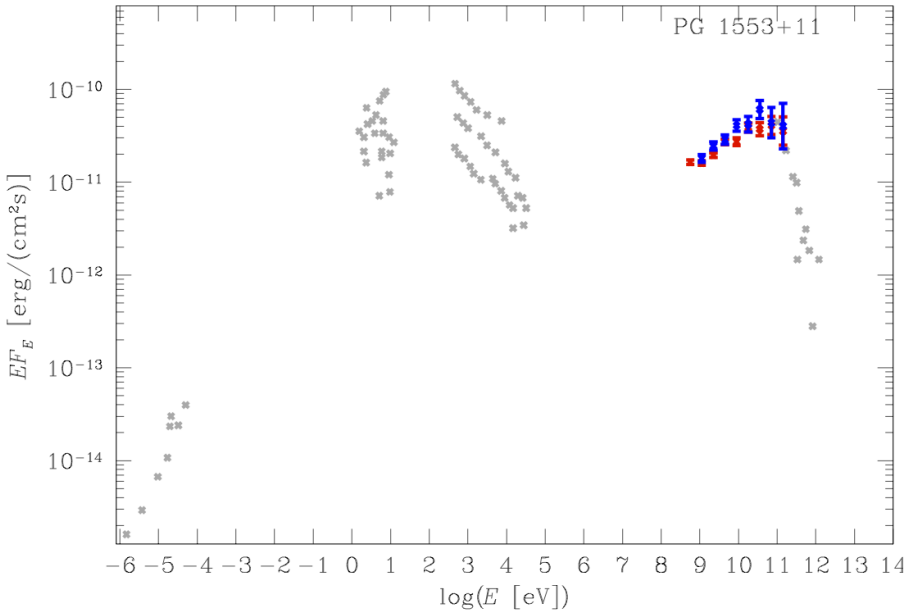

Figure 6.8: Fermi data in the context of the broad-band spectral energy distribution of PG1553+113. Grey data points are from Abdo et al. (2010). Red/blue data points are the same as in Fig. 6.5. Taken from (Tchernin et al. 2013a).

6.5 Constraints on the injected primary proton spectrum combining IC-40 and Fermi observations

In this analysis, the proton spectrum is assumed to have a cut-off power-law distribution, of spectral index γ_p and cut-off energy $E_{max,p}$.

Assuming that the observed γ-ray emission as a purely hadronic origin, we investigate the information on the neutrino spectrum that can be obtained depending on whether the pp or $p\gamma$ interactions dominate. We follow Kelner et al. (2006) to calculate the secondary neutrino and photon spectra produced during pp interactions. This parametrization is optimized in the energy range 10^{11} eV to 10^{17} eV. In the frame of this work, we use the parametrization over a larger energy band of up to 10^{19}eV. For the secondary neutrino and photon spectra from $p\gamma$ interactions, we use the parametrization of Kelner & Aharonian (2008).

Depending if the γ-ray emission is dominated by the neutral pion decay or by the electromagnetic cascade[2], two different methods have been used to set constraints on the hadronic models.

π^0 decay dominated γ-ray spectrum

If the π^0 decay contribution dominates the observed γ-ray emission, as the slope and normalization of neutrino spectra of all flavors approximately follow those of γ-ray spectra (see e.g., Kelner et al. 2006; Kappes et al. 2007, and also Fig. 3.8 and Fig. 3.11), we obtain the simplest estimate of the neutrino spectrum.

The IC-40 limits may impose restrictions on the cut-off energy of the proton spectrum if the estimated neutrino spectrum, extrapolated to higher energy from the γ-ray measurements, intercepts the IC-40 envelope. To this end, the proton spectrum must be relatively hard, but not too hard. Indeed, for a too hard proton spectrum, the π^0 decay photons may initiate an electromagnetic cascade, which would dominate over the neutral pion contribution and hide its spectral features. This implies that a π^0 decay dominated γ-ray spectrum is not expected in the case of $p\gamma$ interactions. Indeed, in such interactions, the secondary particle spectra are hard and peaked at the pion production energy threshold for any value of the parent spectral index (as shown in Fig. 3.11). Furthermore, given that for efficient $p\gamma$ interactions, the density of low energy target photons must be high, $\gamma\gamma$ interactions are expected to take place and to trigger an electromagnetic cascade.

Examples of the expected constraints for the sources PG 1553+113 and Mrk 421 are shown in Figs. 6.9 and 6.10, respectively. One could see that the spectra of these two BL Lacs are slightly harder than $\gamma_p = 2$. For distant sources, the highest energy γ-ray photons can be absorbed by the EBL (see Fig. 3.20). This seems to be the case for PG 1553+113, shown in Fig. 6.9, where the dashed line shows the suppression for the assumed source redshift $z \simeq 0.5$ (Danforth et al. 2010). In this case, the γ-ray high energy cut-off is not representative of the neutrino high energy cut-off and the neutrino flux is expected to extend to higher energies without suppression. As shown, a power law extrapolation of the neutrino spectrum to the TeV-PeV energy band results in a neutrino flux higher than the IC-40 sensitivity, unless the neutrino spectrum has a high-energy cut-off. Based on the γ-ray spectrum observed with the Fermi-LAT satellite, for the two sources PG 1553+113 and Mrk 421, the neutrino data restrict the cut-off in the proton spectrum to be at $E_{max,p} \sim 1 - 10$ TeV. In the case of Mrk 421, the IC-40 sensitivity is at the level of the measured

[2] In the power of the electromagnetic cascade, the contribution of the secondary electrons and positrons is also taken into account.

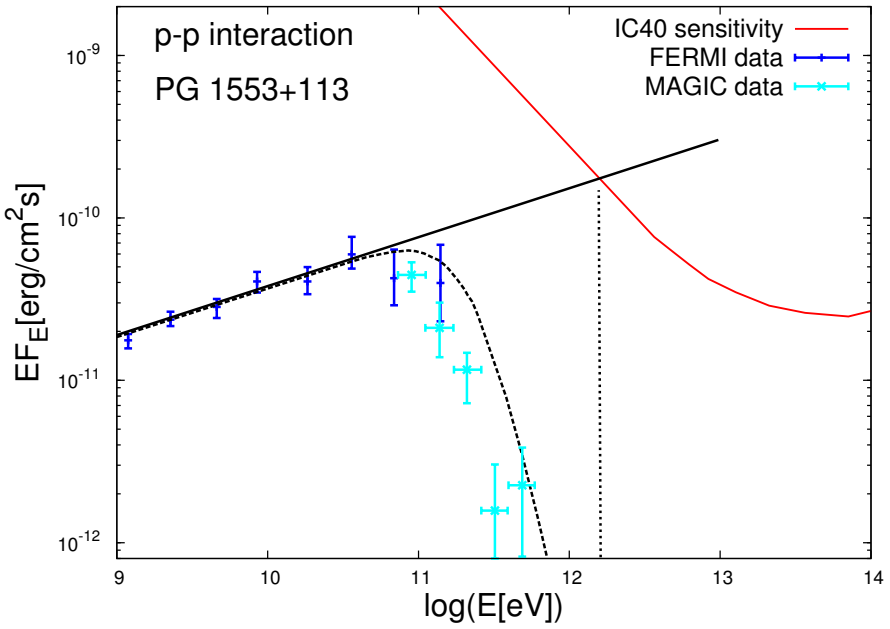

Figure 6.9: γ-ray spectrum of PG 1553+113 recorded by Fermi (blue data points) during the IC-40 observations, compared with the IC-40 sensitivity. Cyan points are MAGIC data from Albert et al. (2009). The red thick curve is the IC-40 sensitivity envelope. The vertical line shows the maximal energy to which the power-law type neutrino spectrum could extend. Taken from (Tchernin et al. 2013a).

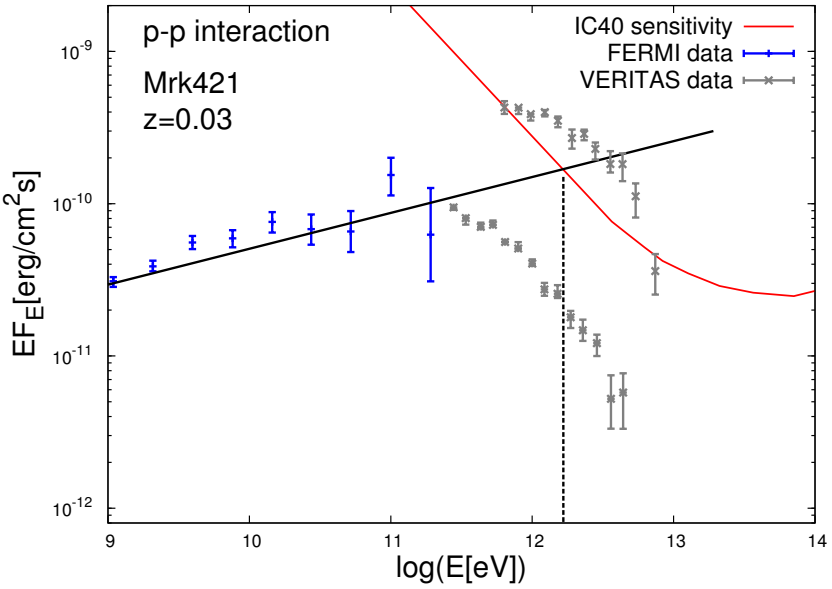

Figure 6.10: Fermi observations (blue points) of Mrk421 during the IC40 period together with maximum and minimum fluxes observed by VERITAS (grey points) in 2008 (Acciari et al. 2011). The vertical line shows the maximal energy to which the power-law type neutrino spectrum could extend. Taken from (Tchernin et al. 2013a).

γ-ray flux from the source in the TeV energy range. Therefore, if the γ-ray emission from blazars is really dominated by the pion decays component, IC-40 results rule out the possibility that AGN are accelerating protons up to the ultra-high-energy cosmic ray band ($\sim 10^{20}$ eV).

After a longer exposure, the sensitivity curve will decrease and the full IceCube detector will have the potential to rule out the model in which the γ-ray emission is dominated by the pion decay component. Otherwise, 1-10 TeV neutrinos should be readily detected by the full IceCube.

Cascade dominated γ-ray spectrum

If the observed flux in the GeV-TeV range is dominated by the cascade emission, rather than by the π^0 decay component, the spectral characteristics of the γ-ray signal could not be used in the estimate of the spectral characteristics of the neutrino signal. In such a case, only the information of the overall power injected in the cascade emission can be used to constrain the expected neutrino emission. As we saw in Sect. 3.1.2, the injected power in electromagnetic cascade and in the neutrino flux of all flavors are comparable for both interaction channels (this is illustrated in Fig. 3.8 and 3.11, for the pp and $p\gamma$ interaction, respectively). Therefore, the observed γ-ray flux is an estimate of the expected neutrino flux for each of the selected sources (see Table 6.1).

Estimating the neutrino flux by γ-ray measurements, the constraints arising from the fact that the neutrino flux should not exceed the sensitivity limit of IC-40 can be expressed as constraints on the two parameters $(\gamma_p, E_{max,p})$ of the primary proton spectrum. These constraints are derived as follows: since the total emitted neutrino power is limited by the electromagnetic observations detected with Fermi, a too low $E_{max,p}$ with a too soft γ_p would result in overproduction of neutrino flux in the energy range where IceCube is most sensitive so that the flux would exceed the IC-40 sensitivity. The constraints for both pp and $p\gamma$ interaction channels are studied. This method

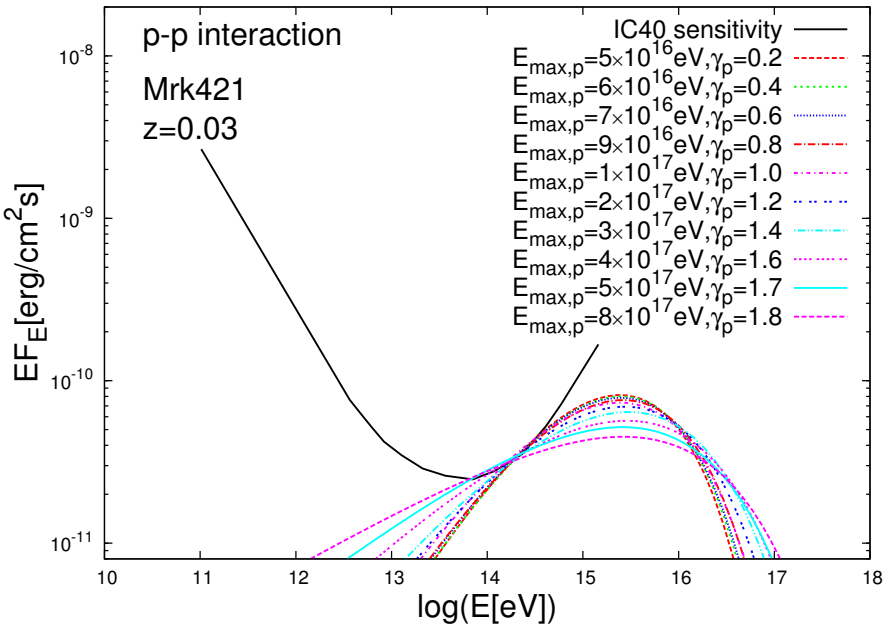

Figure 6.11: Neutrino spectra expected for Mrk 421 for pp interactions and different primary proton spectra characterized by the indicated proton cut-off energy, $E_{max,p}$, and by the proton spectral index, γ_p. The Fermi integrated flux is used for normalization. The black line is the envelope of power law sensitivities of IC-40. Only neutrino fluxes not exceeding the envelope sensitivity are shown. Taken from (Tchernin et al. 2013a).

is illustrated in Fig 6.11 for the source Mrk 421 in the case of pp interactions. In this figure, the neutrino spectra are normalized to the observed γ-ray flux of Mrk 421 and only the neutrino spectra consistent with the IC-40 sensitivity are shown with their corresponding values of γ_p and $E_{max,p}$.

Due to the difference in the cross-sections for the two interaction channels (pp and $p\gamma$), the constraints on the allowed parameter space is expected to be different for both cases.

Constraints on the pp model

Assuming that pp interactions are the dominating interaction channel, the scan of the two parameters γ_p, $E_{max,p}$ produces the exclusion plot shown in Fig 6.12: the excluded range of parameters lies to the left and above each curve. In this figure, only two sources are considered: 3C 454.3 and Mrk 421, because the constraints for the other sources of the sample are weaker (or equivalent, in the case of PKS 1502+106). The quasar 3C 454.3 is the brightest source of the sample (see Table 6.1). It results in the strongest constraints on both $E_{max,p}$ and γ_p. The lower bound of the allowed region ($E_{max,p} \gtrsim 10^{18} - 10^{19}$ eV) indicates that in the framework of pp model with cascade dominated γ-ray emission, blazars should accelerate protons in the UHECR range: otherwise the model is ruled out by this multi-messenger data.

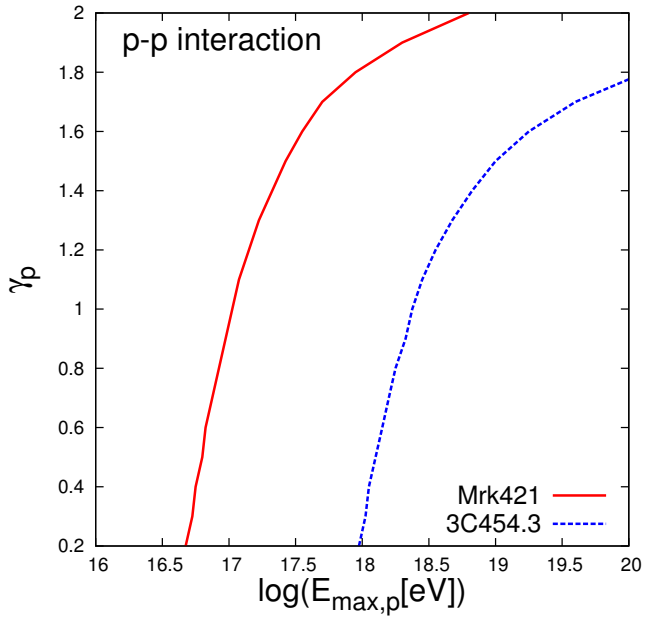

Figure 6.12: Exclusion plot for pp interaction model parameters (in the cascade dominated γ-ray emission case). The excluded range of parameters lies on the left and above each curve. The two curves represent the constrains obtained for the sources Mrk 421 (top) and for 3C 454.3 (bottom). Taken from (Tchernin et al. 2013a).

Constraints on the $p\gamma$ model

Contrary to the pp models which could be characterized by only two parameters, the "minimal" $p\gamma$ model needs at least three parameters. The additional parameter describes the energy or temperature of the soft photons which serve as targets for the $p\gamma$ interactions. In the case of FSRQs, the soft photon field could be produced by the accretion disk, or by the BLR (broad line region, see Sect. 4.3.1). As the spectrum of emission of BLR is formed by re-processing of the emission of the accretion disk spectrum (known as the "big blue bump"), their spectra are expected to be similar. In those cases the typical photon energies can be described by the disk temperature T. This is a simplification of realistic situations, where the disk or BLR spectra are a superposition of the multi-temperature black body spectra. On the contrary, in the case of photons coming from the jet, the soft photon spectrum has a power law shape, and hence the choice of the typical soft photon energy is more problematic. In the first approximation, we limit the analysis to the model where the soft photon field is provided by the accretion disk or the BLR and assume that the disk is characterized by a single temperature T. Then, in the case of 3C 273, we consider also the interaction of the protons with more realistic target photon fields using the multiwavelength observations of this source (see Fig. 6.6).

The allowed range of the parameters $E_{max,p}, \gamma_p$ and T required by the fact that the level of the neutrino flux expected in the purely hadronic $p\gamma$ model should not exceed the envelope of the IC-40 power law flux sensitivities is shown in Fig. 6.13. In this figure, the cross-sections of this 3D allowed volume defined by the conditions T= $const$ = 10^4 K are represented for different sources listed in Tab. 6.1.

The strongest limit on $(E_{max,p}, \gamma_p)$ for fixed values of T comes from the quasar 3C 273. Figure 6.14 shows the excluded region as a function of the temperature for this source (with T$\in$ $[10^3; 10^5]$ K). We can see that for a soft photon field characterized by a temperature of T= 10^4 K, the slope of the proton spectrum of 3C 273 is constrained to be harder than $\gamma_p \lesssim 1.7$ with a cut-off energy $E_{max,p} \geq 10^{18}$ eV. Such hard spectra could be in the range expected for the shock acceleration models (Schlickeiser & Vainio 1998), if the distribution of protons injected by the acceleration process is not significantly modified by the effects of (energy dependent) escape from and attenuation in the source. Lower soft photon temperatures also allow somewhat lower values of $E_{max,p}$ and softer spectral index. However, for all temperatures, $E_{max,p}$ remains in a range higher than $\sim 3 \cdot 10^{17}$ eV, implying that also in the model with $p\gamma$ interactions blazars have to be the UHECR sources for the model to be valid.

To test the robustness of the constraint on the cut-off energy of the proton spectrum, we investigate the dependence on the lower bound on $E_{max,p}$ on the shape of the soft photon spectrum for the blazar 3C 273. As shown in Fig. 6.6, the big blue bump spectrum in 3C 273 could be modeled as a cut-off power-law with the photon index close to 0 and cut-off at 10 eV. Repeating the analysis for such soft photon spectrum provides a constraint on the slope and cut-off energy of the proton spectrum shown in Fig. 6.15. In the particular case of 3C 273, the constraints on $(E_{max,p}, \gamma_p)$ found assuming the realistic accretion disk soft photon spectrum are equivalent to those found for the one-temperature black body spectrum with T$\sim 3 \cdot 10^3$ K. Alternatively, if we consider the soft photon spectrum generated by the synchrotron radiation in the jet of the blazar (dashed curve in Fig. 6.6), the constraints on $(E_{max,p}, \gamma_p)$ are equivalent to the ones obtained assuming the black-body soft photon spectrum with temperature T$\sim$ 10^3 K (see Fig. 6.15). Therefore the details of the shape of the soft photon spectrum do not seem to have a great impact on the rejection bounds that can be set on the basic parameters of the $p\gamma$ hadronic scenario.

6.6 Discussion

Summary and outlook

The constraints on the parameters of pp and $p\gamma$ models of the activity of blazars derived in this study demonstrate the potential of the multi-messenger methods to study astrophysical sources. This new method became available with the start of operation of the IceCube neutrino telescope.

Regarding the pp interactions, when we assume that the GeV electromagnetic emission is dominated by the emission of the cascade, the combination of IC-40 and Fermi data indicate that blazars should be a source of UHECRs (see Fig. 6.12). Interestingly, for the same data, but assuming that the pion decays component dominates the GeV electromagnetic emission, this multi-messenger approach rules out the possibility that AGN are accelerating protons up to ultra-high-energy (Fig. 6.10).

Secondly, considering the case of $p\gamma$ model, the limits imposed by the neutrino data depend on an additional parameter, which is not directly measured. This additional parameter is the typical energy of the soft photons. In a first estimate, we have limited our analysis to the simplest case where the soft photon field has a thermal spectrum, so that the characteristic energy of the soft photons is given by the temperature. From Figs. 6.13 and 6.14, we could see that by fixing the temperature of the soft photon field, we still find relatively tight constraints on the slope and high-energy cut-off of the proton spectrum. For instance, for a sample of the brightest sources, when the temperature is fixed at 10^4 K, the cut-off energies of the proton spectra are allowed to be in

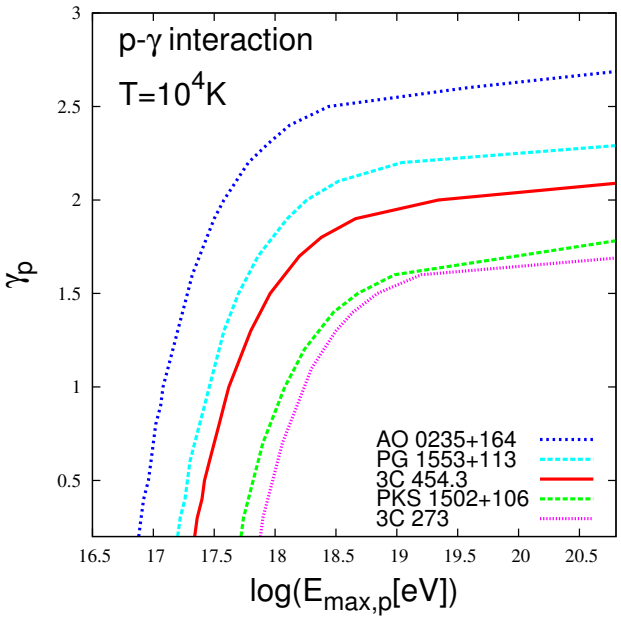

Figure 6.13: Constraints on $(E_{max,p}, \gamma_p)$ deduced in the $p\gamma$ model, assuming T= 10^4K for different sources in Tab. 6.1. The excluded regions lie above the curves. From top to bottom, the constrains are obtained for the sources: AO 0235+164, PG 1553+113, 3C 454.3, PKS 1502+106 and 3C 273. The best constraint is from 3C 273. Taken from (Tchernin et al. 2013a).

the range larger than $10^{17} - 10^{18}$ eV and the slope of the proton spectrum is constrained to be harder than 2.5 (Fig. 6.13). In the case of 3C 273, which provides the best constraints, the cut-off energy of the proton spectrum is bound to be higher than $\sim 10^{18}$ eV and the spectrum harder than about 1.7 (Fig. 6.14). Changing the soft photon field temperature leads to modification of these constraints, somewhat relaxing or strengthening the bounds on $E_{max,p}$ and γ_p, as shown in Fig. 6.14 and Fig. 6.15. Our results show that in our order of magnitude estimate, the constraints have a similar trend for any of the considered soft photon fields.

Interestingly, the set of blazars providing the best constraints on the parameters of pp and $p\gamma$ models is different. Tightest constraints on the pp model parameters are given by the brightest Northern hemisphere blazars. This is not surprising, because the neutrino spectrum in the pp model is expected to be emitted in a broad energy range, including the range in which the IceCube detector is most sensitive (from $\sim$ 10 TeV to $\sim$ 10 PeV). At the same time, the tightest constraints on the $p\gamma$ model parameters are imposed by the bright blazar(s) situated close to the horizon of IceCube detector. This is explained by the fact that in the $p\gamma$ models the neutrino flux is peaked at the energy of the pion production energy threshold (see Fig. 3.11), ie at high energy. Therefore, given that the sensitivity of IceCube at the highest energies improves around the horizon (see Fig. 6.3), the best constraints are achieved for the sources located close to the horizon.

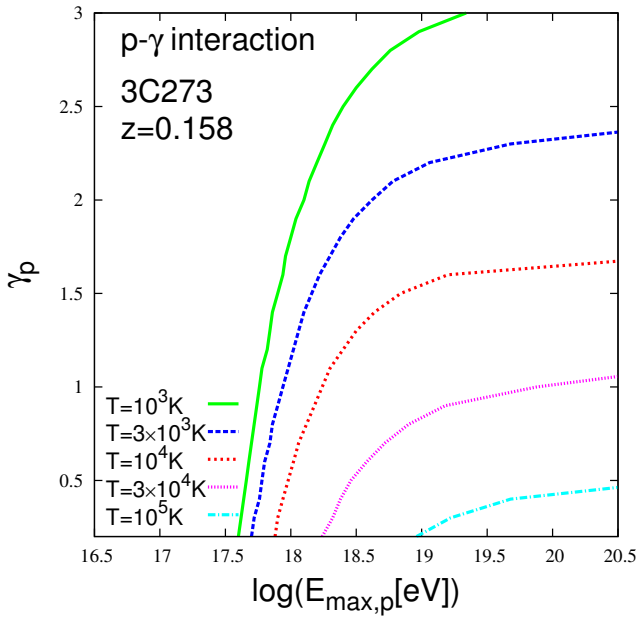

Figure 6.14: As in the previous figure, but only for 3C 273 and for different temperatures of the soft photon field. The lines represent the constrains obtained for the temperatures of (from top to bottom): T= 10^3K, T= $3 \cdot 10^3$K, T= 10^4K, T= $3 \cdot 10^4$K and T= 10^5K. Taken from (Tchernin et al. 2013a).

Remarks and limitations of this analysis

The aim of this analysis is not to test the validity of purely hadronic models and their energetic (in)efficiency. Indeed, our constraints do not depend on the efficiency of pp and $p\gamma$ interactions in the sources: if the efficiency is low, most of the protons would escape from the source, transferring only a small fraction of their power to gamma-rays and neutrinos. However, the equal power re-distribution between the electromagnetic and neutrino components would hold also in this case. Therefore, it may well be that parameters of the source are such that interactions of high-energy protons in the source are inefficient (energy attenuation length is much longer than ct_{esc} where t_{esc} is the escape time of the protons from the source). This would imply that most of the high-energy protons escape in the form of ultra-high-energy cosmic rays, instead of powering the electromagnetic and neutrino emission. Consequently, in this analysis we do not aim at testing the validity of the purely hadronic model itself, we just constrain the model parameters assuming that electromagnetic and neutrino emission is powered by the high-energy proton interactions.

Our study does not apply to the models in which the energy of the proton beam is used for the generation of proton or muon synchrotron emission. In this case the neutrino power of the source might be much smaller than the electromagnetic power. In fact neutrino power could be made arbitrarily small in these scenarios, so that the constraints reported in this study are largely relaxed.

We assumed that γ-rays and neutrinos are arriving simultaneously at the detector. However, the geometry of the electromagnetic cascade could be affected by the deflections of electrons and

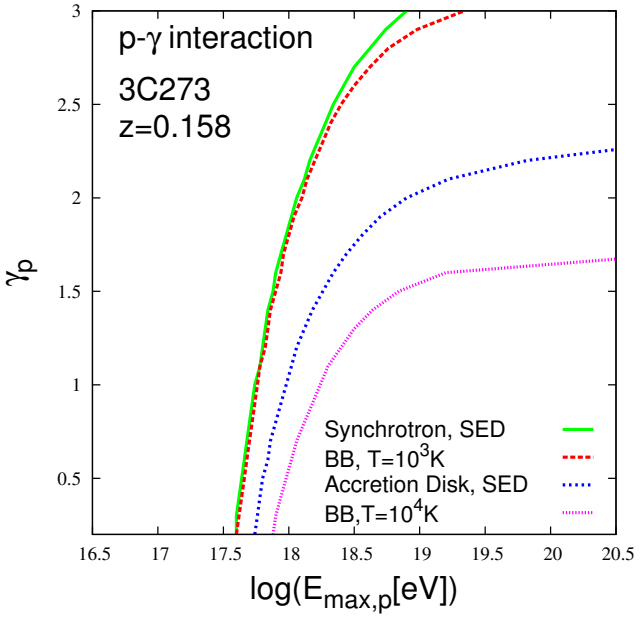

Figure 6.15: Constraints on $(E_{max,p}, \gamma_p)$ deduced in the $p\gamma$ model for proton interactions with different soft photon distributions coming from (from top to bottom): the synchrotron emission (from the SED of 3C 273, Fig. 6.6), a black body (BB) of temperature T= 10^3K, the accretion disk (from the SED of 3C 273, Fig. 6.6) and a black body of temperature T= 10^4K. Taken from (Tchernin et al. 2013a).

positrons by magnetic fields. If the electromagnetic cascade develops at the distance d from the AGN central engine, in a cone with an opening angle $\theta \sim \Gamma^{-1} \sim 0.1$, the characteristic time delay is $d\theta^2/c \sim 1\,[d/30\text{ pc}]$ yr. Our study is based on the neutrino and γ-ray fluxes averaged on ~ 1 yr time scale. If the distance, d, is much larger than ~ 30 pc, the γ-ray and the characteristic time scale of activity of blazars is comparable to one year, and therefore the assumption that γ-ray flux is comparable to the neutrino flux might be violated. In this case the constraints on $(E_{max,p}, \gamma_p)$ derived above from the common γ-ray + neutrino data set might be relaxed.

As we saw in Sect. 3.1.2 , the parametrization of Kelner et al. (2006) slightly overestimates the cross-section measurements from Beringer et al. (2012) at the energy of 10^{17} eV (see Fig. 3.7). In order to quantify how much the use of this parametrization can affect our results, I produced an "updated" parametrization (see Fig. 6.16) based on the cross-section parametrization from Kelner et al. (2006), which I modified to take into account the cross-section data from Beringer et al. (2012). I computed the ratio between the energy flux of the secondary particles produced with the cross-section parametrization of Kelner et al. (2006) and the one of the secondary particles produced with the "updated" cross-section parametrization. For different proton spectral indices ($\gamma_p \in [1:3]$), I obtained that the parametrization of Kelner et al. (2006) overestimates the secondary particle flux to 20% at most. This overestimation is contra-balanced by several underestimations of the neutrino flux. Indeed, the Fermi measurement of the source flux in the 0.1-100 GeV range is an underestimate of the overall electromagnetic luminosity. Indeed, for most of the considered blazars, the spectral energy distribution peaks at the energy covered by the Fermi detector, such that the source flux in the 0.1-100 GeV range might be an underestimation of the bolometric flux by a factor ~2-5. Furthermore, the suppression of the γ-ray flux in the energy band above 100 GeV due to the absorption on the Extragalactic Background Light (EBL, Franceschini et al. 2008) might also cause a slight underestimation of the neutrino power. Therefore, the constraints on the hadronic models of activity of blazars presented here are conservative.

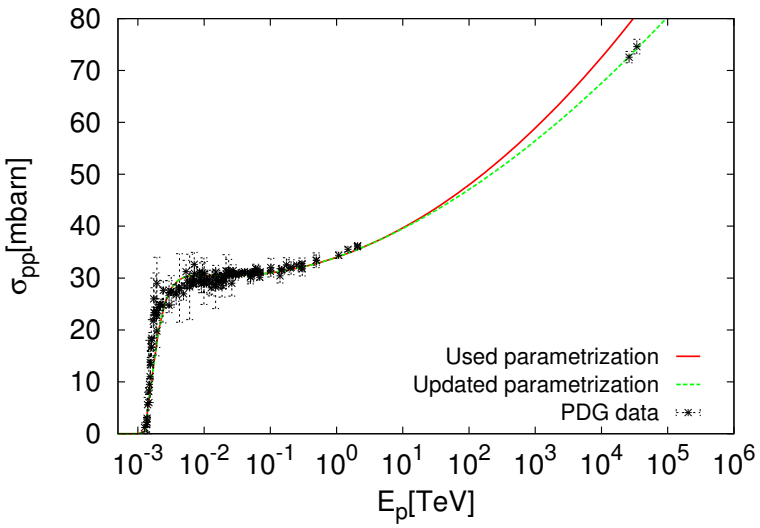

Figure 6.16: Same figure as Fig. 3.7,where has been added the "updated" parametrization for the total inelastic cross-section introduced in the text.

In general, both the distribution of the high-energy protons and the target photon field seen by the high-energy protons in the blazar central engine or jet are highly anisotropic. These anisotropies strongly affect the efficiency of $p\gamma$ interactions in the source and the energy threshold for the pion production. For example, if the high-energy proton beam is generated in the AGN central engine and propagates through the quasi-thermal radiation field produced by the accretion disk, the energy threshold for the pion production would scale with the distance d from the central engine as $(d/R_{disk})^2$, where R_{disk} is the size of the quasi-thermal emission region from the disk. The increase of the threshold energy is due to the fact that the collision angle between the high-energy protons and the disk photons would scale as $\theta \sim R_{disk}/d$. In the first approximation, the increase of the threshold could be equivalently described by the decrease of the characteristic energy/temperature of the soft photons, i.e. by the substitution $\epsilon_{ph} \rightarrow \epsilon_{ph}(R_{disk}/d)^2$ in Eq. [3.11]. Otherwise, if the disk photons are efficiently scattered in the BLR, the proton beam would see an isotropic photon field (in the reference frame of the AGN central engine) and the threshold energy would not change.

In a similar way, if high-energy protons interact with the synchrotron photons generated by the blazar jet moving with the bulk Lorentz factor Γ in the same direction as the proton beam), the collision angle between the high-energy protons and jet photons is $\theta \sim \Gamma^{-1}$, so that the threshold for the pion production scales as Γ^2, compared to the threshold which would be found in the AGN (or observer) reference frame in the case of isotropic distributions of high-energy protons and soft photons. Similarly to the case of the disk radiation, the change of the threshold energy could be described by the substitution $\epsilon_{ph} \rightarrow \epsilon_{ph}/\Gamma^2$ in Eq. [3.11]. The increase of the energy threshold for the pion production could be equivalently described in the reference frame comoving with the jet. In this frame the energies of the soft synchrotron photons and of the protons are a factor Γ^{-1} lower than in the AGN / observer reference frame. Applying Eq. [3.11] to the jet frame proton and soft photon energies, one finds that the threshold energy in the laboratory frame scales as Γ^2.

The constraints on the $p\gamma$ models have been presented in the AGN central engine / AGN host galaxy frame, which is equivalent to the 'observer' reference frame in the case of the low-redshift sources. To keep our results as independent of the (highly uncertain) anisotropy patterns of the high-energy proton and soft photon distributions as possible, we make a scan over different characteristic energies ϵ_{ph} (or temperatures T$\sim \epsilon_{ph}$) of soft photon radiation fields. This is equivalent to taking into account the different possible values of the factor Γ and $(d/R_{disk})^2$ in the substitutions $\epsilon_{ph} \rightarrow \epsilon_{ph}/\Gamma^2$, $\epsilon_{ph} \rightarrow \epsilon_{ph}/(d/R_{disk})^2$ in Eq. [3.11].

The parametrization of $p\gamma$ interaction cross-sections by Kelner & Aharonian (2008) applies for the isotropic target photon distribution, so that it is, strictly speaking, not appropriate for the description of interactions of high-energy protons with photons produced by the accretion disk or jet. However, the precise anisotropy pattern of the photon field in the possible regions of high-energy proton interactions in blazars is not known. Nevertheless, the uncertainties of the numerous parameters / assumptions introduced in the different interaction models would not make the results more precise. Therefore, calculations done assuming isotropic target photon field could be used for the purpose of the order-of-magnitude estimate of the relations between the parent protons and their secondary particles.

Finally, the lower bound on the maximal proton energies derived from the neutrino data provides an indirect constraint on the physical conditions at the acceleration site, in particular on the magnetic field strength B and size R of the acceleration site. This constraint stems from the Hillas

condition

$$E_{max,p} \geq E_{max} = e \cdot B \cdot R = 10^{18} \left[B/10^4 \text{ G}\right] \left[R/10^{12} \text{ cm}\right] \text{ eV}.$$

The bound $E_{max,p} \gtrsim 10^{17} - 10^{18}$ eV translates to the constraint

$$\left[B/10^4 \text{ G}\right] \left[R/10^{12} \text{ cm}\right] > 1.$$

This constraint is satisfied in several components of the blazar, in particular, in the central engine with typical size about the Schwarzschild radius of the black hole and strong magnetic field in excess of kG, in the parsec scale jet with $R \sim 1$ pc and magnetic fields possibly in the mG range and even possibly in the large kiloparsec scale jet with $R \sim 1$ kpc and μG magnetic fields.

Chapter 7

High energy particles and dark matter in galaxy clusters

7.1 Upper-limits on the cosmic ray content of galaxy clusters

7.1.1 Motivation

As introduced in Sect. 4, cosmic ray protons could potentially be accelerated in galaxy clusters (Hillas 1984). For instance, the presence of cosmological shocks during the structure formation processes (see e.g., Vazza et al. 2012), or/and the relativistic outflows of the central AGN (see e.g., Vazza et al. 2013) may trigger particle acceleration. Based on the evidences of the cosmic ray confinement in our Galaxy (see Sect. 4), these accelerated cosmic rays are expected to stay confined in the potential wells of the galaxy clusters (Berezinsky et al. 1997).

These confined cosmic ray protons interact predominantly through pp interactions with the gas in the ICM. This is due to the fact that the density of the low energy photons is too low to have significant $p\gamma$ interactions. Indeed, at the pion production threshold, the cross section for pp interaction is 50 larger than the cross section for $p\gamma$ interactions. Therefore, assuming a density of low energy protons in galaxy clusters of the order of 10^{-2} cm^{-3}, the pp interactions channel dominates over the $p\gamma$ interactions channel if the density of the target radiation is below 0.5 cm^{-3}. Assuming cosmic rays protons of energy of 100 GeV, the energy of the target radiation required for pion production is of about 1 MeV (see Eq. [3.12]). This implies that the luminosity at 1 MeV is required to be larger than $L_{1\mathrm{MeV}} \geq 8 \cdot 10^{53}\,[n_{ph}/0.5\ \mathrm{cm}^{-3}]\,[R/\ \mathrm{Mpc}]^2\,[\epsilon_{ph}/1\ \mathrm{MeV}]$ erg/s for the $p\gamma$ interaction channel to dominate over the pp interaction channel in a cluster of Mpc scale. As galaxy clusters are not bright MeV sources, this implies that the density of target MeV photons is too low to allow efficient $p\gamma$ interactions.

Based on theoretical models and on the density of the target ICM protons observed in X-rays, the radiation produced in the expected pp interactions should be observable with γ-ray telescopes (e.g. Colafrancesco & Blasi 1998; Pfrommer & Enßlin 2004; Pfrommer et al. 2008; Pinzke et al. 2011). However, galaxy clusters are very faint γ-ray sources and the numerous observational studies have resulted in upper limits on the gamma-ray emission only (e.g. Reimer et al. 2003; Perkins 2008; Aharonian et al. 2009; Aleksić et al. 2010; Ackermann et al. 2010; Arlen et al. 2012; Dutson et al. 2013). Therefore, it would be difficult to estimate the neutrino flux from the undetected γ-ray flux and the multi-messenger approach as applied in the previous chapters to the Galactic plane and to the blazars can be hardly applied to galaxy clusters.

Instead, in the present study I use the result of a stacked γ-ray emission of a sample of very bright X-ray galaxy clusters ($f_x(0.1-2.4\mathrm{keV}) > 2 \cdot 10^{-11}\mathrm{erg/s\,cm^2}$). Assuming that these γ-rays are produced by the interactions of the cosmic ray protons with the ICM, this γ-ray upper-limit leads to an average upper-limit on the cosmic ray-to-gas energy ratio. I derive the average cosmic ray-to-gas energy ratio for different proton spectral indices between ∼2 and ∼3.2. Such spectral

indices are expected in simulations of large scale structure formation, in the strong (with a Mach number M≥10) and weak (M∼2) shock limits (see e.g., Vazza et al. 2012).

The importance of the presence of cosmic ray protons in galaxy clusters is two- folds. First the presence of non-thermal component could bias the mass estimation (see Eq. [4.4]) and have impact on our understanding of structure formation (see Sect.4.3.2); second, the detection of cosmic ray protons in galaxy cluster would attest that galaxy clusters are accelerators of cosmic rays and would help us understand the particle acceleration mechanisms in such systems (see e.g., Vazza et al. 2012; Kang & Jones 2007). This study has been published in (Huber et al. 2013).

7.1.2 Selection and stacking of the galaxy clusters

The studied clusters have been selected from the extensive catalog of high X-ray luminosity galaxy clusters HIFLUGCS (Reiprich & Böhringer 2002). From this catalogue, only 53 galaxy clusters have been selected (see list in appendix Sect. .2), based on the following criteria: they should not be located too close from the Galactic plane (whose diffuse emission could be miss-interpreted as arising from the clusters), should not have any known γ-ray point sources located in their vicinity (based on the second year Fermi-LAT catalog (Nolan et al. 2012)) and should be located at low redshift $z < 0.2$, to help the detection of the γ-ray signal.

The stacked analysis has been performed on γ-ray data collected by the Fermi-LAT satellite from 2008-08-04 to 2013-01-31, using a method described in our paper (Huber et al. 2013). For the purpose of my thesis, I would like to concentrate in my contribution to this analysis, where I used the result of this stacking analysis to derive the average cosmic-ray-to-gas energy ratio for the selected sample of galaxy clusters.

Results of the stacked analysis

Galaxy clusters are not resolved with the Fermi-LAT satellite (whose angular resolution is of ∼3° at 100 MeV). Therefore, we consider here the integrated flux over the entire cluster size. In the present analysis, the γ-ray emission is assumed to be the same in all clusters and to have a power-law spectral shape parametrized by $dN/dE|_\gamma = n_0(E/E_{0,\gamma})^{-\gamma_\gamma}$, where γ_γ is the spectral index and n_0 the normalization at the arbitrary energy $E_{0,\gamma}$ (fixed to 1 GeV). The upper-limits have been derived for photon spectral indices γ_γ equal to 2.0, 2.4, 2.8, and 3.2.

Since the evolution histories of cool-core (CC) and non cool-core (NCC) galaxy clusters are different (see Sect. 4.3.2), average γ-ray upper-limits are also provided for these two populations of galaxy clusters. The 95% C.L. upper-limit for the 53 clusters, for the 21 CC clusters of the sample and for the 32 NCC clusters, obtained for power laws with photon indices $\gamma_\gamma = 2.0, 2.4, 2.8,$ and 3.2 integrated from 1 to 300 GeV are summarized in Table 7.1.

As shown, the 95% C.L. upper limits on the gamma-ray emissivity of the galaxy cluster sample is of the order of a few 10^{-11} ph cm^{-2} s^{-1} in the 1 to 300 GeV range for all spectral indices. This limit can be compared to the results of the Fermi collaboration (Ackermann et al. 2014), where they obtained an upper-limit of the level of few 10^{-10} ph cm^{-2} s^{-1} for individual clusters on the energy range above 500 MeV and which is one order of magnitude larger than the result achieved in the present stacked analysis.

Table 7.1: Flux upper limits divided by the sample size on the stacked emission in the 1 − 300 GeV energy band.

Photon index γ_γ	All Flux UL	CC Flux UL	NCC Flux UL
2.0	3.2	4.9	2.8
2.4	3.4	5.7	2.7
2.8	2.9	5.7	2.0
3.2	2.4	5.5	1.5

Column description: 1: Photon index assumed for the analysis. 2: 95% CL flux upper limit on the stacked emission of the entire sample in units of 10^{-11} ph cm^{-2} s^{-1}. 3: Same as 2 for the CC subsample. 4: Same as 2 for the NCC subsample. Adapted from (Huber et al. 2013).

7.1.3 Constraints on the cosmic-ray energy density combining γ-ray with X-ray observations

The observational constraints from Fermi-LAT data were obtained by assuming that the spectral shape of the observed photons follows a single power law. As we saw in Sect.3.1.2, in order to produce a γ-ray spectrum of power-law shape, the parent protons must also be distributed also with a power-law. Therefore, the proton spectrum can be defined as

$$\frac{dN_p(r)}{dE_p} = n_p(r)\left(\frac{E_p}{E_{0,p}}\right)^{-\gamma_p} \exp\left(-\frac{E_p}{E_{max,p}}\right), \tag{7.1}$$

where γ_p is the proton spectral index, n_p the normalization at $E_{0,p}$ and $E_{max,p}$ the proton cut-off energy. For soft proton spectra, the total cosmic ray energy density depends very weakly on the cut-off energy. In this study the cut-off energy has been fixed to $E_{max,p}$=10^{19} eV. The radial dependence comes from the fact that galaxy clusters are extended source whose size is resolvable with the present X-ray telescopes (for instance the angular resolution of ROSAT is of 15" (Aschenbach et al. 1981).

The analysis is performed in the energy range between 1 and 300 GeV, because at lower energy, a power law is a not good approximation of the gamma-ray spectrum resulting from neutral pion decay. Indeed, as we saw in Sect. 3.1.2, in pp interactions the spectrum of the secondary photons coming from neutral pion decay is comparable to the spectrum of the parent protons only above the threshold energy for pion production ($\simeq$1 GeV), while below this limit, the predicted spectrum follows the behavior of the cross-section (see Fig. 3.8 and for instance Kappes et al. 2007; Kelner et al. 2006). This implies that the power-law approximation for the γ-ray emission is not valid below about 1 GeV. This effect is illustrated in Fig. 7.1 where the photon spectrum produced by the interaction of the primary protons with the ambient gas is represented in blue. As one can see, the effective photon index (red curve), which represents the fit of the γ-ray spectrum in the range 1-300 GeV, is harder than the spectral index of the parent protons (black curve). Using the parametrization of Kelner et al. (2006) to produce the γ-ray spectra, I compute for each γ_γ the value of γ_p which reproduces the assumed γ-ray spectrum. For γ_γ=2.0, 2.4, 2.8, and 3.2, I obtain respectively γ_p=2.05, 2.45, 2.85, and 3.25.

For these proton spectra and knowing the density of the target proton (from X-ray observations), I can compute the luminosity density of each cluster of the sample. The collision rate per unit of volume is given by

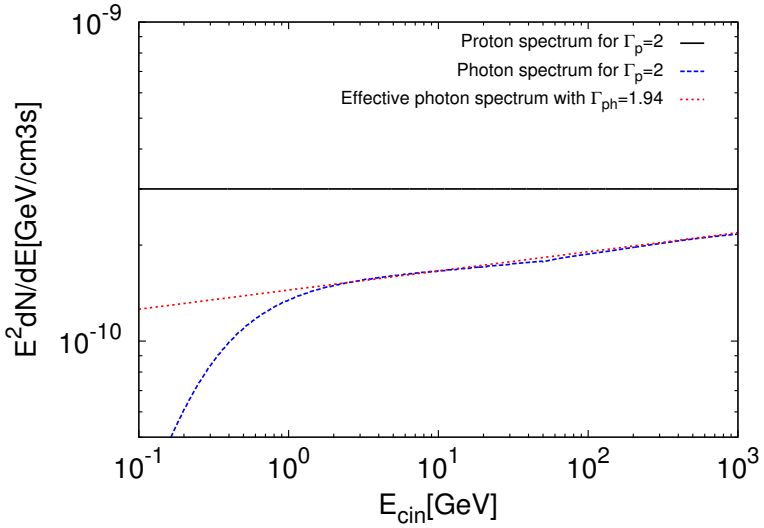

Figure 7.1: The produced photon spectrum (blue) for a proton injected spectrum of $\gamma_p = 2$ and $E_{cut,p} = 10^{15}$eV (black, scaled by an arbitrary factor). The red dotted line represents the best fit of the photon spectra with a simple power law in the energy range [1-300] GeV. The behavior at low energy follows the increase of the cross section at $E_p \sim 1GeV$ (see Fig.. 3.7). Note that the proton spectrum is expressed as function of the kinetic energy, $E_{cin} = E_{tot} - m_p c^2$. Taken from (Huber et al. 2013).

$$\frac{dN}{dtdV}(r) = n_{gas}(r) n_p(r) v_p \sigma_{pp} \quad [1/cm^3 s], \tag{7.2}$$

where n_p is the number density introduced in Eq. [7.1], v_p is the velocity of the cosmic rays, n_{gas} is the number density of the proton target, and σ_{pp} is the cross-section of the interaction (Fig. 3.7). With the collision rate, the luminosity can be derived using the fact that at each interaction, for each neutral pion produced, two photons of energy $E_\gamma = \frac{\zeta}{2k} E_p$ are produced (where ζ is the fraction of energy transferred from the proton to the k produced pions, Kelner et al. 2006). Therefore, the luminosity density resulting from the interactions of these two populations of protons can be obtained as

$$\frac{dL}{dV}(r) = 2kE_{\gamma,\pi^0} \frac{dN}{dtdV}(r) \quad [eV/cm^3 s], \tag{7.3}$$

where the factor $2k$ counts for the photons produced by the decay of the k neutral pions produced in the collision.

Once the luminosity of each cluster is known, the cosmic ray content of these clusters can be constrained as follows. The total energy stored into cosmic rays, E_{CR}, is expressed as a fraction ϵ of the total thermal energy E_{gas}, as $E_{CR} = \epsilon \cdot E_{gas}$. Using $E_{gas} = \frac{2}{3} n_{gas}(r) k_{bol} T_{gas}$, where k_{bol} is the Boltzmann constant, the cosmic ray energy can be written as

$$E_{CR} = \int_V dr^3 \int_{m_p c^2} n_p(r) \left(\frac{E_p}{E_{0,p}}\right)^{-\gamma_p} \exp\left(-\frac{E_p}{E_{max,p}}\right) E_p dE_p = \epsilon \int_V dr^3 \frac{2}{3} n_{gas}(r) k_{bol} T_{gas}. \tag{7.4}$$

In first approximation, the temperature is assumed to be constant over the volume of the cluster.

Then we compute the gamma-ray flux that should be observed in the extreme case where the cosmic rays were in equipartition with the gas (i.e. $\epsilon = 1$ in Eq. [7.4]). The seaked value of ϵ is then given by the ratio of the observed upper-limits to the flux expected when equipartition is assumed. The value of the cosmic ray number density at the center of the cluster required to be in equipartition with the gas is

$$n_{p,0} = \frac{\frac{3}{2} n_{gas,0} k_{bol} T \int_V f_{gas}(r) d^3 r}{\int_{m_p c^2} \left(\frac{E_p}{E_{0,p}}\right)^{-\gamma_p} \exp\left(-\frac{E_p}{E_{max,p}}\right) E_p dE_p \int_V f_p(r) d^3 r}, \tag{7.5}$$

where $n_i(r) = n_{i,0} f_i(r)$ and $f_i(r)$ represents the radial dependence, with $i = p$ or gas.

The radial profile for the density of the thermal gas is assumed to follow an isothermal beta model (Cavaliere & Fusco-Femiano 1976), where the gas density can be parametrized by the function

$$n_{gas}(r) = n_{0,gas} \left(1 + \left(\frac{r}{r_c}\right)^2\right)^{-3\beta/2}, \tag{7.6}$$

where $n_{0,gas}$ is the central density, r_c is the cluster core radius, and β is the slope of the density profile in the outer regions.

In this study, three different cosmic ray radial distributions have been tested. In the first case, $n_p(r)$ is assumed to have the same radial distribution as the thermal gas, ie $f_p(r) = f_{gas}(r)$ (referred to as the isobaric case). In the second case, the cosmic ray-to-thermal energy ratio is assumed to increase with radius as $f_p(r) = f_{gas}(r) \cdot (1 + (r/r_c)^2)^{-0.25}$, which corresponds to $\epsilon(r) \sim r^{0.5}$ (referred to as flatter). This distribution corresponds to the predictions of simulations in which cosmic rays are accelerated at cosmological shocks (see e.g. Vazza et al. 2012; Pinzke & Pfrommer 2010; Donnert et al. 2010). In the third case, a decreasing radial profile has been assumed, using $f_p(r) = f_{gas}(r) \cdot (1 + (r/r_c)^2)^{0.25}$ ($\epsilon(r) \sim r^{-0.5}$, referred to as steeper). This radial dependence is expected in simulations where cosmic rays are injected by a central AGN (e.g. Colafrancesco & Marchegiani 2008; Mathews 2009; Fujita & Ohira 2011).

The luminosity in equipartition of the cluster i in the energy range of interest can be obtained as

$$L_{equip,i} = \int_{V_i} \mathrm{d}^3 r \int_{1\ \mathrm{GeV}}^{300\ \mathrm{GeV}} E_\gamma \, \mathrm{d}E_\gamma \left[\frac{dN_\gamma}{dV dE_\gamma dt}\right]_i, \tag{7.7}$$

where $\frac{dN_\gamma}{dV dE_\gamma dt}$ is obtained as shown in Eq. [3.5], using as proton spectrum Eq. [7.1] with the normalization in equipartition (Eq. [7.5]).

For each individual cluster of the sample, I compute the luminosity in equipartition using the parameters published in Chen et al. (2007). These parameters are: the redshift, the temperature, the electronic gas density (which provides the proton gas density through the relation $n_{0,gas} = n_e/1.21$ valid for fully ionized plasma) and the parameters of the gas density distribution (Eq. [7.6]): the core radius, r_c, and the slope of the density profile, β. Knowing the redshift, the luminosity distance (d_{lum}) of a cluster has been obtained using the parametrization of Pen (1999),

$$d_{lum} = \frac{c}{H_0}\left(z + (1 - \frac{3}{4}\Omega_m) z^2 + (9\Omega_m - 10)\frac{\Omega_m}{8} z^3 + ...\right), \tag{7.8}$$

where $H_0 = 70$ km/s Mpc is the Hubble constant and $\Omega_m = 0.3$ is the matter density normalized by the critical density. This parametrization is valid for z<1. To estimate of the virial radius R_{vir}, I use the scaling relations of Arnaud et al. (2005) between the temperature of the cluster and R_{200} (the radius in which the density is 200 times the critical density of the Universe), making the approximation $R_{vir} \sim R_{200}$

$$R_{vir} \approx R_{200} = \frac{B_{200}}{h(z)} \left(\frac{kT}{5\mathrm{keV}} \right)^{0.57}, \tag{7.9}$$

with $B_{200} = 1674$ kpc and $h(z) = (\Omega_m(1+z)^3 + \Omega_\Lambda)^{0.5}$, with $\Omega_\Lambda = 0.7$. This approximation allows us to estimate the physical radius R_{vir} from R_{200}, which is a measurable quantity.

Once the luminosity is computed, the flux is then given by

$$F_i = \frac{1}{4\pi d_{L,i}^2} L_i, \tag{7.10}$$

with L_i given by Eq. [7.7].

To compare with our upper limits on the stacked populations, we define the expected equipartition flux F_{equip} as the mean of the equipartition fluxes of individual systems,

$$F_{equip}(\Gamma) = \frac{1}{N} \sum_{i=1}^{N} F_i, \tag{7.11}$$

where N is the total number of galaxy clusters in the sample.

Finally, the upper limit on the cosmic ray-to-thermal energy ratio is obtained by taking the ratio of the observed flux to the equipartition flux, as

$$\epsilon(\Gamma) = \frac{UL_{Fermi}}{F_{equip}(\Gamma)}, \tag{7.12}$$

where UL_{Fermi} is the energy flux corresponding to the photon flux obtained in the stacked analysis in the 1-300 GeV energy band (see Table 7.1). The value of ϵ depends both on the assumed spectral index and on cosmic ray density radial distribution.

7.1.4 Results

Among the 53 systems comprising our sample, 32 are classified as NCC, while 21 exhibit CC properties. We note that among our sample CC clusters typically exhibit a lower temperature ($T_{av,CC} \sim 3.2$ keV), and thus a lower mass and thermal energy, than NCC systems ($T_{av,NCC} \sim 5.5$ keV).

The results for the entire sample, as well as for the CC and NCC cluster populations independently and for the three different cosmic ray radial distributions described above, are given in Table 7.2. As can be seen in Table 7.2, for a photon index of 2.0 our upper limits on the cosmic ray-to-thermal energy ratio for the whole sample and the three cosmic ray distributions are in the range ~3-6%.

As we saw in the introduction (Sect. 4.3.2), the mass estimation based on the hydrostatic assumption usually neglect non thermal pressure. Therefore, the presence of a significant cosmic ray component in galaxy clusters could introduce a bias in cluster masses estimation (e.g. Ando & Nagai 2008). In the fully relativistic case ($v_p \rightarrow c$), the limits provided in the present study can be readily transformed into the pressure ratio using the relation $E_{CR}/E_{gas} = 2P_{CR}/P_{th}$, where P_{CR}/P_{th} is the pressure ratio. This assumption is approximately valid, since we are considering only photons with energies > 1 GeV. Thus in the isobaric case, for the average population of photon index of 2.0, we obtain an upper limit on the pressure ratio of $P_{CR}/P_{th} \lesssim 2.2\%$. Our results indicate that the pressure contribution from cosmic rays is small, and thus that the bias in cluster masses induced by the presence of cosmic ray, if existing, would be negligible.

For comparison, using data obtained by the EGRET experiment on board the *Compton Gamma-Ray Observatory*, Reimer et al. (2003) performed a similar study and obtained upper limits on the cosmic ray-to-thermal energy ratio of the order of 10-20% also for a photon index of 2.0. However, thanks to the better sensitivity of Fermi-LAT, our upper limit lies a factor of 3-4 below the upper limits obtained in this study. Recently, Ackermann et al. (2010, 2014) performed a similar analysis on individual and stacked systems and obtained stringent gamma-ray upper limits which constrain the cosmic ray energy density at the level of a few percent of the thermal energy density in the best cases. Similar results were recently obtained on the Coma cluster through a combination of Fermi-LAT and VERITAS data (Arlen et al. 2012), which leads to an upper limit of the order of 2% on the cosmic ray-to-to-thermal pressure ratio. Compared to these studies, our analysis puts constraints on the average population which are slightly below the few best cases for individual systems. The stacking method therefore allows us to bring the constraints on the typical cluster population to the level of the few best individual cases. Recently, Dutson et al. (2013) stacked a sample of 114 clusters including a central radio galaxy with Fermi-LAT, and did not find any evidence of a signal in the stacked population, in agreement with the results presented here.

7.1.5 Discussion

Summary and outlook

In this study, I have used the γ-ray upper-limit of a stacked analysis of 53 galaxy clusters to set constraints on the averaged cosmic ray-to-thermal pressure ratio. I also have treated separately the case of CC and NCC clusters and have derived constraints for these two samples. The idea was to test if the dynamical state of the cluster (relaxed or unrelaxed) can influence the fraction of cosmic-ray content in clusters. The results are shown in Table. 7.2. As we can attest, NCC clusters are generally better constrained than the entire sample, which is better constrained than the CC clusters. This ordering in the strength of the constraints can arise from the fact that the CC clusters that we consider typically exhibit a lower temperature than the NCC clusters, this thus implies that the flux in equipartition is smaller for the CC than for the NCC clusters and that CC clusters are typically less well constrained. It seems therefore that this ordering in the constraints is an artifact of the cluster selection. Consequently, the fraction of cosmic rays in clusters can be considered as being the same in relaxed and unrelaxed clusters. This result can be interpreted as follows: as cosmic ray protons are expected to accumulate during the whole life of the cluster (Berezinsky et al. 1997), by studying the γ-ray emission of galaxy clusters, we are sensitive to the cosmic ray protons accelerated during the whole history of the cluster.

γ_γ	γ_p	cosmic ray distribution	All	CC	NCC
2.0	2.05	Isobaric	4.5	8.5	3.4
		Steeper	3.1	4.9	2.6
		Flatter	6.2	13.3	4.5
2.4	2.45	Isobaric	4.6	9.6	3.3
		Steeper	3.2	5.6	2.4
		Flatter	6.4	15.1	4.2
2.8	2.85	Isobaric	7.0	16.7	4.3
		Steeper	4.8	9.7	3.2
		Flatter	9.6	26.1	5.6
3.2	3.25	Isobaric	10.1	30.7	5.9
		Steeper	7.4	17.8	4.4
		Flatter	14.9	47.8	7.7

Table 7.2: Upper limits on the cosmic ray -to-thermal energy ratio of the parent proton population. Column description: 1: Photon index assumed for the analysis. 2: Corresponding effective proton index (see Fig. 7.1). 3: Assumed radial distribution of the cosmic ray in the cluster. In the "isobaric" case the cosmic ray distribution is assumed to follow the same radial dependence as the gas (Eq. [7.6]). In the "steeper" case the cosmic ray -to-thermal energy ratio decreases with radius as $\epsilon(r) \sim r^{-0.5}$. In the "flatter" case it increases as $\epsilon(r) \sim r^{0.5}$. 4: UL on the cosmic ray-to-thermal energy ratio, in percent, computed using Eq. [7.12] for the entire cluster population. 5: Same as Col. 4 for the CC subsample. 6: Same as Col. 4 for the NCC subsample. Taken from (Huber et al. 2013).

The consequences of the low cosmic ray-to-gas energy content of the level of a few % can help constraining the different models of particle acceleration in galaxy clusters (see Sect. 4.3.2). In the following, I will review some of these implications.

In the case where cosmic rays are injected at merger shocks, in Vazza et al. (2012) the authors estimated that the cosmic ray-to-thermal pressure ratio should slightly increase with radius, from $\sim 1\%$ in the core to $\sim 10\%$ around R_{200}, without any important differences between relaxed and dynamically-active systems. Similar results were obtained by Pinzke & Pfrommer (2010). Since the bulk of the cosmic rays are produced in merger shocks with Mach number in the range $2-4$, we expect the photon index of the resulting proton population to be in the range 2.3 to 2.8. Comparing these predictions with our computation of the cosmic ray-to-thermal pressure ratio (see Table 7.2), for a flatter cosmic ray distribution we can see that our 95% upper limits on the pressure ratio for the entire sample are in the range $3-5\%$ for γ_p in the range 2.3-2.8. These values are similar to the expectations of numerical simulations, and thus our observational results are starting to probe the particle acceleration models assumed in these simulations. For the NCC subpopulation, our upper limits are at the level of $2-3\%$ of the thermal pressure for γ_p in the range 2.3-2.8, which is in slight disagreement with the predictions. Therefore, although these predictions cannot be firmly ruled out yet, it is likely that the acceleration efficiency assumed in these simulations is overestimated. Given that the simulations presented by Vazza et al. (2012) and Pinzke & Pfrommer (2010) are non-radiative (ie, the cooling of the gas is not taken into account, but it is expected to modify the distribution of the cosmic rays, which will be injected at the cluster center by the accretion of the baryonic matter in the potential well) and neglect the injection of cosmic rays by other processes (AGN, SNe), the predicted level of cosmic ray energy density should be treated as a lower bound to the expectations from numerical simulations, which reinforces our result. Therefore, it appears likely that the acceleration efficiency used in existing numerical simulations is overestimated in the case of cosmological shocks.

In some models, the cosmic rays accelerated in the central AGN in CC clusters can heat the gas and prevent the star formation (see Sect. 4.3.2). Different models have been suggested to explain the transfer of the cosmic ray kinetic energy to the gas. In one of the proposed mechanisms, the interactions of relativistic cosmic rays with the gas is considered as heat conveyors (e.g. Colafrancesco & Marchegiani 2008; Mathews 2009; Fujita & Ohira 2011). Considering CC clusters and a proton spectral index of 2.7, Colafrancesco & Marchegiani (2008) found that they could reproduce the observed X-ray temperature profile, given that the cosmic ray radial distribution is steeper than the one of the gas and that the pressure ratio is of the order of $\sim 40-120\%$, depending on the considered clusters. Alternatively, Fujita & Ohira (2012) used a model where cosmic rays are injected in the ICM during AGN intermittent explosions whose outgoing shock waves, followed by the formation of bubbles, heat the gas. This model was applied to the observations made on Perseus. Again, in this case a cosmic ray radial distribution more peaked than that of the gas and a pressure ratio of the order of 1-25% (depending on the distance to the cluster center) were required to explain the observations. Comparing with our observational results, in the case of a cosmic ray profile decreasing with radius and for proton indices between 2.5 and 3.0, we obtain an upper limit on the cosmic ray-to-thermal pressure ratio of 3-5% which is well below the values required to offset cooling. We note that because of the large target densities in the central regions, our analysis is very sensitive to the cosmic ray energy density in the inner regions, especially in the case of a steep cosmic ray radial profile. Therefore, we conclude that the energy density in the central regions of CC clusters is likely lower than what is needed in these models to offset radiative cooling, and heating through cavity expansion and/or shocks is preferred.

Remarks and limitations of this analysis

In this analysis, we assumed that cosmic rays lose energy only via pp interactions and that the neutral pions decay before interacting such that the resulting γ-ray flux is directly related to the primary proton flux. These assumptions are justified in galaxy clusters, because the gas density, magnetic fields, and radiation fields of the ambient medium are low. Nevertheless, other emission mechanisms could contribute to this upper-limit, like the Inverse Compton processes triggered by the co-accelerated or secondary electrons, on the CMB photons. While the γ-ray emission of the secondary electrons is expected to contribute to the γ-ray emission of the neutral pions decay at any time of the cluster evolution, the emission of the primary electrons is expected to contribute just after their acceleration (with a cooling time of about 10^6 yr for TeV electrons on the CMB photons, which is very short compared to the age of the cluster). Therefore, our upper-limits would contain the contribution from the secondary electrons and the limits on the cosmic ray content would be even stronger. However, if the contribution of the secondary electrons were significant, we should see extended radio emissions in all clusters, and not only in NCC (see e.g., Cassano et al. 2010). Therefore, this could be a complementary method to constrain the cosmic ray content of galaxy clusters, using radio observations. However, even if the radio emission has a "long" life time ($\sim$ 2 Gyr for 10 GeV electrons in a μG magnetic field), it is still shorter than the 10 Gyr of the galaxy cluster and the radio emission in clusters does not accumulate. Therefore, using the radio emission to constrain the cosmic rays content would not be so straightforward.

Furthermore, as the γ-ray emission of the central AGN present in the 21 CC clusters was not removed, this implies that the upper-limit on the γ-ray emission from π^0 decay could be lower and the consequent constraints on the cosmic ray content smaller. In this framework, we note that the upper limit obtained here has implications on the typical gamma-ray luminosity of the central AGN itself. Indeed, in the case of Perseus (Abdo et al. 2009b) a bright variable gamma-ray source was detected by Fermi-LAT, corresponding to the central AGN NGC 1275/3C 84 (see also Eckert & Paltani 2009; Colafrancesco et al. 2010; Aleksić et al. 2012). Our non-detection of the stacked CC cluster population with an upper limit $\sim$ 3 orders of magnitude below the gamma-ray flux of NGC 1275 thus shows that the central AGN of Perseus is significantly more active than the typical radio-loud AGN which are at work at the center of CC clusters. A similar conclusion has recently been reached by Dutson et al. (2013).

Our limits on the cosmic ray content are valid in the central part of the cluster, where the X-ray observations are sensitive (Eckert et al. 2012). Therefore these constraints could be released, if cosmic rays would have been transported outwards to lower-density regions (Enßlin et al. 2011; Keshet 2010). Indeed, as we can see in Table 7.2, the obtained constraints are less tight when assuming a flat radial distribution for the cosmic ray, since the density of target protons drops sharply in the outer regions. Based on the difference of density dependence in the Sunyaev-Zel'dovich effect signal (SZ) and X-ray observations (see Sect. 4.3.2), this could thus be interesting to combine the SZ effect measurements with the γ-ray data in order to probe the expected cosmic ray content in the outer region of the cluster. In this case, we could better probe the model in which cosmic rays are accelerated in mergers with a cosmic ray-to-thermal ratio expected to be flat (Vazza et al. 2012; Pinzke & Pfrommer 2010).

Finally, in this analysis we only took into account the photons produced at energy above 1 GeV based on the shape of the photon spectrum which can not be approximated by a power-law at energy below 1 GeV. To alleviate this issue, instead of cutting the low energy part of the spectrum, we could have used directly the γ-ray spectrum predicted from neutral pion decay in the fit of the γ-

ray data. In this case, the result of the fit of the stacked clusters with the method explained in Huber et al. (2013) would have provided directly the value of the cosmic ray-to-thermal energy ratio, given that the normalization of these spectra would have been computed within the equipartition assumption (Eq. [7.5]). This could be the subject of a future work.

7.2 Dark matter content of galaxy clusters: Reconstruction of the lensing potential of the galaxy cluster Abell 1689 using X-ray observations and the Richardson-Lucy deprojection method

7.2.1 Motivation

The combination of observations collected over different wavelengths allowed us in the previous section to constrain the acceleration processes in galaxy clusters. In this section, I would like to show that X-ray and gravitational lensing observations of galaxy clusters can be combined to reconstruct the galaxy clusters gravitational potential wells and to infer the physical state of the gas in different regions of the cluster.

Indeed, the cold dark matter model, favored by substantial theoretical and observational evidence (e.g., Komatsu et al. 2011), predicts the formation of small structures at early times and their later merging into larger systems. Therefore, galaxy clusters are expected to be the latest systems to form. As we saw in Sect. 4.3.2, galaxy clusters are mainly composed by three components: galaxies, hot gas and dark matter. Even if the dark matter is by definition impossible to observe directly, it is expected to follow a universal density profile approximated by the Navarro-Frenk-White profile (NFW, Navarro et al. 1997). Such predictions can be tested using the luminous matter (galaxies and gas), because we expect the baryonic matter to fill the deep gravitational potential, such that its distribution is governed by the depth and the shape of the dark-matter potential well (see e.g. Ettori et al. 2013, for a review). Therefore, the observables provided by the thermal plasma carry information on the gravitational potential.

The physical properties of the ICM can be directly studied in X-rays through thermal bremsstrahlung and line emission and at millimeter wavelengths through the Sunyaev-Zel'dovich (SZ) effect. On the other hand, measurements of gravitational lensing in clusters constrain the gravitational tidal field and thus the curvature of the projected gravitational potential of these clusters. The present study is based on the idea that a simultaneous combination of as many galaxy-cluster observables as possible may lead to a consistent model for the projected cluster potential since, under equilibrium assumptions, all those observables can be combined on the grounds of the gravitational potential.

Apart from improving the reconstruction of the projected cluster potential beyond gravitational lensing, the combination of as many cluster observables as possible will also allow us to cover a wider range of angular or radial scales. Indeed, the joint analysis of weak and strong gravitational lensing allows us to map the dark matter distribution within the entire cluster. Furthermore, because of the dependence of the emissivity on the square of the gas density, X-ray flux and temperature profiles are most reliable in and near the central region of the cluster, while due to the fact that the thermal SZ signal is proportional to the gas pressure integrated over the line-of-sight, the thermal SZ effect has a shallower dependence on the local gas density (Planck Collaboration et al. 2013; Eckert et al. 2013). Hence, owing to the different dependences of different observable signals on angular scales, weak-lensing and thermal-SZ measurements extend to relatively

large distances from the cluster centre, while strong-lensing and X-ray observations are more sensitive to regions near the cluster centre. In combination, more reliable reconstructions of cluster potentials can be expected on all scales.

Another advantage of this joint analysis would be the test the validity of the assumptions made on the physical state of the gas. Indeed, the lensing potential can be recovered without any equilibrium assumptions, while the gravitational potential reconstructed from X-ray and thermal-SZ observations, is recovered assuming hydrostatic equilibrium. In the present work, we will substitute the deprojection method called "onion peeling" (O-P, Kriss et al. 1983), commonly used to deproject the observed two-dimensional surface brightness into a three-dimensional radial profile, by the Richardson-Lucy deprojection method (R-L Lucy 1974, 1994). This latter allows the deprojection of each line-of-sight independently. Therefore, the lensing potential can be compared to the projected potential recovered from observations of the hot ICM to test, at different distance of the cluster center, the validity of the assumptions made on the physical state of the gas.

In the present study, I apply an algorithm developed in Konrad et al. (2013) on the well-studied cluster Abell 1689 to reconstruct the projected cluster potential from the X-ray observations. This is the first time that this algorithm is tested on real data. The work discussed here has been submitted for publication in the journal A&A.

7.2.2 The cluster Abell 1689

The cluster Abell 1689 is a well-known strong lensing cluster located at redshift 0.183 in the Virgo constellation. The multi-wavelength observations performed on this object extend from the mid-infrared, using for instance *ISOCAM* on board of the *ISO* satellite (Fadda et al. 2000), to the X-ray band, using X-ray satellites like *Suzaku* (Kawaharada et al. 2010), *ROSAT* (Allen 1998), *Chandra*[1] (Xue & Wu 2002), and *XMM-Newton* (Andersson & Madejski 2004; Snowden et al. 2008). As for the visible light, the optical signal has been observed using the *Subaru/Suprime-Cam* telescope and the *Hubble Space telescope* (Broadhurst et al. 2005). This list is however not exhaustive.

The main result of these observations is that the cluster Abell 1689 is a dynamically active cluster: kinematics and X-ray studies indicate the presence of a merger aligned with the line-of-sight (see e.g., Andersson & Madejski 2004, and references therein). Combinations of different observations in joint analyses have been performed by many authors and have shown that in the central regions the hydrostatic mass is smaller than the mass estimated from gravitational lensing measurements (see e.g., Peng et al. 2009; Morandi et al. 2011; Miralda-Escude & Babul 1995; Łokas et al. 2006; Sereno et al. 2013). In the following, I will review the main results of these studies.

In Miralda-Escude & Babul (1995), strong lensing and X-ray surface brightness measurements have been combined to test the physical state of the gas near to the cluster center. The authors showed that the observed temperature in the central regions is lower than that expected from hydrostatic equilibrium. As a result, a non-negligible non-thermal pressure component should be present and act against gravity. According to these authors, such a non-thermal pressure support could be associated with the merger process. In a complementary analysis, Łokas et al. (2006) measured the velocity distribution of the galaxies in the field and identified several matter clumps aligned with the line-of-sight through the cluster, which do not interact with the cluster dynamically and could affect the lensing mass estimates without modifying the X-ray mass estimate. This

[1] see also the Chandra catalogue of (Cavagnolo et al. 2009a).

provides an alternative explanation for the mass discrepancy observed between the two methods. In a different analysis of Abell 1689, Peng et al. (2009) combined weak lensing with X-ray data from the *Chandra* satellite. Considering the central part of the cluster out to $R \sim 1000$ kpc/h they found that at radii larger than $R \sim 200$ kpc/h, the X-ray and lensing masses are consistent, whereas they found a discrepancy between the masses at smaller radii. These authors explain this discrepancy by a projection effect. This conclusion agrees with the results of Sereno et al. (2013). In this study, the authors constrained the shape and the orientation of the cluster in a joint analysis of the ICM distribution in the cluster. Using X-ray and SZ measurements, the cluster appears to have a triaxial shape elongated along the line-of-sight. According to these authors, this may explain the mass discrepancy. Finally, in a joint analysis of X-ray surface brightness with strong and weak lensing measurements, Morandi et al. (2011) inferred the fraction of non-thermal pressure required for the cluster to be in hydrostatic equilibrium taking into account the triaxial shape of the cluster. The authors found that 20 % of the total pressure should be non-thermal, most probably contributed to by turbulent gas motion driven by the merger events.

In our Galaxy the turbulent pressure is in equipartition with the cosmic ray pressure and the magnetic field pressure. *A priori*, there is no reason to believe that it should not be the case in galaxy clusters, as the charged particles interact with the magnetic field and are thought to be accelerated by turbulence. Therefore, the 20% turbulent pressure derived by Morandi et al. (2011) gives an upper-limit of 20% to the non-thermal pressure initiated by the cosmic rays in this cluster. However, the results of the previous section limits the cosmic ray content in galaxy clusters to be 4-10 % of the thermal pressure of the gas. Therefore, if Abell 1689 is not different from the clusters we considered in our previous study, this may indicate that the cosmic rays could be in equipartition with the turbulence in this cluster. Nevertheless, even if we assume that cosmic rays initiate 20% of non-thermal pressure in the cluster, the flux arising from the hadronic interactions with the gas in the cluster is of the order of 10^{-12} erg/cm^{2}s, for a proton spectral index of 2 and of $2 \cdot 10^{-13}$ erg/cm^{2}s, for a proton spectral index of 3 (using the parameters of the cluster given by Chen et al. (2007)). Such flux could not be detected with the sensitivity of the Fermi-LAT telescope. Therefore, the hypothesis that the cosmic rays are in equipartition with the turbulence can not be tested.

To sum up, a mass discrepancy has been observed by many studies and different explanations have been suggested. In the studies mentioned above, the regions apparently in hydrostatic equilibrium were mixed by projection effects with regions out of hydrostatic equilibrium. The theoretical expectation that the underlying dark matter distribution can be recovered from the ICM gas distribution can thus not be properly tested. For this purpose, we here propose the following method: 1) To reconstruct a three-dimensional gas distribution, we use a deprojection method which can be applied specifically where the equilibrium assumptions are thought to be valid without using any information from regions where it is known to fail; and 2) we substitute the mass with a direct local observable, i.e. the gravitational potential. This procedure, applied in the present study to a joint analysis of X-ray and lensing observations, is expected to allow us to make a direct comparison between the dark matter and gas distributions and to test the validity of the equilibrium assumptions at each projected radius. Indeed, using the gravitational potential should render the comparison with gravitational lensing measurement more straightforward, as the gravitational potential is directly observable from the lensing measurements. Applying this method with different geometries (spherical and triaxial) should remove the degeneracy between the different possible explanations concerning the mass discrepancy. In the present study, we test this algorithm for the first time on a real cluster assuming spherical symmetry. The generalization to a spheroidal shape

is ongoing.

In the following sections, I will apply this method as outlined in Konrad et al. (2013). First, we recover the three-dimensional gravitational potential from the observed X-ray data assuming hydrostatic equilibrium, then we project it and finally, we compare its projection with the lensing potential. With this method, we expect to be able to test for each projected radius the validity of the equilibrium assumptions. In the present study, we test this algorithm for the first time on a real cluster assuming spherical symmetry. The generalization to a spheroidal shape is ongoing.

7.2.3 The Richardson-Lucy deprojection method

In this section, I would like to introduce the main points of the R-L deprojection method and to compare them with the ones of the O-P deprojection method, which is the standard deprojection method in X-ray astronomy.

Historically, the R-L deprojection method has been introduced by Lucy (1994, 1974) to recover the tridimensional quantity (f) from the two-dimensional quantities (g), taking into account that we do not have access to the quantity g, but only to the observed quantity $\tilde{g}$, which is embedded in uncertainties. The R-L method proposes to recover f with an iterative procedure. In this approach, the value of f is estimated using the maximum Likelihood, where the projection of f is fitted on the observed data $\tilde{g}$ for each line-of-sight independently.

I will now review in a few steps the main idea of the R-L method.

The variable s is the projected radius defined as $r = \sqrt{s^2 + z^2}$, with z the coordinate along the line-of-sight and r the tridimensional radius. The observed projected quantity g(s) and the three-dimensional function of interest f(r) are related by

$$g(s) = \int f(\sqrt{s^2 + z^2})dz = \int f(r)P(s|r)dr. \tag{7.13}$$

Where $P(s|r)$ is the kernel of the projection. In the case of spherical symmetry, we have $P(s|r) \propto r/\sqrt{r^2 - s^2}$. The method proposed by Lucy (1974) is based on the Bayes' theorem for conditional probability,

$$f(r) = \int g(s)Q(r|s)ds, \tag{7.14}$$

where $Q(r|s)$ is given by

$$Q(r|s) = \frac{f(r)P(s|r)}{g(s)}. \tag{7.15}$$

with $g(s)$ given by Eq.[7.13].

As the kernel $Q(r|s)$ is a function of $f(r)$, it can not be used directly to solve Eq. [7.14]. Instead Lucy (1974, 1994) suggested an iterative solution for it. With an initial guess for $f(r)$ ($f_0(r)$) and assuming that $P(s|r)$ is known, one obtains an estimate for $g_0(s)$ using Eq. [7.13] and one can estimate the deprojection kernel in the first iteration step as

$$Q_0(r|s) = \frac{f_0(r)P(s|r)}{g_0(s)}.$$

Then, the value of $f(r)$ in the first iteration can be estimated as

$$f_1(r) = f_0(r) \int \tilde{g}(s) Q_0(r|s) ds. \tag{7.16}$$

Iteratively, one obtains $f_{i+1}(r)$ as function of $f_i(r)$, $g_i(s)$ and $\tilde{g}(s)$, through Eq. [7.16] and [7.15]:

$$f_{i+1}(r) = f_i(r) \int \frac{\tilde{g}(s)}{g_i(s)} P(s|r) ds. \tag{7.17}$$

The iteration converges when $g_i(s)$ tends to $\tilde{g}(s)$, therefore, when the estimated projected potential obtained for a given f tends to the observed quantity $\tilde{g}(s)$. The optimal value of $f(r)$ is the result of the fit.

As each line-of-sight is deprojected independently, in order to obtain a smooth solution for the observable f, Lucy (1974) introduced a smoothing scale, L. By construction, this method fits first the large scale fluctuations and latter the small scale ones, which are mostly due to statistical errors of the observation of g. This implies that after a given number of iterations, the method starts being sensitive to the statistical fluctuations and it worsens the estimate of f. However, given that the maximum Likelihood gets better with the increase of the number of iterations, the optimal number of iterations is not easy to find. To alleviate this issue, in Lucy (1994), the authors introduced a regularization parameters, α, which prevents the iteration from being continued into the regime in which only the statistical fluctuations are being fitted. This parameter weights the penalty to the maximum Likelihood. The value of the penalty is adjusted depending on the complexity of the estimated f: once the statistical noise starts to be fitted, the function f becomes more complex and the value of the penalty decreases, making the fit worst. In Lucy (1994), the fit is performed on a likelihood function which takes into account these two parameters: α, which controls the level of suppression of the small-scale fluctuations and L, the smoothing scale for the reconstruction.

The choice of this two parameters is not easy (see e.g., Majer et al. 2013). However, in a first estimate, L should be at least as large as the distance between two successive data points. As for the value of α, one could start with a small value and increase its value until the function starts to follow the expected results. A small value of α indicating that the noise is fitted together with the data in the reconstruction.

On the other hand, the concept of the O-P method is purely geometrical (Kriss et al. 1983). This method assumes that the cluster has an onion-like shell structure, with a uniform emissivity in each of the concentric spherical shells. The three-dimensional profile of the emissivity is then recovered from the surface brightness map in an iterative way from ring to ring progressing from the outskirts to the centre of the cluster. Furthermore, as the errors associated with each line-of-sight are correlated, if the number of events is overestimated in a ring, the same quantity needs to be underestimated in an adjacent ring, which can produce fluctuations in the deprojected radial profile (see e.g., Ameglio et al. 2007).

This implies that the O-P method is non-local, in the sense that to reconstruct the three-dimensional shell at a given radius, the results of the deprojection of all shells at larger radii are needed. However, the R-L deprojection method, is local in the sense that even though the information collected at one image point is integrated over a long line-of-sight, the two-dimensional profile is deprojected along each line-of-sight independently (see e.g., Reblinsky 2000; Puchwein & Bartelmann

2006), such that the deprojected function is evaluated independently at each image point. This implies that this algorithm can be applied on data sets with incomplete coverage.

This feature of local deprojection is most relevant for our study since the information provided by gravitational-lensing measurements that we use here is local as well. Indeed, in the SaWLens method developed by Merten et al. (2009), the observations of weak gravitational lensing give information on the local galaxy density.

Both deprojection methods can be generalize to intrinsically spheroidal cluster bodies, by modifying the (de)projection kernel (see e.g., Reblinsky 2000; Puchwein & Bartelmann 2006, for the R-L method) and (see e.g., Buote & Humphrey 2012a, for the O-P method).

7.2.4 Assumptions of the method

The general reconstruction formalism outlined in Konrad et al. (2013) is based on the following assumptions. This assumptions have been introduced in Sect. 4.3.2.

- The ICM is in hydrostatic equilibrium with the cluster gravitational potential

$$\nabla P = -\rho \nabla \Phi \ , \tag{7.18}$$

  where Φ denotes the Newtonian gravitational potential, while P and ρ are the gas pressure and density, respectively.

- The gas equation of state follows the polytropic relation,

$$\frac{P}{P_0} = \left(\frac{\rho}{\rho_0}\right)^{\gamma_{poly}} \ , \tag{7.19}$$

  where the suffix 0 denotes values for the pressure and for the gas density at an arbitrary radius r_0 and where γ_{poly} is the polytropic index.

- The gas is ideal

$$P = \frac{\rho}{\bar{m}} k_{\rm B} T_{gas} \ , \tag{7.20}$$

  where T_{gas} is the gas temperature, $k_{\rm B}$ is Boltzmann's constant and $\bar{m}$ the mean mass of a gas particle.

- The bolometric bremsstrahlung emissivity, j_x, can be written as

$$j_x = C T_{gas}^{1/2} \rho^2 \ , \tag{7.21}$$

  where C is an amplitude formed by all relevant physical constants. The bremsstrahlung emission is assumed to dominate the X-ray observations. This assumption is justified as long as the temperature of the plasma does not fall below $\sim 2\,$keV and the Fe XXV-Fe XXVI line complex at $6 - 7\,$keV is avoided (Peterson & Fabian 2006). This is the case of the cluster Abell 1689, whose temperature has been measured to fall between 2 keV and 10 keV (Kawaharada et al. 2010).

- Apart from the natural constants and the averaged parameters, all quantities introduced above are assumed to depend on the cluster-centric radius. This dependence is not written explicitly in order to simplify the notation. The polytropic index is assumed to be constant across the cluster. While this has been shown not to be true in general, this can be a good approximation as long as the core of the cluster is avoided (see e.g. Tozzi & Norman 2001; Capelo et al. 2012; Eckert et al. 2013).
- The cluster is assumed to be spherically symmetric.

7.2.5 Deprojection of the cluster Abell 1689

In this section, we will compare the results of the R-L deprojection method obtained using the algorithm developed in Konrad et al. (2013) with those obtained by Eckert et al. (2012, 2013) using the O-P deprojection method. Both deprojection methods will be applied on the surface-brightness profile extracted from the *ROSAT*/PSPC data in the $0.4 - 2$ keV (Eckert et al. 2011). The X-ray observables on which the two methods will be tested are the emissivity profile, the density profile and the temperature profile of the cluster.

The three-dimensional emissivity

The X-ray surface-brightness deprojected using the O-P and R-L methods is shown in Fig. 7.2. To obtain these results, the parameters of the R-L method are set to $\alpha = 0.01$ and $L = 300\,\mathrm{kpc}$. As mentioned above, these parameter values are quite low with respect to the expectations (see Konrad et al. 2013, for more details), and imply that the regulation term introduced in the R-L method is not very effective in the case of Abell 1689.

The mean value and the error bars of the recovered emissivity are obtained using a Monte-Carlo (MC) method based on the R-L deprojection method: the value of the surface brightness profile is randomized within each radial ring, according to a Gaussian distribution, whose mean is the observed value and whose width is given by the error bars. After 10000 simulations, the deprojected value and its error is given by the mean and 1σ deviation of the resulting distribution.

Further investigations with simulated clusters have shown that the results of the reconstruction depend very little on the values chosen for the regularisation parameters. Testing wide ranges for both α and L, typically covering an order of magnitude, changes the recovered potentials routinely by much less than the statistical uncertainties.

We should emphasize that the regularization term is controlled by the difference of the potential reconstructions between subsequent iterations steps, which vanishes progressively as the iteration proceeds. The regularization is thus gradually switched of towards the end of the iteration. In the present analysis, the number of iterations has been fixed to 10, which corresponds to the number of iterations at which the algorithm converges, as no significant changes in the emissivity profile were observed when a larger number of iterations was used.

This is endorsed by our result showing that the emissivity profiles obtained with both methods agree very well within the error bars. We can see, however, that the outermost points of the profile are different in the two techniques, which can be attributed to edge effects (see e.g., McLaughlin 1999). The large error bars in the outermost points are caused by the weakness of the signal at large radii.

The three-dimensional density profile

The bolometric emissivity is a function of the gas density and temperature (see Eq. [7.21]). In the specific case of Abell 1689, the cluster temperature profile has been measured to fall between 2 keV and 10 keV by Kawaharada et al. (2010). This implies that if we consider the energy range [0.4; 2] keV, the emissivity depends only weakly on the temperature and the density profile can be expressed as a function of the emissivity $j_{[0.4;2]}$, as

$$\rho(r) \propto \sqrt{j_{[0.4;2]}(r)} \, . \tag{7.22}$$

Figure 7.3 shows the density profile obtained using Eq. [7.22] with the three-dimensional emissivity shown in Fig. 7.2. On the same figure is shown the density profile derived in Eckert et al. (2013) using the O-P method. Again, we see that the density profile deprojected with the two methods coincide well.

The three-dimensional temperature profile

To extract the temperature profile, we use the polytropic relation (Eq. [7.19]), the ideal gas equation (Eq. [7.20]) and Eq. [7.22], which is valid in the energy band [0.4;2] keV.

The temperature profile can be expressed as

$$T(r) \propto \rho(r)^{\gamma_{poly}-1} \propto j_{[0.4;2]}(r)^{(\gamma_{poly}-1)/2} \, . \tag{7.23}$$

Figure 7.4 shows the temperature profile reconstructed with a polytropic index of $\gamma_{poly} = 1.19 \pm 0.04$. The polytropic index $\gamma_{poly} = 1.19 \pm 0.04$ (with 1σ error) results from a fit of the pressure profile observed by Planck Collaboration et al. (2013) using the reconstructed density profile (Eq. [7.22]) and the polytropic and gas ideal equations (following the method outlined in Eckert et al. 2013). For completeness, we also fitted Eq. [7.23] to the joint *XMM-Newton* and *Suzaku* data and obtained $\gamma_{poly} = 1.17 \pm 0.03$. This latter is consistent with our earlier result. On the same figure are also shown the temperature profiles obtained using other techniques: in dark-blue is shown the temperature profile taken from Eckert et al. (2013), which has been derived from the combination of the density profile extracted in Eckert et al. (2013), with the SZ pressure profile from Planck (Planck Collaboration et al. 2013), using the gas ideal equation (Eq. [7.20]); while in pink and light-blue are respectively shown, the temperature profiles obtained by spectral fitting of data taken with the *Suzaku* (Kawaharada et al. 2010) and *XMM-Newton* (Snowden et al. 2008) satellites.

Furthermore, the decrease in the temperature profile is well reproduced by our method, which supports the validity of the polytropic assumption (Eq. [7.19]).

7.2.6 Reconstruction of the lensing potential

The lensing potential is recovered from observations of the distorted images of distant background galaxies. The distortion (shear and magnification) of those images is related to linear combinations of second derivatives of the lensing potential of a foreground cluster. This distortion is due to the gravitational field of a deep potential well between the observer and the background galaxies. In the case of weak lensing measurements, the distortion of individual galaxies is too weak to be observed, but the distortion averaged over a sufficiently number of neighboring galaxies is used to estimate the gravitational field of the foreground galaxy cluster. Indeed, in a large enough sample,

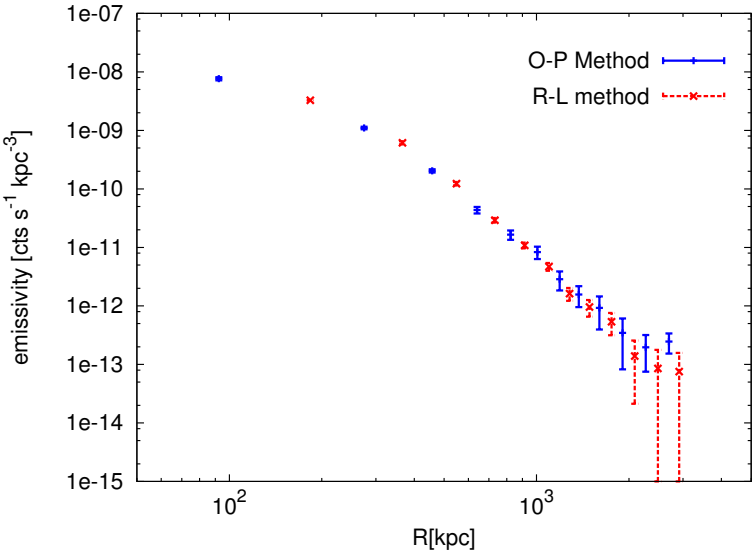

Figure 7.2: Emissivity obtained applying the R-L and the 'onion peeling' (O-P) methods on the ROSAT surface-brightness profile (Eckert et al. 2012). The reconstructed emissivity using the R-L method has been normalized to the O-P data points within a spherical shell delimited by the radii in the range [183; 2700] kpc. Submitted in A&A.

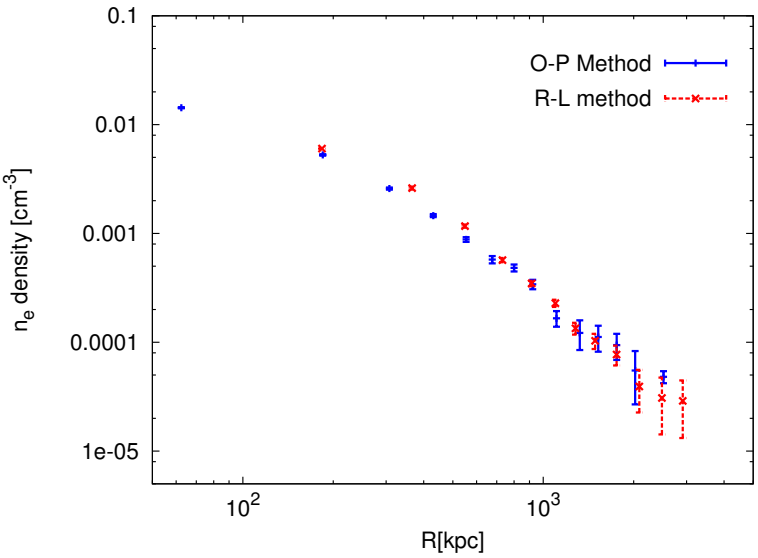

Figure 7.3: Electron-density profile taken from (Eckert et al. 2012) recovered from the O-P deprojection method compared to the reconstructed profile obtained from the R-L deprojection method [Eq. (7.22)]. The reconstructed density using the R-L method has been normalized to the O-P data points within a spherical shell delimited by the radii in the range [183; 2515] kpc. Submitted in A&A.

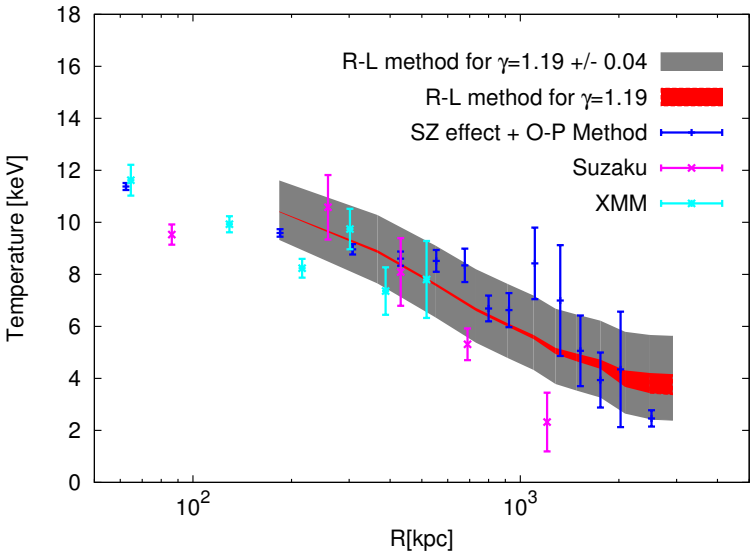

Figure 7.4: Observed temperature profile compared to temperature profile obtained from the reconstructed emissivity profile via Eq. (7.23) with $\gamma = 1.19 \pm 0.04$. Dark blue: profile derived from combined X-ray and thermal-SZ measurements (Eckert et al. 2013); light blue: XMM observations (Snowden et al. 2008); pink: Suzaku observations (Kawaharada et al. 2010); red: mean value and errors on the reconstructed profile for $\gamma = 1.19$; gray: mean value and errors on the reconstructed profile for $\gamma = 1.19 \pm 0.04$. The mean and the error bars were obtained with a Monte-Carlo method based on the R-L deprojection. The reconstructed temperature profile has been normalized to the data points from Eckert et al. (2013) within a spherical shell delimited by the radii in the range [183; 2515] kpc. Submitted in A&A.

the random intrinsic orientation of the background galaxies is expected to average out, and the ellipticity induced by lensing can be measured. The lensing potential observations used here are recovered with SaWLens in a non-parametric way from weak-lensing data.

The reconstructed projected potential ψ is the projection along the line-of-sight of the three-dimensional gravitational potential Φ.

$$\psi(\theta) = 2\frac{D_{ls}}{D_l D_s}\int dz \Phi(D_l\theta, z). \tag{7.24}$$

Where D_{ls}, D_l, D_s are the angular diameter distances from the lens to the sources, from the observer to the lens, and from the observer to the source, respectively. Based on the assumptions mentioned in Sect. 7.2.4, and following the method outlined in Konrad et al. (2013), the three-dimensional gravitational potential can be expressed in terms of the X-ray emissivity. Here I will review the main steps of this reconstruction.

Integrating the hydrostatic equilibrium equation (Eq. [7.18]) with the polytropic equation (Eq. [7.19]), the tridimensional gravitational potential can be rewritten as function of the density profile, giving

$$\left(\frac{\rho(r)}{\rho_0}\right)^{\gamma_{poly}-1} = -\frac{\gamma_{poly}-1}{\gamma_{poly}}\frac{\rho_0}{P_0}(\Phi(r)-\Phi_0) \equiv \phi(r) \tag{7.25}$$

where Φ_0 is the tridimensional potential at r_0.

Following Konrad et al. (2013), we have defined the above quantity as the dimension-less potential ϕ (using that P/ρ has the dimension of the spare of the velocity). Therefore, the density, temperature and emissivity profiles can be expressed as a function of ϕ, as

$$\rho(r) = \rho_0\phi(r)^{1/(\gamma_{poly}-1)}; \tag{7.26}$$

and

$$T_{gas}(r) = \frac{\bar{m}P(r)}{\rho(r)k_B} = \frac{\bar{m}P_0}{\rho_0 k_B}\phi(r). \tag{7.27}$$

For the temperature profile, we use both the polytropic (Eq. [7.19]) and the gas ideal equation (Eq. [7.20]). Therefore, the X-ray emissivity (Eq. [7.21]) can be written as

$$j_x(r) = CT_{gas}(r)^{1/2}\rho(r)^2 \propto \phi^{1/2}\phi(r)^{2/(\gamma_{poly}-1)} \propto \phi(r)^{\frac{3+\gamma_{poly}}{2(\gamma_{poly}-1)}}. \tag{7.28}$$

In this equation, we use the bolometric emissivity (j_x) and not the emissivity restricted to the energy band [0.4;2] keV. To recover the bolometric emissivity from the energy restricted one, we compute the ratio between the bolometric flux and the restricted flux for each radius, using the temperature profile and the thin-plasma code APEC (Smith et al. 2001, fixing the metallicity to 0.3). This factor is then used to recover the bolometric emissivity from the restricted one.

We can inverse this equation and use the definition of the dimension-less potential (Eq. [7.25]) to express the tridimensional potential as function of the emissivity:

$$\phi(r) \propto j_x(r)^\eta\ , \quad \eta = \frac{2(\gamma_{poly}-1)}{3+\gamma_{poly}}. \tag{7.29}$$

The reconstructed three-dimensional dimension-less gravitational potential is then projected along the line-of-sight.

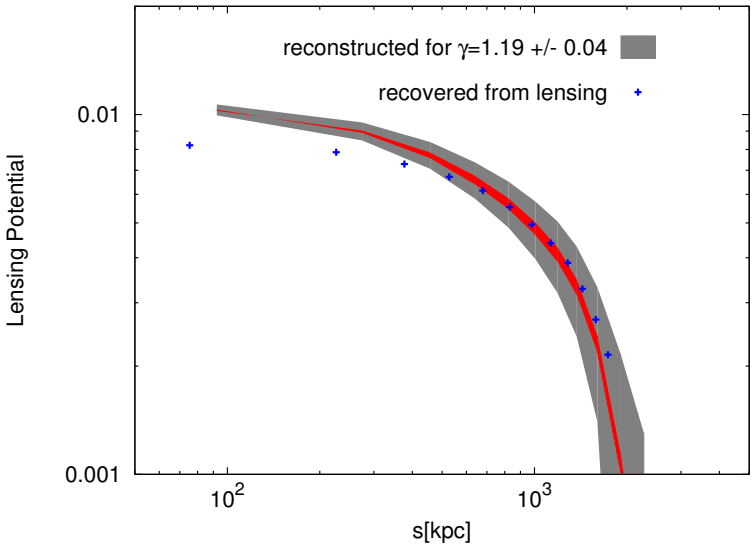

Figure 7.5: Opposite sign of the projected gravitational potential reconstructed using the method described in Konrad et al. (2013) compared to the potential recovered from weak gravitational lensing as function of the projected radius s. The projected potential reconstructed from the X-ray emission has been obtained assuming a polytropic index $\gamma = 1.19 \pm 0.04$ (see the text for details). The potential recovered by lensing is shown in blue; the mean projected potential obtained from X-ray observations with $\gamma = 1.19 \pm 0.04$ is shown in red; and the uncertainties of the latter are shown in gray. The mean and errors have been obtained using a Monte-Carlo method to randomize the algorithm described in Konrad et al. (2013). The reconstructed lensing potential has been normalized to the lensing data within a circular shell region delimited by the radii in the range [92; 1734] kpc. Submitted in A&A.

In Fig. 7.5, we show the opposite sign of the reconstructed, two-dimensional potential, assuming a polytropic index $\gamma = 1.19 \pm 0.04$. Mean values (for $\gamma = 1.15, 1.19$, and 1.23) are shown in red, while the corresponding uncertainties estimated with the Monte Carlo method are shown in gray. This profile is compared with the lensing potential obtained from weak lensing (Merten et al. 2009). As shown, at radii $\gtrsim 0.5$ Mpc the curvature of our reconstructed potential profile agrees well with the one of the reconstructed lensing profile within the error bars, even though the potential reconstructed from the X-ray emission appears slightly less curved. The discrepancy at small radii and the slight curvature change at larger radii may be caused by the lack of resolution in the weak-lensing measurement and by the other assumptions made (sphericity, polytropic and equilibrium assumptions). Those points will be discussed further in the next section.

7.2.7 Discussion

In this study we used the R-L deprojection method to recover the three-dimensional gas distribution in Abell 1689 from its X-ray surface brightness. We then converted this gas distribution into a three-dimensional gravitational potential that we subsequently projected for comparison with the lensing potential. Using the R-L deprojection method is advantageous because it allows deprojecting the X-ray observables independently along each line-of-sight, and the treatment of data sets with incomplete coverage. This therefore allows the exclusion from the analysis of regions

where the equilibrium assumptions may not hold. As a result, a substantial amount of information becomes available by the direct comparison of the lensing potential with the projected potential reconstructed from X-ray emission (Fig. 7.5).

For example, the agreement between the two reconstructed potentials at radii from 500 – 2000 kpc indicates that the assumptions underlying the derivation of the projected potential from X-ray observations, namely hydrostatic equilibrium, polytropic stratification and the ideal-gas equation of state [Eqs. (7.18)-(7.21)] are not substantially violated in the cluster Abell 1689 within this radial range. Nevertheless, we can observe a slight discrepancy between the potentials curvature: the potential recovered from lensing is flatter than the one reconstructed from the X-ray observations. This flattening can be produced by the large resolution limit present in the weak-lensing measurements ($\sim$ 100kpc, see e.g., Bartelmann 2003, for a review), which can smooth the data, so that the lensing potential recovered from weak-lensing measurements appears flatter than the potential recovered from X-ray observations. This discrepancy is expected to vanish if more potential observables are taken into account. For instance, a combined strong and weak-lensing reconstruction is expected to yield a better match in the region close to the cluster centre, as the strong lensing is sensitive to this region.

At small radii ($R \lesssim 500$ kpc), however, the two projected potentials differ. Such a discrepancy in the central region of the cluster was also found by Peng et al. (2009); Andersson & Madejski (2004); Morandi et al. (2011); Miralda-Escude & Babul (1995); Łokas et al. (2006); Sereno et al. (2013), as mentioned in the introduction. This could be explained by a modification of the balance between the physical processes in the inner part of the cluster. It may indicate that some of the assumptions made should not be used in the central part of the cluster.

For instance, the polytropic assumption with constant polytropic index may not be valid in the central part of cool-core clusters, because the radiative cooling near the centre renders the cooling time shorter than the Hubble time (e.g., Fabian 1994). Cooling alters the polytropic equation by lowering the temperature of the gas, which implies that the temperature profile does not increase toward the centre as the gas density does, but rather decreases. Therefore, the assumption of a constant polytropic index is not expected to be correct at the cluster centre. However, the assumption that the gas follows the polytropic equation seems to be valid in Abell 1689, with a fitted polytropic index of $\gamma = 1.19 \pm 0.04$ (Fig. 7.4).

On the other hand, the assumption of hydrostatic equilibrium is likely valid in the central regions of cool-core clusters because of the deep gravitational potential (see for instance Fig. 2 of Lau et al. 2009). This may not be the case in non-cool core clusters. Indeed, as has been shown for instance by Mahdavi et al. (2013), departure from the equilibrium assumption is expected in unrelaxed clusters. The authors compared the lensing mass with the mass obtained under hydrostatic equilibrium assumptions for a sample of clusters at $R \lesssim R_{500}$ ($\sim$ 1.34 Mpc in the case of Abell 1689) and concluded that the departure from the equilibrium assumption is different between relaxed and merging clusters: while for cool-core clusters, almost no bias is observed between the lensing and the hydrostatic mass, for non cool-core clusters, a bias of 15-20% is present. Abell 1689 is known to experience a merging event aligned with the line-of-sight, and therefore, the gas is not expected to be in hydrostatic equilibrium near the cluster centre (see also e.g., Nelson et al. 2012; Morandi et al. 2011). This may contribute to the discrepancy at small radii observed in Fig. 7.5.

Furthermore, any departure from spherical symmetry could bias the estimate of the cluster mass, and in the case where the major axis of the cluster is preferentially aligned with the line-of-

sight, it should lead to an over-estimation of the lensing mass with respect to the X-ray mass. This is consistent with the conclusions of Lee & Suto (2003, 2004), who showed that in non-spherical clusters, the dark matter profile is always more sensitive to triaxiality than the gas distribution from X-ray measurements. This small dependence of the X-ray measurements on the cluster shape was also observed in Buote & Humphrey (2012a,b), where the authors computed the biases in the observables obtained by applying a spherical O-P deprojection method on clusters with significant triaxiality. They conclude that spherical averaging biases the observables by a small factor ($< 1\,\%$) with respect to a triaxial deprojection.

Therefore, in the case of Abell 1689, the non-sphericity of the cluster could explain the discrepancy at small radii between the X-ray and lensing projected potential profiles, but interestingly, it does not seem to affect strongly the reconstruction of the potential in the region $500 - 2000$ kpc.

At large radii ($R \gtrsim R_{500}$), simulations tend to show that due to mixing of the ICM with the infalling material from the large scale structure, the equilibrium assumptions are not valid anymore (see e.g, Reiprich et al. 2013, for a review). The deviation from the hydrostatic equilibrium can be due to residual gas motions or incomplete thermalization of the ICM (Mahdavi et al. 2013). Such phenomena are expected in the outskirts of clusters, where matter is accreted and substructures as clumps are more likely to be found (Nagai & Lau 2011; Vazza et al. 2013; Zhuravleva et al. 2013), so that our reconstruction method is not expected to be valid at radii larger than $R_{500}(\sim 1.339$ Mpc, for Abell 1689). However, as the lensing data used in our study do not extend to much larger radii than R_{500}, we cannot test this statement. Extrapolating lensing data points to larger radii, we do not find significant differences between X-ray and lensing information in this radial range.

Remarks and limitations of the analysis

In this study, we provided a general proof of concept of potential reconstruction combining X-ray data with weak lensing measurements. This study is part of project which consists in combining all observables provided by galaxy clusters: strong and weak gravitational lensing, X-ray surface-brightness and temperature, galaxy kinematics and the thermal Sunyaev-Zel'dovich effect into a joint construction of one consistent model for the projected cluster potential.

The advantages of the R-L method with respect to the O-P method may be clearer if we had applied this algorithm to a cluster which undergoes a merger at large distance from the cluster center. Indeed, in the O-P method, the regions at large distances from the cluster center are iteratively mixed to the regions closer to the cluster center. Therefore, I would not expect the lensing potential to be well reconstructed with the O-P method. Applying the R-L method to this same cluster is expected to shed light on the regions where the equilibrium assumptions are correct (Eqs. [7.18]-[7.21]). I would expect that the comparison of the two reconstructed potential obtained using the two deprojection methods with the observed lensing potential would show the advantages of the R-L method with respect to the O-P method. Such a comparison could already be done on the cluster Abell 1689, but I doubt that we would see any difference between the two reconstructed potentials, because the equilibrium assumptions seem to hold in the whole cluster, except near to the center, such that the value of the observable at large radius will not affected by the fact that at the cluster center, the equilibrium assumptions are not valid.

Furthermore, combining the two analyses performed in this chapter (Sect. 7.1 and 7.2), we can deduce that the discrepancy observed at small radii between X-ray and lensing observations can not be explained by the presence of cosmic rays only. Indeed, in Sect. 7.1 their contribution to

the total pressure has been constrained to be below of a 4-10 %, ie below the 20% of non-thermal pressure required by the study of (Morandi et al. 2011) to explain the mass discrepancy between X-ray and lensing measurements at the cluster center. Nevertheless, these results do not rule out the possibility that the cosmic rays are in equipartition with the turbulence in Abell 1689, and that both effects contribute to the 20% of non-thermal pressure.

Chapter 8

Service work for INTEGRAL

I did my PhD at the ISDC Data Center for Astrophysics where the data of the satellite INTEGRAL are collected and analyzed. Therefore, I had the opportunity to take part in some of the science achieved with this mission during my shifts, as scientist on duty. In this chapter, I will review this mission and the results related to my activities as scientist on duty.

8.1 The INTEGRAL mission and the instruments on-board

The INTERnational Gamma-RAy Laboratory (INTEGRAL) satellite is a European Space Agency (ESA) mission (Winkler et al. 2003). It has been launched in 2002 with the goal of studying the high energy sources from the optical band to the γ-ray band. The INTEGRAL satellite follows an eccentric orbit and enters a new revolution every 3 days.

The INTEGRAL satellite hosts on board five instruments: the spectrometre SPI, the imager IBIS, the two X-ray monitors JEM-X and an optical telescope (OMC; see Fig. 8.1).

The SPI spectrometer (SPectrometer on INTEGRAL, Vedrenne et al. 2003) is sensitive in the energy band 20 keV-8 MeV and is designed to perform high resolution spectroscopy, achieving an energy resolution of 2.2 keV at 1.33 MeV.

The second instrument, the IBIS imager (Imager on-Board INTEGRAL Satellite, Ubertini et al. 2003), is sensitive to photons in the 15 keV-2 MeV. IBIS is made of two detector planes: the ISGRI instrument (INTEGRAL Soft Gamma-Ray Imager, Lebrun et al. 2003) which operates in the 15-400 keV band and the PICsIT instrument (Pixellated Imaging Caesuim Iodide Telescope, Di Cocco et al. 2003), which is sensitive in the range 180 keV-2 MeV. When photons interact in both detectors, the angle of incidence of the photons can be reconstructed.

The JEMX X-ray monitor (Joint European Monitor in X-rays, Lund et al. 2003) is sensitive in the 3-35 keV energy band. It is devoted to the spectral, imaging and timing study of the sources detected by the other instruments on-board in softer energy bands. The field of view is smaller than that of ISGRI. JEMX consists of two identical instruments called JEM-X1 and JEM-X2. These are currently used simultaneously to observe relevant astrophysical events.

The OMC optical camera (Optical Monitoring Camera, Mas-Hesse et al. 2003) is designed for the optical follow-up of the sources detected with the other instruments on-board and collects the light curves of a selected sample of sources in the field of view simultaneously with the high-energy observations.

The hard X-ray and gamma-ray photons are so penetrating that each of the high-energy instruments on-board INTEGRAL is using a coded mask. Coded masks are made of absorbing material and holes with a pre-defined pattern. This technique is illustrated in Fig. 8.2: the shadow of the mask allows to determine the position of the source with respect to the detector.

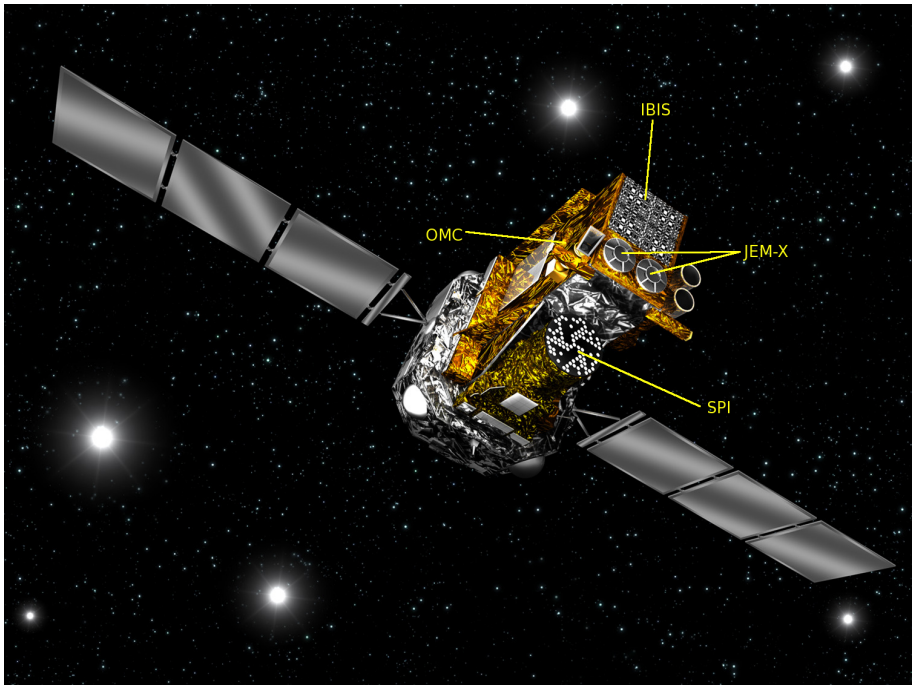

Figure 8.1: Illustration of the INTEGRAL spacecraft with the instrument onboard. Credit: ESA.

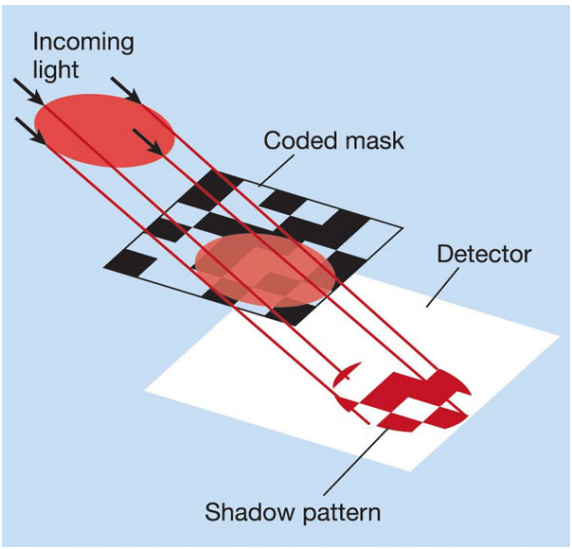

Figure 8.2: Illustration of the coded mask technique. Credit: White (2004).

INTEGRAL data are first collected at the Mission Operation Center (MOC) in Darmstadt and then immediately provided to the INTEGRAL Data Center (ISDC) for processing and quick-look analysis (Courvoisier et al. 2003a).

8.2 Activities related to INTEGRAL duties

The INTEGRAL Science data centre receives the satellite telemetry in near real time from the MOC. An INTEGRAL observation consists of many short pointings lasting about 2 ks each. These ”science windows” can be mosaicked to achieve a deeper sensitivity.

At the ISDC, an operator and a scientist on duty (scody) are in charge of checking the data quality and of providing any relevant scientific information to the operation coordinator. The specific activities of the scody consist in the search for new sources that may turn-on in X-rays during the INTEGRAL observation (using the quick-look analysis software, QLA), in the detection of a unusual activity of a known source and in the verification of the Gamma-ray burst alerts automatically detected by the INTEGRAL Burst Alert System (IBAS).

There exist also ToO (Target of Opportunity) observations, which are particular observations requested by scientists in advance and are activated in cases where the source meets a trigger criterion.

8.3 Astronomer’s Telegram

Every time that a relevant astronomical event is observed with INTEGRAL, an Astronomer’s Telegram (ATel) can be published to inform the scientific community. During my shifts, I was the witness of three interesting events which led to the publication of ATels. After the discovery of the events, part of the data analysis was done by the owner of the data.

8.3.1 Flaring activity and cyclotron line in GX 304-1 observed with INTEGRAL (ATel #3902)

The source GX 304-1

This source is an high mass X-ray binary which has been first detected during a balloon experiment in 1967 by SAS-3 (McClintock et al. 1977). Many observations of this source have followed, for instance with INTEGRAL (Klochkov et al. 2012a), Swift-BAT (Krimm et al. 2010), RXTE-ASM (Devasia et al. 2011), MAXI/GSC (Yamamoto et al. 2009), Suzaku (Mihara et al. 2010), and with Fermi-GBM (Jenke et al. 2012).

This binary system hosts a massive and fast rotating Be star and a neutron star. The phenomenological understanding of the X-ray variability of this system can be sketched as follows: due to the rotation of the Be star, a decretion disk forms perpendicular to the rotation axis of the Be star (see e.g., Porter & Rivinius 2003). As the decretion disk is confined to within a few stellar radii at the most, while the neutron star orbit is usually much wider and eccentric, the interaction between the disk and the compact object takes place only at periastron. During this interaction material from the decretion disk is accreted onto the rotating neutron star due to the strong gravitational field of this object. In this model, the magnetic field configuration of the neutron star can be described as a dipole. When the ram pressure of the accreted flow equals the magnetic field pressure, the matter is funnelled along the field lines onto the magnetic poles. The gravitational

potential energy of the accreting matter is converted into kinetic energy. Due to shocks in the accretion flow, the kinetic energy is then dissipated in X-rays and hot spots form on the neutron star surface close to its magnetic poles (see, e.g., Caraveo 2008).

If the rotation axis is inclined with respect to its magnetic axis, the X-ray emission is observed to be modulated by the spin period of the compact object. These periodical episodes of accretion , related to the periastron passage, are called type I outbursts and can reach an X-ray luminosity as high as $L_X \approx 10^{36-37}$erg/s.

There exist also Type II (or giant) outbursts, which are characterized by a larger X-ray emission than the type I outburst, with an outburst duration which can last for several binary orbits. Such large outburst durations can be explained if the Be star undergoes episodes of very strong mass ejection. As this material spreads around in the binary systems, the neutron star can accrete matter from it for a long time.

Some binary systems exhibit cyclotron resonance scattering features (CRSF), which are the results of the interaction of the electrons with the magnetic field. These lines are expected in highly magnetized accreting X-ray pulsars ($B \approx 10^{11} - 10^{13}$ G) (see Heindl et al. 2004, for a review), when the de Broglie radius of the electron becomes comparable to its Larmor radius. In this case, the energy of the electron perpendicularly to the magnetic field lines is quantized in Landau levels (the electrons can only occupy cyclotron orbits of discrete energies) and the discrete energy levels are given by $E_e = E_{cycl}n$, where the $E_{cycl} = 11.6(B/10^{12}\mathrm{G})$ keV is the fundamental Landau level and n the harmonics (Schönherr et al. 2007). Photons of energy $E = nE_{cycl}$ are scattered by the electrons in the plasma. Therefore, an absorption-like feature is produced in the photon spectrum at energies $E = nE_{cycl}$.

Such lines are of particular interest as they directly probe the strength of the magnetic field at the neutron star surface. GX 304-1 has been recently established as a cyclotron line source (Yamamoto et al. 2011). Such lines are also reported in the present ATel (Klochkov et al. 2012b).

ATel #3902 (Klochkov et al. 2012b)

The INTEGRAL monitoring of the on-going outburst of the transient accreting pulsar GX 304-1 with a Be optical companion revealed strong flaring activity with X-ray flux variations by a factor of 2 on a time scale of 1 hour (18-80 keV). The INTEGRAL observations started around MJD 55943. The maximum flux level measured by ISGRI so far is 964 +/- 2 mCrab in the 20-40 keV range. The cyclotron resonance scattering feature is present in the ISGRI and SPI spectra of the source. In the ISGRI data taken around MJD 55944, it can be modeled with a Gaussian absorption line with a best fit centroid energy of 52.4 +/-1.3 keV and a width (sigma) of 6+/-1 keV. Due to the possibility that the observations are affected by solar flares, the actual line position might be subject to systematic uncertainties at the level of a few keV. The detailed spectral study is ongoing. We thank the INTEGRAL team for the effective communication and prompt scheduling of the TOO observations.

8.3.2 INTEGRAL detection of a new outburst of A 0535+262 (ATel #3173)

The source A 0535+262

A 0535+262 is an X-ray pulsar in a binary system with the Be star HDE 245770. This binary system has been discovered during a giant outburst in 1975 (Rosenberg et al. 1975). In this system,

the accretion of the material from the Be star on the compact star is a similar to the one outlined above in the case of GX 304-1.

Since its discovery, A 0535+262 has been detected in quiescent states (Motch et al. 1991; Negueruela et al. 2000; Orlandini et al. 2004), with a luminosity of about $L_x \ll 10^{37}$ erg/s. This indicates that the source undergoes limited accretion also during its quiescent state. Furthermore, the detection of quasi-periodic oscillations seems to show that an accretion disk is present around the compact star. This quiescent state has been interrupted by type I outbursts (Finger et al. 1996) and by more powerful, type II outbursts, where the luminosity reached $L_x \sim 10^{36-37}$ erg/s and $L_x > 10^{37}$ erg/s, respectively. In the whole activity history of this source, 5 giant outbursts have been detected (Nagase et al. 1982; Sembay et al. 1990; Makino et al. 1989; Finger et al. 1994; Tueller et al. 2005). Cyclotron lines have been detected in the spectrum of A 0535+262 and a magnetic field of 10^{12} G at the neutron star surface has been inferred (Caballero 2009).

In the observations reported here (Tchernin et al. 2011), the system enters in a new giant outburst.

ATel #3173 (Tchernin et al. 2011)

During the on-going calibration observations of the Crab, INTEGRAL detected the Be X-ray binary A 0535+262 during a new bright X-ray outburst (see also Atel #3166). The observations on which this telegram is based were performed from 2011 Feb. 16 at 11:50 to 2011 Feb. 17 at 15:55 (UTC). The source is detected at an average flux of 1.5 and 0.8 Crab in the 20-40 keV and 40-80 keV energy bands, respectively. The IBIS/ISGRI lightcurve shows a remarkable increase in the count-rate, thus suggesting that the currently on-going event is probably another giant outburst from the source. Further INTEGRAL observations of the region around A 0535+262 are currently planned until 2011 Feb. 19. Observations with other instruments are encouraged.

8.3.3 INTEGRAL/IBIS observations of the Galactic center region at the epoch of the short Fermi/LAT flare (ATel #3170)

The Fermi-LAT instrument detected a 20 s burst coming from a position consistent with the Galactic center (ATel #3170). From the same location, the SWIFT detected a significant emission from the source SAX J1747.0-2853 (Kennea et al. 2011) and suggested that this could have been the emitter of the flare observed by the Fermi-LAT. SAX J1747.0 - 2853 is a neutron star transient which shows high variability but with a low luminosity. It has been observed by INTEGRAL (Fiocchi et al. 2011), Swift/XRT (Kennea et al. 2011), BeppoSAX (Natalucci et al. 2000; Campana et al. 2000), ASCA (Murakami et al. 2000), RXTE (Wijnands et al. 2001; Markwardt et al. 2000), Chandra (Wijnands et al. 2002) and Fermi-LAT (Vasileiou et al. 2011).

The idea of the INTEGRAL team was to use the INTEGRAL data to investigate what happened there and localize the source of the burst. INTEGRAL was indeed pointing by chance in the same direction of the Fermi-LAT at the time of the burst. In the present ATel is reported an extended analysis of these data.

They used observed science windows around the time and position reported by the Fermi-LAT. They detected the emission from many other sources, SAX J1750.8-2900, 1E1743.1-2852 (a low mass X-ray binary, Vaiana et al. 1981) and IGR J17507-2856 (a gamma-ray source, Courvoisier et al. 2003b) but no significant emission from the source identified by SWIFT, SAX J1747.0-2853.

As mentioned in this ATel, the region around SAX J1747.0 - 2853 is very crowded and the angular resolution may not be good enough to resolve all objects in this region. This may explain these controversial results.

ATel #3170 (Fiocchi et al. 2011)

The Galactic Center was in the IBIS/ISGRI field-of-view during the epoch of the gamma-ray flare observed recently by Fermi/LAT (ATEL#3162). During the 20s interval of the flare IBIS/ISGRI did not detect any emission from SAX J1747.0-2853, located at 10degrees off-axis, with a 3sigma upper limit of 250mCrab in the 20-60 keV band. We have also analyzed two separate time slots of 6 and 7 pointings, respectively: (a) 2011 Feb. 10, 11:41-18:41 UT, and (b) 2011 Feb. 12, 04:09-10:09 UT. The retrieved data belong to the near-real time INTEGRAL archive. The first period includes the gamma-ray flare, the second one was selected because the source position was most optimal, i.e., about 6-8 degrees off-axis, the closest to the Galactic center region. The second slot is only a few hours apart from the Swift/XRT observation of SAX J1747.0-2853 (ATEL #3163), during which very bright emission from this source was reported. SAX J1747.0-2853 was not detected in the IBIS/ISGRI images produced in the range 20-60 keV and we find 3 sigma upper limits of 6 mCrab for period (a) and 4 mCrab for period (b). Conversely, during a 10.4 ks period including the XRT observation, we have an indication of faint activity of the source found by comparing with the images taken with periods (a) and (b). However, since the source is blended and located only 9.5 arcmin from 1E1743.1-2852, we cannot claim for a clear detection. We note that in both periods IBIS/ISGRI detects emission from a region consistent with the position of the transient X-ray burster SAX J1750.8-2900. The average flux is 14.5 +/- 1.2 mCrab (20-60 keV) during both periods and the 90% c.l. position error is 2.2 arcmin. The IBIS survey catalog version 4 (Bird et al. 2010, ApJS 186, 1) lists a candidate transient source (classified as "blended"), IGR J17507-2856, at about 5' from the position of SAX J1750.8-2900. IGR J17507-2856 is a faint source known to appear sporadically in the survey maps. Within the limits of our analysis both sources are compatible with the observed site of emission, although our results are suggesting that the detected source is most probably SAX J1750.8-2900. For this detection, we encourage follow-up observations to identify the source of emission seen with IBIS/ISGRI. Finally, we thank the ISDC for providing us the results of their quick look analysis.

Chapter 9

Conclusion & Outlook

Since their discovery about 100 years ago, the cosmic rays have been observed over a broad range of energy, up to 10^{20} eV. However, due to the ubiquitous magnetic field, no firm ideas of the acceleration sites of UHECR have been yet established.

In this perspective, the study of the neutral secondary particles produced in cosmic ray interactions in the source are an indirect but promising way to determine where the observed cosmic rays are accelerated. This multi-messenger approach based on γ-ray and neutrino observations has only recently started thanks to the recently built IceCube neutrino detector and to the development of the γ-ray astronomy, with the Fermi satellite. In this thesis, I combined γ-ray and neutrino observations to test this multi-messenger approach on different γ-ray sources.

I investigated the possibility of the detection of a neutrino signal from the Galactic plane with IceCube (Tchernin et al. 2013b). Knowing that the diffuse γ-ray emission of the Galactic plane is dominated by the neutral pion decay, the Galactic plane should also be a bright source of neutrinos. The Galactic plane scan performed in this study allowed us also to predict which Galactic region should be detectable within the IceCube life-time. As the IceCube detector is optimized for the detection of the neutrino signal of sources located in the Northern hemisphere, the two hemispheres have been treated separately.

One of the most important result of our study has been the prediction that among all the sources located in the Northern hemisphere, only the neutrino signal from the Cygnus region could be potentially detected after about ten-twenty years of exposure. This result was based on phenomenological concepts, but it may potentially be confirmed by the recent data analysis performed by the IceCube collaboration (IceCube Collaboration et al. 2014). In this analysis, the IceCube collaboration performed a stacking analysis of six MILAGRO TeV sources and obtained that the stacked signal was consistent with a probability of 2% with background fluctuations. As from these six sources, four were located in the Cygnus region, this may confirm our result that the neutrino signal from the Cygnus region may be detected after a longer exposure time.

Then, in the second part of this Galactic plane analysis, I computed the exposure time necessary to detect the neutrino signal arising from sources located in the Southern hemisphere. This analysis has been performed with an hypothetic detector similar to the IceCube detector, but sensitive to sources located in the Southern hemisphere. The results show that a few sources would be already detectable within 5 years of exposure time at a 5σ level. Most of these potentially detectable sources are located in the Galactic ridge. This led to another substantial result. Indeed, the IceCube collaboration recently developed a data analysis which is sensitive to the Southern hemisphere. Based on this analysis method, the IceCube collaboration detected a bunch of high energy neutrinos, whose direction is consistent with the Galactic Ridge of our Galaxy (Aartsen et al. 2014b; Neronov et al. 2013). Therefore, this discovery may be in agreement with our results. However the poor angular resolution of these events implies that this neutrino direction is also consistent with other models, even with extragalactic sources. Nevertheless, thanks to this

neutrino detection, the neutrino astronomy and the multi-messenger approach can start and better constraints on the potential cosmic ray acceleration sites can be set. Furthermore, this latter result provides a strong argument in favor of the deployment of the km^3 scale VHE neutrino detector in the Northern hemisphere, like KM3NeT (Kappes & KM3NeT Consortium 2007).

Then moving to larger scales, I combined the neutrino and γ-ray observations collected on the brightest TeV blazars (Tchernin et al. 2013a). For these sources, the origin of the γ-ray emission is unknown and could be from leptonic or hadronic origin. For this reason, the analysis was different to the Galactic plane analysis, as the aim was then not to determine if a known neutrino source could be detected, but to constrain the parameter space of purely hadronic scenarios of activity of blazars, based on the combined neutrino and γ-ray data,

In this study, with my co-authors I assumed that the observed electromagnetic emission comes purely from high-energy proton interactions via pp and/or $p\gamma$ channels and used this assumption to estimate the level of neutrino flux which was subsequently compared to the IceCube sensitivity. Assuming that the observed γ-ray emission was dominated by the electromagnetic cascade, this analysis indicated that harder spectra than E^{-2} proton spectra and cut-off energies in the UHECR band are favored by IceCube limits. These results have been derived from phenomenological expectations with half of the IceCube detector (IC-40) (Abbasi et al. 2011) and only one year exposure. As the IC-40 sensitivity is already comparable (in terms of the energy flux) with the electromagnetic fluxes of the brightest blazars observed by the Fermi satellite, a larger exposure time should help us to confirm or rule out hadronic models for blazars.

In the last part of my thesis, I considered galaxy clusters. Based in one hand, on the model of our own Galaxy and, on the other hand on the X-ray observations of the gas in these systems, cosmic rays are expected to be confined in these large systems and to interact with the intercluster gas via pp interactions. Therefore, a γ-ray flux and a neutrino flux are expected to arise from the produced pions. However, at the opposite to these expectations, galaxy clusters are very faint γ-ray sources, which have not yet been detected with the Fermi detector.

In the present study, I used the γ-ray upper-limits of a stacking analysis of a sample of bright X-ray galaxy clusters to derive constraints on the average cosmic ray content in this sample. Different cosmic ray radial distributions (flatter, steeper or the same as the one of the thermal gas) and different cosmic ray proton spectral indices ($\gamma_p \in [2.05, 3.25]$) have been tested. The obtained upper-limits on the cosmic ray-to thermal energy ratio range between 3 to 15%, for the considered cosmic ray radial and spectral distributions. In this thesis, I show that these upper-limits are starting to probe the particle acceleration models of cosmic ray injection at cosmological shocks used in numerical simulations (Vazza et al. 2012; Pinzke & Pfrommer 2010). This result seems to indicate that the acceleration efficiency assumed in these simulations is overestimated.

In this thesis I also reported my contribution to a project, where I studied with my co-authors how well X-ray and lensing data can be combined on the ground of the projected gravitational potential. To this end, I applied the reconstruction method developed in Konrad et al. (e.g., 2013) on the well-known cluster Abell 1689. The result demonstrates that the two-dimensional, projected potential recovered from information contained in X-ray observations is in good agreement with the lensing potential. This is therefore an encouraging step forward for the reconstruction of cluster gravitational potentials based on joint analyses.

CHAPTER 10

Publication list

Articles:

- *"Reconstruction of the projected gravitational potential of Abell 1689 from X-ray measurements"*
  C. Tchernin, C.L. Majer, S. Meyer, E. Sarli, D. Eckert, M. Bartelmann, submitted in A&A (2014);

- *"PeV neutrinos from interactions of cosmic rays with the interstellar medium in the Galaxy"*
  A.Neronov, D. Semikoz and **C. Tchernin**,C. 2014, Phys. Rev. D 9, 103002;

- *"Probing the cosmic-ray content of galaxy clusters by stacking Fermi-LAT count maps"*
  B. Huber, **C. Tchernin**, D. Eckert, C. Farnier, A. Manalaysay, U. Straumann and R. Walter, 2013, A&A, 560, A64;

- *"Neutrino signal from extended Galactic sources in IceCube"*
  C. Tchernin, J.A. Aguilar, A. Neronov, T. Montaruli, 2013, A&A, 560, A67;

- *"An exploration of hadronic interactions in blazars using IceCube"*
  C. Tchernin, J.A. Aguilar, A. Neronov, T. Montaruli, 2013, A&A, 555, A70.;

- *"Measuring the correlation length of intergalactic magnetic fields from observations of gamma-ray induced cascades"*
  A.Neronov, A.M.Taylor, **C. Tchernin** and Ie. Vovk, 2013, A&A, 554, A31;

Proceedings:

- *"An exploration of hadronic interactions in blazars using multi-messenger data"* talk held in RICAP-13 on the 22.05.12,
  C. Tchernin, J.A. Aguilar, A. Neronov, T. Montaruli, Elsevier Nuclear Inst. and Methods in Physics Research, A (2013), http://dx.doi.org/10.1016/j.nima.2013.10.065.

ATels:

- *"INTEGRAL/IBIS observations of the Galactic center region at the epoch of the short Fermi/LAT flare"*
  M. Fiocchi, C. Sanchez-Fernandez, L. Natalucci, E. Kuulkers, A. Bazzano, A. J. Bird, E. Bozzo, J. Chenevez, C. Ferrigno, V. Sguera, **C. Tchernin**, ATel #3170;

- *"INTEGRAL detection of a new outburst of A 0535+262"*
  C. Tchernin, C. Ferrigno, E. Bozzo, ATel #3173;

- *"Flaring activity and cyclotron line in GX 304-1 observed with INTEGRAL"*
  D. Klochkov, A. Santangelo, R. Staubert, V. Doroshenko, G. Puehlhofer, C. Ferrigno, E. Bozzo, **C. Tchernin**, I. Caballero, P. Kretschmar, I. Kreykenbohm, J. Wilms, K. Pottschmidt, R. E. Rothschild, C. A. Wilson-Hodge, V. McBride, G. Schoenherr, ATel #3902;

GCN:

- *"XRF 120118A: an X-ray flash detected by INTEGRAL"*
  D. Gotz; S. Mereghetti, J. Borkowski, C. Ferrigno, E. Bozzo, **C. Tchernin**, GRB Coordinates Network, Circular Service, 12849, 1 (2012).

Appendices

.1 Diffusive Shock Acceleration mechanism

The first order Fermi acceleration or Diffusive Shock Acceleration mechanism (see e.g., Axford et al. 1977; Krymskii 1977; Bell 1978) is associated with particle acceleration at shock waves. Usually, perturbations propagate at the speed of sound, however, in the case of a shock wave, the disturbance propagates at supersonic speed and a discontinuity in the fluid velocity forms between the regions behind (region 2) and ahead (region 1) from the shock (see Fig. 1, panel a)). In both regions, the gas can be described by the thermodynamic quantities p_i, ρ_i and T_i ($i = 1, 2$), which are respectively, the pressure, density and temperature. In the region 1, where the disturbance has not arrived yet, the gas can be considered as at rest, while in the region 2, the gas moves at the supersonic speed U of the disturbance.

Based on the conservation of the flux of mass, energy and pressure between the two regions, the density ratio of the gas in front and behind the shock can be written as

$$\frac{\rho_2}{\rho_1} = \frac{\gamma_{hc} + 1}{(\gamma_{hc} - 1) + 2/M^2}. \tag{1}$$

Where γ_{hc} is the ratio of specific heat capacities and $M = U/c_1$ the Mach number of the shock, which is defined as the velocity ratio of the gas in the disturbed (2) and undisturbed region (1), c_1.

In the case of strong waves, the shock wave moves at a supersonic speed ($U \gg c_1$), such that $M \gg 1$. In this case, the density ratio of the gas in the two regions becomes $\rho_2/\rho_1 = (\gamma_{hc} + 1)/(\gamma_{hc} - 1)$. In the case of fully ionized plasma, the gas can be considered as monoatomic, which implies $\gamma_{hc} = 5/3$ and $\rho_2/\rho_1 = 4$.

Based on the conservation of mass flux between the two regions: $\rho_1 v_1 = \rho_2 v_2$, the velocity ratio between the regions can be derived as $v_1/v_2 = 4$.

Assuming that a particle crosses the shock from up- to downstream, the particle energy in the downstream region can be obtained using the Lorentz transformations (assuming that the coordinate x is perpendicular to the shock), given

$$E' = \Gamma_V (E + p_x V). \tag{2}$$

Where Γ_V is the Lorentz factor of the shock. Using the fact the particle is relativist ($E = pc$), while the shock is not ($\Gamma_V = 1$), one obtains $(E' - E)/E = \Delta E/E = (V/c)cos(\theta)$, where θ is the angle between the direction of the shock and the one of the particle.

Once the particles cross the shock, they scatter on the magnetic field irregularities and the velocity distribution of the particles becomes isotropic in the reference frame of the moving fluid, in either sides of the shock (see Fig. 1, panels c) and d)). The averaging over the angles weighted by the probability that the particle approaches the shock, leads an energy gain for the particle of $\Delta E/E = (2/3)(V/c)$. The average energy of the particle after a round trip (up- to down- and back to upstream) can be obtained as the energy of the particle + twice the energy gain per crossing. One can define the average energy gain per round trip as $\beta = E/E_0 = 1 + (4/3)(V/c)$, where E_0 is the initial particle energy before acceleration. After k round trips, the particle has the energy $E = E_0 \beta^k$. Now assuming that N_0 particles where initially in the upstream region (region 1), and that each particle has the probability P to remain in the accelerating region, after k round trips, the number of particles accelerated to $E = E_0 \beta^k$ is $N = N_0 P^k$.

Therefore, the differential energy spectrum can be derived as

$$\frac{dN}{dE} \propto E^{(ln(P)/ln(\beta))-1}. \tag{3}$$

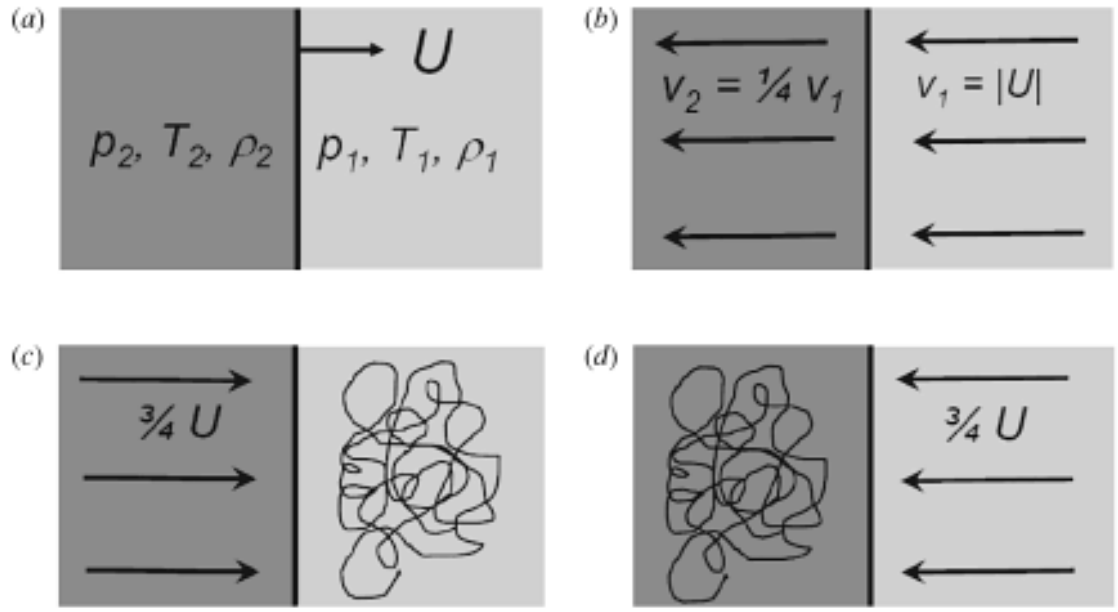

Figure 1: Scheme of the dynamics of high energy particles in the vicinity of a strong shock, as seen in different reference frames: a) in the laboratory frame, b) in the shock rest frame, c) in the rest frame of the upstream gas, with a velocity distribution isotropized by the scatterings on the magnetic fields irregularities, d) in the rest frame of the downstream gas, with a velocity distribution isotropized by the scatterings on the magnetic fields irregularities. Taken from (Longair 2011).

The accelerated particle energy distribution is a power-law. Now, let us derive the spectral index ($(ln(P)/ln(\beta))$) of this distribution. The particle in the upstream region sees the shocked gas coming towards it at a speed $V = U - (1/4)U = (3/4)U$ (see Fig. 1, panels c) and d)). Therefore, with $ln(\beta) = ln(1 + (4/3)(V/c)) \approx U/c$, and $ln(P) = ln(1 - U/c) \approx -U/c$ (see Fig. 1, panel b)), we obtain

$$\frac{dN}{dE} \propto E^{-2}. \tag{4}$$

Therefore, if strong shocks are present and if the energy distribution of the particles in either side of the shock are isotropically distributed in angle, the accelerated particle spectrum is expected to be distributed with a power-law of spectral index equal to 2. As strong shocks are expected to be present in many different astrophysical sources (see Sect.4), this gives rise to the historically 'universal' power law spectrum of accelerated particles (e.g., Krymskii 1977).

For this acceleration to take place, the particles are assumed to be present in the both sides of the shock front and to propagate at velocity much higher than the speed of the shock, with a Larmor radius larger than the thickness of the shock, but smaller than the Coulomb mean free path of the particle (collision-less shock).

For completeness, for non relativistic shocks which satisfy $r \equiv v_1/v_2 < 4$, the accelerated particle distribution is also a power-law, $N(E) \propto E^{-q+2}$, where q is given by $q = 3r/(r - 1)$ (Longair 2011).

.2 List of the galaxy clusters used in Sect. 7.1

Cluster	l (°)	b (°)	Redshift z	M_{500} (in 10^{14} $M_{\odot}$)	Cool core
2A0335p096	176.25	-35.07	0.0349	2.79	yes
A0085	115.05	-72.06	0.0556	8.08	yes
A0119	125.70	-64.10	0.0440	8.98	–
A0133	149.76	-84.23	0.0569	4.30	yes
A0262	136.58	-25.09	0.0161	0.94	yes
A0399	164.36	-39.47	0.0715	7.74	–
A0401	164.18	-38.87	0.0748	8.38	–
A0478	182.41	-28.30	0.0900	8.85	yes
A0496	209.59	-36.49	0.0328	4.81	yes
A0548w	230.49	-25.26	0.0424	1.00	–
A0576	161.42	26.24	0.0381	4.61	–
A1060	269.63	26.51	0.0114	2.50	–
A1367	235.31	73.01	0.0216	7.42	–
A1413	226.19	76.78	0.1427	9.77	–
A1644	304.90	45.50	0.0474	7.34	yes
A1656	58.08	87.96	0.0232	9.95	–
A1736	312.58	35.10	0.0461	2.17	–
A1775	31.92	78.71	0.0757	4.19	–
A1795	33.79	77.16	0.0616	9.87	yes
A1800	40.47	77.07	0.0748	5.94	–
A1914	67.20	67.46	0.1712	11.84	–
A2142	44.23	48.69	0.0899	14.33	–
A2151	31.58	44.52	0.0369	1.60	yes
A2244	58.80	36.35	0.0970	5.48	–
A2255	93.92	34.92	0.0800	7.86	–
A2256	111.10	31.74	0.0601	12.12	–
A2597	65.34	-64.85	0.0852	3.71	yes
A2634	103.45	-33.06	0.0312	4.51	–
A2657	96.65	-50.30	0.0404	6.06	–
A2877	293.13	-70.88	0.0241	6.88	–
A3112	252.95	-56.09	0.0750	4.36	yes
A3158	265.07	-48.97	0.0590	5.75	–
A3266	272.09	-40.17	0.0594	19.24	–
A3391	262.36	-25.16	0.0531	6.04	–
A3395	263.18	-25.13	0.0498	9.48	–
A3528n	303.70	33.85	0.0540	4.49	–
A3528s	303.78	33.64	0.0551	2.76	yes
A3530	304.00	32.51	0.0544	4.34	–
A3532	304.44	32.48	0.0539	6.63	–
A3558	311.98	30.74	0.0480	6.71	–
A3560	312.73	29.00	0.0495	2.77	–
A3562	313.31	30.35	0.0499	3.51	–

Continued on next page

Table 1 – *Continued from previous page*

Cluster	l (°)	b (°)	Redshift z	M_{500} (in 10^{14} $M_\odot$)	Cool core
A3571	316.32	28.55	0.0397	8.76	–
A3581	323.13	32.85	0.0214	0.93	yes
A3921	322.03	-47.97	0.0936	6.59	–
EXO0422m086	203.3	-36.16	0.0390	2.72	yes
Fornax	236.72	-53.63	0.0046	1.29	yes
HydraA	242.93	25.09	0.0538	4.07	yes
MKW4	276.91	62.31	0.0200	0.69	yes
NGC1550	190.98	-31.85	0.0123	0.68	yes
NGC499	130.50	-28.94	0.0147	0.33	yes
NGC5044	311.23	46.10	0.0090	0.49	yes
NGC507	130.64	-29.13	0.0165	0.46	yes

Table 1: The sample of 53 clusters used for the stacking. The values for redshift z and cluster mass M_{500} are taken from (Chen et al. 2007). The classification of cool cores is done using (Cavagnolo et al. 2009b) and (Chen et al. 2007). Taken from (Huber et al. 2013).

Bibliography

Aartsen, M. G., Abbasi, R., Abdou, Y., et al. 2013a, Physical Review Letters, 111, 021103

Aartsen, M. G., Abbasi, R., Abdou, Y., et al. 2013b, Phys. Rev. D 8, 042004

Aartsen, M. G., Ackermann, M., Adams, J., et al. 2014a, ArXiv e-prints

Aartsen, M. G., Ackermann, M., Adams, J., et al. 2014b, ArXiv e-prints

Aartsen, M. G., Ackermann, M., Adams, J., et al. 2014c, ArXiv e-prints

Abbasi, R., Abdou, Y., Abu-Zayyad, T., et al. 2010a, Astroparticle Physics, 34, 48

Abbasi, R., Abdou, Y., Abu-Zayyad, T., et al. 2011, ApJ, 732, 18

Abbasi, R. U., Abu-Zayyad, T., Al-Seady, M., et al. 2010b, Physical Review Letters, 104, 161101

Abbasi, R. U., Abu-Zayyad, T., Allen, M., et al. 2008, Physical Review Letters, 100, 101101

Abdo, A. A., Abeysekara, U., Allen, B. T., et al. 2012, ApJ 53, 159

Abdo, A. A., Ackermann, M., Ajello, M., et al. 2011a, ApJ 27, 129

Abdo, A. A., Ackermann, M., Ajello, M., et al. 2011b, ApJ 34, 28

Abdo, A. A., Ackermann, M., Ajello, M., et al. 2009a, Physical Review Letters, 103, 251101

Abdo, A. A., Ackermann, M., Ajello, M., et al. 2009b, ApJ 99, 31

Abdo, A. A., Ackermann, M., Ajello, M., et al. 2009c, ApJ 99, 817

Abdo, A. A., Ackermann, M., Ajello, M., et al. 2010, ApJ 08, 1310

Abdo, A. A., Ackermann, M., Ajello, M., et al. 2009d, ApJ 00, 1059

Abdo, A. A., Allen, B., Berley, D., et al. 2007, The Astrophysical Journal, Letters 58, L33

Abraham, J., Abreu, P., Aglietta, M., et al. 2008, Physical Review Letters, 101, 061101

Abraham, J., Abreu, P., Aglietta, M., et al. 2010, Physical Review Letters, 104, 091101

Acciari, V. A., Aliu, E., Arlen, T., et al. 2011, ApJ 38, 25

Ackermann, M., Ajello, M., Albert, A., et al. 2014, ApJ 87, 18

Ackermann, M., Ajello, M., Allafort, A., et al. 2011a, ApJ 43, 171

Ackermann, M., Ajello, M., Allafort, A., et al. 2013, Science, 339, 807

Ackermann, M., Ajello, M., Allafort, A., et al. 2010, The Astrophysical Journal, Letters 17, L71

Ackermann, M., Ajello, M., Allafort, A., et al. 2011b, Science, 334, 1103

Ackermann, M., Ajello, M., Atwood, W. B., et al. 2012, ApJ 50, 3

Actis, M., Agnetta, G., Aharonian, F., et al. 2011, Experimental Astronomy, 32, 193

Adrián-Martínez, S., Ageron, M., Aguilar, J. A., et al. 2012, Journal of Instrumentation, 7, 8002

Aguilar, J. A. 2013, Nuclear Physics B Proceedings Supplements, 237, 250

Aguilar, M., Alberti, G., Alpat, B., et al. 2013, Physical Review Letters, 110, 141102

Aharonian, F., Akhperjanian, A. G., Anton, G., et al. 2009, Astronomy and Astrophysics 95, 27

Aharonian, F., Akhperjanian, A. G., Aye, K.-M., et al. 2005a, Science, 307, 1938

Aharonian, F., Akhperjanian, A. G., Barres de Almeida, U., et al. 2008, Astronomy and Astrophysics 77, 353

Aharonian, F., Akhperjanian, A. G., Bazer-Bachi, A. R., et al. 2006a, Nature 39, 695

Aharonian, F., Akhperjanian, A. G., Bazer-Bachi, A. R., et al. 2005b, Astronomy and Astrophysics 37, L7

Aharonian, F., Akhperjanian, A. G., Bazer-Bachi, A. R., et al. 2006b, ApJ 36, 777

Aharonian, F. A. 2000, New Astronomy , 377

Aharonian, F. A., Akhperjanian, A. G., Bazer-Bachi, A. R., et al. 2005c, Astronomy and Astrophysics 42, L25

Aharonian, F. A., Akhperjanian, A. G., Kankanian, A. S., et al. 1991, International Cosmic Ray Conference, 2, 615

Ahn, E.-J., Engel, R., Gaisser, T. K., Lipari, P., & Stanev, T. 2009, Phys. Rev. D 0, 094003

Ahrens, J., Bahcall, J. N., Bai, X., et al. 2004, Nucl.Phys.Proc.Suppl 8, 519

Albert, J., Aliu, E., Anderhub, H., et al. 2008, ApJ 74, 1037

Albert, J., Aliu, E., Anderhub, H., et al. 2009, Astronomy and Astrophysics 93, 467

Alcaraz, J. 1999, International Cosmic Ray Conference, 5, 88

Aleksić, J., Alvarez, E. A., Antonelli, L. A., et al. 2012, Astronomy and Astrophysics 39, L2

Aleksić, J., Antonelli, L. A., Antoranz, P., et al. 2010, ApJ 10, 634

Aleksić, J., Antonelli, L. A., Antoranz, P., et al. 2011, ApJ 26, 58

Allen, S. W. 1998, Monthly Notices of the Royal Astronomical Society 96, 392

Allen, S. W., Evrard, A. E., & Mantz, A. B. 2011, Annual Review of Astron and Astrophys 9, 409

Aloisio, R., Berezinsky, V., & Gazizov, A. 2011, Astroparticle Physics, 34, 620

Ameglio, S., Borgani, S., Pierpaoli, E., & Dolag, K. 2007, Monthly Notices of the Royal Astronomical Society 82, 397

Amenomori, M., Ayabe, S., Caidong, et al. 2000, Phys. Rev. D 2, 112002

Anchordoqui, L. A., Barger, V., Cholis, I., et al. 2013, ArXiv e-prints

Andersson, K. E. & Madejski, G. M. 2004, ApJ 07, 190

Ando, S. & Nagai, D. 2008, Monthly Notices of the Royal Astronomical Society 85, 2243

Andres, E., Askebjer, P., Barwick, S. W., et al. 2000, Astroparticle Physics, 13, 1

ANTARES Collaboration. 1999, ArXiv Astrophysics e-prints

Apel, W. D., Arteaga-Velázquez, J. C., Bekk, K., et al. 2011, Physical Review Letters, 107, 171104

Apel, W. D., Arteaga-Velàzquez, J. C., Bekk, K., et al. 2013, Phys. Rev. D 7, 081101

Arlen, T., Aune, T., Beilicke, M., et al. 2012, ApJ 57, 123

Arnaud, M., Pointecouteau, E., & Pratt, G. W. 2005, Astronomy and Astrophysics 41, 893

Asakimori, K., Burnett, T. H., Cherry, M. L., et al. 1993, International Cosmic Ray Conference, 4, 708

Aschenbach, B. 1998, Nature 96, 141

Aschenbach, B., Braeuninger, H., Briel, U., et al. 1981, Space Science Reviews 0, 569

Aschenbach, B., Iyudin, A. F., & Schönfelder, V. 1999, Astronomy and Astrophysics 50, 997

Atkins, R., Benbow, W., Berley, D., et al. 1999, ArXiv Astrophysics e-prints

Atwood, W. B., Abdo, A. A., Ackermann, M., et al. 2009, ApJ 97, 1071

Ave, M. 1999, International Cosmic Ray Conference, 1, 365

Axford, W. I., Leer, E., & Skadron, G. 1977, International Cosmic Ray Conference, 11, 132

Balkanov, V. A., Belolaptikov, I. A., Bezrukov, L. B., et al. 2000, Nuclear Physics B Proceedings Supplements, 87, 405

Barbiellini, G., Basini, G., Bellotti, R., et al. 1995, International Cosmic Ray Conference, 3, 657

Bartelmann, M. 2003, in Astronomical Society of the Pacific Conference Series, Vol. 301, Matter and Energy in Clusters of Galaxies, ed. S. Bowyer & C.-Y. Hwang, 255

Bartelmann, M. & Schneider, P. 2001, Physics Reports 40, 291

Beatty, J. 1999, International Cosmic Ray Conference, 5, 61

Bednarek, W. & Protheroe, R. J. 1997, Monthly Notices of the Royal Astronomical Society 87, L9

Bell, A. R. 1978, Monthly Notices of the Royal Astronomical Society 82, 147

Berezinsky, V. 2013, ArXiv e-prints

Berezinsky, V. S., Blasi, P., & Ptuskin, V. S. 1997, ApJ 87, 529

Berezinsky, V. S., Gaisser, T. K., Halzen, F., & Stanev, T. 1993, Astroparticle Physics, 1, 281

Beringer, J. et al. 2012, Phys.Rev., 010001

Bignami, G. F., Boella, G., Burger, J. J., et al. 1974, in The Context and Status of Gamma-Ray Astronomy, ed. B. G. Taylor, 307–322

Bird, D. J., Corbató, S. C., Dai, H. Y., et al. 1995, in American Institute of Physics Conference Series, Vol. 338, Intersections between Particle and Nuclear Physics, ed. S. J. Seestrom, 839–854

Blandford, R. & Eichler, D. 1987, Physics Reports 54, 1

Blasi, P., Gabici, S., & Brunetti, G. 2007, International Journal of Modern Physics A, 22, 681

Bloom, S. D. & Marscher, A. P. 1996, ApJ 61, 657

Borione, A., Cronin, J. W., Covault, C. E., et al. 1993, in American Institute of Physics Conference Series, Vol. 276, Very High Energy Cosmic-Ray Interactions, ed. L. Jones, 207–211

Broadhurst, T., Takada, M., Umetsu, K., et al. 2005, The Astrophysical Journal, Letters 19, L143

Brown, S. & Rudnick, L. 2011, Monthly Notices of the Royal Astronomical Society 12, 2

Bruel, P. 2010, Journal of Physics Conference Series, 203, 012020

Budnev, N. M., Besson, D., Chvalaev, O. A., et al. 2010, ArXiv e-prints

Buote, D. A. & Humphrey, P. J. 2012a, Monthly Notices of the Royal Astronomical Society 20, 1693

Buote, D. A. & Humphrey, P. J. 2012b, Monthly Notices of the Royal Astronomical Society 21, 1399

Burns, J. O. 1990, The Astronomical Journal 9, 14

Caballero, I. 2009, PhD thesis, IAAT University of Tuebingen

Campana, S., Israel, G. L., & Stella, L. 2000, IAU Circulars 401, 1

Capelo, P. R., Coppi, P. S., & Natarajan, P. 2012, Monthly Notices of the Royal Astronomical Society 22, 686

Caraveo, P. A. 2008, Astronomische Nachrichten, 329, 191

Casolino, M., Mikhailov, V., & PAMELA Collaboration. 2003, International Cosmic Ray Conference, 6, 3477

Cassano, R., Brunetti, G., & Venturi, T. 2011, Journal of Astrophysics and Astronomy, 32, 519

Cassano, R., Ettori, S., Giacintucci, S., et al. 2010, The Astrophysical Journal, Letters 21, L82

Cassidy, M., Fortson, L. F., Fowler, J. W., et al. 1997, International Cosmic Ray Conference, 5, 189

Cavagnolo, K. W., Donahue, M., Voit, G. M., & Sun, M. 2009a, VizieR Online Data Catalog, 218, 20012

Cavagnolo, K. W., Donahue, M., Voit, G. M., & Sun, M. 2009b, The Astrophysical Journal Supplement Series 82, 12

Cavaliere, A. & Fusco-Femiano, R. 1976, Astronomy and Astrophysics 9, 137

Celotti, A., Fabian, A. C., & Rees, M. J. 1998, Monthly Notices of the Royal Astronomical Society 93, 239

Cesarsky, C. J. 1980, Annual Review of Astron and Astrophys 8, 289

Chen, Y., Reiprich, T. H., Böhringer, H., Ikebe, Y., & Zhang, Y.-Y. 2007, Astronomy and Astrophysics 66, 805

Chevalier, R. A. 1977, Annual Review of Astron and Astrophys 5, 175

Chiarusi, T. & Spurio, M. 2010, European Physical Journal C, 65, 649

Chiba, N., Hashimoto, K., Hayashida, N., et al. 1991, International Cosmic Ray Conference, 2, 700

Colafrancesco, S. & Blasi, P. 1998, Astroparticle Physics, 9, 227

Colafrancesco, S. & Marchegiani, P. 2008, Astronomy and Astrophysics 84, 51

Colafrancesco, S., Marchegiani, P., & Giommi, P. 2010, Astronomy and Astrophysics 19, A82

Courvoisier, T. J.-L. 1998, Astronomy & Astrophysics Reviews , 1

Courvoisier, T. J.-L., Walter, R., Beckmann, V., et al. 2003a, Astronomy and Astrophysics 11, L53

Courvoisier, T. J.-L., Walter, R., Rodriguez, J., Bouchet, L., & Lutovinov, A. A. 2003b, IAU Circulars 063, 3

Danforth, C. W., Keeney, B. A., Stocke, J. T., Shull, J. M., & Yao, Y. 2010, ApJ 20, 976

Daum, K. 1995, Z. Phys., C66, 417

de Jager, O. C., Funk, S., & Hinton, J. 2005, International Cosmic Ray Conference, 4, 239

de Marzo, C., Ambriola, M., Bellotti, R., et al. 2000, Nuclear Physics B Proceedings Supplements, 87, 433

de Plaa, J., Werner, N., Bleeker, J. A. M., et al. 2007, Astronomy and Astrophysics 65, 345

Dermer, C. D. 1986, Astronomy and Astrophysics 57, 223

Devasia, J., James, M., Paul, B., & Indulekha, K. 2011, Monthly Notices of the Royal Astronomical Society 17, 348

Di Cocco, G., Caroli, E., Celesti, E., et al. 2003, Astronomy and Astrophysics 11, L189

Donnert, J., Dolag, K., Cassano, R., & Brunetti, G. 2010, Monthly Notices of the Royal Astronomical Society 07, 1565

Drury, L. O. 1983, Reports on Progress in Physics, 46, 973

Dutson, K. L., White, R. J., Edge, A. C., Hinton, J. A., & Hogan, M. T. 2013, Monthly Notices of the Royal Astronomical Society 29, 2069

Eckert, D., Molendi, S., Gastaldello, F., & Rossetti, M. 2011, Astronomy and Astrophysics 29, A133

Eckert, D., Molendi, S., Vazza, F., Ettori, S., & Paltani, S. 2013, Astronomy and Astrophysics 51, A22

Eckert, D. & Paltani, S. 2009, Astronomy and Astrophysics 95, 415

Eckert, D., Vazza, F., Ettori, S., et al. 2012, Astronomy and Astrophysics 41, A57

Edwards, P. G., Fujii, H., Fujimoto, M., et al. 1993, International Cosmic Ray Conference, 2, 426

Enßlin, T., Pfrommer, C., Miniati, F., & Subramanian, K. 2011, Astronomy and Astrophysics 27, A99

Enßlin, T. A. & Brüggen, M. 2002, Monthly Notices of the Royal Astronomical Society 31, 1011

Ettori, S., Donnarumma, A., Pointecouteau, E., et al. 2013, Space Science Reviews 77, 119

Fabian, A. C. 1994, Annual Review of Astron and Astrophys 2, 277

Fadda, D., Elbaz, D., Duc, P.-A., et al. 2000, Astronomy and Astrophysics 61, 827

Fanaroff, B. L. & Riley, J. M. 1974, Monthly Notices of the Royal Astronomical Society 67, 31P

Fang, K., Fujii, T., Linden, T., & Olinto, A. V. 2014, ArXiv e-prints

Feldman, G. J. & Cousins, R. D. 1998, Phys. Rev. D, 57, 3873

Feretti, L., Giovannini, G., Govoni, F., & Murgia, M. 2012, Astronomy & Astrophysics Reviews 0, 54

Fermi, E. 1949, Physical Review, 75, 1169

Fichtel, C. E., Hartman, R. C., Kniffen, D. A., et al. 1975, ApJ 98, 163

Finger, M. H., Wilson, R. B., & Hagedon, K. S. 1994, IAU Circulars 931, 1

Finger, M. H., Wilson, R. B., & Harmon, B. A. 1996, ApJ 59, 288

Finley, J. P. & VERITAS Collaboration. 2001, International Cosmic Ray Conference, 7, 2827

Fiocchi, M., Sanchez-Fernandez, C., Natalucci, L., et al. 2011, The Astronomer's Telegram, 3170, 1

Fletcher, R. S., Gaisser, T. K., Lipari, P., & Stanev, T. 1994, Phys. Rev. D 0, 5710

Franceschini, A., Rodighiero, G., & Vaccari, M. 2008, Astronomy and Astrophysics 87, 837

Fujita, Y. & Ohira, Y. 2011, ApJ 38, 182

Fujita, Y. & Ohira, Y. 2012, ApJ 46, 53

Funk, S., Hinton, J. A., Pühlhofer, G., et al. 2007, ApJ 62, 517

Gabici, S. & Aharonian, F. A. 2014, ArXiv e-prints

Gaensler, B. M. & Slane, P. O. 2006, Annual Review of Astron and Astrophys 4, 17

Gaisser, T. K. 2012, Astroparticle Physics, 35, 801

Gandhi, R. 2001, Nuclear Physics B Proceedings Supplements, 91, 453

Gandhi, R., Quigg, C., Hall Reno, M., & Sarcevic, I. 1996, Astroparticle Physics, 5, 81

Gemmeke, H., Kleifges, M., Kopmann, A., et al. 2001, International Cosmic Ray Conference, 2, 769

Ghisellini, G. & Madau, P. 1996a, Monthly Notices of the Royal Astronomical Society 80, 67

Ghisellini, G. & Madau, P. 1996b, Monthly Notices of the Royal Astronomical Society 80, 67

Giacinti, G., Kachelrieß, M., & Semikoz, D. V. 2012, Physical Review Letters, 108, 261101

Ginzburg, V. L. & Syrovatskii, S. I. 1964, The Origin of Cosmic Rays

Glushkov, A. V., D'Yakonov, M. N., Egorov, T. A., et al. 1993, Rossijskaya Akademiya Nauk Izvestiya Seriya Fizicheskaya, 57, 91

Gould, R. J. & Schreder, G. P. 1967, Phys.Rev., 155, 1404

Graff, P. B., Georganopoulos, M., Perlman, E. S., & Kazanas, D. 2008, ApJ 89, 68

Greisen, K. 1966, Physical Review Letters, 16, 748

Guzik, T. G. 1999, International Cosmic Ray Conference, 5, 9

Hartman, R. C., Bertsch, D. L., Bloom, S. D., et al. 1999, The Astrophysical Journal Supplement Series 23, 79

HAWC Collaboration, Abeysekara, A. U., Alfaro, R., et al. 2013, ArXiv e-prints

Healy, M. D. 2008, International Cosmic Ray Conference, 4, 377

Heindl, W. A., Rothschild, R. E., Coburn, W., et al. 2004, in American Institute of Physics Conference Series, Vol. 714, X-ray Timing 2003: Rossi and Beyond, ed. P. Kaaret, F. K. Lamb, & J. H. Swank, 323–330

Higdon, J. C., Lingenfelter, R. E., & Ramaty, R. 1998, The Astrophysical Journal, Letters 09, L33

Hillas, A. M. 1984, Annual Review of Astron and Astrophys 2, 425

Hoffman, K. D. 2009, New Journal of Physics, 11, 055006

Hofmann, W. 2012

Hofmann, W. & H.E.S.S. Collaboration. 2001, International Cosmic Ray Conference, 7, 2785

Honda, M., Kajita, T., Kasahara, K., Midorikawa, S., & Sanuki, T. 2007, Phys. Rev. D 5, 043006

Hooper, D. & Serpico, P. D. 2007, Physical Review Letters, 99, 231102

Huangs, A., Antoni, T., Apel, W. D., et al. 2003, International Cosmic Ray Conference, 2, 985

Huber, B., Tchernin, C., Eckert, D., et al. 2013, Astronomy and Astrophysics 60, A64

Hümmer, S., Rüger, M., Spanier, F., & Winter, W. 2010, ApJ, 721, 630

IceCube Collaboration. 2013, Science, 342

IceCube Collaboration, Aartsen, M. G., Abbasi, R., et al. 2013a, ArXiv e-prints

IceCube Collaboration, Aartsen, M. G., Abbasi, R., et al. 2013b, ArXiv e-prints

IceCube Collaboration, Aartsen, M. G., Ackermann, M., et al. 2014, ArXiv e-prints

Jenke, P., Finger, M. H., Wilson-Hodge, C. A., & Connaughton, V. 2012, The Astronomer's Telegram, 4547, 1

Jui, C. C. H. & the Telescope Array Collaboration. 2012, Journal of Physics Conference Series, 404, 012037

Kachelrieß, M., Serpico, P. D., & Teshima, M. 2007, Astroparticle Physics, 26, 378

Kalmykov, N., Ostapchenko, S., & Pavlov, A. 1997, Nucl.Phys.Proc.Suppl., 52B, 17

Kamae, T., Karlsson, N., Mizuno, T., Abe, T., & Koi, T. 2006, ApJ 47, 692

Kang, H. & Jones, T. W. 2007, Astroparticle Physics, 28, 232

Kang, H., Rachen, J. P., & Biermann, P. L. 1997, Monthly Notices of the Royal Astronomical Society 86, 257

Kang, H., Ryu, D., & Jones, T. W. 1996, ApJ 56, 422

Kappes, A., Hinton, J., Stegmann, C., & Aharonian, F. A. 2007, ApJ, 656, 870

Kappes, A. & KM3NeT Consortium, f. t. 2007, ArXiv e-prints

Katagiri, H., Enomoto, R., Ksenofontov, L. T., et al. 2005, The Astrophysical Journal, Letters 19, L163

Kawaharada, M., Okabe, N., Umetsu, K., et al. 2010, ApJ 14, 423

Kelner, S. R. & Aharonian, F. A. 2008, Phys. Rev. D, 78, 034013

Kelner, S. R., Aharonian, F. A., & Bugayov, V. V. 2006, Phys. Rev. D, 74, 034018

Kennea, J. A., Evans, P. A., Krimm, H., et al. 2011, The Astronomer's Telegram, 3163, 1

Keshet, U. 2010, ArXiv e-prints

Klochkov, D., Doroshenko, V., Santangelo, A., et al. 2012a, Astronomy and Astrophysics 42, L28

Klochkov, D., Santangelo, A., Staubert, R., et al. 2012b, The Astronomer's Telegram, 3902, 1

Komatsu, E., Smith, K. M., Dunkley, J., et al. 2011, The Astrophysical Journal Supplement Series 92, 18

Konrad, S., Majer, C. L., Meyer, S., Sarli, E., & Bartelmann, M. 2013, Astronomy and Astrophysics 53, A118

Krimm, H. A., Barthelmy, S. D., Baumgartner, W., et al. 2010, The Astronomer's Telegram, 2538, 1

Kriss, G. A., Cioffi, D. F., & Canizares, C. R. 1983, ApJ 72, 439

Krymskii, G. F. 1977, Akademiia Nauk SSSR Doklady, 234, 1306

Kurahashi, N. & for the IceCube Collaboration. 2014, ArXiv e-prints

Lagage, P. O. & Cesarsky, C. J. 1983, Astronomy and Astrophysics 25, 249

Lau, E. T., Kravtsov, A. V., & Nagai, D. 2009, ApJ 05, 1129

Learned, J. G. & Pakvasa, S. 1995, Astroparticle Physics, 3, 267

Lebrun, F., Leray, J. P., Lavocat, P., et al. 2003, Astronomy and Astrophysics 11, L141

Lee, J. & Suto, Y. 2003, ApJ 85, 151

Lee, J. & Suto, Y. 2004, ApJ 01, 599

Lemiere, A., Slane, P., Gaensler, B. M., & Murray, S. 2009, ApJ 06, 1269

Link, J. T., Binns, W. R., Cummings, J. R., et al. 2000, in APS Meeting Abstracts, 16004

Łokas, E. L., Prada, F., Wojtak, R., Moles, M., & Gottlöber, S. 2006, Monthly Notices of the Royal Astronomical Society 66, L26

Longair, M. S. 2011, High Energy Astrophysics

Lucy, L. B. 1974, The Astronomical Journal 9, 745

Lucy, L. B. 1994, Astronomy and Astrophysics 89, 983

Lund, N., Budtz-Jørgensen, C., Westergaard, N. J., et al. 2003, Astronomy and Astrophysics 11, L231

Mahdavi, A., Hoekstra, H., Babul, A., et al. 2013, ApJ 67, 116

Majer, C. L., Meyer, S., Konrad, S., Sarli, E., & Bartelmann, M. 2013, ArXiv e-prints

Makino, F., Cook, W., Grunsfeld, J., et al. 1989, IAU Circulars 769, 1

Malkov, M. A. & O'C Drury, L. 2001, Reports on Progress in Physics, 64, 429

Manchester, R. N., Bell, J. F., Camilo, F., et al. 2002, in Astronomical Society of the Pacific Conference Series, Vol. 271, Neutron Stars in Supernova Remnants, ed. P. O. Slane & B. M. Gaensler, 31

Mannheim, K. 1993, Astronomy and Astrophysics 69, 67

Mannheim, K. & Biermann, P. L. 1992, Astronomy and Astrophysics 53, L21

Markevitch, M. 2010, ArXiv e-prints

Markwardt, C. B., Marshall, F. E., & Swank, J. H. 2000, IAU Circulars 377, 1

Mas-Hesse, J. M., Giménez, A., Culhane, J. L., et al. 2003, Astronomy and Astrophysics 11, L261

Mathews, W. G. 2009, The Astrophysical Journal, Letters 95, L49

Mazzotta, P. & Giacintucci, S. 2008, The Astrophysical Journal, Letters 75, L9

McClintock, J. E., Nugent, J. J., Li, F. K., & Rappaport, S. A. 1977, The Astrophysical Journal, Letters 16, L15

McLaughlin, D. E. 1999, The Astronomical Journal 17, 2398

McNamara, B. R. & Nulsen, P. E. J. 2007, Annual Review of Astron and Astrophys 5, 117

Menanteau, F., Hughes, J. P., Sifón, C., et al. 2012, ApJ 48, 7

Merten, J., Cacciato, M., Meneghetti, M., Mignone, C., & Bartelmann, M. 2009, Astronomy and Astrophysics 00, 681

Meynet, G. & Maeder, A. 2003, Astronomy and Astrophysics 04, 975

Mihara, T., Yamamoto, T., Suzuki, M., et al. 2010, The Astronomer's Telegram, 2779, 1

Miniati, F., Ryu, D., Kang, H., & Jones, T. W. 2001, ApJ 59, 59

Miniati, F., Ryu, D., Kang, H., et al. 2000, ApJ 42, 608

Miralda-Escude, J. & Babul, A. 1995, ApJ 49, 18

Mittal, R., Hudson, D. S., Reiprich, T. H., & Clarke, T. 2009, Astronomy and Astrophysics 01, 835

Morandi, A., Limousin, M., Rephaeli, Y., et al. 2011, Monthly Notices of the Royal Astronomical Society 16, 2567

Morlino, G. & Caprioli, D. 2012, Astronomy and Astrophysics 38, A81

Motch, C., Stella, L., Janot-Pacheco, E., & Mouchet, M. 1991, ApJ 69, 490

Mücke, A. & Protheroe, R. J. 2001, Astroparticle Physics, 15, 121

Mücke, A., Protheroe, R. J., Engel, R., Rachen, J. P., & Stanev, T. 2003, Astroparticle Physics, 18, 593

Mucke, A., Rachen, J. P., Engel, R., Protheroe, R. J., & Stanev, T. 1999, PASA 6, 160

Murakami, H., Sakano, M., Koyama, K., Furusho, T., & Sakamoto, T. 2000, IAU Circulars 379, 3

Murase, K., Inoue, S., & Nagataki, S. 2008, The Astrophysical Journal, Letters 89, L105

Murgia, M., Govoni, F., Feretti, L., et al. 2004, Astronomy and Astrophysics 24, 429

Nagai, D. & Lau, E. T. 2011, The Astrophysical Journal, Letters 31, L10

Nagano, M. 2009, New Journal of Physics, 11, 065012

Nagase, F., Hayakawa, S., Kunieda, H., et al. 1982, ApJ 63, 814

Natalucci, L., Bazzano, A., Cocchi, M., et al. 2000, The Astrophysical Journal, Letters 43, L73

Navarro, J. F., Frenk, C. S., & White, S. D. M. 1997, ApJ 90, 493

Negueruela, I., Reig, P., Finger, M. H., & Roche, P. 2000, Astronomy and Astrophysics 56, 1003

Nellen, L., Mannheim, K., & Biermann, P. L. 1993, Phys. Rev. D 7, 5270

Nelson, K., Rudd, D. H., Shaw, L., & Nagai, D. 2012, ApJ 51, 121

Neronov, A. & Ribordy, M. 2009, Phys. Rev. D 0, 083008

Neronov, A. & Semikoz, D. V. 2012, Phys. Rev. D 5, 083008

Neronov, A., Semikoz, D. V., & Tchernin, C. 2013, ArXiv e-prints

Nolan, P. L., Abdo, A. A., Ackermann, M., et al. 2012, The Astrophysical Journal Supplement Series 99, 31

Norbury, J. W. & Townsend, L. W. 2007, Nuclear Instruments and Methods in Physics Research B, 254, 187

Nozaki, M., Streitmatter, R., Yamamoto, A., et al. 1995, International Cosmic Ray Conference, 3, 579

Obermeier, A., Boyle, P., Hörandel, J., & Müller, D. 2012, ApJ 52, 69

Oliva, A. & on behalf of the AMS collaboration. 2013, ICRC 2013 contribution: 1266

Orlandini, M., Bartolini, C., Campana, S., et al. 2004, Nuclear Physics B Proceedings Supplements, 132, 476

Osborne, J. L., Roberts, E., & Wolfendale, A. W. 1973, Journal of Physics A Mathematical General, 6, 421

Parizot, E. 2000, Astronomy and Astrophysics 62, 786

Paz Arribas, M., Schwanke, U., Sushch, I., et al. 2012, ArXiv e-prints

Pen, U.-L. 1999, The Astrophysical Journal Supplement Series 20, 49

Peng, E.-H., Andersson, K., Bautz, M. W., & Garmire, G. P. 2009, ApJ 01, 1283

Perkins, J. S. 2008, in American Institute of Physics Conference Series, Vol. 1085, American Institute of Physics Conference Series, ed. F. A. Aharonian, W. Hofmann, & F. Rieger, 569–572

Peterson, J. R. & Fabian, A. C. 2006, Physics Reports 27, 1

Pfrommer, C. & Enßlin, T. A. 2004, Astronomy and Astrophysics 13, 17

Pfrommer, C., Enßlin, T. A., & Springel, V. 2008, Monthly Notices of the Royal Astronomical Society 85, 1211

Pierre Auger Collaboration, Abraham, J., Abreu, P., et al. 2007, Science, 318, 938

Pierre Auger Collaboration, Abreu, P., Aglietta, M., et al. 2011, Journal of Cosmology and Astroparticle Physics , 22

Pinzke, A. & Pfrommer, C. 2010, Monthly Notices of the Royal Astronomical Society 09, 449

Pinzke, A., Pfrommer, C., & Bergström, L. 2011, Phys. Rev. D 4, 123509

Pittori, C. 2003, Chinese Journal of Astronomy and Astrophysics Supplement, 3, 517

Planck Collaboration, Ade, P. A. R., Aghanim, N., et al. 2013, Astronomy and Astrophysics 50, A131

Porter, J. M. & Rivinius, T. 2003, Publications of the Astronomical Society of the Pacific 15, 1153

Puchwein, E. & Bartelmann, M. 2006, Astronomy and Astrophysics 55, 791

Rachen, J. P. & Mészáros, P. 1998, Phys. Rev. D 8, 123005

Rädel, L. & Wiebusch, C. 2013, Astroparticle Physics, 44, 102

Rando, R. & for the Fermi LAT Collaboration. 2009, ArXiv e-prints

Rebel, H. & Sima, O. 2012, Rom.J.Phys., 57, 472

Reblinsky, K. 2000, Astronomy and Astrophysics 64, 377

Reimer, A. 2012, Journal of Physics Conference Series, 355, 012011

Reimer, O., Pohl, M., Sreekumar, P., & Mattox, J. R. 2003, ApJ 88, 155

Reiprich, T. H., Basu, K., Ettori, S., et al. 2013, Space Science Reviews 77, 195

Reiprich, T. H. & Böhringer, H. 2002, ApJ 67, 716

Resvanis, L. K. & Nestor Collaboration. 2006, Journal of Physics Conference Series, 39, 447

Romeyer, A. 2003, PhD thesis

Rosenberg, F. D., Eyles, C. J., Skinner, G. K., & Willmore, A. P. 1975, Nature 56, 628

Rossetti, M., Eckert, D., Cavalleri, B. M., et al. 2011, Astronomy and Astrophysics 32, A123

Ryu, D., Kang, H., Hallman, E., & Jones, T. W. 2003, ApJ 93, 599

Sarazin, C. L. 1986, Reviews of Modern Physics, 58, 1

Sarazin, C. L. 1999, ApJ 20, 529

Sarazin, C. L. 2008, in Lecture Notes in Physics, Berlin Springer Verlag, Vol. 740, A Pan-Chromatic View of Clusters of Galaxies and the Large-Scale Structure, ed. M. Plionis, O. López-Cruz, & D. Hughes, 1–4020

Sarcevic, I. 2009, Nuclear Instruments and Methods in Physics Research A, 604, 88

Sarli, E., Meyer, S., Meneghetti, M., et al. 2013, ArXiv e-prints

Schlickeiser, R. & Vainio, R. 1998, Astrophysics & Space Science 64, 457

Schönherr, G., Wilms, J., Kretschmar, P., et al. 2007, Astronomy and Astrophysics 72, 353

Sembay, S., Schwartz, R. A., Orwig, L. E., Dennis, B. R., & Davies, S. R. 1990, ApJ 51, 675

Seo, E. S. 2012, Astroparticle Physics, 39, 76

Sereno, M., Ettori, S., Umetsu, K., & Baldi, A. 2013, Monthly Notices of the Royal Astronomical Society 28, 2241

Sikora, M., Kirk, J. G., Begelman, M. C., & Schneider, P. 1987, The Astrophysical Journal, Letters 20, L81

Smith, R. K., Brickhouse, N. S., Liedahl, D. A., & Raymond, J. C. 2001, The Astrophysical Journal, Letters 56, L91

Snowden, S. L., Mushotzky, R. F., Kuntz, K. D., & Davis, D. S. 2008, Astronomy and Astrophysics 78, 615

Sokolsky, P. & HiRes Collaboration. 2011a, Nuclear Physics B Proceedings Supplements, 212, 74

Sokolsky, P. & HiRes Collaboration. 2011b, Nuclear Physics B Proceedings Supplements, 212, 74

Stecker, F. W. 1971, NASA Special Publication, 249

Stecker, F. W. 1979, ApJ 28, 919

Stenger, V. F. 1978, Acoustical Society of America Journal, 64, 105

Strong, A. W., Moskalenko, I. V., & Reimer, O. 2004, ApJ 13, 962

Sugizaki, M., Mitsuda, K., Kaneda, H., et al. 2001, The Astrophysical Journal Supplement Series 34, 77

Surdo, A., ARGO-YBJ Collaboration, Bernardini, P., et al. 2003, International Cosmic Ray Conference, 1, 5

Takeda, M., Hayashida, N., Honda, K., et al. 1998, Physical Review Letters, 81, 1163

Tchernin, C., Aguilar, J. A., Neronov, A., & Montaruli, T. 2013a, Astronomy and Astrophysics 55, A70

Tchernin, C., Aguilar, J. A., Neronov, A., & Montaruli, T. 2013b, Astronomy and Astrophysics 60, A67

Tchernin, C., Aguilar, J. A., Neronov, A., & Montaruli, T. 2014, Nuclear Instruments and Methods in Physics Research A, 742, 191

Tchernin, C., Ferrigno, C., & Bozzo, E. 2011, The Astronomer's Telegram, 3173, 1

The ANTARES Collaboration, Adrián-Martínez, S., Albert, A., et al. 2013, ArXiv e-prints

The Fermi-LAT collaboration, :, Abdo, A. A., et al. 2010, ArXiv e-prints

The Fermi-LAT Collaboration. 2012, ArXiv e-prints

The Telescope Array Collaboration, Abbasi, R. U., Abe, M., et al. 2014, ArXiv e-prints

Thompson, D. J., Bertsch, D. L., Fichtel, C. E., et al. 1993, The Astrophysical Journal Supplement Series 6, 629

Tozzi, P. & Norman, C. 2001, ApJ 46, 63

Tsunesada, Y. & for the Telescope Array Collaboration. 2011, ArXiv e-prints

Tueller, J., Ajello, M., Barthelmy, S., et al. 2005, The Astronomer's Telegram, 504, 1

Ubertini, P., Lebrun, F., Di Cocco, G., et al. 2003, Astronomy and Astrophysics 11, L131

Urry, C. M. & Padovani, P. 1995, Publications of the Astronomical Society of the Pacific 07, 803

Vaiana, G. S., Cassinelli, J. P., Fabbiano, G., et al. 1981, ApJ 45, 163

van Weeren, R. J., Röttgering, H. J. A., Brüggen, M., & Hoeft, M. 2010, Science, 330, 347

Vasileiou, V., Chiang, J., Omodei, N., et al. 2011, The Astronomer's Telegram, 3162, 1

Vazza, F., Brüggen, M., & Gheller, C. 2013, Monthly Notices of the Royal Astronomical Society 28, 2366

Vazza, F., Brüggen, M., Gheller, C., & Brunetti, G. 2012, Monthly Notices of the Royal Astronomical Society 21, 3375

Vedrenne, G., Roques, J.-P., Schönfelder, V., et al. 2003, Astronomy and Astrophysics 11, L63

Venters, T. M. 2010, ApJ 10, 1530

VERITAS Collaboration, Aliu, E., Arlen, T., et al. 2011, Science, 334, 69

Véron-Cetty, M.-P. & Véron, P. 2006, Astronomy and Astrophysics 55, 773

Voit, G. M. 2005, Reviews of Modern Physics, 77, 207

Völk, H. J., Aharonian, F. A., & Breitschwerdt, D. 1996, Space Science Reviews 5, 279

Völk, H. J. & Atoyan, A. M. 1999, Astroparticle Physics, 11, 73

Völk, H. J. & Atoyan, A. M. 2000, ApJ 41, 88

von der Linden, A., Allen, M. T., Applegate, D. E., et al. 2014, Monthly Notices of the Royal Astronomical Society 39, 2

Waizmann, J.-C., Ettori, S., & Bartelmann, M. 2013, Monthly Notices of the Royal Astronomical Society 32, 914

Weinstein, A. & for the VERITAS Collaboration. 2009, ArXiv e-prints

Werner, K., Liu, F.-M., & Pierog, T. 2006, Physical Review C: Nuclear Physics 4, 044902

White, N. 2004, Nature 28, 264

Whiteoak, J. B. Z. & Green, A. J. 1996, Astronomy & Astrophysics, Supplement 18, 329

Wijnands, R., Méndez, M., Markwardt, C., et al. 2001, ApJ 60, 892

Wijnands, R., Miller, J. M., & Wang, Q. D. 2002, ApJ 79, 422

Williamson, R., Benson, B. A., High, F. W., et al. 2011, ApJ 38, 139

Winkler, C., Courvoisier, T. J.-L., Di Cocco, G., et al. 2003, Astronomy and Astrophysics 11, L1

Xue, S.-J. & Wu, X.-P. 2002, ApJ 76, 152

Yamamoto, T., Nakahira, S., Kawai, N., et al. 2009, The Astronomer's Telegram, 2297, 1

Yamamoto, T., Sugizaki, M., Mihara, T., et al. 2011, Publications of the Astronomical Society of Japan 3, 751

Yanasak, N. E., Wiedenbeck, M. E., Mewaldt, R. A., et al. 2001, ApJ 63, 768

Yüksel, H., Stanev, T., Kistler, M. D., & Kronberg, P. P. 2012, ApJ 58, 16

Zatsepin, G. T. & Kuz'min, V. A. 1966, Soviet Journal of Experimental and Theoretical Physics Letters, 4, 78

Zayarnaya, I. S. 2008, Physics of Atomic Nuclei, 71, 280

Zeimann, G. R., Stanford, S. A., Brodwin, M., et al. 2013, ApJ 79, 137

Zha, M. 2012, Nucl.Instrum.Meth., A692, 77

Zhuravleva, I., Churazov, E., Kravtsov, A., et al. 2013, Monthly Notices of the Royal Astronomical Society 28, 3274